Coherence and Collisions in Ultracold ^{87}Rb^{133}Cs Molecules

Jacob Andrew Blackmore

This thesis presents work towards the development of a quantum simulator based on ^{87}Rb^{133}Cs molecules using a bulk sample of up to ~ 4000 molecules at temperatures of ~ 1 μK.

We demonstrate coherent control over the molecules' internal state using resonant microwave fields. We test this coherence by performing high resolution Ramsey spectroscopy of the first rotational transition and observing how the contrast of the spectroscopic fringes decay. We are able to affect the coherence of the superposition using an external laser field, as the two component states have a significant differential AC Stark shift. We extend this microwave control by including an additional microwave field, demonstrating the Autler-Townes effect with hyperfine state resolution and transfer between two hyperfine states in $N = 0$.

We study the internal structure of the molecule in the presence of external fields focussing on controlling the differential AC Stark shift between the rotational ground state and the first excited state. We investigate the effect of the off-resonant light on the internal structure in static magnetic and electric fields. In the DC electric field we use two models to describe the molecular structure, demonstrating that at modest values of the electric field the nuclear spin angular momentum is decoupled from the rotational angular momentum of the molecule, this enables us to construct a set of optimum trapping parameters for states with $M_N = 0$.

Through careful measurements of the molecular lifetime we are able to determine that molecular losses are limited by two-body collisions. By introducing a time dependent intensity modulation to our optical trap we are further able to determine that the dominant loss process in bulk samples of ultracold ^{87}Rb^{133}Cs molecules is the laser excitation of collision complexes.

Finally, we investigate the collisional properties of ^{87}Rb^{133}Cs with ^{87}Rb and ^{133}Cs atoms. We find that the loss is caused by single molecule-single atom collisions and sub-universal over a wide range of magnetic fields.

Coherence and Collisions in Ultracold ^{87}Rb^{133}Cs Molecules

Jacob Andrew Blackmore

A thesis submitted in partial fulfilment
of the requirements for the degree of
Doctor of Philosophy

Department of Physics
Durham University

September 2020

Contents

List of Figures

List of Tables

List of Publications

The following publications were completed during the course of this work:

- [1] P. D. Gregory, J. A. Blackmore, J. Aldegunde, J. M. Hutson, and S. L. Cornish, *ac Stark effect in ultracold polar $^{87}Rb^{133}Cs$ molecules*, Physical Review A **96**, 021402(R) (2017)

- [2] J. A. Blackmore, L. Caldwell, P. D. Gregory, E. M. Bridge, R. Sawant, J. Aldegunde, J. Mur-Petit, D. Jaksch, J. M. Hutson, B. E. Sauer, M. R. Tarbutt, and S. L. Cornish, *Ultracold molecules for quantum simulation: rotational coherences in CaF and RbCs*, Quantum Science and Technology **4**, 014010 (2018).

- [3] P. D. Gregory, M. D. Frye, J. A. Blackmore, E. M. Bridge, R. Sawant, J. M. Hutson, and S. L. Cornish, *Sticky collisions of ultracold RbCs molecules*, Nature Communications **10**, 3104 (2019)

- [4] R. Sawant, J. A. Blackmore, P. D. Gregory, J. Mur-Petit, D. Jaksch, J. Aldegunde, J. M. Hutson, M. R. Tarbutt, and S. L. Cornish, *Ultracold polar molecules as qudits*, New Journal of Physics **22**, 013027 (2020).

- [5] P. D. Gregory, J. A. Blackmore, S. L. Bromley, and S. L. Cornish, *Loss of ultracold $^{87}Rb^{133}Cs$ molecules via optical excitation of long-lived two-body collision complexes*, Physical Review Letters **124**, 163402 (2020)

- [6] J. A. Blackmore, R. Sawant, P. D. Gregory, S. L. Bromley, J. Aldegunde, J. M. Hutson and S. L. Cornish, *Controlling the ac Stark effect of RbCs with dc electric and magnetic fields*, Physical Review A *accepted* (2020)

- [7] J. A. Blackmore, P. D. Gregory, S. L. Bromley and S. L. Cornish, *Coherent Manipulation of the Internal State of Ultracold $^{87}Rb^{133}Cs$ Molecules with Multiple Microwave Fields*, Physical Chemistry Chemical Physics *accepted* (2020)

Declaration

I confirm that no part of the material offered has previously been submitted by myself for a degree in this or any other University. Where material has been generated through joint work, the work of others has been indicated.

Jacob Andrew Blackmore

Durham, September 2020

The data and analysis presented within this thesis are available at:
DOI:10.15128/r1sf2685106

This work has been supported by the Engineering and Physical Sciences Research Council.

Acknowledgements

A PhD is rarely easy (for the record I am writing these acknowledgements at home in the middle of the 2020 coronavirus pandemic) and it takes effort from a whole team to complete one. It would be unfair to not celebrate the fantastic people who have helped me through this journey here.

Firstly I would like to thank my supervisor Simon Cornish. I joined Simon's group briefly as a summer student during my undergraduate studies and during that time it seems I was somehow was able to convince him that he should let me work for four years on the RbCs machine. Over the time that I have been his student there have been ups and downs but with his clear guidance and leadership I was able to thrive: hopefully one day I'll remember all of his 5 steps for a measurement!

I would also like to take the time to personally thank the lab's post-doc Phil Gregory, who taught me everything I could dream to know about the machine, how to be a better scientist and crucially when (and when not) to ignore Simon! It has been a pleasure to work with him over the last few years due to his level head, calm demeanour and incisive technical mind. I am sure that he will continue to guide further students and postdocs as he has done for me for many more years. I am also indebted to Liz Bridge, Ana Rakonjac and Rahul Sawant for teaching me about academic life and sharing their skills and talents with me whilst they were in Durham. I also thank the rest of the ever-expanding Cornish group for helping to improve my baking skills.

To all of my fellow QLM[1] students I would like to say thank you for creating such a warm and welcoming atmosphere, the group truly is special and we

[1]It is always AtMol in our hearts

should all be proud of it. In particular I would like to shout-out to my fellow 2016 intake and grad course friends (Mew, Nick, Paul, Lucy and Renju) for being there every step of the way: I am sure that this will not be the last we see of each other. I also thank everyone else who came by to knock on the door to lab 60 over the years, whether that was to borrow optics, steal screws or just to remind me that it was time for the pub!

Speaking of the pub... What kind of student would I be to neglect to mention my second supervisor (and previously my undergraduate advisor) Ifan Hughes? Ifan's refreshing guidance on university life was always well-received and his cheerful attitude never failed to liven my spirits, particularly when sheltering from rainy evenings in the Vic. I am so happy to have known him and look forwards to returning to Durham to keep in touch. You should all buy his books.

Beyond Durham I thank my A-level physics teachers Mr S. Lawrence and Dr J. Theobald, without whom I would never have made it to Durham University and may have never even considered physics research. My family, who have put up with me over the last 8 years of physics also deserve recognition for their unquestioning support, I would not have been able to reach the end without them.

Finally special thanks go to Sam, for putting up with my whinging about the lab. She supported me when I was down and celebrated when I was up. There is no-one else I would have rather had by my side through a PhD and I am excited for where we will both go in the future. All I can say is "thank you".

Chapter 1

Introduction

1.1 Ultracold Atoms and Extending Interactions

Ultracold atomic gases have opened the door to new avenues of research in quantum science and technology. In part this is due to the quantum control that has been developed alongside the continued growth of the field. Two technologies that are of chief interest to us are quantum *computers* and quantum *simulators*. For our purposes we consider quantum computers to be devices that perform an abstract calculation using quantum particles through the application of discrete processes called "gates". A quantum simulator on the other hand uses a tunable quantum apparatus to emulate a complex system that cannot be fully studied numerically. In both of these technologies the key is to have two controlled quantum systems that can "talk" to one another. As such working towards these technologies is often considered a quest for interactions.

The interactions in ultracold neutral atomic gases are typically limited to contact interactions, which only occur on the length scale of collisions. There are two common ways that atomic ensembles are extended to include long-range interactions. The first is to use Rydberg atoms [8, 9], which are neutral atoms excited to very high principal quantum number n, typically these are $n \gg 10$. These states have large *electric* dipole moments, d_e, (on the order

of $10^2 - 10^3$ D) and so have strong interactions, given by

$$V_{\mathrm{dd}}^{\mathrm{elec}} = \frac{d_e^2}{4\pi\epsilon_0 r^3} \times \left(1 - 3\cos^2\theta\right), \tag{1.1}$$

for aligned dipoles. In the above r is the separation between the dipoles and θ is the angle between the dipoles and the line connecting the pair. For Rydbergs $V_{\mathrm{dd}}^{\mathrm{elec}} \sim h \times 10$ MHz at $r = 1$ µm. These states have lifetimes limited by radiative decay which occurs on a timescale $\lesssim 1$ ms. The second solution is to use highly magnetic atoms such as ultracold gases of Er [10], Dy [11] or Cr [12]. These atoms have ground states which have high angular momentum and so a large permanent *magnetic* dipole moment, μ, which gives an interaction between pairs of atoms

$$V_{\mathrm{dd}}^{\mathrm{mag}} = \frac{\mu_0\mu^2}{4\pi r^3} \times \left(1 - 3\cos^2\theta\right). \tag{1.2}$$

For these atoms $V_{\mathrm{dd}}^{\mathrm{mag}} \sim h \times 1$ Hz at 1 µm. However because these atoms possess a dipole moment in the ground state they are not prone to radiative losses and so have much longer lifetimes.

There is a third option though, provided you are willing to leave the world of atoms behind: ultracold heteronuclear molecules. Like Rydberg atoms these molecules have a permanent electric dipole moment, though it is much smaller (~ 1 D) which gives dipole-dipole interactions $V_{\mathrm{dd}} \sim h \times 0.1$ kHz at 1 µm. Like the highly magnetic atoms this dipole moment, in the molecule frame, is present in the molecule's ground state. As there is nowhere for the molecule to decay to, the timescale of experiments is only limited by the typically second-scale collisional lifetime.

Our work focuses on the ^{87}Rb^{133}Cs isotopologue, hereafter referred to as RbCs for simplicity. Our long-term goal is to use these molecules in a quantum simulator to study complex quantum many-body systems. In this work we present proof-of-concept measurements towards building a quantum simulator using RbCs molecules.

1.2 Production of Ultracold Molecules

There are currently two routes to ultracold temperatures for molecules, these are known as the *direct* and *indirect* methods. The direct method of cool-

ing ultracold molecules starts with the goal of taking molecules which are formed in their ground state and cooling them to ultracold temperatures using laser cooling techniques on suitable molecules to form MOTs and tweezer traps. The other method for producing samples of ultracold molecules is to exploit the atomic cooling techniques and then form the molecules from the pre-cooled atomic gases. These techniques are known as "indirect" as the molecules are produced at ultracold temperatures, so do not need further cooling. The two methods that we will consider as indirect are association using a resonant laser (photoassociation) and association on a magnetic Feshbach resonance (magnetoassociation). Both of which (broadly) follow a three step sequence:

1. Cool atomic gases to a high phase-space density.
2. Transfer the atoms into a molecular bound state.
3. Transfer the molecules from their initial state to a desired state adiabatically.

Step (1) can be readily achieved using conventional cooling techniques, they will be built upon an atomic MOT for homonuclear species or dual atomic MOTs for heteronuclear species. Cooling to ultracold temperatures will require additional techniques, the specifics of the cooling in the Durham RbCs experiment will be described in Section 2.1.1.

1.2.1 Direct Laser Cooling

Taking an idea directly from the world of atomic physics where laser cooling has been critical to many modern experiments there are now several groups that have cooled molecular species using laser light. To explain the differences between laser cooling of molecules and the laser cooling of atoms we will briefly revise the principles of laser cooling which are much the same for molecules as for atoms: each photon carries a small amount of momentum related to the optical wavelength (λ) given by: h/λ. Light can therefore be used to exert a small force on objects such as atoms or molecules. When the object absorbs a photon it becomes excited and eventually decays back to

the ground state emitting another photon in the process, this spontaneous emission has no net momentum contribution *i.e.* a photon is emitted into a random direction. Over many cycles this averages out to no net effect on the momentum. For a typical alkali atom the most probable velocity at room temperature is $\sim 200\ \mathrm{m\,s^{-1}}$ (> 400 mph) and reaching $v = 0$ would take $\sim 10^4$ photons, this is typically easy in atoms as they possess closed transitions where following a cycle of absorption and spontaneous emission the atom returns to the state it started in.

Taking the lessons learnt from laser cooling of atomic species DiRosa wrote criteria for a suitable molecule for laser cooling [13]. These are:

1. A short upper state lifetime.
2. A highly diagonal Franck-Condon matrix.
3. No intervening electronic states.

All three criteria are based around finding a way to scatter enough photons to slow the molecules down. Criterion (1) tells us that cooling molecules with laser light requires the use of electronic transitions, as rotational and vibrational transitions have much longer lifetimes (and smaller photon momenta). Criteria (2) and (3) are concerned with ensuring that the optical transition used is suitably closed.

It is finding a molecule that has a sufficiently closed cycling transition which forms a major challenge to laser-cooling molecules. During an electronic transition there is no selection rule on vibration, instead the decays to different vibrational levels are determined by the overlap of the relevant wavefunctions. The Franck-Condon matrix describes this overlap of different electronic and vibrational states, the more diagonal this matrix the more likely the molecule is to conserve the vibrational quantum number in a decay from an electronically excited state. In experiment multiple vibrational repumps are necessary to close the transition further, typically 3 or 4 are used. Intervening electronic states give a molecule additional decay pathways, though the effect can be minimised if the coupling between the excited state and the intermediate is sufficiently small. Unlike the vibrational branching rotational transitions have a strict selection rule associated with them ($\Delta N = 0, \pm 1$).

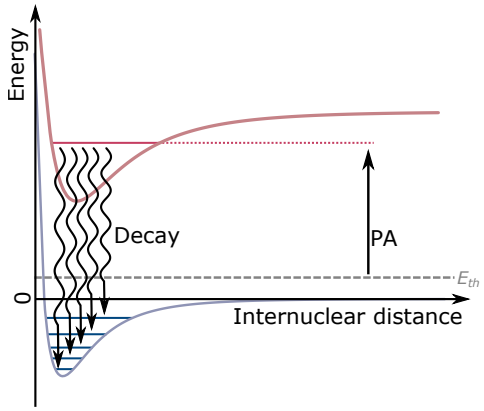

Figure 1.1: Photoassociation of molecules. A laser (PA) is resonant with the transition between a free atom pair of energy E_{th}, shown by the dashed grey line, and an excited molecular bound state $(AB)^*$, the dotted red line. Decays from this excited state possible to multiple levels (solid blue lines) in the ground electronic potential, as governed by the Franck-Condon factors.

Rotational branching can therefore be restricted by cooling on a transition $N = 1 \rightarrow 0$, this however gives more sub-levels in the ground state which adds more complications.

Despite the additional complications that laser cooling molecules directly adds to an experiment there are multiple groups that have created magneto-optical traps (MOTs) of diatomic SrF [14], CaF [15, 16] and YO [17] with cooling demonstrated for SrOH [18], YbF [19], YbOH [20], CaOH [21], $CaOCH_3$ [22] and BaH [23]. There are in addition many groups which are striving to cool more and more molecular species, it is not unreasonable to expect that eventually there will be more molecular species being laser cooled than atomic species.

1.2.2 Photoassociation

Photoassociation spectroscopy has proved to be an important tool in understanding molecular potentials [24, 25] as well as promising additional uses including in precision metrology [26, 27]. The use we will be considering in this section is the creation of ground state molecules from an ultracold atomic gas, though the principle is the same for spectroscopy.

In one-photon photoassocation two atoms, which we shall label A and B, which are colliding with an incident thermal energy E_{th} can be excited by a resonant laser, labelled PA in figure 1.1. This laser takes the atoms to an excited state of the molecular potential: labelled $(AB)^*$. The energy required for this process is less than that required to excite either atom to their own excited states. This excited state has a finite lifetime as such some time after the pair is excited to $(AB)^*$ it then decays to the ground electronic state of the molecule.

Using single-photon photoassociation for the formation of ground state molecules has several limitations. The first is that, for photoassociation rates to be useful, the molecular bound state $(AB)^*$ must have a significant overlap with the atomic continuum: this is only true for high lying vibrational states. The likely decays are therefore from a high vibrational state in an excited potential to high vibrational states in the ground potential, though there are some exceptions where decay to low vibrational numbers is possible [28–32]. The other issue that affects one-photon photoassociation is that the process is incoherent, molecules cannot be coherently broken apart in the same way that the Feshbach molecules discussed in Section 1.2.3 can be, this limits the imaging techniques that can be used to either ionisation and detection on a suitable detector [28, 33] or photodissociation and absorption imaging [34]. Finally because the population of the ground state is through spontaneous decays of the excited states not only are different vibrational states populated but different rotational and hyperfine states can be as well, though rotational pure samples have been created in some species such as ^{85}Rb^{133}Cs [35].

1.2.3 Magnetoassociation

Arguably the most successful route to ultracold molecules has been magnetoassociation on a magnetic Feshbach resonance [36, 37]. Molecules of KRb [38], Cs_2 [39], Rb_2 [40], RbCs [41, 42], NaK [43], NaRb [44], NaLi [45] and NaCs [46] have been formed this way. It is worth highlighting that there are two methods commonly referred to as magnetoassociation in the literature. One method involves using a resonant RF field with the magnetic bias field held close to an interspecies Feshbach resonance. The other method, and

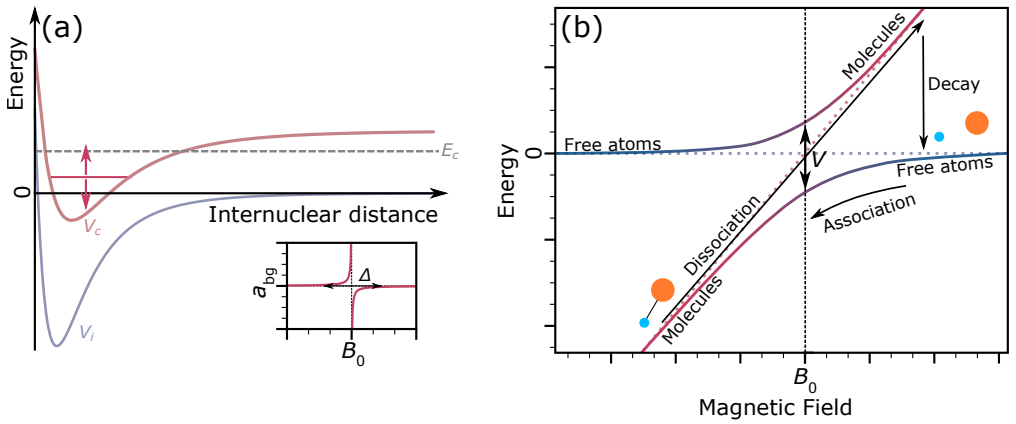

Figure 1.2: Magnetoassociation on a magnetic Feshbach resonance. (a) Two atoms, colliding with energy E_c, on the open incoming channel (V_i) can couple to a bound state in the closed channel V_c. At ultracold temperatures the incoming energy tends to the incoming channel threshold ($E = 0$). The position of the bound state can be tuned with respect to this threshold using a magnetic field, as described in the text. Inset is shown the variation of the scattering length near the Feshbach resonance. (b) A simplified energy level scheme for magneto association, relative to the energy of free atoms. The solid lines show the avoided crossing used for association. The dotted lines indicate the magnetic field dependence of free atoms (blue) and molecules (red) if the two states were not coupled.

the one that we will describe, involves adiabatically sweeping the magnetic field across an interspecies Feshbach resonance. Following magnetoassociation the molecules are in a high lying vibrational level, but only a single rotational and hyperfine state. Transfer between different molecular states is therefore much easier than when considering photoassociation. Typically transfer from the weakly bound state to a more tightly bound one is accomplished with stimulated Raman adiabatic passage (STIRAP), which will be covered in section 2.1.3.

A magnetic Feshbach resonance is the result of a molecular bound state and a free atomic state being degenerate in energy. Because the molecular state and the atomic state have a different magnetic moment an external magnetic field can be used to tune its position with respect to the free atoms. This is illustrated in figure 1.2(a), the atoms are initially on the incoming channel labelled V_i with energy E_c which at ultracold temperatures tends towards the incoming channel threshold ($E = 0$). Inset to the figure is an illustration of the scattering length (a) as a function of magnetic field (B) around the

Feshbach resonance which follows

$$a(B) = a_{\text{bg}} \left(1 - \frac{\Delta}{B - B_{\text{res}}}\right). \tag{1.3}$$

Where B_{res} is the centre of the resonance, a_{bg} is the scattering length in the absence of any resonances and Δ defines the width of the resonance. Control of the scattering length around a magnetic Feshbach resonance has been critical to the formation of BECs of ^{85}Rb and ^{133}Cs as well as novel states of matter such as quantum droplets [47, 48], dipolar supersolids [49–51], bright solitary matter-waves [52] and perhaps most notably observation of the BEC-BCS crossover in Fermi gases [53, 54].

Molecules can be formed on a Feshbach resonance by exploiting that, because of a coupling between the molecular bound state and the atomic state, the resonance doesn't cause the energy levels to cross. Instead an avoided crossing, as shown in figure 1.2(b) opens up. Starting with the magnetic field above the resonance and then ramping it down adiabatically ensures that the atom pair follows the energy level into the bound molecular state. The critical ramp speed, below which the following is adiabatic, can be arrived at by considering the avoided crossing in a Landau-Zener model

$$\left.\frac{\mathrm{d}B}{\mathrm{d}t}\right|_{\text{crit}} = \frac{V^2}{h|\Delta\mu|}. \tag{1.4}$$

In the above V is the energy difference between the two energy levels at the position of the resonance, as shown in figure 1.2(b) and $\Delta\mu$ is the differential magnetic moment between the two states. The process can be reversed by crossing back over the resonance: from low field to high. However it is not necessary to follow this adiabatically, if the crossing speed is too quick the atoms will remain bound together as a molecule but they will eventually dissosciate back into the free atomic state which is more energetically favourable.

1.3 Applications of Ultracold Molecules

Ultracold atoms have been used across many applications including, but not limited to: precision measurement of time [55] and external fields [56, 57];

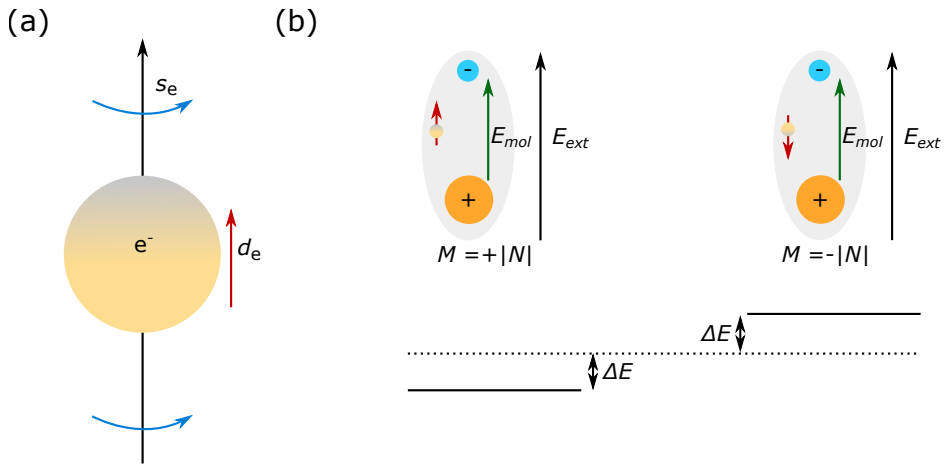

Figure 1.3: Measurement of an electronic EDM using an ultracold polar molecule. (a) An electron with a charge distribution along the spin axis has a dipole moment d_e along the same axis. (b) Illustration of the scheme typical for a measurement of the eEDM. When all other interactions are accounted for the eEDM gives a small shift to a state: ΔE. This is maximal when it is aligned or anti-aligned to the internal electric field of the molecule E_{mol}. By measuring the energy difference between the $+|N|$ and $-|N|$ states the value of d_e can be constrained.

quantum simulation [58, 59]; and quantum computation [60]. We must ask ourselves, why should we go to the effort of working on ultracold molecules? In this section we will approach this question and summarise four places where ultracold molecules are either at the forefront of quantum science or have additional strengths over ultracold atoms.

1.3.1 High precision measurement of fundamental constants

One arena in which cold and ultracold molecules have found themselves to be uniquely suited is the precision study of fundamental constants. Measurements have been made on the variation of the fine-structure constant (α) [61], tests of the electron-to-proton mass ratio (μ) [62] and (perhaps most notably) a search for a non-zero electronic electric dipole moment (eEDM). In this third endeavour the leading groups currently use YbF [63] and ThO [64] though there are proposals to use BaF [65] as well as more exotic polyatom-

ics. It is important to note that current experiments have not used *ultra*cold molecules, instead using molecules that have been slowed. Great effort is being put into using truly ultracold molecules to extend the measurement time, thereby also increasing the precision even further.

The search for an eEDM has proved to be incredibly important to fundamental physics research. Several extensions to the standard model introduce additional time symmetry violations which ultimately lead to a potentially measurable dipole moment. An illustration of the principle behind an eEDM measurement is shown in figure 1.3(b). In short an electric field is used to polarise the molecules, within the molecule an electric field is generated as it is polarised, E_{mol}. Depending on the state that the molecules are in the electronic dipole moment will be either aligned or anti-aligned to the molecule's internal field. This leads to an energy shift of the form

$$\Delta E = \mathbf{d}_{\text{e}} \cdot \mathbf{E}_{\text{mol}}. \tag{1.5}$$

The value of ΔE can be measured by using high-resolution spectroscopic probes of the internal molecular structure. By comparison to a suitable "spectator" state to account for the systematic shifts the value of d_e can be obtained [63, 64].

1.3.2 Molecular Qubits

Currently there are many different architectures that are being considered for qubits. The leading architecture currently is the superconducting circuit as chosen by traditional computing giants like Google [66], Intel [67] and IBM [68]. Other architectures have been considered with their own strengths and weaknesses, trapped ions for instance are the leaders in gate fidelity [69]. In 2001 DeMille proposed using ultracold polar molecules as qubits [70]. The essence of the proposal is that molecules are trapped in a periodic potential formed by a standing-wave optical trap. An electric field which varies along the length of the trap is used to make each of the qubits spectroscopically addressable, with the qubit states identified with the ground and first excited states. In the last two decades there have been many advancements in the field of quantum technology. In this section we will be briefly outlining two

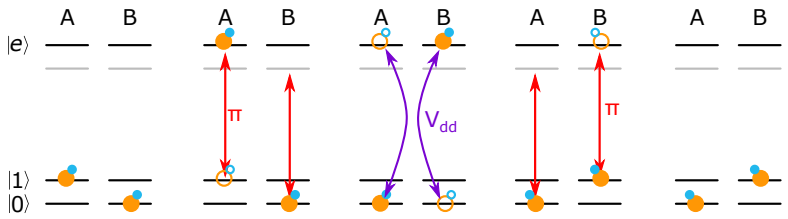

Figure 1.4: The iSWAP gate of [71]. Molecule A is initially in $|1\rangle$ and molecule B is in $|0\rangle$ both in the rotational ground state. A microwave π-pulse drives A to $|e\rangle$ but not B. The dipole-dipole interaction (V_{dd}) allows the excitation to hop between A and B. A second microwave pulse drives B from $|e\rangle$ to $|1\rangle$ completing the SWAP operation.

new proposals for molecular quantum gates: a key element necessary to using ultracold molecules as qubits.

In [71] Ni *et al.* proposed an implementation of an iSWAP gate that would be suitable for $^1\Sigma$ states. The iSWAP gate takes a pair of molecules in the product state $|0\rangle\,|1\rangle$ and transfers the excitation such that the output is $|1\rangle\,|0\rangle$ or vice-versa. Along with single qubit rotations their iSWAP gate forms a universal set, meaning that any quantum computation can be solved. In this implementation a collection of ultracold molecules are held in moveable tweezer traps and the qubit states $|0\rangle$ and $|1\rangle$ are two hyperfine states in the rotational ground state. In this formulation there is a need for a third, intermediate state $|e\rangle$ which is in the first rotational excited state. Crucially $|e\rangle$ has to have a transition dipole moment connecting to both $|1\rangle$ and $|0\rangle$, this is possible through hyperfine mixing in an applied magnetic field. The mechanism by which this gate is implemented is remarkably simple: a microwave π-pulse on the $|1\rangle \rightarrow |e\rangle$ transition; the two molecules in the gate are then able to interact for a time $t_{\mathrm{gate}} = (\pi r^3)/(2D)$ where r is the distance between the molecules and D is a dipole-dipole interaction strength[1]; following the interaction a second π-pulse drives the transition $|e\rangle \rightarrow |1\rangle$. This scheme is illustrated in figure 1.4(a). To protect the state of the other molecules off-resonant light could be used to AC-Stark shift them from resonance with the microwave field.

An alternative gate implementation which does not require an additional ex-

[1]This will depend on the species, the states used and the orientation of the two molecules.

cited state was proposed by Hughes *et al.* [72]. Their entanglement gate does not perform the SWAP operation, instead the ideal operation is represented in the computational basis ($|1\rangle|1\rangle, |1\rangle|0\rangle, |0\rangle|1\rangle, |0\rangle|0\rangle$) by

$$T = \begin{pmatrix} 1 & 0 & 0 & 0 \\ 0 & \frac{e^{i\phi}}{2} & -\frac{e^{i\phi}}{2} & -\frac{1}{\sqrt{2}} \\ 0 & -\frac{e^{i\phi}}{2} & \frac{e^{i\phi}}{2} & -\frac{1}{\sqrt{2}} \\ 0 & \frac{1}{\sqrt{2}} & \frac{1}{\sqrt{2}} & 0 \end{pmatrix}, \tag{1.6}$$

where ϕ is a controllable phase shift. In this implementation the state $|0\rangle$ is in the rotational ground state and $|1\rangle$ is in the excited state. Despite not being an easily identifiable logic gate this operation, along with one-qubit controls, forms a universal gate set [73]. The basic principle of the gate presented transfers a pair of ground state molecules to the Bell state $|\Psi_+\rangle = (|0\rangle|1\rangle + |1\rangle|0\rangle)/\sqrt{2}$. The transfer is accomplished by holding two molecules close enough together that the dipole-dipole interaction becomes significant enough to split the degeneracy between $|\Psi_+\rangle, |1\rangle|1\rangle$ and $|0\rangle|0\rangle$. A shaped microwave pulse, with a fixed detuning, is then able to reproduce equation (1.6) with fidelity > 0.999.

1.3.3 Molecular Qudits

This section summarises the results in Sawant *et al.* [4].

One of the challenges that is associated with the production of a quantum computer under the 2-level qubit paradigm is that of scalability [74]. In short: producing enough individual qubits that can be externally controlled and together form a Hilbert space large enough to perform a useful calculation without interference from the environment is extremely challenging. We can ease the problem of scalability by not restricting ourselves to two-level systems and instead utilising d-level qudits.

Quantum computers are often only considered to be useful when they are able to perform calculations beyond even the most powerful classical computers[2]. Typically this point is expected to be reached for about 50 two-level qubits,

[2]In the literature this is often termed "quantum supremacy", though there is some debate about the appropriateness of the term [75].

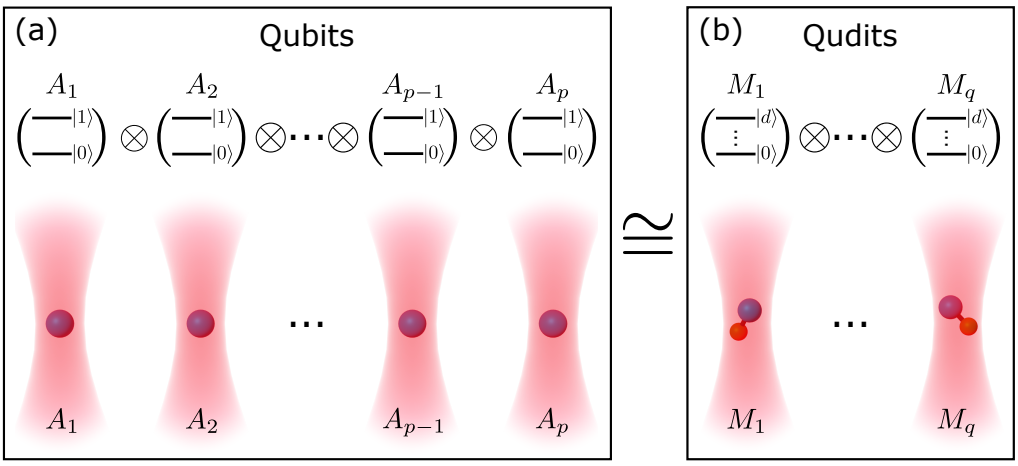

Figure 1.5: A comparison of qubits and qudits in optical tweezer arrays. (a) Using p traditional two-level atomic qubits to form a Hilbert space of dimension 2^p. (b) Using d internal levels of q molecules forms a Hilbert space of d^q. To create a space of the same dimension as in (a) requires $q = p/\log_2(d)$. Clearly for $d > 2$ fewer quantum elements are required for qudits than for qubits.

with a team from Google AI Quantum recently demonstrating a significant quantum advantage for $p = 53$ [66]. If we were to use a quantum system of dimension d then only $\sim 50/\log_2(d)$ qudits would be required, which is approximately 15 for $d = 10$. This scaling law is illustrated in figure 1.5, where the qubits' state-space is represented by the products of several two-level atoms whilst the qudits' state-space requires fewer d-level molecules.

Molecules provide an interesting system to consider producing qudits in, as alongside the hyperfine and electronic degrees-of-freedom possessed by atoms they also have rotation and vibration. The rotational and hyperfine degrees-of-freedom in ultracold molecules are readily controlled using microwaves[3]. By analysing the internal structure of RbCs we were able to find states to form $d = 8$ qudits in the rotational ground state, with a gate time of 1 ms. The qudit is formed by multiple levels in the rotational ground state, and gates are formed by microwave operations between the rotational ground state and the first excited state. An alternative formulation, with the same gate time, would enable us to form a qudit with d up to 21, a single qudit therefore would have equal computational power to 4 qubits. In practice however these excited states are more prone to dephasing due to differential

[3]See Chapter 4 for details of the microwave control in the Durham RbCs experiment.

AC Stark shifts in optical traps.

1.3.4 Quantum Simulation

The motivation for using molecules for quantum simulation stems from the ability to engineer controllable long-range interactions between spins via the electric dipole-dipole interaction between molecules i and j

$$V_{ij}^{\mathrm{DD}} = \frac{1}{4\pi\epsilon_0}\frac{\boldsymbol{d}_i \cdot \boldsymbol{d}_j - (\boldsymbol{d}_i \cdot \hat{\boldsymbol{e}}_{ij})(\boldsymbol{d}_j \cdot \hat{\boldsymbol{e}}_{ij})}{r_{ij}^3}\,. \tag{1.7}$$

Here molecule i has electric dipole moment $\boldsymbol{d}_i$ and position vector $\boldsymbol{r}_i$; $\boldsymbol{r}_{ij} = \boldsymbol{r}_i - \boldsymbol{r}_j = r_{ij}\hat{\boldsymbol{e}}_{ij}$. This form differs from equation (1.2) as we have not assumed that the dipole moments are aligned. Typical achievable dipole moments are ~ 1 D, leading to a dipole-dipole interaction energy $\sim h \times 1$ kHz between neighbouring molecules spaced by 532 nm in an optical lattice ($\lambda = 1064$ nm).

There are two limits that are relevant for experiments on quantum simulation with ultracold molecules. The first is the weak lattice limit: here the molecules can tunnel between neighbouring sites and so there is an on-site interaction and a dc electric field aligns the permanent dipole moments of the molecules. The many-body physics of this system is captured in the extended Bose-Hubbard model [76, 77]

$$H_{\mathrm{BH}} = -T\sum_{\langle i,j\rangle} b_i^\dagger b_j + \frac{V}{2}\sum_{i\neq j}\frac{n_i n_j}{r_{ij}^3} - \mu\sum_i n_i. \tag{1.8}$$

The first term in this many-body Hamiltonian describes the kinetic energy, with hopping amplitude T and bosonic creation/annihilation operators for site i are $b_i^\dagger/b_i$. The second-term is the repulsive dipole-dipole interaction with strength $V = d^2/a^3$ where a is the lattice spacing and $r_{ij} = |\boldsymbol{r}_i - \boldsymbol{r}_j|$ for the normalised lattice vectors $\boldsymbol{r}$. The final term includes the chemical potential μ and the number operator for site i,n_i. Theoretical studies [76, 77] of this system show the emergence of superfluid, supersolid and Mott solids of varying fractional density. These varied phases of matter can be studied by tuning the lattice depth (and thereby the tunnelling rate) or the strength of the dipole-dipole interaction.

The other limit is the "tight binding" limit, here the lattice depth is sufficiently high that molecules cannot tunnel to neighbouring sites. It is then

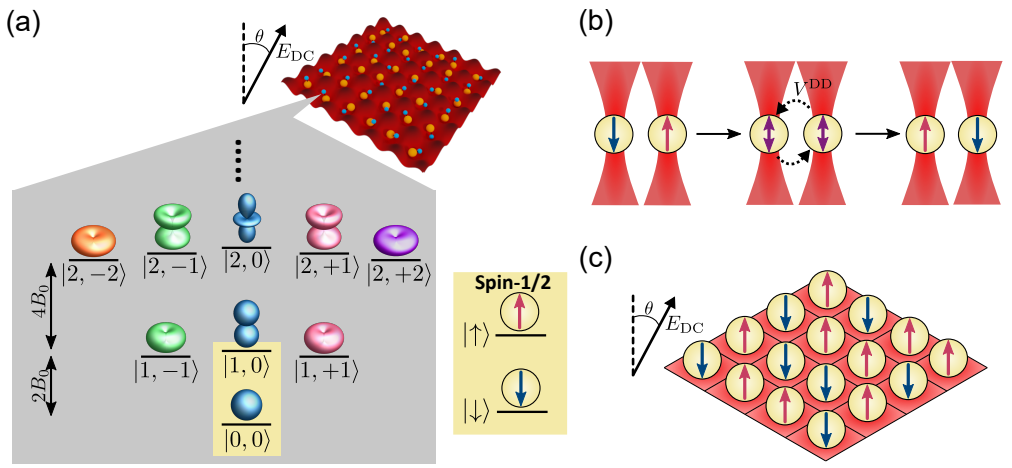

Figure 1.6: Using polar molecules for quantum simulation. (a) Pseudo-spins can be encoded in the internal rotational states of molecules (blue-orange dumbbells) confined in regular arrays. In this example, we map the two spin states $\uparrow, \downarrow$ onto the rotational states $|N = 0, M_N = 0\rangle$ and $|1, 0\rangle$. The energy separation between these states is set by the rotational constant B_0 and lies in the microwave domain. (b) Dipole-dipole interactions (V^{DD}) lead to spin-exchange (or spin flip-flop) interactions between adjacent molecules, here shown confined in individual tightly-focussed optical tweezers. (c) In a deep optical lattice, the molecules can be used to simulate models of quantum magnetism, such as the XXZ model described in the text. The applied static electric field can be used to tune the model parameters.

possible to encode pseudo-spins in the molecular rotational states in order to realise various models of quantum magnetism. For example, in the proposal by Barnett *et al.* [78] they mapped $|\downarrow\rangle$ with the ground state ($N = 0, M_N = 0$) of a $^1\Sigma$ potential. The excited state $|\uparrow\rangle$ is mapped to any of the states with $N = 1$. In figure 1.6(a) we identify $|\uparrow\rangle$ with $|1, 0\rangle$ and $|\downarrow\rangle$ with $|0, 0\rangle$ to also demonstrate a spin-1/2 system. The resonant dipole-dipole interaction between these pseudo-spin states leads to two-body "flip-flop" or spin-exchange interactions, shown in figure 1.6(b) for tweezer-confined molecules. For a collection of molecules pinned to the sites of a two-dimensional (2D) lattice this two-body interaction leads to the well-known XXZ spin Hamiltonian [79, 80]

$$H_{\mathrm{XXZ}} = \sum_{i \neq j} \left[\frac{J_X}{2} \left(S_i^+ S_j^- + S_i^- S_j^+ \right) + J_Z S_i^z S_j^z \right]. \tag{1.9}$$

In this Hamiltonian the first term describes the spin-exchange interaction,

the second term describes the the two coupling constants are given by

$$J_X = \frac{1 - 3\cos^2\theta_{ij}}{4\pi\epsilon_0 r_{ij}^3} d_{\uparrow\downarrow}^2, \tag{1.10a}$$

$$J_Z = \frac{1 - 3\cos^2\theta_{ij}}{4\pi\epsilon_0 r_{ij}^3} \left(d_{\uparrow\uparrow} - d_{\downarrow\downarrow}\right), \tag{1.10b}$$

with $d_{s_i s_j} = |\langle s_i| \boldsymbol{d} |s_j\rangle|$ for $|s\rangle \in \{|\uparrow\rangle, |\downarrow\rangle\}$ and θ_{ij} the angle between the molecular dipole moments and the intermolecular vector [79–81]. By controlling the angle of the applied electric field these two parameters can be tuned for performing simulations of different many-body systems.

1.4 Thesis Overview

This thesis is structured as follows:

In Chapter 2 we detail the key pieces of experimental apparatus used to create our samples of ultracold polar molecules. We pay particular attention to the microwave and electric field apparatus which are key to our control of the rotational state of the molecule.

Chapter 3 covers the physics of molecular structure in great detail. We start by determining the behaviour of a rigid rotor in AC and DC electric fields, examining the pendular states of the molecule. We then construct a Hamiltonian that includes the hyperfine structure in a completely uncoupled basis. We end the chapter by presenting theoretical calculations for RbCs in AC and DC electric fields as well as in static magnetic fields.

In Chapter 4 we demonstrate coherent control over the internal state of the molecule using resonant one and two-photon microwave pulses. We demonstrate Ramsey interferometry with high contrast and no loss of coherence over the ~ 3 ms we can observe the molecules for. To extend our investigation we apply a beam from the optical dipole trap to the molecule cloud and observe that the coherence is lost rapidly. With a comparison to a theoretical calculation of the AC Stark shift we find some regions where we can extend this coherence to a $1/e$ time of 0.7 ms. We conclude with an outlook that extends our two-photon work to performing quantum simulations of the SSH model in synthetic dimensions.

Chapter 5 contains an exploration of the internal structure of the molecule in laser fields at $\lambda = 1550$ nm and at $\lambda = 1064$ nm where we characterise the polarisability and compare to theoretical predictions. We additionally find an unexpected two-photon transition within the molecule at $\lambda \approx 1064.5$ nm. We conclude by exploring the limits of the "magic angle" formulation by exploring the polarisation dependence of the AC Stark shift in applied DC electric and magnetic fields.

In Chapter 6 we explore the collisional properties of the RbCs molecule in detail. We start by establishing that the kinetics are second-order indicating that the rate-limiting step involves two molecules which we attribute to the

formation of collision complexes. We compare our results to a single channel model inspired by quantum defect theory which indicates that only approximately two-thirds of the molecules that reach short range are lost. Using an intensity modulated trap we are able to measure the lifetime and excitation rate of the complexes formed, which both agree with the theoretical prediction that optical excitation limits the lifetime of the molecule. We conclude this chapter by exploring the collisional behaviour of RbCs in mixtures with Rb and Cs atoms at fields near 20 G and near 181.5 G, we find no evidence of resonant behaviour and losses in both mixtures are approximately a factor of 5 below the zero-temperature universal limit.

Chapter 2

Experimental Apparatus

The RbCs apparatus in Durham is the result of well over a decade of development and work by a multitude of students and postdocs [82–88]. Within this work very little has been done to change the experiment on a hardware level as it still stands as a cutting edge apparatus. This is the advantage of a Ph.D. in a well established laboratory. However there are some limitations related to how the experiment has developed which are worth considering. In this chapter we will discuss some of the details relating to the experimental hardware used to perform the experiments presented in this thesis. We will start with a description of the methods we use to produce the RbCs molecules. We will then describe the vacuum system, the apparatus for magnetic fields and the systems used for generating electric fields and for removing the residual charge build-up between experimental cycles. Finally we will conclude by describing our microwave equipment and, using finite element method calculations, determine how well polarised they are.

2.1 How to make RbCs

RbCs, as a bialkali, is an example of an associated molecule. In this section we will briefly cover the three steps needed to produce a sample using our apparatus.

2.1.1 Atomic Mixture

The Durham RbCs apparatus uses a two chamber design. The first is a pyramid MOT which acts as a source for the ^{87}Rb and ^{133}Cs gases. The initial samples are sourced from pairs of alkali metal dispensers which are mounted on opposing edges of the pyramid MOT chamber. From the pyramid, atoms are transferred via an imbalance in the trapping beams into an ultra-high vacuum glass cell (the "science cell") where we produce two conventional 6-beam MOTs. The clouds are separated to minimise interspecies collisions by an additional push beam, which displaces the ^{87}Rb MOT centre. A brief compressed MOT phase is used to overlap the traps for both species and match the geometry of the MOT to the magnetic trap. We use both sets of lasers to perform polarisation-gradient cooling in optical molasses to reach sub-Doppler temperatures. Both species are then optically pumped into low-field seeking states ($f_{\mathrm{Rb}} = 1, m_{\mathrm{Rb}} = -1$), ($f_{\mathrm{Cs}} = 3, m_{\mathrm{Cs}} = -3$) before loading into the magnetic quadrupole trap.

Additional cooling in the magnetic trap is achieved by forced RF evaporation of the Rb atoms which sympathetically cools the Cs through interspecies collisions[85, 86]. Both species are then loaded into the crossed 1550 nm dipole trap. The atoms are transferred into the high-field seeking states of their respective hyperfine manifolds ($f_{\mathrm{Rb}} = 1, m_{\mathrm{Rb}} = +1, f_{\mathrm{Cs}} = 3, m_{\mathrm{Cs}} = +3$). We achieve this by moving the zero of the magnetic quadrupole field over the atomic cloud whilst coupling the lowest and highest magnetic sublevels with RF radiation, transferring the atoms using rapid adiabatic passage. Following this stage the quadrupole field and the 20 G magnetic bias field add in such a way to form a uniform field gradient pointing upwards, we choose the strength and direction of this field gradient ($\sim 30\ \mathrm{G\,cm^{-1}}$) to levitate both species against gravity.

By reducing the intensity of the trapping light further we can allow the most energetic atoms to escape, evaporatively cooling our mixture. Because of the difference in polarisablity the ^{133}Cs atoms "see" a deeper potential from the optical dipole trap throughout, which is well suited to continued sympathetic cooling by the ^{87}Rb. Previously this cooling sequence was used to bring both species to BEC [89]. Practically a doubly-degenerate mixture is not useful for

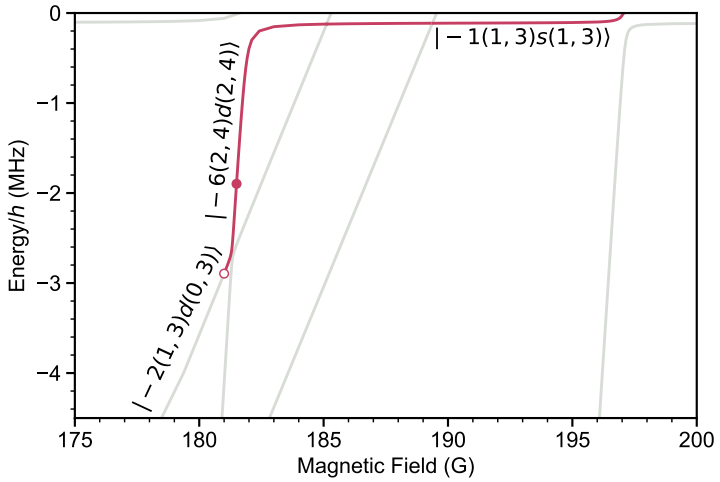

Figure 2.1: The relevant Feshbach states for magnetoassociation. The states are labelled by $|n(f_{\mathrm{Rb}}, f_{\mathrm{Cs}})L(m_{\mathrm{Rb}}, m_{\mathrm{Cs}})\rangle$, as described in the text. The magnetic field where Stern-Gerlach separation is used to separate the atomic and molecular clouds is marked by the unfilled point. The magnetic field at which STIRAP is performed is marked by the filled point.

production of molecules as the large interspecies scattering length makes the two clouds immiscible and prevents efficient magneto-association. Following this process we have a mixture of ^{87}Rb and ^{133}Cs atoms at a phase-space density of approximately 0.1 and a temperature of ~ 300 nK.

2.1.2 Magneto-association

As discussed in Section 1.2.3, when a free atomic state meets a bound molecular state at a Feshbach resonance there is an avoided crossing. By ramping the magnetic field over this resonance adiabatically we can take pairs of atoms with quantum numbers f_i and m_i, for i = Rb,Cs, and associate them into molecules in a single quantum state [90]. We label these states as $|n(f_{\mathrm{Rb}}, f_{\mathrm{Cs}}), L(m_{\mathrm{Rb}}, m_{\mathrm{Cs}})\rangle$. The quantum numbers to label the molecular state are L which is the quantum number for end-over-end rotation of the molecule, represented by a letter $s, p, d, f...$ for $0, 1, 2, 3...$; and n which is the vibrational number counting down from the least bound state: $n = -1$. Each of the Feshbach states has a total angular momentum projection $M = m_{\mathrm{Rb}} + m_{\mathrm{Cs}} + M_L = 4$.

We start the association process with the magnetic field held above the two lowest interspecies Feshbach resonances at ~ 212 G, two magnetic field ramps are necessary to form molecules in the desired state. The initial 250 $\mathrm{G\,s^{-1}}$ magnetic field ramp crosses a Feshbach resonance at $\sim$197 G which forms molecules in a weakly bound state, which runs nearly parallel to the free atomic energy as shown in figure 2.1. A second ramp across an avoided crossing at $\sim$ 182 G transfers the molecules into $|-2(1,3), d(0,3)\rangle$ via the $|-6(2,4)d(2,4)\rangle$ state. To remove the remaining atoms we exploit that, in this Feshbach state, the molecules and atoms have very different magnetic moment to mass ratios. We increase the magnetic field gradient such that the molecules are exactly levitated. This over levitates the atoms and throws them out of the top of the trap, we name this part of the experiment the "Stern-Gerlach separation".

The ground state of the molecule has no appreciable magnetic moment and so we must transfer the molecules to a pure optical potential, we do this before the STIRAP transfer. The 1550 nm optical dipole trap is increased in intensity over 20 ms, this adiabatic compression raises the temperature of the sample as the trap frequency increases with the square-root of intensity, the final temperature of the molecules is ~ 1 μK. Crucially however the phase-space density of the sample is preserved through this compression. Finally, to prepare for the STIRAP transfer, the magnetic field is ramped again so that the Feshbach molecules are in the state $|-6(2,4)d(2,4)\rangle$. The overall efficiency of this process is such that from clouds of $\sim 10^5$ atoms about 5000 Feshbach molecules will be produced.

2.1.3 STIRAP

The final stage in the ground state molecule production sequence is stimulated Raman adiabatic passage (STIRAP) from the weakly bound Feshbach state to the rovibronic ground state. The system consists of two lasers labelled "Pump" and "Stokes". The Pump laser drives transitions between the Feshbach state, $|F\rangle = |-6(2,4), d(2,4)\rangle$ and an excited state: $|E\rangle = |b^3\Pi_1, v = 29, J = 1, M = 4\rangle$. $|E\rangle$ is chosen due to its strong coupling to both an accessible Feshbach state and to the ground state $|G\rangle =$

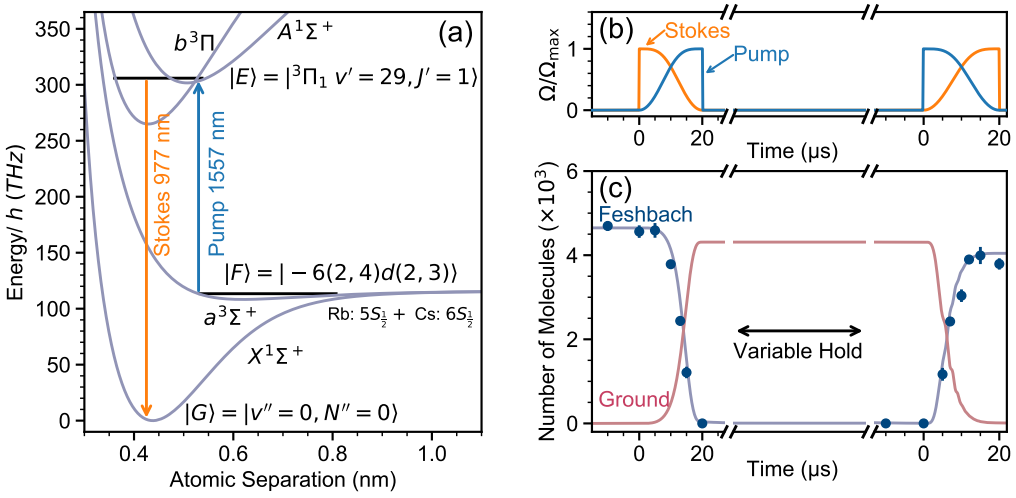

Figure 2.2: The STIRAP sequence used in the RbCs experiment. (a) Relevant potentials for STIRAP, reproduced from [91]. Spin-orbit coupling is not included. (b) The pulse sequence used, the time axis is shared with (c). (c) Molecule transfer from the Feshbach state with $n = -6$ to the ground state. Only molecules in the Feshbach state can be dissociated and imaged. Data is reproduced from [92].

$|X^1\Sigma^+, v = 0, N = 0, M_F = +5\rangle$. The Stokes laser drives the second leg of the two-photon transition from $|E\rangle \rightarrow |G\rangle$. We show the levels involved in figure 2.2(a). It should be highlighted that although the Feshbach state is a high energy level of the $a^3\Sigma$ potential, transfer to the $X^1\Sigma$ ground state is possible because, due to spin-orbit coupling, the $b^3\Pi$ excited state has significant singlet character.

To describe the STIRAP process we first consider an ideal three-level system. In the basis $\{|F\rangle, |E\rangle, |G\rangle\}$ the Hamiltonian is[1]

$$H_{3-\text{level}} = \hbar \begin{pmatrix} 0 & \Omega_P/2 & 0 \\ \Omega_P/2 & \Delta_P & \Omega_S/2 \\ 0 & \Omega_S/2 & \Delta_P - \Delta_S \end{pmatrix}, \tag{2.1}$$

where subscript "P" refers to the Pump laser and "S" to the Stokes laser. When the three level system is on two-photon resonance, *i.e.* $\Delta_P - \Delta_S = 0$ the three level Hamiltonian has an eigenstate $|a\rangle$ that has no $|E\rangle$ component

$$|a\rangle = \cos(\theta_{mix})|F\rangle - \sin(\theta_{mix})|G\rangle, \tag{2.2}$$

[1] A diagram of the Λ energy level scheme can be found in figure 4.8.

where θ_{mix} is the "mixing angle" and is defined with respect to the Rabi frequencies Ω_{P}, Ω_{S} as

$$\tan\left(\theta_{\text{mix}}\right) = \frac{\Omega_{\text{P}}}{\Omega_{\text{S}}}. \tag{2.3}$$

Thus as Ω_{P} becomes zero whilst $\Omega_{\text{S}} \neq 0$ the state $|a\rangle$ becomes entirely $|F\rangle$, similarly when $\Omega_{\text{S}} \to 0$ then $|a\rangle \to |G\rangle$. In the idealised system there is no loss of molecules to state $|E\rangle$, however in the experiment this is limited by the adiabaticity of the transfer. The conditions for efficient transfer are [92]

$$\frac{\tilde{\Omega}^2}{\pi^2\gamma} \gg \frac{1}{\tau} \gg D, \tag{2.4}$$

in this expression γ is the natural linewidth of the excited state, D is the linewidth associated with the frequency difference between the lasers, $\tilde{\Omega}^2 = \Omega_{\text{P}}^2 + \Omega_{\text{S}}^2$ and τ is the transfer time. The two limits on our hardware and control are therefore, the transfer must be slower than the rate $\tilde{\Omega}^2/\gamma$ and faster than D. The first is achieved by using states with high transition strengths as available laser power is typically a practical limit. The second criterion is met by using lasers with narrow linewidths, we estimate that our STIRAP lasers have a linewidth of $\lesssim 1$ kHz, details of the apparatus can be found in Gregory *et al.* [93].

The pulse sequence that we use for ground state transfer follows two sinusoids and is shown in figure 2.2(b), with the current hardware this transfer process takes ≈ 20 μs. During this time the optical trap is switched off to remove spatially-varying AC Stark shifts [94]. Using this sequence we achieve a maximum transfer efficiency of 92(1)% [92]. The STIRAP process completes the formation of the RbCs sample, however we have no current means to directly detect the molecules as there are no closed transitions suitable for absorption or fluorescence imaging. Currently to image our molecular clouds we reverse the STIRAP process and dissociate the molecules back into atoms. We then take in-situ absorption images of both clouds and average the number of atoms within each to determine our molecule numbers. This process is hyperfine state selective, molecules in states other than $|G\rangle$ are unable to undergo the reverse process and so are not imaged.

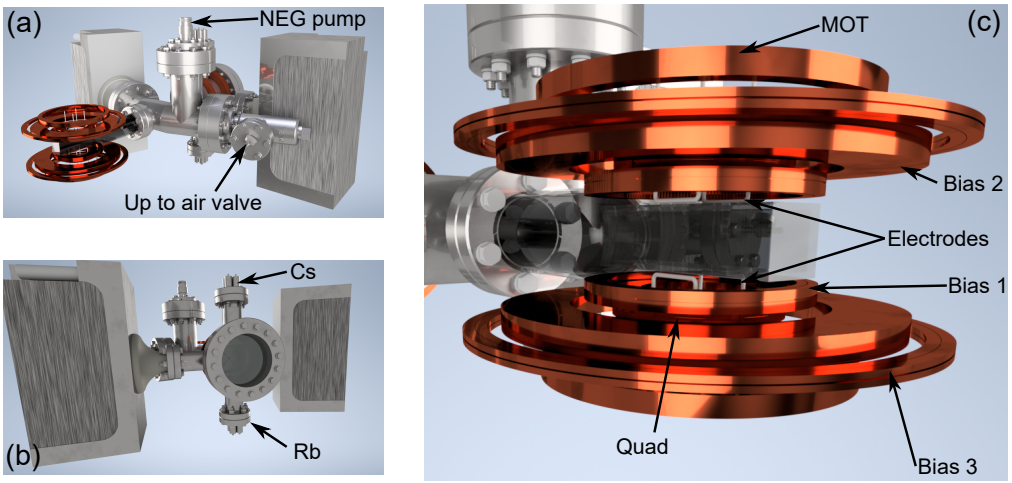

Figure 2.3: Rendered CAD models of the vacuum apparatus used in the RbCs experiment. (a) View of the science cell side of the apparatus. Support structures have been removed. (b) View of the pyramid MOT side of the apparatus. The feedthroughs for the alkali metal dispensers are labelled by the species. The mirror for the pyramid MOT can be seen through the viewport. (c) Close up of the second MOT. Each of the coils labelled is one of a pair, arranged symmetrically about the glass cell.

2.2 Vacuum System

The centrepiece of any ultracold physics experiment is the vacuum system. As mentioned earlier the apparatus we use is a two-chambered design. Within the first chamber is a pyramid mirror, used for the pyramid MOT. This first chamber has its own 40 $\mathrm{L\,s^{-1}}$ vacuum pump. The pyramid MOT is loaded directly from alkali metal dispensers and is used to produce a beam of cold atoms, which move through a hole at the apex of the pyramid mirror into the second chamber.

The second chamber is a fused silica glass cell, measuring 2 cm×2 cm×8.3 cm. This cell is where the experiments are actually performed and so is referred to as the "science cell". The science cell is pumped using a 55 $\mathrm{L\,s^{-1}}$ vacuum pump and is connected to the pyramid MOT chamber by a narrow tube to maintain two orders of magnitude difference in pressure between the two chambers. A render showing both chambers can be found in figure 2.3 with a close-up of the science cell (and surrounding equipment) in figure 2.3(c).

Currently this apparatus is suitable for the production of bulk samples of

ultracold RbCs molecules, and studying their properties as an ensemble. To advance further towards quantum simulation there are two next-generation apparatuses being constructed to study RbCs on the single-molecule level. These will benefit from increased optical access around their science cells, which is heavily restricted in the current apparatus due to the optics required for the two MOTs in the second chamber.

2.3 Magnetic Fields

The apparatus is equipped with six pairs of coils for the generation of magnetic fields and magnetic field gradients. Of the six pairs five surround the science cell, and can be seen in figure 2.3(c). The sixth coil pair is responsible for the quadrupole field on the pyramid MOT and so is configured in an anti-Helmholtz arrangement. Two of the five coil pairs around the science cell are also in an anti-Helmholtz configuration, the inner coil pair is used for the magnetic trap and levitation gradients whilst the outer coils are used for the second MOT. The remaining three coil pairs are all in a Helmholtz arrangement, and are labelled from inside to out Bias 1, Bias 2 and Bias 3. Bias 1 and Bias 2 are used to generate the largest magnetic fields required by our apparatus (> 1000 G) however currently only ~ 200 G is necessary for our magneto-association sequences and so Bias 2 is disconnected. Bias 3 is the outermost Helmholtz coil pair and is used to perform rapid ($\sim$ ms) and small changes to the magnetic field. In our association sequence Bias 1 provides a magnetic field just below the ~ 181 G used for STIRAP whilst Bias 3 is used to carefully control the field through the association sequence.

Each of the coils pairs is controlled by a bank of metal oxide semiconductor field-effect transistors (IXFN230N10-ND) which, when coupled with our feedback electronics, enables us to control the current in the coil to approximately 1 part in 10^3. The coils on the science cell side of the apparatus are powered by supplies that can deliver > 400 A, whilst the pyramid MOT coils are limited to ~ 30 A. To be able to cope with the power dissipation by such large currents each coil is wound from hollow copper wire with a square cross-section, during operation a barrier cooler pumps distilled water through this area dissipating up to 2 kW of heat.

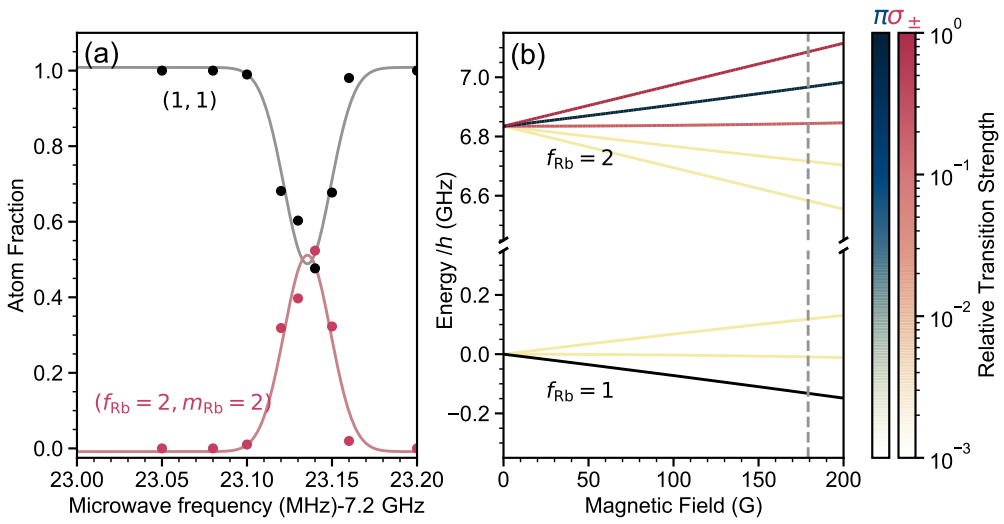

Figure 2.4: Calibrating the magnetic field using the hyperfine structure of ^{87}Rb. (a) Microwave spectroscopy of $(f_{\mathrm{Rb}} = 1, m_{\mathrm{Rb}} = 1) \rightarrow (2, 2)$. The solid lines are Gaussian fits to the data. (b) The hyperfine structure of the $5^2S_{1/2}$ ground state of ^{87}Rb used for magnetic field calibrations. The transitions which can be driven by different polarisations of microwaves are coloured by their transition strength relative to the strength of the $(1, 1) \rightarrow (2, 2)$ transition. The hyperfine ground state $(1, 1)$ is coloured black. The dashed grey line indicates the magnetic field that corresponds to the spectroscopy in (a).

To probe the magnetic field at the location of the molecules we perform microwave spectroscopy on the hyperfine transitions of the alkali atoms we have trapped. For the works presented in this thesis we typically use the $(f_{\mathrm{Rb}} = 1, m_{\mathrm{Rb}} = 1) \rightarrow (2, 2)$ transition in ^{87}Rb, which has a differential magnetic moment of $\sim h \times 2.1\ \mathrm{MHz\,G^{-1}}$. We probe this transition using microwave spectroscopy, however it is only allowed by a magnetic dipole moment. In this frequency range ~ 5 GHz $\leftrightarrow\sim 13$ GHz we can access up to 35 dBm of microwave power, which is coupled into a microwave horn. With this equipment we can achieve Rabi frequencies on the scale of kHz. Following the microwave spectroscopy we split the atomic cloud by state with a magnetic field gradient, where the $(2, 2)$ state is forced down and the $(1, 1)$ state is levitated. This leads to a vertical separation between the two clouds. An example spectrum is shown in figure 2.4(a).

To extract the magnetic field we construct the Breit-Rabi diagram (shown in figure 2.4(b)) using the Hamiltonian

$$H = H_{\mathrm{HF}} + H_{\mathrm{Zeeman}}. \tag{2.5}$$

Where H_{HF} contains the hyperfine structure, which in the $5^2S_{1/2}$ ground state is dominated by the direct nuclear spin-electron spin coupling. The Zeeman term is given by

$$H_{\mathrm{Zeeman}} = g_l l_z \mu_{\mathrm{B}} B + g_s s_z \mu_{\mathrm{B}} B + g_i i_z \mu_{\mathrm{N}} B, \tag{2.6}$$

where μ_{B} is the Bohr magneton, μ_{N} is the nuclear magneton, l is the orbital angular momentum, s is the electron spin angular momentum and i is the nuclear spin angular momentum. The values of the three relevant g-factors are phenomenally well known [95] and so error due to conversion between magnetic field and frequency is minimal compared to the spectroscopic error, using this technique we can determine the central value of the magnetic field to ~ 5 mG. By using the width of a Gaussian fitted to our spectroscopy (in the case of figure 2.4(a) this is 32(5) kHz) we can also determine that our magnetic field is only stable to ~ 20 mG over the 1 ms microwave pulse. Repeated measurements at the same settings indicate that the magnetic field is stable to ~ 55 mG day-to-day.

2.4 Optical Traps

Our apparatus is equipped with two optical dipole traps, operating at two different wavelengths. A diagram showing these is shown in figure 2.5. The first, and oldest, is the $\lambda = 1550$ nm crossed optical dipole trap. The light for this trap is sourced from an IPG photonics ELR-30LP-SF Er-doped fibre laser, outputting a maximum of 30 W. This light is divided into two beams using a polarising beam splitter and a 100 MHz difference in frequency is applied to the beams using two acousto-optical modulators (AOMs) to remove interference effects. These AOMs are also used to control the intensity of the light using a servo loop with ~ 50 kHz bandwidth, the power in each beam is monitored using the light that leaks through the final mirrors. Both beams are focussed through the glass cell. Over time the waists have varied between 65 μm and 110 μm, likely due to thermal degradation of the optical surfaces near the laser output. Each beam has an independent $\lambda/2$-waveplate for control over the polarisation, because the light is almost normally incident on the walls of the glass cell there is no measureable variation in reflectiv-

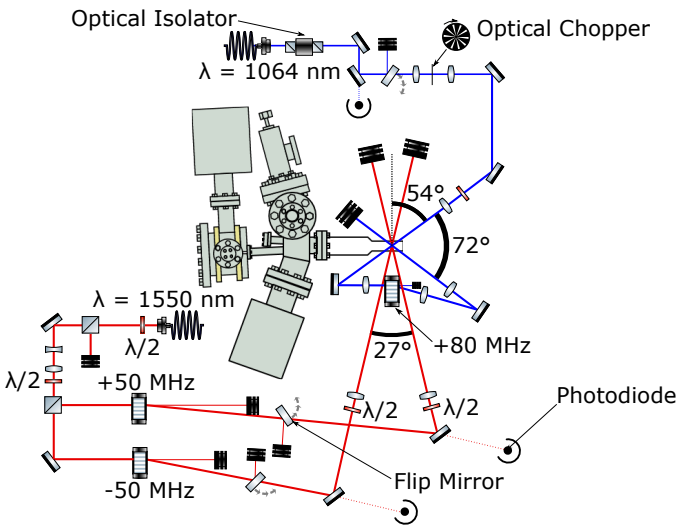

Figure 2.5: The optical traps in the RbCs apparatus (not to scale). The $\lambda = 1550$ nm is shown in red, the $\lambda = 1064$ nm trap is shown in blue. The arrangement of the 1064 nm trap is for the intensity-modulated trap in Chapter 6.2.1, for the spectroscopy in Chapter 5.3 the optical chopper is removed and the second pass is blocked.

ity with polarisation. This trapping potential has been largely untouched, barring realignments, as even small changes in the beam waists or alignment can significantly reduce the efficiency of the evaporation in the dipole trap.

The second trap operates at a wavelength of 1064 nm and has two main configurations for the results discussed in this thesis. The first configuration, and the one shown in figure 2.5, is the intensity-modulated or time-averaged trap. The light is delivered from a Coherent Mephisto Nd:YAG laser, configured in a master-oscillator power amplifier (MOPA) configuration though an NKT photonic crystal fibre. The light intensity is stabilised before being coupled into the fibre for delivery using similar electronics to the 1550 nm trap. On this laser system the photodiode for the power servo monitors the transmission through the second of a pair of steering mirrors near the fibre out-coupler. The time-averaged trap is arranged in a bow-tie configuration, the first pass has a waist of 107(1) µm whilst the second pass, which is frequency shifted by +80 MHz by an AOM, has a waist of 74(1) µm. As in the 1550 nm trap we can control the polarisation of the laser light using a $\lambda/2$ waveplate, however control of the polarisation is not independent between the two beams. Careful control over the polarisation is necessary because at the shallow angle of incidence of the laser beam (54°) there is a significant

difference in the reflectivity for s- and p- polarised light [96]. The intensity modulation is achieved using an optical chopper, to reduce the impact of diffraction on the trap we focus the beam through the chopper so that the waist is significantly smaller than the gaps in the chopper wheel. The alternative arrangement for the 1064 nm laser system is as a single beam for spectroscopic measurements, in this arrangement the optical chopper and the optics for focussing through it are removed and the second pass through the cell is blocked.

2.5 Electric Fields

Our apparatus is equipped with a system to generate DC electric fields, these are used to align the intrinsic dipole moment of the molecule to the external field by coupling states of opposite parity. The fields are generated by applying high voltages to four out-of-vacuum steel electrodes. The electrodes are highlighted in figure 2.3(c). The high voltages necessary are generated by two up to 5 kV Stanford Research Systems PS350 power supplies of opposing polarity. The lower two electrodes are connected to positive polarity whilst the upper two are connected to negative polarity. This ensures that the electric field points vertically in our apparatus and so aligns with the magnetic bias field. To determine the uniformity of our electric field we perform a simple simulation, approximating each of the steel electrodes as an infinite conductor held at a fixed voltage. The calculation we perform returns values that are normalised to that in the center of the cell and can be seen in figure 2.6(a), we match the calculation to the experimental data in chapter 5 for quantitative analysis[2]. The results of our simulation can be seen in figure 2.6, at the centre of the cell we can reach a maximum electric field of $\sim 1.5\ \mathrm{kV\,cm^{-1}}$ for a potential difference of 10 kV applied between the electrodes. We note that because we only have four electrodes and our molecules are located at an electric field maxima that we expect only a small electric field gradient across the cloud, however we do have a significant electric field curvature which contributes to non-uniformity.

[2]These measurements are also in agreement with an older finite element method simulation and previous measurements [42, 88].

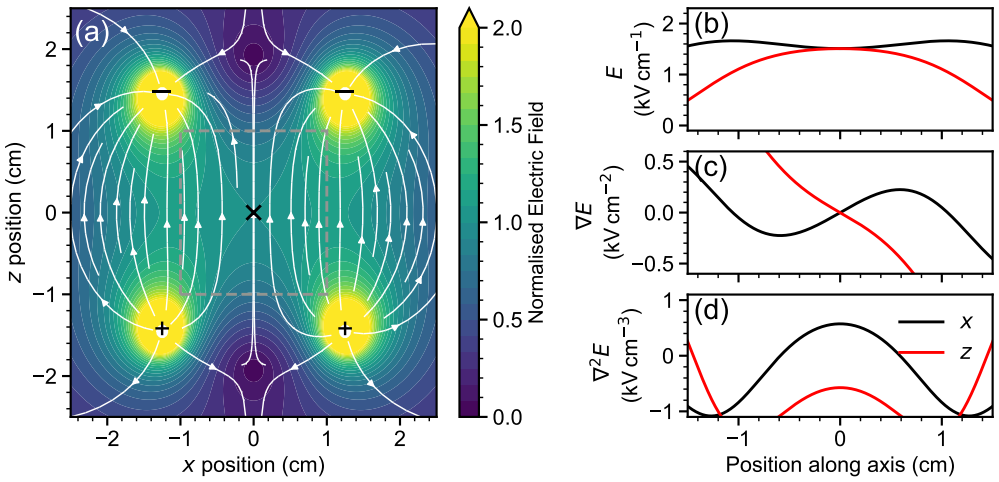

Figure 2.6: A simulation of the electric field within the RbCs apparatus. (a) The electric field between the electrodes in the apparatus, the colour indicates the magnitude $|E|$ whilst the arrow indicates the direction. The calculation approximates the arrangement as four infinitely long wires. The polarity of the electrode with respect to the common ground is indicated by $\pm$. The numerical result is rescaled to an experimental calibration for a potential difference of 10 kV. The dashed grey box indicates the bounds of the glass cell. The position of the molecules is indicated by the X. (b) The electric field along x (black) and z (red) axes through the point marked by an x in (a). (c) As in (b) but showing the gradient of E. (d) As in (b) but showing the curvature of E.

The power supplies that we use have a large intrinsic capacitance and so switching the output voltage on or off can take a large amount of time (multiple s). For experiments we want to use electric fields that are on for time scales comparable to our microwave spectroscopy (typically a few ms) or STIRAP transfer (several µs). To speed up switching we use a Behlke HTS-61-03-GSM switch with a high voltage capacitor (capacitance = 4.7 nF) in parallel as an external switching circuit for each power supply [88]. The trigger input for the high voltage is isolated from our FPGA control card with an external optical link. Using this arrangement we can switch from 0 V to 5 kV in ~ 1 µs and from 5 kV to 0 V in 0.3 µs [88].

Whilst we have the potential to apply up to ± 5 kV to our electrodes our limiting factor is not the maximum voltage we have available and is instead due to the fused silica of our glass cell. At high electric field ($E_{\mathrm{DC}} > 1\ \mathrm{kV\,cm^{-1}}$) the glass becomes measurably polarised with the accumulated charges creating a significant electric field. This additional electric field persists even when the

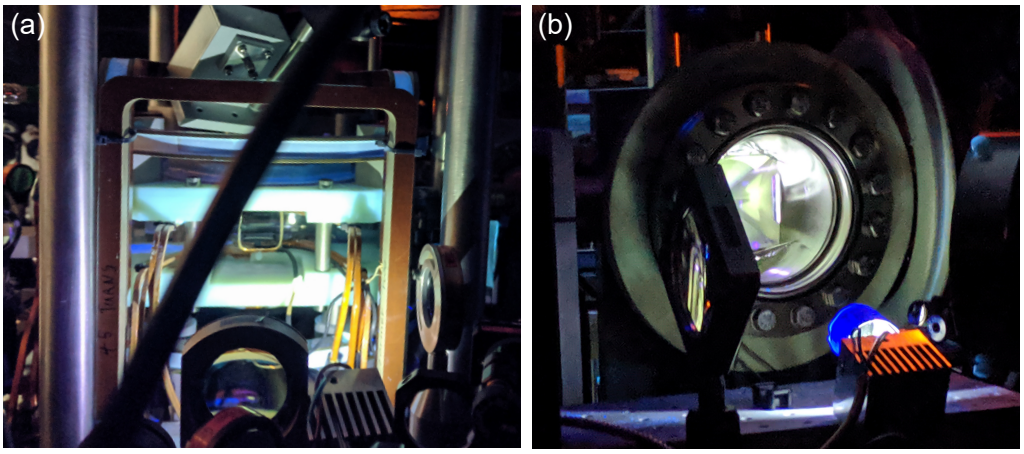

Figure 2.7: Illumination of the RbCs apparatus under the UV ($\lambda_0 = 365$ nm) light used to remove remnant electrical charges. (a) The science-cell side of the apparatus. The Rb microwave horn can be seen, as can the G-10 mounts and the supports for the magnetic field coils. (b) The pyramid MOT side of the apparatus, the pyramid mirror is visible through the viewport.

external voltages are removed and can be significant enough to Stark shift the molecules away from resonance with our STIRAP lasers [87]. To prevent the gradual build up of charges even when operating below this point we apply up to 3 W of UV light with centre wavelength 365 nm to our cell and viewport from LedEngin LZ4-44UV00-0000 light emitting diode (LED) arrays. Each LED array is mounted to an aluminium heatsink to dissipate the approximately 10 W of waste heat generated and they are controlled using a TTL signal from our experimental control. The areas illuminated by the LED arrays can be seen in figure 2.7, we are unable to collimate the light on the science cell side of the apparatus due to space restrictions. We find that there is no measurable difference in the electric field when we power the UV LED arrays for 1 s between experimental cycles.

2.6 Microwaves

Controlling the rotational and hyperfine state of the RbCs molecule requires fields with frequency $\sim$ 1GHz, this is well within the microwave portion of the electromagnetic spectrum. The first step to understanding microwave fields

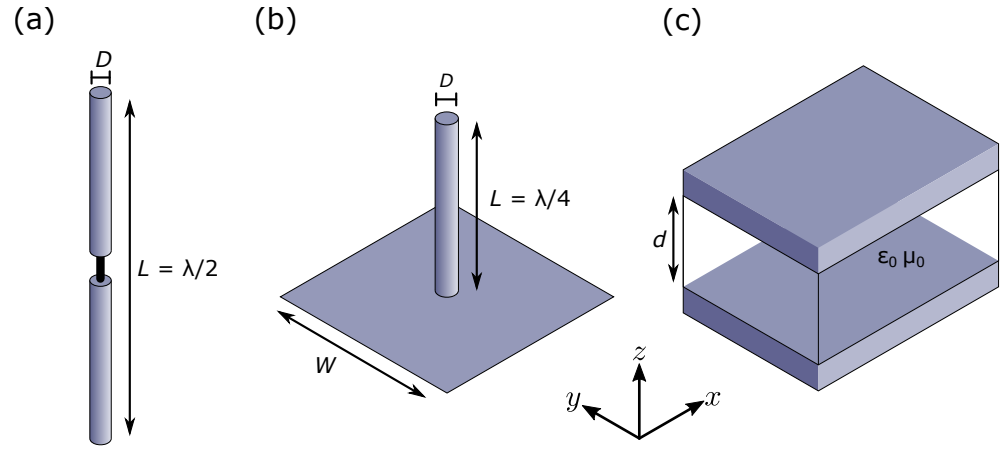

Figure 2.8: The models and geometry that are important for this section. (a) A dipole antenna, the overall length is $\lambda/2$ and is modelled as two conducting cylinders of diameter D separated by an ideal insulator, which is also able to act as a 50 Ω feed line. (b) The monopole antenna, which has one conducting cylinder, again of diameter D and length $\lambda/4$, is mounted onto a square grounded conducting plane of side-length W. (c) The microwave waveguide, two conducting plates are separated by an air gap of size d along the z axis.

in the RbCs apparatus is to start with the fields emitted by the simple antennas that we have developed. We build up the modelling, starting with the simple theoretical description of a Hertzian dipole before discussion of simulations of the $\lambda/4$ antennas used in the experiment. We additionally consider the environment around the cell, and the impact that has on the microwave field polarisation by considering the physics of microwave waveguides.

2.6.1 Emission Patterns

To consider the Hertzian dipole[3] as an antenna design is already misleading, the structure is inherently theoretical; a line of charge of (infinitesimal) length dl is driven by a current of the form $I_0 e^{i\omega t}$. We can derive the field that is emitted from this structure by first finding the vector potential $\vec{A}(\vec{R}, t)$, where

[3]sometimes the "Hertzian Doublet"

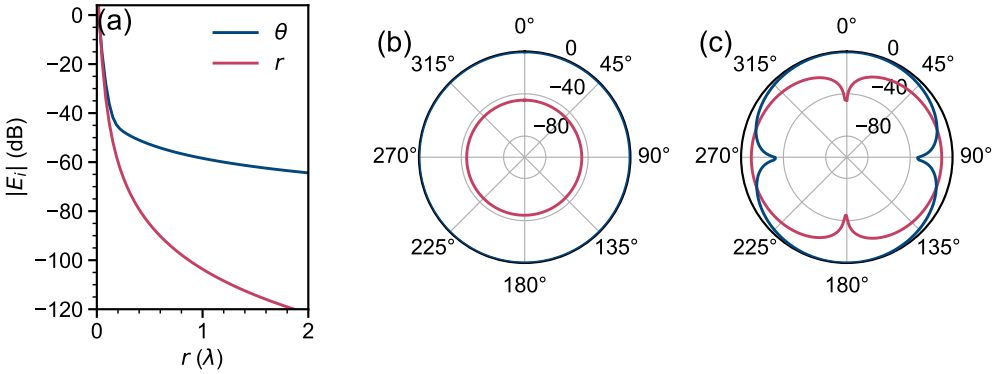

Figure 2.9: Emission patterns of a perfect Hertzian dipole antenna. (a) The electric field strength in the θ and r directions, as a function of the distance from the antenna in the $z = 0$ plane. The strength of the E field is in decibels with respect to the θ-polarised field at $r = 0$. By $r = \lambda$ the r-polarised component is already a factor of 50 dB weaker than the θ-polarised component. (b) The directivity pattern in the $x - y$ plane at $r = \lambda$. The colours indicate which direction the field is polarised as in (a), the strength is in decibels with respect to the maximum of the θ-polarised field with 0 dB on the circumference of the plot. (c) The directivity pattern in the $x - z$ plane at $r = \lambda$, the colours indicate which direction the field is polarised as in (a).

$\vec{R}$ is a coordinate in space and t is time

$$\begin{aligned}\vec{A}(\vec{r}) &= \frac{\mu_0}{4\pi}\int \frac{\vec{J}(\vec{R}', t_r)}{|\vec{R} - \vec{R}'|}\,\mathrm{d}^3\vec{R}' \\ &= \frac{\mu_0}{4\pi r} I_0 e^{-ikr}\hat{\vec{z}}\,\mathrm{d}l\end{aligned} \tag{2.7}$$

where t_r is the "retarded time" and is given by $t_r = t + |r - r'|/c$ and k is the angular wavenumber $\omega/c = 2\pi/\lambda$. We have also implicitly used the Lorenz gauge[4] to simplify future steps. The molecule couples most strongly to the electric field component of the microwave field we shall only calculate $\vec{E}$ for which we only need the vector potential

$$\begin{aligned}\vec{E}(\vec{r'}, t_r) &= \frac{\nabla \times (\nabla \times \vec{A})}{i\omega\mu_0\epsilon_0} \\ &= \frac{I_0 Z_0 \mathrm{d}l}{2\pi} e^{-ikr}\left[\frac{1}{2}\left(\frac{ik}{r} + \frac{1}{r^2} - \frac{i}{kr^3}\right)\sin(\theta)\hat{\vec{\theta}} + \left(\frac{1}{r^2} - \frac{i}{kr^3}\right)\cos(\theta)\hat{\vec{r}}\right]\end{aligned} \tag{2.8}$$

[4]the condition for this gauge is: $\nabla\cdot\vec{A} + \frac{1}{c^2}\frac{\mathrm{d}\phi}{\mathrm{d}t} = 0$, this allows us to write $\vec{E} = -\nabla\phi - \frac{\partial\vec{A}}{\partial t}$ and $\vec{B} = \nabla \times \vec{A}$

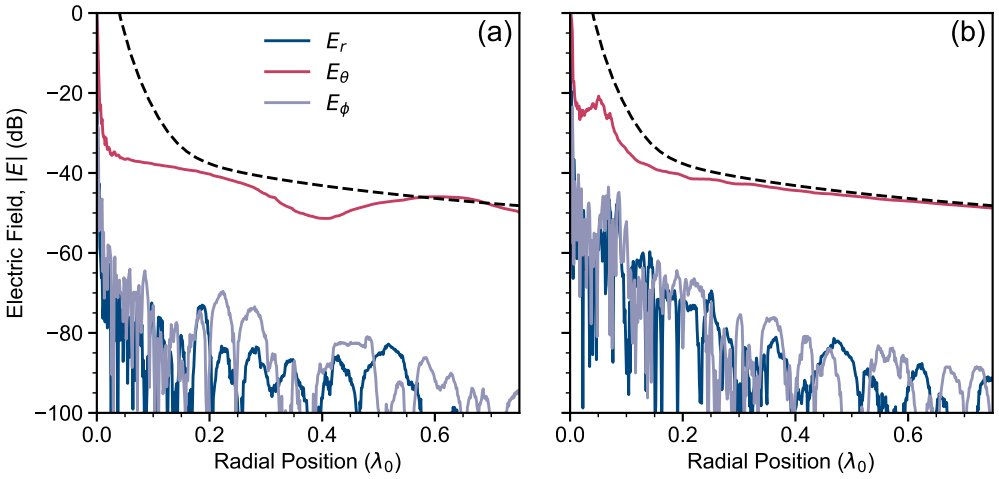

Figure 2.10: The polarisation from a dipole (a) and monopole (b) antenna from a finite element method (FEM) simulation in COMSOL. In both panels the dashed line indicates the $1/r$ decay of $|E_\theta|$ for a Hertzian dipole. The simulations indicate that the antennas are exceptionally well polarised with 60 dB of difference between the θ component and the two orthogonal components in the $z = 0$ plane. The simulation is set to use $\lambda_0 = 30$ cm for both antenna designs.

Where, in the above expression, we have used that $Z_0 = \sqrt{\mu_0/\epsilon_0} \approx 377\ \Omega$ is the impedance of free-space and $\vec{\theta}$, $\vec{r}$ are vectors that point in the altitude and radial directions respectively. We have plotted the E_θ and E_r components in figure 2.9.

In the far-field only the terms that fall as $1/r$ survive, as such we can see that the radiated electric field only has a component in the θ-direction. In the plane defined by $z = 0$ this means that the field is linear and vertically polarized with no dependence on x or y other than through the distance from the origin r. In the near-field regime there is also a component that is $\pi/2$ out of phase which points along the radial direction, the field therefore should circulate in the r, θ plane. Where the near-field ends and the far-field begins is a semantic matter, there is no hard-and-fast rule: however the characteristic length scale is typically a wavelength.

We began the analysis of this system by stating that the Hertzian doublet is not a real antenna design and that the structures are smaller than the wavelength. A common approximation to this system is the half-wave dipole where the overall length is $\lambda/2$, as shown in figure 2.8(a). An analytical form

of the emission pattern in the far field can be arrived at through a process known as pattern multiplication [97]

$$\vec{E} \approx \frac{iZ_0 I_0}{4\pi r} e^{-ikr} \left[\frac{\cos\left(\frac{kl}{2}\cos(\theta)\right) - \cos\left(\frac{kl}{2}\right)}{\sin(\theta)} \right] \hat{\vec{\theta}}. \tag{2.9}$$

The difference between this formula and the idealised Hertzian dipole is actually minimal as such we use this as a benchmark for our numerical calculations.

The transition $N = 0 \rightarrow 1$ has a transition frequency of ~ 1 GHz, correspondingly the wavelength is approximately 30 cm. For space reasons we do not use a half-wave dipole for our microwave antennas as these would have to be ~ 15 cm in length which begins to become prohibitively long to fit into our apparatus. Instead we use a simplified design, known as a quarter-wave monopole. In essence it is a single conductor connected to the microwave source mounted on a grounding plane, and behaves similarly to the dipole antenna. We are chiefly concerned with the polarisation purity of the antenna in both the near- and far-field regimes. We are concerned with both as one antenna is located significantly less than one wavelength away from the molecules. To determine the electric fields that are being generated by our design we create an idealised model, illustrated in figure 2.8(b), and use the finite element method (FEM) solver in COMSOL multiphysics RF. For our simulation we use a side length $W = \lambda/10$, $D \ll \lambda$ and simulate a region less than a wavelength from the centre of the antenna, this is appropriate for our closest antenna. We show the field components along r, θ and ϕ directions as a function of the radial coordinate for this simulation and, as a benchmark, for a dipole antenna in figure 2.10. The far-field behaviour of the two designs is remarkably similar, with only the θ component surviving to long ranges: this simulation indicates that our antennas are as close to perfectly polarised as we could reasonably require. An additional simulation also confirms that the emission pattern matches that of the ideal dipole.

2.6.2 Effect of the Surroundings

Within the RbCs apparatus in Durham there are numerous coils required for the MOT, magnetic trap and magneto-association stages of the experi-

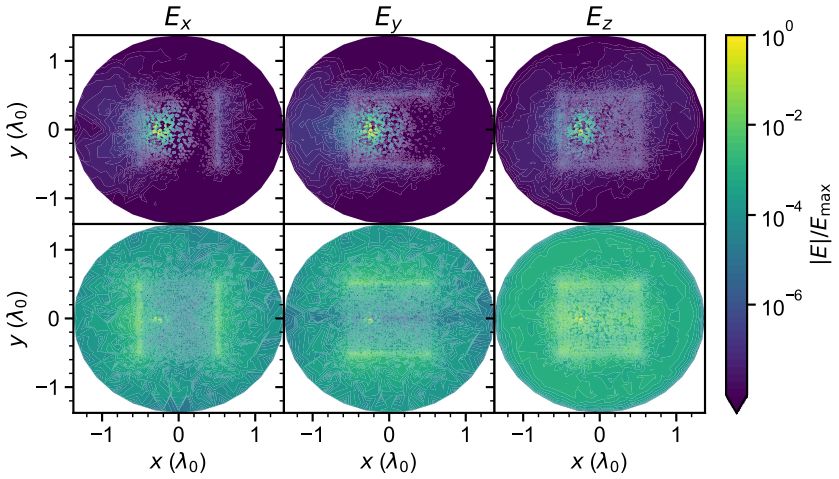

Figure 2.11: The propagation of an electric field between two plates spaced by $\lambda_0/10$, originating from a point microwave source simulated using COMSOL multiphysics RF. The upper panels show the propagation of a field initially polarised along the y direction. The lower panels show the propagation for a field initially polarised along the z direction. Both sets of panels are normalised independently. We have split the field into the three polarisation components along the Cartesian x, y, z axes. We see that for both polarisations there is a significant electric field strength for all three polarisations, showing that the plates mix the polarisation.

ment. As well as the G-10 mounts and the support structures necessary to hold the coils in place. Naturally this forms a structure within which the microwaves either cannot propagate within, or where they are strongly attentuated. For the purposes of modelling we treat this as a bulk object with openings significantly smaller than one wavelength.

The simplest waveguide structure one can envisage is the parallel plate waveguide, this consists of two infinite conducting plates which are separated by a dielectric, usually in the radio-frequency regime this is considered to be air but can in principle be any electrically permittive medium, in the microwave spectrum it is not unusual for the medium to be the dielectric in a circuitboard. Within the region between the two plates only certain transverse modes can propagate, these are labelled TE for transverse electric; TM for transverse magnetic; TEM for transverse electromagnetic. We can determine which modes are allowed by considering the boundary conditions to the problem, starting for the TE modes for a wave propagating along the y axis in figure 2.8(c) and given that the electric fields must be zero at the locations

of the plates, and so the allowed modes have wavenumbers given by

$$k = \frac{n\pi}{d}, n \in 1, 2, 3, ... \tag{2.10}$$

The frequency at which propagation in a TE mode is possible is given by the cut-off frequency, which is determined by the cut-off wavenumber i.e. $n = 1$

$$f_c = \frac{k_c}{2\pi\sqrt{\mu\epsilon}} \tag{2.11}$$

the closest coils in the RbCs experiment is the pair for Bias 1, with an inner separation of 32.5(1) mm [84]. If we use this value for the separation of the plates we find that $f_c = 4.6$ GHz, so any EM waves of wavelength longer than 65 mm will be attenuated by the waveguide structure.
We can calculate the length over which each of the fields decays, within the waveguide the component of the field along the propagation direction is given by $\exp(-i\beta y)$ with

$$\beta = \sqrt{k^2 - \left(\frac{n\pi}{d}\right)^2}, \tag{2.12}$$

where for $k < k_c$ β is imaginary and the propagating field decays away over a length scale given by the difference in wavenumbers between the TE mode and the applied field. For our example above and an incident field with $\lambda = 30$ cm this length scale is 8 cm, these cut-off modes are known as "evanescent".

To gain a qualitative understanding on how the coils in our experiment will impact the polarisation purity of our antennas we set up a simplified computational model. We use a pair of square plates which are spaced by 3 cm and with side lengths of 30 cm for a simulation wavelength of $\lambda_0 = 30$ cm, this accurately reflects the spacing of the coils for bias 1 and the extent of the G-10 mounts. For our source we do not use the monopole antenna discussed previously: the reason for this is that the structures necessary for an accurate full simulation requires a finer mesh and so more computational resources. Instead as a source we use an idealised point emitter located at $y = 0$ and $x = -7.5$ cm and repeat the simulation for two polarisations: along the horizontal y axis and along the vertical z axis. For analysis we only consider the fields along the $z = 0$ plane, corresponding to the exact centre of the parallel plates, shown in figure 2.11 after averaging over 5 periods of oscillation. For both sources we observe that there is a significant

electric field component along all three axes, but this is most obvious for an initial y polarisation (upper panels of figure 2.11). This tells us that we cannot purely rely on polarisation to isolate individual transitions. We have observed this effect experimentally by observing slow Rabi oscillations when using the "incorrectly" polarised antenna for a transition.

Chapter 3

Molecular Structure

The Hamiltonian (H) relevant to our experiments can be split into terms that depend on internal (H_{Int}) and external degrees of freedom (H_{Ext}). In a diatomic molecule there are many energy scales which we must consider to properly describe the internal structure. The Hamiltonian of such a molecule is given by

$$H_{\mathrm{Int}} = H_{\mathrm{Electronic}} + H_{\mathrm{Vibration}} + H_{\mathrm{Rotation}} + H_{\mathrm{HF}}. \tag{3.1}$$

where this Hamiltonian contains terms for electronic ($H_{\mathrm{Electronic}}$), vibrational ($H_{\mathrm{Vibration}}$) and rotational (H_{Rotation}) excitations as well as the hyperfine interactions between the constituent atoms in the molecule (H_{HF}). When constructed accurately this Hamiltonian contains all of the information about the internal structure of the molecule and illustrates the large number of degrees-of-freedom that the structure provides. The internal structure of the RbCs molecule is shown in figure 3.1 to illustrate the various energy scales.

The interaction between the internal structure and external fields is described by H_{Ext}, for our purposes we describe it with three terms

$$H_{\mathrm{Ext}} = H_{\mathrm{Zeeman}} + H_{\mathrm{DC}} + H_{\mathrm{AC}}. \tag{3.2}$$

The three terms we consider are the interaction between a molecule and a DC magnetic field (H_{Zeeman}), a DC electric field (H_{DC}) and an AC electric field (H_{AC}).

In this chapter we will begin by discussing the electronic and vibrational structure briefly, particularly as it relates to RbCs. The later sections of

this chapter will be dedicated to the rotational structure of the vibronic (vibrational & electronic) ground state of a diatomic molecule which we will represent as a rigid rotor. We will then show, in detail, the interplay between hyperfine, Stark and Zeeman structures and the different ways these are represented in a molecule. We conclude the chapter with theoretical hyperfine structure calculations for RbCs.

3.1 Hund's Cases

Before we begin the detailed description of the internal structure of the molecule we shall cover some idealised cases for the coupling of electronic and rotational angular momenta. These cases are known as Hund's cases and are labelled (a-e). We will cover only the cases relevant to the RbCs molecule: (a) and (c), which are illustrated in figure 3.2. The terms we shall use for angular momentum will follow [98]:

- $\boldsymbol{L}$: The total orbital angular momentum of the electrons,
- $\boldsymbol{S}$: The total spin of the electrons,
- $\boldsymbol{J}$: The total angular momentum,
- $\boldsymbol{N}$: The total angular momentum without spin; $\boldsymbol{N} = \boldsymbol{J} - \boldsymbol{S}$,
- $\boldsymbol{R}$: The rotational angular momentum of the nuclei; $\boldsymbol{R} = \boldsymbol{N} - \boldsymbol{L}$,
- $\boldsymbol{I}$: The total nuclear spin.

Hund's case (a)

In this case the total orbital angular momentum $\boldsymbol{L}$ is strongly coupled to the internuclear axis by electrostatics and more weakly to $\boldsymbol{S}$ by spin-orbit coupling. The components along the internuclear axis of $\boldsymbol{L}$ and $\boldsymbol{S}$ are both well-defined and labelled as Λ and Σ respectively. These two components add to form Ω, which is the magnitude of a vector pointed along the internuclear axis. The total angular momentum vector, $\boldsymbol{J}$, is the vectorial sum of $\boldsymbol{\Omega}$ with the nuclear rotational angular momentum $\boldsymbol{R}$.

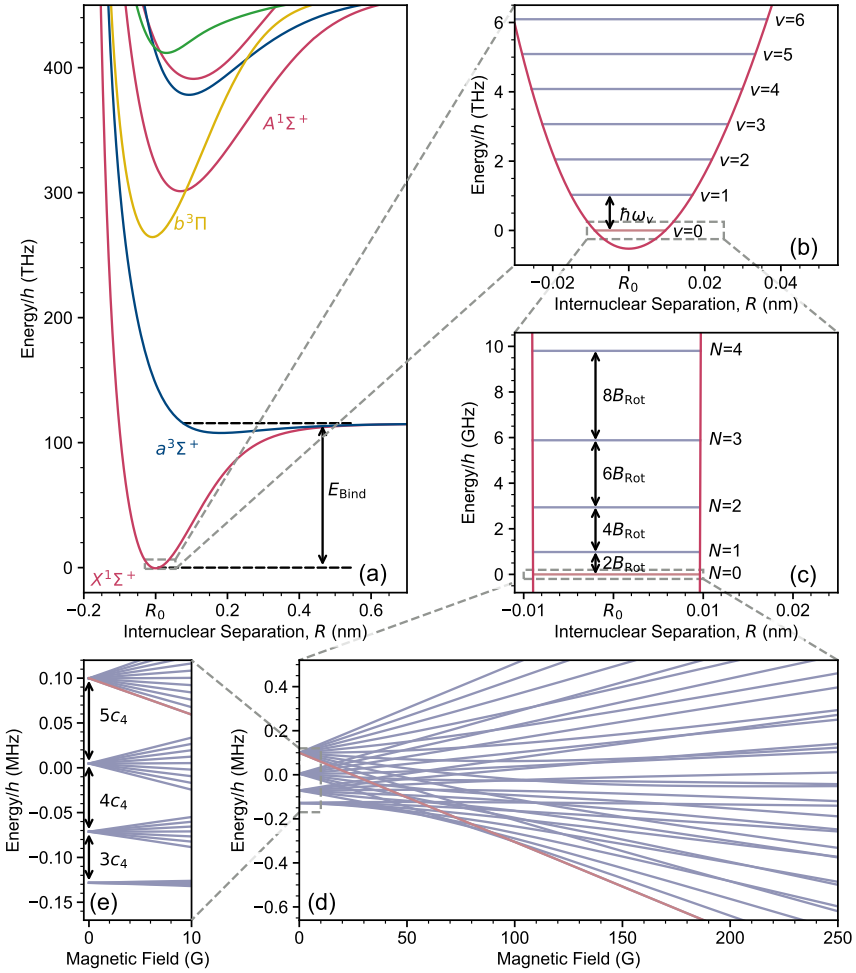

Figure 3.1: The structure of the RbCs molecule at various energy scales. (a) The molecular potentials as a function of the distance from the equilibrium nuclear position R_0 [91]. The four lowest energy potentials are labelled. Highlighted are the Feshbach $[n = -6(f_{\text{Rb}} = 2, f_{\text{Cs}} = 4), L = 2(m_{\text{Rb}} = 2, m_{\text{Cs}} = 3)]$ and ground $(v = 0, N = 0, M_F = 5)$ states. (b) The vibrational structure near the bottom of the $X^1\Sigma^+$ potential for small distances from $R_0 = 0.43$ nm. Each of the vibrational lines is separated by $\hbar\omega_v$, where ω_v is the vibration frequency. (c) The rotational structure of $v = 0$, as a function of distance from R_0. As the rotational quantum number increases the separation between neighbouring states also increases in multiples of the rotational constant B_{Rot}. (d) The Zeeman structure of $N = 0$ as a function of applied magnetic field. The state with $(N = 0, M_F = +5)$ is highlighted. (e) A zoom on the low field region in (d) showing the $F = 2, 3, 4, 5$ manifolds separated by the scalar spin-spin coupling constant c_4.

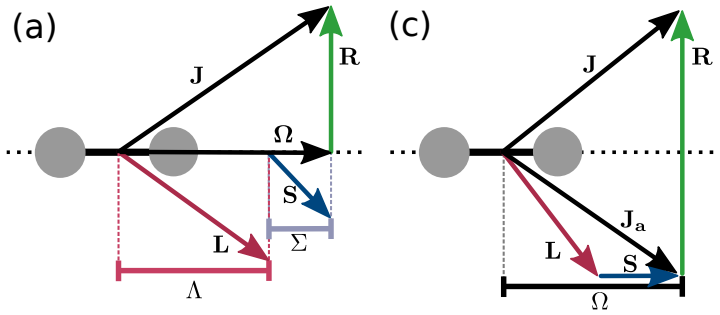

Figure 3.2: A schematic of Hund's cases (a) and (c) as relevant for the RbCs molecule.

This case is typically a good representation of low-lying J states [99]. The appropriate quantum numbers to describe the basis states are $(S, \Sigma, \Lambda, \Omega, J)$ [98].

Within this case we can also describe the coupling of the nuclear spins to the molecular rotation, using Dunn's case (a_β) [98, 100]. In this case the total nuclear spin $\boldsymbol{I} = \boldsymbol{i}_{\mathrm{Rb}} + \boldsymbol{i}_{\mathrm{Cs}}$ couples to the total angular momentum $\boldsymbol{J}$ to form a grand total angular momentum $\boldsymbol{F} = \boldsymbol{J} + \boldsymbol{I}$. Using this scheme the basis states can be labelled by the quantum numbers $(S, \Sigma, \Lambda, \Omega, J, I, F)$.

Hund's case (c)

In case (c) the spin-orbit coupling between $\boldsymbol{L}$ and $\boldsymbol{S}$ is much stronger and so Λ and Σ cannot be defined. In this case both $\boldsymbol{L}$ and $\boldsymbol{S}$ couple to form $\boldsymbol{J_a} = \boldsymbol{L} + \boldsymbol{S}$, with projection Ω on the internuclear axis. This new angular momentum adds vectorially to $\boldsymbol{R}$ to form the total angular momentum $\boldsymbol{J}$.

This coupling scheme is usually applicable to molecules with large internuclear separations [99]. Near the dissociation limit and at short range potentials are often labelled by Ω, alongside other quantum numbers. The good quantum numbers for this case are (J_a, Ω, J) [98]. In RbCs this case is appropriate for the description of molecules in a Feshbach state.

3.2 Electronic Structure

The largest energy separation in molecules, typically $h \times 100\,\mathrm{THz}$, is due to the electronic degree-of-freedom. In this thesis a detailed understanding

of the electronic structure is not necessary, outside of what is necessary to describe the STIRAP process described in Chapter 2 and the two-photon spectroscopy shown later in Chapter 5. However it is worthwhile to discuss briefly.

The total molecular wavefunction is the product of a wavefunction for the component nuclei ψ_{N} and an electronic wavefunction ϕ_{e}. Because of the differences in masses between the nuclei and electrons the motion of the nuclei is much slower than the electrons and so, via the Born-Oppenheimer approximation, the electronic wavefunctions vary slowly with the nuclear coordinates $\boldsymbol{r} = \{r, \Theta, \Phi\}$. This allows the Schrödinger equation to be written for ψ_{N}

$$\left[-\frac{\hbar^2}{2\mu}\frac{1}{r^2}\frac{\partial}{\partial r}\left(r^2\frac{\partial}{\partial r}\right) + \frac{\langle\phi_e|\,\boldsymbol{R}^2\,|\phi_e\rangle}{2\mu r^2} + E_e(r)\right]\psi_N(\boldsymbol{r}) = E\psi_N(\boldsymbol{r}). \tag{3.3}$$

Here μ is the reduced mass of the molecule.

What we therefore term "the electronic structure" are actually then the electronic eigen-energies (E_e) which vary as a function of the nuclear separation. These energies act as potentials which define the range over which the nuclear wavefunction exists. The general form of these potentials is to increase toward infinity as $r \to 0$ (due to Coulomb repulsion) and to tend to the free atomic levels as $r \to \infty$. If there is a minimum between these two points, and the potential is deep enough, the electronic structure is able to support bound states. The position of this minimum is called the "equilibrium separation" R_0.

Each of these potentials can be described by a "term symbol": $n^{(2S+1)}\Lambda^{\pm}_{\Omega}$. By analogy with the spectroscopic notation used in atoms Λ is represented by a capital Greek letter starting with Σ for $\Lambda = 0$, Π for $\Lambda = 1$ continuing following the s, p, d, f... pattern. The value of n is represented by a letter, starting at X then A, B, C... counting up in energy, in some places the case of the letter is used to indicate that a potential has a different spin multiplicity (the value of $2S + 1$) to the ground state. n can be omitted and replaced by Ω for certain potentials [91]. The $\pm$ superscript represents the inversion symmetry in a plane which includes the internuclear axis. Figure 3.1(a) shows examples of the lowest potentials for the RbCs molecule, calculated neglecting spin-orbit coupling by Fahs *et al.* [91].

3.3 Vibrational Structure

The vibrational energy of the molecule is associated with motion around the equilibrium separation. We can arrive at an equation for the radial motion of the nuclei by substituting $\psi_N(\boldsymbol{r}) = f_{v,N}\,{}^{\Lambda}X_{N,M_N}\,r^{-1}$ where $f_{v,N}$ is the radial wavefunction and ${}^{\Lambda}X_{N,M_N}$ is the angular wavefunction. By substituting into equation (3.3) we can form a radial equation

$$\left[\frac{-\hbar^2}{2m}\frac{\mathrm{d}^2}{\mathrm{d}r^2} - E_{\mathrm{Rot}} + E_e(r)\right] f_{v,N} = E\, f_{v,N}. \tag{3.4}$$

Here one term has already been simplified to the rotational energy (E_{Rot}), this will be covered in much greater detail in the next section. To solve this equation we will consider only behaviour around the potential minimum. Taylor expanding the potential near the minimum gives

$$E_e(R) \approx E_e(R_0) + \frac{B_e}{2}(r - R_0)^2. \tag{3.5}$$

and so we can immediately recognise that the vibrational energy is exactly the quantum harmonic oscillator. This gives energy levels

$$E_{\mathrm{vib}} = \hbar\omega_v \left(v + \frac{1}{2}\right), \tag{3.6}$$

with the vibrational angular frequency $\omega_v = \sqrt{B_e/m}$. For the $X^1\Sigma$ state of RbCs the $v = 0 \to 1$ transition energy is $h \times 1.49270\,\mathrm{THz}$ [101]. This short derivation illuminates two features of the vibrational structure: firstly the vibrational ground state does not coincide with the minimum of the electronic potential (as can be seen in figure 3.1(b)) there is a zero-point energy of $\hbar\omega_v/2$. Secondly, as the wavefunctions are those for the harmonic oscillator, they behave like Hermite polynomials and so, for $v' \neq v$, are orthogonal, hence one can arrive at a selection rule $\Delta v = \pm 1$.

However for vibronic transitions (that is: transitions involving changing vibrational *and* electronic state) the potential minimums and vibrational frequencies can be vastly different and so the argument that the wavefunctions for $v \neq v'$ are orthogonal breaks down. In this case the overlap of the radial wavefunctions, known as the Franck-Condon factor, governs the strength of different transitions. In experiment, particularly those related to the laser cooling of molecules, a multitude of vibrational transitions are allowed [102, 103].

3.4 Rotational structure and the rigid rotor

The previous sections have dealt with what we shall term the "gross" structure of the molecule: the largest energies. In this section we will cover, in detail, the derivation of an effective Hamiltonian for the rotational and hyperfine structure. We will neglect both E_{vib} and E_e in this discussion as ro-vibrational and rovibronic transitions are not relevant to molecules prepared in the electronic and vibrational ground states.

The coarsest energy level we will consider in our new "effective" Hamiltonian is that of rotation. In RbCs rotational energies are in the microwave part of the spectrum with energies $\sim h \times 1\,\text{GHz}$. The rotational term can be arrived at by treating the molecule as a rigid rotor which is symmetric about the internuclear axis, the associated kinetic energy is [104]

$$\begin{aligned} T &= \frac{1}{2I_a}(R_a^2 + R_b^2) + \frac{1}{2I_c}R_c^2 \\ &= \frac{1}{2I_a}R^2 + \left(\frac{1}{2I_c} - \frac{1}{2I_a}\right)R_c^2, \end{aligned} \tag{3.7}$$

where a, b and c are the principal axes of the system, conventionally c is chosen to be the internuclear axis. In equation (3.7) I_i is the moment of inertia about axis i and R_i is the rotational angular momentum about axis i. For axis a the moment of inertia is given by $I_a = I_0 = mR_0^2$, where m is the reduced mass of the molecule. We can discard the terms in R_c as their eigenvalues are proportional to $\pm\Lambda$ (which is zero for Σ potentials). Making the substitution for the rotational constant $B_0 = \hbar^2/2I_0$ and setting $R = J = N$ for $\Lambda = \Sigma = 0$ gives the rigid rotor energy levels

$$E_{\text{Rigid}}(N) = B_0 N(N+1). \tag{3.8}$$

As there is no potential energy associated with the rotation of the molecule, provided it is rigid, the Schrödinger equation is identical to the angular part of that for the hydrogen atom. Its wavefunctions are thus [105]

$$\psi_{\text{R}} = A_{\text{R}} e^{-iM_N\phi} P_N^{M_N}\left[\cos(\theta)\right] = Y_{N,M_N}(\theta,\phi) \tag{3.9}$$

where θ and ϕ are the polar and azimuthal angles about z respectively. $P_N^{M_N}$ is the associated Legendre polynomial and A_{R} is a normalisation constant.

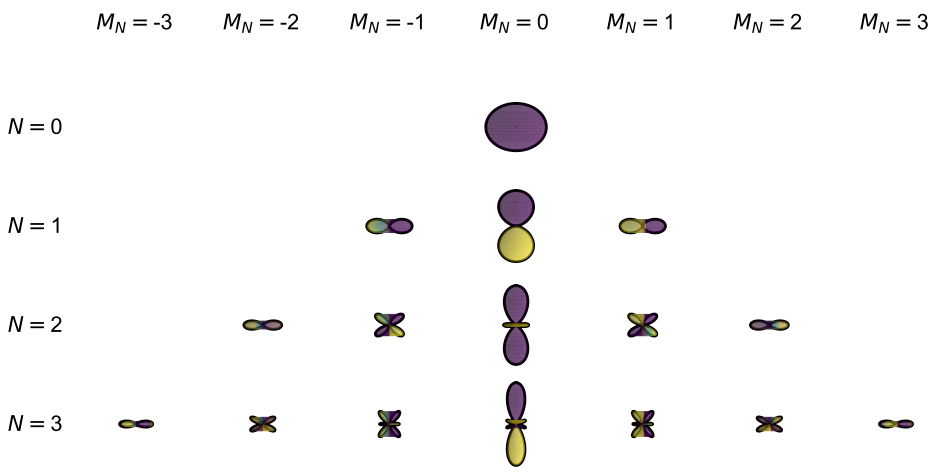

Figure 3.3: The probability density of the wavefunctions, Y_{N,M_N}, for $N \leq 3$ for a rigid rotor, the colour indicates the phase. The wavefunctions are being viewed along the x axis, with the solid black line showing cuts through the $y-z$ plane. Scales are consistent for each N but not between states of different N.

The functions Y_{M,M_N} are the spherical harmonics, which will come in handy later to determine the matrix elements of various Hamiltonians. These wavefunctions are shown in figure 3.3 for $N \leq 3$.

However real molecules can vibrate and so are not rigid, to include this requires solving the radial equation for separations about the equilibrium position R_0. Doing so introduces an additional effective potential due to the centrifugal distortion of the molecule, which leads to a correction to the eigenenergy of the form

$$E_{\text{Centrifugal}} = -D_0 N^2 (N+1)^2. \tag{3.10}$$

In principle there are also higher order terms which couple vibration and rotation to higher powers. For the low rotation states only this first distortion term is relevant, for RbCs this shifts the energy of $N = 1$ by $h \times 800\,\text{Hz}$. Our rotational Hamiltonian's matrix elements are then given by

$$\langle N, M_N | \, H_{\text{Rot}} \, | N', M_N' \rangle = (E_{\text{Rigid}} + E_{\text{Centrifugal}}) \delta_{M_N, M_N'} \delta_{N,N'}, \tag{3.11}$$

which is diagonal in the $|N, M_N\rangle$ basis and so the wavefunctions in equation (3.9) are still valid.

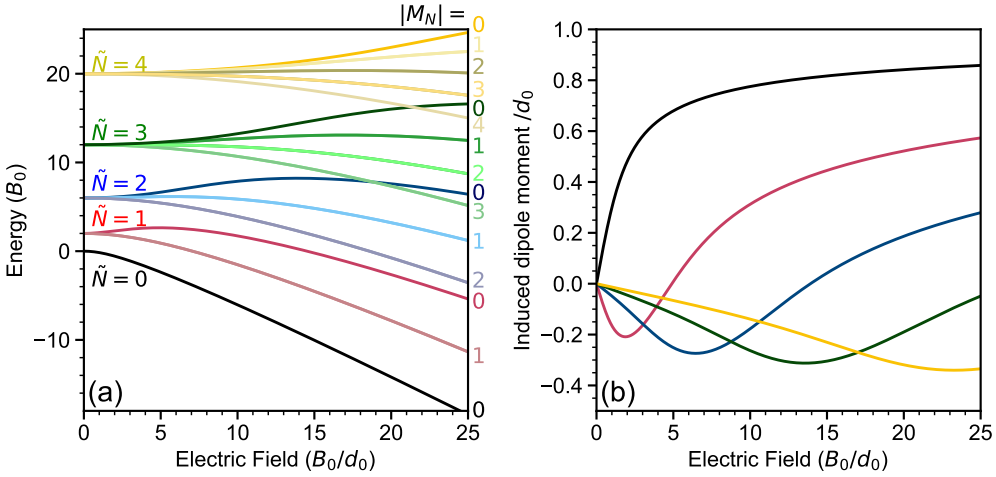

Figure 3.4: The DC Stark shift of a rigid rotor molecule. (a) The pendular states with $\tilde{N} \leq 4$, the magnitude of M_N is indicated where a given energy level crosses the vertical axis. The electric field is given in units of the ratio of the rotational constant to the intrinsic dipole moment. For RbCs this is $B_0/d_0 \approx 0.785\ \mathrm{kV\,cm^{-1}}$ (b) The induced dipole moment of this molecule in units of the permanent dipole moment (d_0) for states with $M_N = 0$, calculated using equation (3.20).

3.5 Rigid Rotor and Electric Fields

In this section we will describe a simple model of a charged rigid rotor in an electric field. This will enable us to describe the AC and DC Stark effects for polar molecules.

3.5.1 DC Stark Effect

In any heteronuclear molecule there is a slight difference in charge along the internuclear axis due to the differing number of protons between the two nuclei. This charge distribution gives the molecules an intrinsic dipole moment. This dipole moment exists only within the molecular reference frame. In the laboratory the molecules follow the rotational wavefunctions shown in figure 3.3 and have no specified orientations and so the average dipole moment is zero. Applying an electric field to the molecules couples states of opposing parity, inducing a dipole moment in the molecules in the laboratory frame. The Hamiltonian for the DC Stark effect can be written

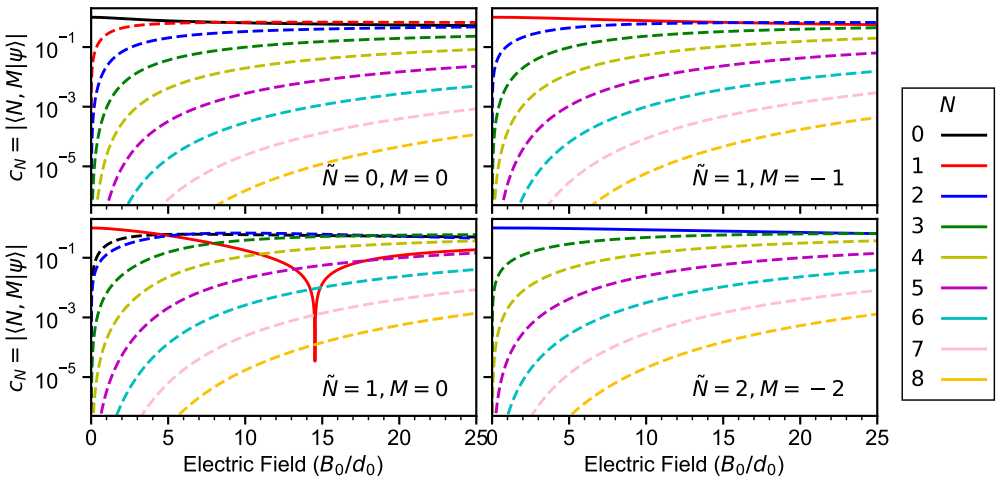

Figure 3.5: The state composition of four pendular states is shown as a function of applied electric field. The component in the rotational state which they adiabatically connect to at zero electric field is shown as a solid line, with all other components shown as dashed. As the electric field increases it becomes clear that higher rotational states contribute more to the state composition and so labelling states by N is no longer appropriate. The pole in $\tilde{N} = 1, M = 0$ is due to a zero crossing of the $|N = 1, M_N = 0\rangle$ component.

as:

$$H_{\mathrm{DC}} = -d_0 \boldsymbol{E} \cdot \hat{\boldsymbol{n}}, \tag{3.12}$$

where $\hat{\boldsymbol{n}}$ is a unit vector which points in the direction of the internuclear axis and d_0 is the molecule-frame intrinsic electric dipole moment. Let us assume that the electric field is pointed along the z-axis, which the molecules are also quantised along. Equation (3.12) becomes

$$H_{\mathrm{DC}} = -d_0 E \cos(\theta). \tag{3.13}$$

Our total Hamiltonian now resembles a spherical pendulum with potential energy associated with the position along the z axis. The eigenstates of this new system, so-called "pendular states", are given by superpositions of the spherical harmonics [106]

$$\left|\psi_{\tilde{N},M_N}\right\rangle = \sum_{N,M} c_{N,M} Y_{N,M} = \sum_{N,M} c_{N,M} \left|N, M\right\rangle \tag{3.14}$$

the $\tilde{N}$ is used to indicate that N is no longer a good quantum number but that we can still count up in energy for each $|M_N|$. As the eigenstates for this Hamiltonian can be expressed as superpositions of our rotational

wavefunctions we will continue to use the $|N, M_N\rangle$ basis when discussing the charged rigid rotor model. The evolution of some example states is shown in figure 3.5, where it becomes clear that using (N, M_N) as labels is inappropriate.

To determine the new wavefunctions and the associated energies we shall calculate the matrix elements of equation (3.13) the $|N, M_N\rangle$ basis. Remembering from equation (3.9) once again that these wavefunctions are the spherical harmonics $Y_{N,M_N}(\theta, \phi)$ the matrix elements are

$$\begin{aligned}\langle N, M_N| H_{\mathrm{DC}} |N', M'_N\rangle = \\ -d_0 E \int\int Y^*_{N,M_N}(\theta,\phi)\cos(\theta)Y_{N',M'_N}(\theta,\phi)\mathrm{d}^2\Omega,\end{aligned} \tag{3.15}$$

where the integral is over the surface of a sphere *i.e.* in spherical polar coordinates $\mathrm{d}^2\Omega = \sin(\theta)\mathrm{d}\theta\mathrm{d}\phi$, $0 \leq \theta \leq \pi$, $0 \leq \phi \leq 2\pi$. We can use the substitution $\cos(\theta) = Y_{1,0} \times \sqrt{4\pi/3}$ to rewrite this expression entirely in the form of spherical harmonics. This allows us to use the known integral formula for the product of three spherical harmonics [107]

$$\begin{aligned}&\int\int Y_{A,i}(\theta,\phi)Y_{B,j}(\theta,\phi)Y_{C,k}(\theta,\phi)\mathrm{d}^2\Omega \\ &= \left[\frac{(2A+1)(2B+1)(2C+1)}{4\pi}\right]^{1/2} \begin{pmatrix} A & B & C \\ 0 & 0 & 0 \end{pmatrix} \begin{pmatrix} A & B & C \\ i & j & k \end{pmatrix}.\end{aligned} \tag{3.16}$$

Combined with the definition that $Y^*_{N,M_N} = (-1)^{M_N} Y_{N,-M_N}$ we can arrive at the result

$$\begin{aligned}\langle N, M_N| H_{\mathrm{DC}} |N', M'_N\rangle = &- d_0 E \sqrt{(2N+1)(2N'+1)}(-1)^{M_N} \\ &\times \begin{pmatrix} N & 1 & N' \\ -M_N & 0 & M'_N \end{pmatrix} \begin{pmatrix} N & 1 & N' \\ 0 & 0 & 0 \end{pmatrix}.\end{aligned} \tag{3.17}$$

The last two terms in parenthesise are Wigner-3j coefficients[1] and show that the DC Stark effect mixes states with the same M_N but N different by 1. For $N = 0, 1$ and $M_N = 0, -1, 0, 1$ the DC Stark effect is given by the matrix

$$H_{\mathrm{DC}} = -d_0 E \begin{pmatrix} 0 & 0 & \sqrt{\frac{1}{3}} & 0 \\ 0 & 0 & 0 & 0 \\ \sqrt{\frac{1}{3}} & 0 & 0 & 0 \\ 0 & 0 & 0 & 0 \end{pmatrix}. \tag{3.18}$$

[1]The Wigner-3j symbols are similar to the Clebsch-Gordon coefficients and describe the addition of two angular momenta in terms of a third [108].

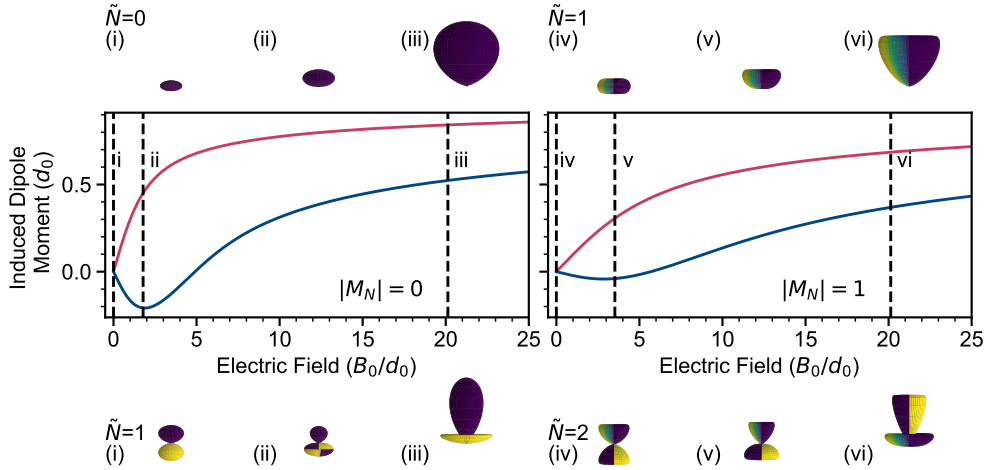

Figure 3.6: The dipole moment for pendular states with $M_N = 0$ (left) and $|M_N| = 1$ (right). At key points the probability density of the wavefunction is illustrated as in figure 3.3. For $\tilde{N} \neq M_N$ the dipole moment is briefly oriented anti-parallel to the applied electric field, shown as a distortion of the wavefunctions along the $-z$ axis at (ii) and (v).

We can interpret this matrix as showing us the couplings between the lowest two rotational levels. In this simplified case there are only the $N = 0, 1$, $M_N = 0$ states that are being coupled as no other states satisfy the rules enforced by equation (3.17). We can also observe that there are no diagonal elements, these would correspond to the simple shifting of energy levels without mixing. In figure 3.4(a) the DC Stark shift of the lowest pendular states is shown as a function of applied electric field.

Dipole moments

We can now sensibly ask the question, what is the dipole moment induced by the DC electric field? The lab-frame dipole moment of a state $|\psi\rangle$ is given by the appropriate expectation value of the dipole operator

$$\langle\psi|\,\boldsymbol{d}\,|\psi\rangle\,. \tag{3.19}$$

where $\boldsymbol{d}$ has components along all three axes. If we are only concerned with the z component (the one along the external DC electric field) then we find

$N \to N+1$	$d_z(d_0)$	$d_\pm(d_0)$
0	$\frac{1}{\sqrt{3}}$	$-\frac{1}{\sqrt{3}}$
1	$\frac{2}{\sqrt{15}}$	$-\sqrt{\frac{2}{5}}$
2	$\frac{3}{\sqrt{35}}$	$-\sqrt{\frac{3}{7}}$
3	$\frac{4}{3\sqrt{7}}$	$-\frac{2}{3}$
4	$\frac{5}{3\sqrt{11}}$	$-\sqrt{\frac{5}{11}}$
5	$\frac{6}{\sqrt{143}}$	$-\sqrt{\frac{6}{13}}$
6	$\frac{7}{\sqrt{195}}$	$-\sqrt{\frac{7}{15}}$
7	$\frac{8}{\sqrt{255}}$	$-2\sqrt{\frac{2}{17}}$
8	$\frac{9}{\sqrt{323}}$	$-\frac{3}{\sqrt{19}}$
9	$\frac{10}{\sqrt{399}}$	$-\sqrt{\frac{10}{21}}$
10	$\frac{11}{\sqrt{483}}$	$-\sqrt{\frac{11}{23}}$

Table 3.1: The transition dipole moments for the π transitions $|N,0\rangle \to |N+1, M_N = 0\rangle$ and the spin-stretched $\sigma_\pm$ transitions $|N, |M_N| = N\rangle \to |N+1, |M_N| = N+1\rangle$.

that

$$\begin{aligned}\frac{\mathrm{d}\left\langle\psi_i\right| H \left|\psi_i\right\rangle}{\mathrm{d}E} &= \frac{\mathrm{d}\mathcal{E}_i}{\mathrm{d}E} \\ &= \frac{\mathrm{d}\mathcal{E}_i^{\mathrm{Rot}}}{\mathrm{d}E} + \frac{\mathrm{d}\mathcal{E}_i^{\mathrm{DC}}}{\mathrm{d}E} \\ &= 0 - \frac{\mathrm{d}(E\left\langle\psi_i\right| d_z \left|\psi_i\right\rangle)}{\mathrm{d}E} \\ &= -\left\langle\psi_i\right| d_z \left|\psi_i\right\rangle ,\end{aligned} \tag{3.20}$$

where $\mathcal{E}_i$ is the eigenenergy associated with eigenstate $|\psi_i\rangle$. The value of this induced dipole moment is shown in figure 3.4(b) for $\tilde{N} \leq 4$ and $M_N = 0$. We also show the induced dipole moment and its relation to the shape of the wavefunction in figure 3.6, plotting the wavefunction in this way illustrates the common interpretation that the electric field "aligns" the molecules along the z axis.

We can also explicitly calculate the terms in the $|N, M_N\rangle$ basis. If we replace

$\boldsymbol{E}$ with $\hat{z}$ in equation (3.15) then the matrix elements become

$$\begin{aligned}\langle N, M_N|\, d_z\, |N', M'_N\rangle = \\ d_0 \int\int Y^*_{N,M_N}(\theta,\phi)\cos(\theta) Y_{N',M'_N}(\theta,\phi)\mathrm{d}^2\Omega \\ = d_0\sqrt{(2N+1)(2N'+1)}(-1)^{M_N} \\ \times \begin{pmatrix} N & 1 & N' \\ -M_N & 0 & M'_N \end{pmatrix}\begin{pmatrix} N & 1 & N' \\ 0 & 0 & 0 \end{pmatrix}.\end{aligned} \tag{3.21}$$

It is worth highlighting a key property of this formula. If we set $N = N'$ then equation (3.21) is exactly zero, we can interpret this as for any of the pure rotational states there is no laboratory-frame dipole moment! The physical reason for this is that the spherical harmonics have a definite parity whilst for a dipole moment to exist this symmetry must be broken.

To determine the remaining elements of the dipole operator we can use foresight to calculate for $\sigma_+ = (\hat{x} + i\hat{y})/\sqrt{2}$, $\sigma_- = (\hat{x} - i\hat{y})/\sqrt{2}$ and $\pi = \hat{z}$, which are the matrix elements for transitions that change M_N by $+1$, -1 and 0 respectively. These are represented by the terms $d_j = d_0 Y_{1,j}$ and so give

$$\begin{aligned}&\langle N, M_N|\, d_j\, |N', M'_N\rangle = \\ &d_0 \int\int Y^*_{N,M_N}(\theta,\phi) Y_{1,j}(\theta,\phi) Y_{N',M'_N}(\theta,\phi)\mathrm{d}^2\Omega = \\ &d_0\sqrt{(2N+1)(2N'+1)}(-1)^{M_N}\begin{pmatrix} N & 1 & N' \\ -M_N & j & M'_N \end{pmatrix}\begin{pmatrix} N & 1 & N' \\ 0 & 0 & 0 \end{pmatrix},\end{aligned} \tag{3.22}$$

where $j = -1, 1, 0$ for σ_+, σ_-, π transitions.

Dipole-Dipole Interactions

The reason to care about the preceding section is to arrive at a system of permanent dipoles that can be engineered to interact. This necessiates a brief journey into many-body physics. If we consider a system of two molecules in the plane, as in figure 3.7, then classically the dipole-dipole interaction is given by

$$V_{\mathrm{dd}} = \frac{\boldsymbol{d_1}\cdot\boldsymbol{d_2} - 3(\boldsymbol{d_1}\cdot\hat{\boldsymbol{R}})(\boldsymbol{d_2}\cdot\hat{\boldsymbol{R}})}{r^3}. \tag{3.23}$$

To transform this equation into a quantum-mechanical form we must replace the vectors $\boldsymbol{d_i}$ with the expectation values of operators. As the dipole oper-

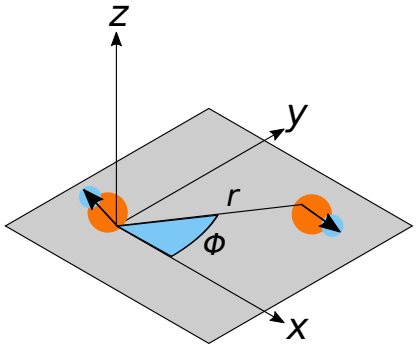

Figure 3.7: The coordinate system used to define the interaction between two molecules. The z axis is fixed by an external electric or magnetic field and is used as a quantisation axis. The molecules are confined to the perpendicular $x-y$ plane.

ators we have previously determined would act on separate state-spaces for molecules i and j it is convenient to form a new ij state space. We will represent the dipole operators for the k-th molecule as $\boldsymbol{D}_k^{(q)}$, where q represents a spatial axis. Explicitly this is

$$\begin{aligned} D_i^{(q)} &= d_i^{(q)} \otimes \mathbb{1}_j, \\ D_j^{(q)} &= \mathbb{1}_i \otimes d_j^{(q)}. \end{aligned} \tag{3.24}$$

We additionally construct the vector of operators $\boldsymbol{D}_k = (D_k^{(x)}, D_k^{(y)}, D_k^{(z)})$ such that we can expand out the scalar products in Cartesian coordinates. Noting that, with our constraint that the molecules lie in the plane, $\boldsymbol{R} = (r\cos(\Phi), r\sin(\Phi), 0)$. The dipole-dipole interaction then becomes

$$\begin{aligned} V_{\text{dd}} = \frac{1}{r^3}\Bigg(&\left[D_i^{(x)} D_j^{(x)} \left[1 - 3\cos^2(\Phi)\right] + D_i^{(y)} D_j^{(y)} \left[1 - 3\sin^2(\Phi)\right]\right] \\ &- 3\cos(\Phi)\sin(\Phi)\left[D_i^{(x)} D_j^{(y)} + D_i^{(y)} D_j^{(x)}\right] + D_i^{(z)} D_j^{(z)}\Bigg). \end{aligned} \tag{3.25}$$

However for calculations on molecules that have quantum numbers N, M_N these Cartesian operators are not convenient. Using the same form as in equation (3.22) we can convert the dipole operators into ones for circularly polarised light. Doing so, and expanding out the trigonometric functions gives [109]:

$$\begin{aligned} V_{\text{dd}} = \frac{1}{r^3}\Bigg(&\left[D_i^{(0)} D_j^{(0)} + \frac{D_i^{(+)} D_j^{(-)} + D_i^{(-)} D_j^{(+)}}{2}\right] \\ &- \frac{3}{2}\left[D_i^{(+)} D_j^{(+)} e^{-2i\Phi} + D_i^{(-)} D_j^{(-)} e^{+2i\Phi}\right]\Bigg). \end{aligned} \tag{3.26}$$

This form of the dipole-dipole interaction is often used in quantum magnetism Hamiltonians such that molecules can represent pseudo-spins on a tight lattice. I will outline how one could do so here.

The first step is to define a useful basis to work in. Commonly these are the lowest rotational or pendular states with $M_N = 0$ [72, 106], which have on-site Ising energies as well as "flip-flop" interactions. Our basis is for the states: $\{|\downarrow_k\rangle = |\tilde{N} = 0, M_N = 0\rangle_k,\ |\uparrow_k\rangle = |1, 0\rangle_k\}$, $|\Psi_{ij}\rangle \in \{|\downarrow_i\downarrow_j\rangle, |\downarrow_i\uparrow_j\rangle, |\uparrow_i\downarrow_j\rangle, |\uparrow_i\uparrow_j\rangle\}$. We then calculate the matrix elements for molecules i, j, noting that we expect there to be 16 elements (a 4×4 matrix) due to the number of basis states

$$H_{ij} = \sum_{n,m} \left|\Psi_{ij}^n\right\rangle \left\langle\Psi_{ij}^n\right| V_{\mathrm{dd}} \left|\Psi_{ij}^m\right\rangle \left\langle\Psi_{ij}^m\right|, \tag{3.27}$$

for $0 \leq n, m \leq 4$. We can also note here that the states we have chosen as a basis only have matrix elements for $D_k^{(0)}$ and so the Hamiltonian for the interaction between i and j is given by the matrix

$$H_{ij} = \frac{1}{r^3} \begin{pmatrix} d_\downarrow^2 & 0 & 0 & d_{\uparrow\downarrow}^2 \\ 0 & d_\downarrow d_\uparrow & d_{\uparrow\downarrow}^2 & 0 \\ 0 & d_{\uparrow\downarrow}^2 & d_\downarrow d_\uparrow & 0 \\ d_{\uparrow\downarrow}^2 & 0 & 0 & d_\uparrow^2 \end{pmatrix}, \tag{3.28}$$

where $d_\downarrow$ and $d_\uparrow$ correspond to the expectation value of $\boldsymbol{d}$ for $|\downarrow\rangle$ and $|\uparrow\rangle$ respectively. The terms $d_{\downarrow\uparrow}$ are the transition dipole matrix elements $|\downarrow\rangle \rightarrow |\uparrow\rangle$, values of these for the bare rotational states can be found in Table 3.1. The diagonal elements of this Hamiltonian correspond to Ising energies. The terms in $|\uparrow_i\downarrow_j\rangle\langle\downarrow_i\uparrow_j|$ and the conjugate, correspond to flip-flop interactions. The terms in $|\uparrow_i\uparrow_j\rangle\langle\downarrow_i\downarrow_j|$ and its conjugate are also flip-flops, but because there is a requirement of two spin excitations these are often far off-resonant and so neglected.

3.5.2 AC Stark Effect

The AC Stark shift caused by light with electric field $\boldsymbol{E}$ is governed by the Hamiltonian

$$H_{\mathrm{AC}} = -\boldsymbol{E} \cdot \boldsymbol{\alpha} \cdot \boldsymbol{E}. \tag{3.29}$$

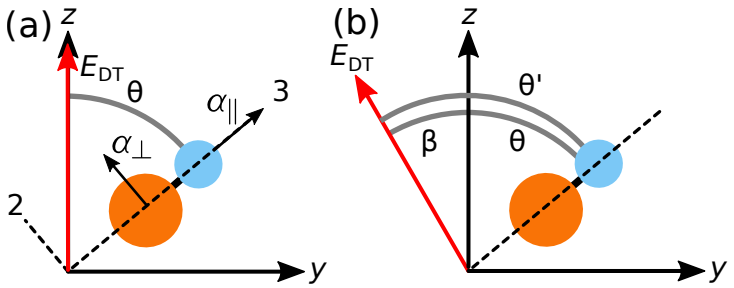

Figure 3.8: The coordinate systems needed to describe the polarisability of the RbCs molecule. (a) A linearly polarised dipole trapping laser, propagating along x (perpendicular to the page), is polarised along z, which also acts as the quantisation axis for a molecule. Highlighted are two of the components of the polarisability $\alpha_{\|}$ and $\alpha_{\perp}$ and their axes in the molecule's coordinate system. The third component is perpendicular to the page with magnitude $\alpha_{\perp}$. (b) The dipole trapping laser's polarisation is rotated by β about x. This forms a new coordinate system where the inter-nuclear axis of the molecule is at an θ' to the electric field of the laser.

Where the polarisability, $\boldsymbol{\alpha}$, of a molecule is given by the tensor:

$$\boldsymbol{\alpha} = \begin{pmatrix} \alpha_{11} & \alpha_{12} & \alpha_{13} \\ \alpha_{21} & \alpha_{22} & \alpha_{23} \\ \alpha_{31} & \alpha_{32} & \alpha_{33} \end{pmatrix}, \tag{3.30}$$

if we use the coordinate system shown in figure 3.8(a) this tensor can be simplified as $\alpha_{11} = \alpha_{22} = \alpha_{\perp}$, $\alpha_{33} = \alpha_{\|}$ and all other terms are zero. At first it is convenient to assume that the molecule, lying at some angle θ to the z axis, has z-polarised light incident. For this case the electric field in the molecule's coordinate frame (with numerical labels) is

$$\boldsymbol{E} = E \begin{pmatrix} 0 \\ \sin(\theta) \\ \cos(\theta) \end{pmatrix}, \tag{3.31}$$

where $E = |\boldsymbol{E}|$ is the magnitude of the laser's electric field. Expanding out equation (3.29) gives the expression

$$H_{\mathrm{AC}} = \left[\alpha_{\|} \cos^2(\theta) + \alpha_{\perp} \sin^2(\theta)\right] \times |E|^2, \tag{3.32}$$

we can replace the E^2 with a scaled intensity $I/(2\epsilon_0 c)$ from the definition of the Poynting vector [110]. Equation (3.32) can be rewritten in a

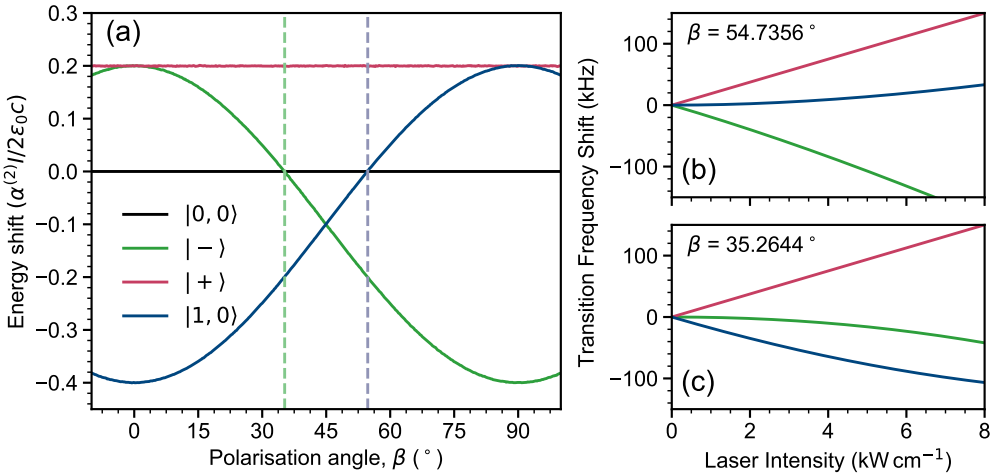

Figure 3.9: The AC Stark shift of an RbCs-like rigid rotor. (a) The AC Stark shift of the lowest two rotational levels is shown as a function of the angle β. The dashed vertical lines indicate the magic angles. The states are determined in the rigid rotor basis, $|\pm\rangle$ corresponds to the linear superpositions: $|N=1, M_N=+1\rangle \pm |N=1, M_N=-1\rangle/\sqrt{2}$. (b) The intensity dependence of the transition frequencies between $(N=0, M_N=0)$ and the states in $N=1$ at the magic angle 54.7356°. The lines are coloured as in (a). We have used the values of the polarisability for RbCs at $\lambda = 1064$ nm to perform this calculation. (c) As in (b) but at the second magic angle: 35.2644°.

more convenient form by making the substitutions $\alpha^{(0)} = (\alpha_\parallel + 2\alpha_\perp)/3$ and $\alpha^{(2)} = 2 \times (\alpha_\parallel - \alpha_\perp)/3$

$$H_{\mathrm{AC}} = \left(\alpha^{(0)} + \alpha^{(2)} P_2\left[\cos(\theta)\right]\right) \times \frac{I}{2\epsilon_0 c}, \tag{3.33}$$

$\alpha^{(0)}$ is known as the isotropic part of the polarisability and has no angular dependence, whilst $\alpha^{(2)}$ is the anisotropic part, with its term depending on the second Legendre polynomial $P_2(x) = (3x^2 - 1)/2$. We can now calculate the matrix elements which correspond to the first, $H^{(0)}_{\mathrm{AC}}$, and second, $H^{(2)}_{\mathrm{AC}}$, terms in equation (3.33). As with the DC Stark effect we will use our knowledge that the wavefunctions in the $|N, M_N\rangle$ basis are given exactly by the spherical

harmonics

$$\begin{aligned}\langle N, M_N|\, H_{\mathrm{AC}}^{(0)}\, |N', M_N'\rangle = \\ \frac{I\alpha^{(0)}}{2\epsilon_0 c}\int\int Y_{N,M_N}^{*}(\theta,\phi)\, Y_{N',M_N'}(\theta,\phi)\,\mathrm{d}^2\Omega = \\ \frac{I\alpha^{(0)}}{2\epsilon_0 c}\delta_{N,N'}\delta_{M_N,M_N'},\end{aligned} \tag{3.34a}$$

$$\begin{aligned}\langle N, M_N|\, H_{\mathrm{AC}}^{(2)}\, |N', M_N'\rangle = \\ \frac{I\alpha^{(2)}}{2\epsilon_0 c}\times\sqrt{\frac{4\pi}{5}}\int\int Y_{N,M_N}^{*}(\theta,\phi)\, Y_{2,0}(\theta,\phi)\, Y_{N',M_N'}(\theta,\phi)\,\mathrm{d}^2\Omega = \\ \frac{I\alpha^{(2)}}{2\epsilon_0 c}\times\sqrt{(2N+1)(2N'+1)}(-1)^{M_N}\times \\ \begin{pmatrix} N & 2 & N' \\ M_N & 0 & -M_N' \end{pmatrix}\begin{pmatrix} N & 2 & N' \\ 0 & 0 & 0 \end{pmatrix}.\end{aligned} \tag{3.34b}$$

Where in equation (3.34a) we have used the orthonormality of the spherical harmonics to remove terms where $N \neq N'$ and $M_N \neq M_N'$, which gives us the expected diagonal Hamiltonian. In equation (3.34b) we have first rewritten $P_2\left[\cos(\theta)\right]$ as a spherical harmonic $Y_{2,0}$ with an appropriate normalisation constant, this is so that we can then use equation (3.16) to perform the integration.

Whilst these terms are correct it is somewhat limiting to only be able to describe lasers polarised along the z axis. If we want to rotate the polarisation of our laser by an angle β we must first rewrite the term for the anisotropic Stark shift[2] in a new coordinate system, which we will designate with θ', ϕ' [107]

$$\begin{aligned}\frac{2\epsilon_0 c}{\alpha^{(2)} I}\times H_{\mathrm{AC}}^{(2)}(\theta',\phi') &= \sqrt{\frac{4\pi}{5}}Y_{2,0}(\theta',\phi') \\ &= \sqrt{\frac{4\pi}{5}}\sum_M D_{M,0}^2(0,\beta,0)Y_{2,M}(\theta,\phi)\end{aligned} \tag{3.35}$$

where $D_{M,0}^2(\alpha,\beta,\gamma)$ is the Wigner rotation matrix. In our example the rotation was simply about the propagation axis (x) so only one of the three Euler angles was necessary and we can make the substitution $D_{M,0}^2(0,\beta,0) =$

[2]Because the isotropic shift has no angular dependence it is the same in all coordinate systems.

$d^2_{M,0}(\beta)$ *i.e.* replacing the Wigner rotation matrix for the *reduced* Wigner rotation matrix. Substituting this into equation (3.34b) gives

$$\begin{aligned}
&\langle N, M_N|\, H^{(2)}_{\mathrm{AC}}\, |N', M'_N\rangle \\
&= \frac{I\alpha^{(2)}}{2\epsilon_0 c} \times \sqrt{\frac{4\pi}{5}} \int\int Y^*_{N,M_N}(\theta,\phi)\, Y_{2,0}(\theta',\phi')\, Y_{N',M'_N}(\theta,\phi)\, \mathrm{d}^2\Omega \\
&= \frac{I\alpha^{(2)}}{2\epsilon_0 c} \times \sqrt{\frac{4\pi}{5}} \int\int Y^*_{N,M_N}(\theta,\phi) \left(\sum_M d^2_{M,0}(\beta) Y_{2,M}(\theta,\phi)\right) Y_{N',M'_N}(\theta,\phi)\, \mathrm{d}^2\Omega \\
&= \frac{I\alpha^{(2)}}{2\epsilon_0 c} \times \sum_M d^2_{M,0}(\beta) \sqrt{(2N+1)(2N'+1)}(-1)^{M_N} \\
&\qquad\qquad \times \begin{pmatrix} N & 2 & N' \\ M_N & M & -M'_N \end{pmatrix} \begin{pmatrix} N & 2 & N' \\ 0 & 0 & 0 \end{pmatrix}.
\end{aligned} \tag{3.36}$$

These terms are not immediately obvious and we will describe some special cases shortly. It is important to note that we have non-zero elements for $|N' - N| = 0, 2$ and $0 \leq |M'_N - M_N| \leq 2$.

The first special case is where $\beta = 0$ or when equation (3.36) reduces to equation (3.34b). In this case the matrix elements, for $N = N' = 1$ are

$$\langle 1, M_N|\, H^{(2)}_{\mathrm{AC}}(0)\, |1, M'_N\rangle = -\frac{1}{2\epsilon_0 c} \begin{pmatrix} -\frac{1}{5}(\alpha^{(2)} I) & 0 & 0 \\ 0 & \frac{2\alpha^{(2)} I}{5} & 0 \\ 0 & 0 & -\frac{1}{5}(\alpha^{(2)} I) \end{pmatrix}, \tag{3.37}$$

and so the AC Stark effect is (mostly) diagonal when the electric field of the trapping laser is along the quantisation axis. The Hamiltonian is only mostly diagonal as there are higher order terms such as: $-2\epsilon_0 c \times \langle 0, 0|\, H^{(2)}_{\mathrm{AC}}\, |2, 0\rangle = \alpha^{(2)} I/\sqrt{5}$.

Another case that may be of interest is when the trapping laser is polarised perpendicularly to the z axis, $\beta = 90°$

$$\langle 1, M_N|\, H^{(2)}_{\mathrm{AC}}(90°)\, |1, M'_N\rangle = -\frac{1}{2\epsilon_0 c} \begin{pmatrix} \frac{\alpha^{(2)} I}{10} & 0 & -\frac{1}{10}(3\alpha^{(2)} I) \\ 0 & -\frac{1}{5}(\alpha^{(2)} I) & 0 \\ -\frac{1}{10}(3\alpha^{(2)} I) & 0 & \frac{\alpha^{(2)} I}{10} \end{pmatrix}. \tag{3.38}$$

In this case only states with $M_N = 0$ are un-mixed, with $M_N = \pm 1$ being coupled by the off-diagonal elements. We also have non-zero matrix elements

for $\langle 0,0|\, H^{(2)}_{\rm AC}\, |2,0\rangle$ and $\langle 0,0|\, H^{(2)}_{\rm AC}\, |2,\pm 2\rangle$ and similar for higher N.

The final case we will show is a little more difficult to immediately recognise, if we start by giving the matrix elements for the $N = N' = 1$ states for an arbitrary value of β

$$\begin{aligned}&\langle 1, M_N|\, H^{(2)}_{\rm AC}(\beta)\, |1, M'_N\rangle \\ &= -\frac{\alpha^{(2)} I}{2\epsilon_0 c}\begin{pmatrix} \frac{1-3\cos^2(\beta)}{10} & \frac{3\cos(\beta)\sin(\beta)}{5\sqrt{2}} & \frac{-3\sin^2(\beta)}{10} \\ \frac{3\cos(\beta)\sin(\beta)}{5\sqrt{2}} & \frac{3\cos^2(\beta)-1}{5} & -\frac{3\cos(\beta)\sin(\beta)}{5\sqrt{2}} \\ \frac{-3\sin^2(\beta)}{10} & -\frac{3\cos(\beta)\sin(\beta)}{5\sqrt{2}} & \frac{1-3\cos^2(\beta)}{10} \end{pmatrix},\end{aligned} \tag{3.39}$$

where we see that all the diagonal terms in M_N have the same angular dependence[3], give-or-take a factor of -1, and so for a special angle we can remove all the diagonal terms at once. The value of this angle is $\beta_{\rm Magic} = \arccos\left(1/\sqrt{3}\right) \approx 54.7356°$. The matrix elements then reduce to

$$\langle 1, M_N|\, H^{(2)}_{\rm AC}(\beta_{\rm Magic})\, |1, M'_N\rangle = -\frac{\alpha^{(2)} I}{2\epsilon_0 c}\begin{pmatrix} 0 & \frac{1}{5} & -\frac{1}{5} \\ \frac{1}{5} & 0 & -\frac{1}{5} \\ -\frac{1}{5} & -\frac{1}{5} & 0 \end{pmatrix}. \tag{3.40}$$

There are indeed now no diagonal elements in the matrix for the AC Stark effect, however as we show in figure 3.9(b), this doesn't mean there are no energy shifts.

3.6 Hyperfine

In a heteronuclear molecule there are two nuclei with their own intrinsic nuclear spins, their interactions cause small (when compared to the rotational structure) changes in the energy level structure. The effect of the interactions between nuclear spins is called the hyperfine structure, we have not described the "fine" structure as in the electronic ground state of bialkalis $S = 0$. In this section we will consider the hyperfine structure of a general bialkali AB, *i.e.* $A, B \in \{\mathrm{Li}, \mathrm{Na}, \mathrm{K}, \mathrm{Rb}, \mathrm{Cs}, \mathrm{Fr}\}$, with a few references specifically to RbCs.

The hyperfine Hamiltonian consists of three terms [98, 111, 112]

$$H_{\rm HF} = H_{\rm Quad} + H_{\rm Spin-Spin} + H_{\rm Spin-Rotation}. \tag{3.41}$$

[3]This dependence extends beyond $N = 1$ as well.

The first term is the nuclear quadrupole interaction and is non-zero only for nuclei with $i > 1/2$. This term arises from the interaction between the nuclear quadrupole and the electronic electric field gradient. This term is given by [113, 114]

$$H_{\text{Quad}} = \sum_{j=\text{A,B}} -(eqQ)_j \frac{3(\boldsymbol{i}_j \cdot \boldsymbol{N})^2 + 3/2(\boldsymbol{i}_j \cdot \boldsymbol{N}) - \boldsymbol{i}_j^2 \cdot \boldsymbol{N}^2}{2i_j(2i_j - 1)(2N - 1)(2N + 3)}, \tag{3.42}$$

$(eqQ)_j$ is the quadrupole coupling constant of nucleus j. This term only has an impact on states with $N > 0$.

The second term that we will consider is $H_{\text{Spin-Spin}}$, which itself consists of two terms, the first is the *scalar* spin-spin interaction

$$H^{(0)}_{\text{Spin-Spin}} = c_4 \boldsymbol{i}_\text{A} \cdot \boldsymbol{i}_\text{B}, \tag{3.43}$$

which arises from electron-mediated dipolar interactions. For RbCs in the ground state at zero magnetic field this term is dominant[4]. The next term is the *tensor* spin-spin interaction which also includes direct magnetic dipolar interactions as well as indirect contributions. It is given by the expression [115]

$$H^{(1)}_{\text{Spin-Spin}} = c_3 \frac{3(\boldsymbol{i}_\text{A} \cdot \boldsymbol{N}) \cdot (\boldsymbol{i}_\mathbf{B} \cdot \boldsymbol{N}) + 3(\boldsymbol{i}_\text{B} \cdot \boldsymbol{N}) \cdot (\boldsymbol{i}_\text{A} \cdot \boldsymbol{N}) - 2N(N+1)(\boldsymbol{i}_\text{A} \cdot \boldsymbol{i}_\text{B})}{(2N + 3)(2N - 1)}. \tag{3.44}$$

The final term we must consider to accurately represent the hyperfine structure with no external fields is $H_{\text{Spin-Rotation}}$, which arises from the interaction between the magnetic moments of the nuclei and the magnetic field generated by the rotation of the molecule. This is given by

$$H_{\text{Spin-Rotation}} = \sum_{j=\text{A,B}} c_j \boldsymbol{N} \cdot \boldsymbol{i}_j. \tag{3.45}$$

The hyperfine structure splits the $2N + 1$ rotational sub-levels into $(2N + 1)(2i_\text{A} + 1)(2i_\text{B} + 1)$ sub-levels. In RbCs this gives 32 sub-levels in the ground state and 96 in the first excited state. In the ground state these levels are divided into manifolds, defined by $F = 2, 3, 4, 5$ and separated by multiples of the scalar spin-spin coupling constant. This splitting is highlighted in figure 3.1(e) where the Zeeman structure at low magnetic fields are shown.

[4]The usage of c_3 and c_4 as the symbols for the coefficients is based on convention. The terms have been presented in order of significance to the ground state structure of RbCs

3.6.1 Zeeman Effect

When compared to the atomic case the magnetic interaction in the molecule is extremely weak, as both electrons are paired they do not provide a magnetic moment and so only the nuclei contribute. The interaction with magnetic field is therefore weaker by the ratio $\mu_{\mathrm{N}}/\mu_{\mathrm{B}}$. The Zeeman term in the Hamiltonian therefore has only nuclear spin and rotational components

$$H_{\mathrm{Zeeman}} = -g_{\mathrm{r}}\mu_{\mathrm{N}}\boldsymbol{N}\cdot\boldsymbol{B} - \sum_{j=\mathrm{A,B}} g_{\mathrm{N}}^{j}\mu_{\mathrm{N}}\boldsymbol{i}_j\cdot\boldsymbol{B}. \tag{3.46}$$

As the magnetic field has terms which act separately on $\boldsymbol{N}$ and $\boldsymbol{i}_{\mathrm{A}}, \boldsymbol{i}_{\mathrm{B}}$ the action of the magnetic field is to split the initially degenerate F states into distinct, decoupled states. In the limit of very high magnetic field the states are well described by the quantum numbers $(N, M_N, m_{\mathrm{A}}, m_{\mathrm{B}})$, whilst at low field the states are well represented with basis states (N, F, M_F).

The Zeeman structure of $N = 0$ in the RbCs molecule is shown in figure 3.1(d) and (e). At low fields the $F = 2, 3, 4, 5$ manifolds are clear and separated by multiples of the scalar spin-spin coupling constant c_4.

3.7 Application to ^{87}Rb^{133}Cs

In this section we combine the results from this chapter to form a full description of the RbCs molecule in external fields. We will describe the evolution of the structure first with the application of magnetic fields, then with DC electric fields. Finally we compare the AC Stark structure to illustrate how the DC electric field can decouple the rotational structure from the nuclear spin and hyperfine structure.

In figure 3.10(a) we show the evolution of the hyperfine states under an increasing applied magnetic field, in this field regime the states in both the ground rotational state and the excited state are being split by their value of M_F. In our apparatus, we produce RbCs molecules at a magnetic field of 181.5 G in the spin stretched state ($M_N = 0, m_{\mathrm{Rb}} = 3/2, m_{\mathrm{Cs}} = 7/2$), which has $M_F = +5$. Under these conditions, this is the lowest hyperfine state in $N = 0$. At this magnetic field, F is no longer a good quantum number

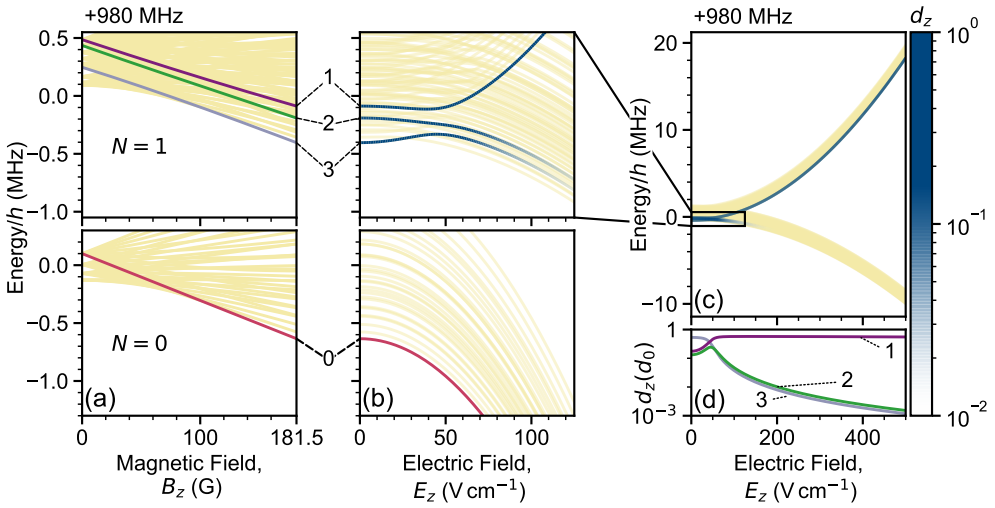

Figure 3.10: The Zeeman and Stark shifts in RbCs with hyperfine structure. (a) The energy of the hyperfine states is shown as a function of the applied magnetic field strength. The states with grand total angular momentum projection $M_F = +5$ are highlighted. In $N = 0$ there is only one state, labelled 0. In $N = 1$ (upper panel) there are three, labelled by an index i in inverted energy order at $E = 0$. (b) The Zeeman split hyperfine energy levels are shown as a function of applied DC electric field strength. The region shown in the upper panel of (b) is highlighted in (c) which shows a larger range of electric field. (d) The transition dipole moment d_z for the π transitions is shown as a function of applied electric field. For high electric field there is only one transition with appreciable transition strength.

but transitions with $\Delta M_F = 0, \pm 1$, provided $\Delta N = 1$, can have a non-zero strength. We have highlighted the three possible transitions with $\Delta M_F = 0$, which correspond to energy levels with $M_F = +5$ and $N = 1$ in figure 3.10(a). Because of the hyperfine interactions described in section 3.6 these states have components with different nuclear spin projections.

In figure 3.10(b) we show the same states at 181.5 G but apply a small electric field < 150 V cm^{-1}. In the ground rotational state all the energy levels remain parallel as each state has the same rotational projection $M_N = 0$. In the first excited state however there is first a pattern of crossings and avoided crossings as the states split according to $|M_N|$. In $N = 1$ the $M_N = 0$ branch is higher in energy than that with $M_N = \pm 1$. In figure 3.10(b) we have coloured each of the lines by the value of the transition dipole moment $|\langle 0| d_z |i\rangle|$ where $|i\rangle$ represents each of the states in $N = 1$. In figure 3.10(c) we take the electric field further to 500 V cm^{-1}. In this figure we have highlighted the region from

figure 3.10(b) to show the rapid change in energy due to the DC Stark shift, which is approximately quadratic with electric field strength. At 400 V cm^{-1} only one state (labelled 1) has any appreciable transition dipole moment with the ground state. We show the evolution of the transition dipole moment as in figure 3.10(b) by shading the appropriate energy level in the Stark map, we also show the numerical values in figure 3.10(d) for the highlighted states in figure 3.10(a).

The application of the DC electric field has split the rotational structure into energy levels characterised by the quantum number M_N. Although there are 32 copies of each level with a given M_N, split by the nuclear Zeeman interaction, the hyperfine interactions no longer have a significant impact on the energy level structure. Each hyperfine state vector $|\Psi_{\mathrm{HF}}\rangle$ is now well represented by

$$|\Psi_{\mathrm{HF}}\rangle = \left|\psi_{\tilde{N},M_N}\right\rangle \otimes |i_{\mathrm{Rb}}, m_{\mathrm{Rb}}\rangle \, |i_{\mathrm{Cs}}, m_{\mathrm{Cs}}\rangle \,, \tag{3.47}$$

where $\left|\psi_{\tilde{N},M_N}\right\rangle$ are the pendular states as given in equation (3.14) and $|i_{\mathrm{Rb}}, m_{\mathrm{Rb}}\rangle \, |i_{\mathrm{Cs}}, m_{\mathrm{Cs}}\rangle$ represent the nuclear spin states.

We now consider the AC Stark shift of RbCs in an off-resonant optical field ($\lambda = 1064$ nm) in two experimentally relevant regimes in figure 3.11. The first is where the 181.5 G magnetic field and hyperfine interactions leave the nuclear spins coupled and where $|\Psi_{\mathrm{HF}}\rangle = |N, M_F\rangle$, this is shown in figure 3.11(a). For $\beta \neq 0°$ the AC Stark effect creates a complex pattern of crossings and avoided crossings, and so the polarisability can only be adequately described locally by the intensity dependent $\mathrm{d}f/\mathrm{d}I$. For the special case of $\beta = 0°$ the Hamiltonian governing the AC Stark shift is almost diagonal, as shown in equation (3.37) and the AC Stark shift is linear, though the transition dipole matrix element does not remain constant for all π transitions. We contrast this behaviour with that when a 300 V cm^{-1} electric field is applied as shown in figure 3.11(b). In this case the hyperfine state vectors are given by equation (3.47) and, for all values of β, the AC Stark shift is linear and so the local polarisability $\mathrm{d}f/\mathrm{d}I$ is independent of intensity.

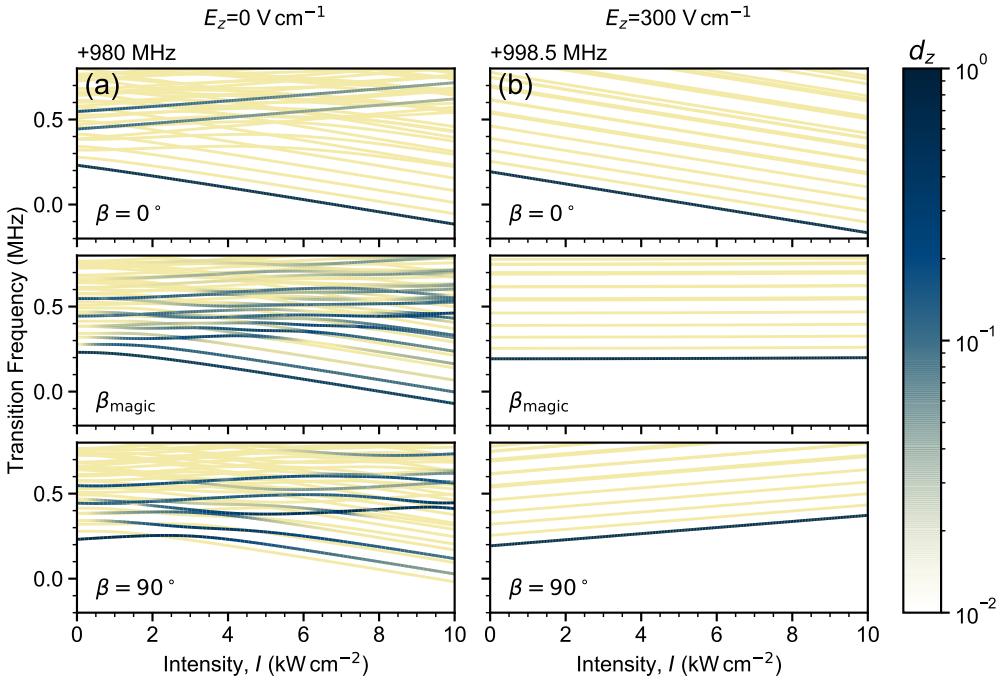

Figure 3.11: A comparison of the AC Stark shift of the transitions to $N = \tilde{N} = 1$ from the hyperfine ground state of RbCs at $\lambda = 1064$ nm without (a) and with an applied electric field of 300 V cm^{-1} (b). We consider three polarisation angles, $\beta = 0°$, β_{magic} and $90°$ in all three cases the Stark structure is vastly simplified . The individual energy levels are shaded by the π transition dipole moment.

3.7.1 Value of Coupling constants

To calculate the energy levels of RbCs the many coupling constants throughout the Hamiltonian must be included. All of the values necessary for the models presented in this chapter are given in Table 3.2. Additionally we present the python 3.7 source code used for performing these calculations in Appendix B.

Constant	Description	Value	Source
i_{Rb}	^{87}Rb nuclear spin	3/2	
i_{Cs}	^{133}Cs nuclear spin	7/2	
d_0	Dipole moment	1.225(3)(8) D	[42]
E_0	Binding energy	$h \times 114\,268\,135.25(3)$ MHz	[92]
$B_{v=0}$	Rotational constant	$h \times 490.173\,994(45)$ MHz	[116]
$D_{v=0}$	Centrifugal distortion constant	$h \times 213.0(3)$ Hz	[101]
$(eQq)_{\mathrm{Rb}}$	^{87}Rb quadrupole coupling constant	$-h \times 809.29(1.13)$ kHz	[116]
$(eQq)_{\mathrm{Cs}}$	^{133}Cs quadrupole coupling constant	$h \times 59.98(1.86)$ kHz	[116]
c_{Rb}	^{87}Rb nuclear spin-rotation coupling constant	$h \times 29.4$ Hz*	[111]
c_{Cs}	^{133}Cs nuclear spin-rotation coupling constant	$h \times 196.8$ Hz*	[111]
c_3	Tensor spin-spin coupling constant	$h \times 192.4$ Hz*	[111]
c_4	Scalar spin-spin coupling constant	$h \times 19.019(105)$ kHz	[116]
g_r	Rotational g-factor	0.0062 *	[111]
$g_{\mathrm{Rb}}(1-\sigma_{\mathrm{Rb}})$	Shielded ^{87}Rb nuclear g-factor	1.8295(24)	[116]
$g_{\mathrm{Cs}}(1-\sigma_{\mathrm{Cs}})$	Shielded ^{133}Cs nuclear g-factor	0.7331(12)	[116]

Table 3.2: Values of the coupling constants relevant to the RbCs hyperfine Hamiltonian. Constants for which the values have been determined using the density-functional theory of [111] have been indicated with an asterisk (*).

Chapter 4

Coherent Control of Molecular States

To realise the potential of ultracold molecules as a viable tool for quantum science we must be able to control the internal degrees of freedom of the molecule. Because of the different energy scales of the molecular degrees of freedom, as shown in figure 3.1, we can spectroscopically choose to address some whilst neglecting others. We choose to focus on the rotational degree of freedom as the associated transition frequencies ($\sim$ 1 GHz) are experimentally convenient as they are in the microwave part of the spectrum. This choice allows us to neglect the electronic and vibrational structure however we must include effects due to the hyperfine structure.

Within the rotational levels we will begin by describing our prior work controlling the internal state and identifying the transitions with theory [116]. We will then describe proof of concept measurements made using a two-level Ramsey system, where the effects of the AC Stark shift (described in greater detail in Chapter 5) on the coherence time are measured. We then expand our discussion to two-photon transitions between rotational levels with measurements of the Autler-Townes effect, Raman spectroscopy and measuring the coherence of a superposition between hyperfine levels in the rotational ground state. Finally we conclude by discussing the use of rotational levels in RbCs molecules as a synthetic lattice dimension.

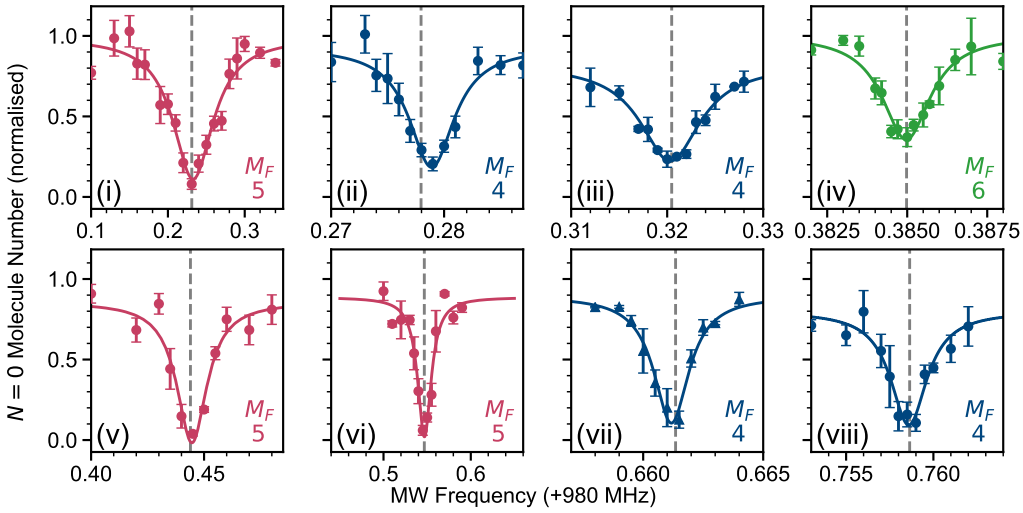

Figure 4.1: Spectroscopy from [116]: reproduced with permission. The 8 transitions with a strong enough dipole moment to drive are shown, the vertical dashed line is the predicted line centre using the molecular constants in Table 3.2. In all cases the microwave Rabi frequency (Ω) and pulse time (τ) are constrained such that $\Omega t < \pi$.

4.1 Internal State Control

The STIRAP process transfers our molecules into a single quantum state of the $X^1\Sigma^+$ electronic potential. To be able to truly exploit the rich internal structure of the molecule we must be able to transfer between the internal states of a given electronic potential. The lowest energy transfers that are electric dipole allowed are transitions between rotational states. In [116] we demonstrated coherent one-photon transfer between rotational and hyperfine states. In this section we will briefly summarise and review those results.

With our two microwave antennas we are able to produce microwave fields polarised along z and y, in principle these are capable of only driving π and $\sigma_\pm$ transitions respectively[1]. In a true rigid rotor these fields would mean we could drive only three possible transitions: $\Delta M_N = -1, 0, 1$, however with the nuclear spins of the Rb and Cs nuclei and hyperfine mixing there are actually 10 transitions which could be driven. This is because the good quantum numbers at 181.5 G are not N, M_N but instead N, M_F. We label states by $(N, M_F)_i$, where i is an index starting from 1 to distinguish states

[1]We actually find that both antennas produce a strong z polarised component, further discussion of this phenomenon is in Chapter 2.6.

by energy at 181.5 G when there are multiple states with the same values of N and M_F.

The strength of a given transition is determined by the squared modulus of the transition dipole moment, which can be reduced by the magnetic field and hyperfine interactions mixing states with different nuclear spin projections. We can illustrate this with an example, which is simplest in the uncoupled basis. The ground state ($N = 0, M_F = +5$) is spin-stretched and so in the uncoupled basis can be represented by $|g\rangle = |N = 0, M_N = 0, m_{\mathrm{Rb}} = 3/2, m_{\mathrm{Cs}} = 7/2\rangle$. For our illustrative example we will take the lowest energy transition $(0, +5) \rightarrow (1, +5)_1$ which is a π transition. At 181.5 G this excited state can only be written as a superposition of multiple states with different nuclear spins but the same M_F [116]

$$|e\rangle = 0.925\,|1, 0, 3/2, 7/2\rangle + 0.087\,|1, 1, 3/2, 5/2\rangle - 0.370\,|1, 1, 1/2, 7/2\rangle\,. \quad (4.1)$$

The electric dipole operator does not affect the nuclear spin degree of freedom and so, because the transition dipole moment for a π transition is given by $\langle g|\, d_z\, |e\rangle$ only the component with the same nuclear spins contributes *i.e.* the first term in equation (4.1). The rigid rotor would have a transition dipole moment of $d_0/\sqrt{3}$, as shown in Table 3.1, therefore the state we are interested in has a dipole moment of $0.925 \times d_0/\sqrt{3} \approx 0.53\ d_0$, or only 85% of the transition strength. For some states this mixing is more severe, weakening the transitions such that they are not observable. As such we only observe 8 of the 10 allowed transitions: these are shown in figure 4.1 and the fitted centres at 181.5 G are summarised in Table 4.1.

We use our hyperfine state selective spectroscopy to determine the values of constants in the molecular Hamiltonian, all the best-fit values are given in Table 3.2. We constrained these constants by repeating the spectroscopy in figure 4.1 at a higher magnetic field of ~ 204.4 G. Because of the interplay between the Zeeman effect and the hyperfine structure these 16 spectroscopic points are enough to constrain 7 of the hyperfine constants. The remaining values are either fixed by measurements in [42, 101] or to theoretical results in [111].

Having characterised the hyperfine structure in an applied magnetic field we are able to demonstrate coherent single-photon control of the internal

State $(N, M_F)_i$	Transition Strength	Magnetic Field (G)	f_{Theory} (kHz)	f_{exp} (kHz)
$(1,5)_1$	0.7314	181.507(2)	980,231.07	980,233(2)
$(1,4)_1$	0.0238	181.484(1)	980,277.96	980,278.9(2)
$(1,4)_2$	0.0461	181.487(1)	980,320.47	980,320.4(2)
				980,321.300(12)*
$(1,6)$	1.0000	181.541(2)	980,384.98	980,384.97(6)
				980,385.569(8)*
				980,385.698(3)*
$(1,5)_2$	0.0027	181.507(2)	980,443.97	980,444.8(7)
$(1,4)_3$	1×10^{-8}	181.5	980,508.39	
$(1,5)_3$	0.0086	181.507(2)	980,546.75	980,546.9(7)
$(1,4)_4$	2×10^{-8}	181.5	980,613.24	
$(1,4)_5$	0.0004	181.487(1)	980,661.35	980,661.15(6)
$(1,4)_6$	0.0044	181.487(1)	980,758.64	980,758.6(1)

Table 4.1: A summary of the spectroscopic data presented in [116]. The entries marked by an asterisk (*) are Ramsey measurements from this work performed in free-space with a nominal magnetic field of 181.5 G, for which we anticipate less than 55 mG of variation day-to-day. States are identified by $(N, M_F)_i$, where i is used to identify states with the same quantum numbers by their energy at 181.5 G. The transition strength $|\langle 0|\, d\, |e\rangle|^2$ is given for transitions from $|0\rangle = |N = 0, M_F = 5\rangle$, relative to the transition $(0,5) \rightarrow (1,6)$. The states $(1,4)_3$ and $(1,4)_4$ are not observed because their transition dipole moments are too small.

structure. This coherence is characterised by Rabi oscillations in free space which do not observably dephase in our $\sim$ ms interaction time. Using these techniques we were able to transfer molecules to the spin-stretched state in $N = 2$ and to a state in $N = 0$ for which the nuclear spin projections are changed [116].

4.2 Derivation of the Ramsey lineshape

In this section we will cover the derivation of the Ramsey lineshape. Our derivation will begin by describing the time dependent interaction between a two-level atom or molecule with an AC field. We then apply this time

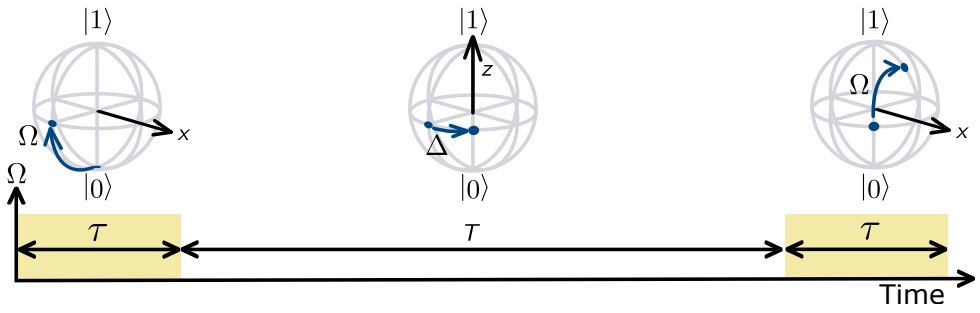

Figure 4.2: A schematic view of a typical Ramsey sequence. Molecules are initially in $N = 0$, the south pole. These are driven up to the equator by near-resonant microwaves of Rabi frequency Ω, where they precess about the polar axis with angular frequency Δ. A second microwave pulse rotates the molecular state about the same axis as the first but only transfers a fraction of the population to $N = 1$.

dependence to the Ramsey sequence to determine a lineshape. Throughout we will neglect additional, nearby, hyperfine levels as in the experiment we can tune our microwave fields to address only a single hyperfine state, as shown in figure 4.1. Similarly we will not include the spontaneous decay of the excited states as this does not affect our molecule on the timescale of experiment.

The Hamiltonian for a two level atom within a frame that co-rotates with an applied electromagnetic field, of angular frequency ω, within the rotating wave approximation is

$$H = \frac{\hbar}{2}\begin{pmatrix} \Delta & \Omega e^{i\phi} \\ \Omega e^{-i\phi} & -\Delta \end{pmatrix}, \tag{4.2}$$

where $\Delta = \omega - \omega_0$ is the detuning of the microwave field frequency from the resonant frequency ω_0. We have set the zero of energy to be exactly between the two energy levels. We have explicitly made the Rabi frequency of the field ($\Omega e^{i\phi}$) complex. The phase angle (ϕ) in a single sequence corresponds to an arbitrary global phase and can usually be disregarded. However in later discussions it will prove useful to have arbitrary phase differences between microwave pulses. To determine how an arbitrary state evolves under this Hamiltonian we need to construct the time evolution operator, starting from the equation of motion [117]

$$U_{\mathrm{MW}} = \exp\left[-\frac{it}{\hbar}H\right], \tag{4.3}$$

which will enable us to study the dynamics of the system. We arrive at this by diagonalising the Hamiltonian, which has two eigenstates

$$|+\rangle = \frac{1}{\Omega}\begin{pmatrix} e^{i\phi}[\Delta + \Omega'] \\ \Omega \end{pmatrix} \tag{4.4a}$$

$$|-\rangle = \frac{1}{\Omega}\begin{pmatrix} e^{i\phi}[\Delta - \Omega'] \\ \Omega \end{pmatrix}, \tag{4.4b}$$

corresponding to eigen-energies of $\pm\hbar\Omega'/2$ where Ω' is the effective Rabi frequency $\sqrt{\Omega^2 + \Delta^2}$. To now determine the expression for U_{MW} we simply diagonalise the Hamiltonian given in equation (4.2)

$$\begin{aligned} \tilde{H} &= D^{-1} H D \\ &= \frac{\hbar}{2}\begin{pmatrix} \frac{\Omega e^{-i\phi}}{2\Omega'} & \frac{\Omega' - \Delta}{2\Omega'} \\ -\frac{\Omega e^{-i\phi}}{2\Omega'} & \frac{\Omega' + \Delta}{2\Omega'} \end{pmatrix}\begin{pmatrix} \Delta & \Omega e^{-i\phi} \\ \Omega e^{-i\phi} & -\Delta \end{pmatrix}\begin{pmatrix} \frac{e^{i\phi}[\Delta+\Omega']}{\Omega} & \frac{e^{i\phi}[\Delta-\Omega']}{\Omega} \\ 1 & 1 \end{pmatrix} \\ &= \frac{\hbar}{2}\begin{pmatrix} \Omega' & 0 \\ 0 & -\Omega' \end{pmatrix}. \end{aligned} \tag{4.5}$$

Finally we rearrange this expression and substitute into equation (4.3) to find our time evolution operator

$$\begin{aligned} U_{\mathrm{MW}}(\Delta, \Omega, \phi, t) &= D \exp\left[-\frac{it}{\hbar}\tilde{H}\right] D^{-1} \\ &= \begin{pmatrix} \cos\left(\frac{\Omega' t}{2}\right) - \frac{i\Delta}{\Omega'}\sin\left(\frac{\Omega' t}{2}\right) & \frac{-i\Omega}{\Omega'}e^{i\phi}\sin\left(\frac{\Omega' t}{2}\right) \\ \frac{-i\Omega}{\Omega'}e^{-i\phi}\sin\left(\frac{\Omega' t}{2}\right) & \cos\left(\frac{\Omega' t}{2}\right) + \frac{i\Delta}{\Omega'}\sin\left(\frac{\Omega' t}{2}\right) \end{pmatrix}, \end{aligned} \tag{4.6}$$

where t is the time elapsed since the interaction between the field and the molecule began.

The operator in equation (4.6) describes a single rotation on the Bloch sphere. The axis of rotation is controlled by the detuning Δ and phase ϕ of the microwave pulse. Within a single pulse the phase is global and so can be neglected, as such we choose to describe $\Delta = 0$, $\phi = 0$ rotations as being about the x axis, as shown in figure 4.2. The angle that the state vector is rotated by is given by $\Omega' t$. Allowing this operator to continue to act on the same state leads to oscillation in the populations in $|0\rangle$ and $|1\rangle$. These oscillations are known as "Rabi oscillations" or "Rabi flopping". We consider

that molecules are initially in state $|0\rangle = \left(\begin{smallmatrix}1\\0\end{smallmatrix}\right)$ and that we are concerned only with the population remaining in the initial state, which evolves as

$$\begin{aligned} |\langle 0|\psi(t)\rangle|^2 &= |\langle 0| U_{\mathrm{MW}} |\psi_0\rangle|^2 \\ &= \left|\cos\left(\frac{\Omega' t}{2}\right) - \frac{i\Delta}{\Omega'}\sin\left(\frac{\Omega' t}{2}\right)\right|^2 \\ &= \cos^2\left(\frac{\Omega' t}{2}\right) + \frac{\Delta^2}{\Omega'^2}\sin^2\left(\frac{\Omega' t}{2}\right), \end{aligned} \tag{4.7}$$

where, for $\Omega' t = \pi$ and $\Delta = 0$, the population is perfectly transferred from $|0\rangle$ to $|1\rangle$ and vice versa.

In figure 4.2 a schematic of the Ramsey method is shown, with the axes that the populations rotate around indicated for each stage of the sequence. The diagram shows an idealised case where a near-perfect $\pi/2$ pulse puts the molecules into a superposition, then due to a small frequency difference between the microwaves and resonance: a phase rotation around the equator occurs. Finally a second pulse, about the same axis as the first, maps the phase accumulated onto the ground state population. To describe this sequence mathematically we can use U_{MW}. We shall assume that the magnitude of Rabi frequency Ω, pulse time τ, evolution time T and detuning Δ are fixed in a single sequence but allow the phase of the second pulse ϕ to vary with respect to the first, which we fix to be $\phi_0 = 0$. The population in the ground state is given by

$$\begin{aligned} |\langle 0|\psi\rangle|^2 =& |\langle 0| U_{\mathrm{MW}}(\Delta,\Omega,\phi,\tau)\cdot U_{\mathrm{MW}}(\Delta,0,0,T)\cdot U_{\mathrm{MW}}(\Delta,\Omega,0,\tau)|0\rangle|^2 \\ =& \frac{1}{8\Omega'^4}\times\Big[3\left(\Delta^4+\Omega^4\right)+3\Omega'^4+2\Delta^2\Omega'^2 \\ &+4\Omega^2\Bigg(\Delta\Omega'\left[2\sin(\tau\Omega')-\sin(2\tau\Omega')\right]\sin(\Delta T+\phi) \\ &-2\sin^2\left(\frac{\tau\Omega'}{2}\right)\cos(\Delta T+\phi)\left[\left(\Delta^2+\Omega'^2\right)\cos(\tau\Omega')+\Omega^2\right]\Bigg) \\ &+8\Delta^2\Omega^2\cos(\tau\Omega')+2\Omega^4\cos(2\tau\Omega')\Big]. \end{aligned} \tag{4.8}$$

The population in the excited state is found by instead projecting $\langle 1|$ onto

$|\psi\rangle$

$$|\langle 1|\psi\rangle|^2 = \frac{\Omega^2 \sin^2\left(\frac{\tau\Omega'}{2}\right)}{\Omega'^4} \times \left([\Delta + \Omega'] \cos\left[\frac{1}{2}(\Delta T + \tau\Omega' + \phi)\right] + [\Omega' - \Delta] \cos\left[\frac{1}{2}(\Delta T - \tau\Omega' + \phi)\right] \right)^2 . \tag{4.9}$$

It is worth noting that we have made no assumptions about the value of the detuning with respect to the strength of the microwave field, as such this is a general formula. We have also neglected the natural linewidth of the excited state in this discussion: for microwave excitation of RbCs molecules this is appropriate as the $N = 1$ radiative lifetime is $1/\Gamma_0 \sim 6 \times 10^3$ years [118].

4.3 Ramsey Interferometry in Free Space

Since Ramsey's original work [119], his method of separated oscillatory fields now known as the Ramsey method, has been at the forefront of precision measurement in atomic and molecular physics [61, 120–122]. Within molecular physics the Ramsey method has an additional benefit: a superposition of rotational states with opposite parity will have a non-zero electric dipole moment in the laboratory frame. This means that, within the Ramsey sequence, there are also dipole-dipole interactions. In this section we will discuss the application of the Ramsey method described in section 4.2 to rotational superpositions in RbCs.

We begin our investigation of the Ramsey method in RbCs by considering the simple case of molecules in free-space. We prepare a superposition of the spin-stretched states $|0\rangle = |N = 0, M_F = +5\rangle$ and $|1\rangle = |1, +6\rangle$, as the associated transition has the largest transition moment available between $N = 0$ and $N = 1$. For our first measurement we fix $T = 600\,\mu\text{s}$ and use a Rabi frequency $\Omega/2\pi \approx 5\,\text{kHz}$. Figure 4.3 shows the high-contrast fringes that result. The fringes have spacing $\approx 1.5\,\text{kHz}$ and an envelope function that has a width set by $1/(2\tau) \approx 10$ kHz. By fitting equation (4.8) to the data, with only the centre frequency f_0 as a free parameter, we can determine $f_0 = 980.385\,569(8)\,\text{MHz}$. We have only quoted a statistical uncertainty having not investigated potential systematic effects. This hertz-level uncertainty is a three orders-of-magnitude improvement on our previous uncertainty, as

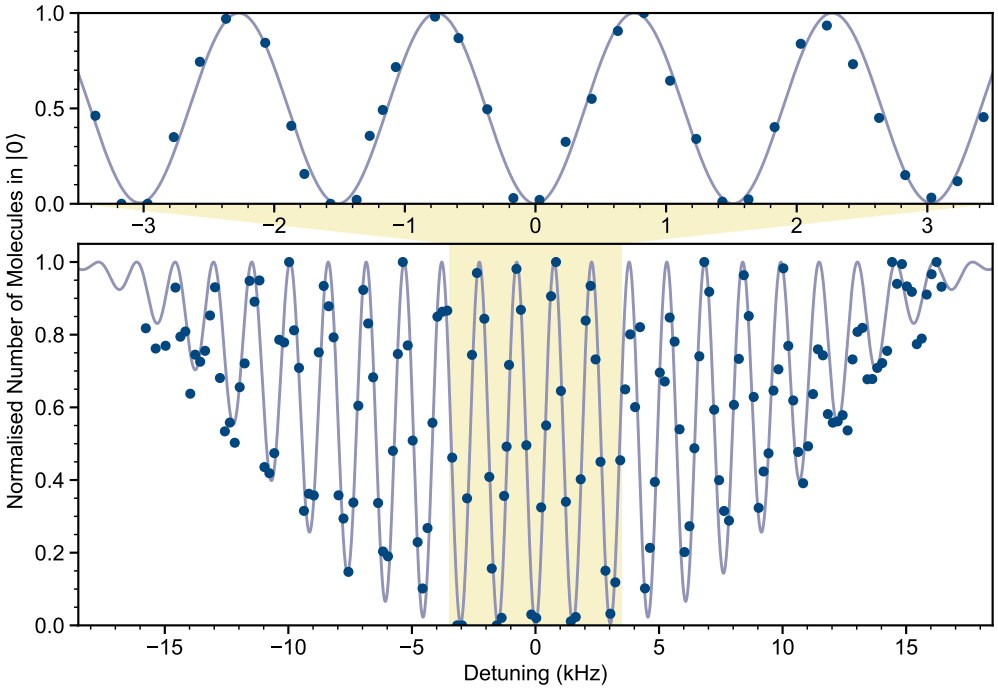

Figure 4.3: High resolution spectroscopy performed using the Ramsey method. The molecule number, normalised to that with no applied microwaves, is shown as a function of the microwave detuning. Each point represents a single experimental run. The $\pi/2$ pulses each have duration $\tau = 47.8\,\mu s$ and the superposition evolves for $T = 600\,\mu s$. The solid line is a fit to equation (4.8) with only the centre frequency as a free parameter. It yields a resonant frequency of 980.385 569(8) MHz, the error quoted is purely statistical.

shown in Table 4.1. This marks a necessary step to be able to observe dipole-dipole interactions between individual molecules in an optical lattice, at a spacing of 500 nm a typical interaction energy is $\sim h \times$ kHz. At our current density (2×10^{11} cm^{-3}) in a bulk gas the interactions are several orders of magnitude weaker $\sim h \times 10$ Hz We investigate the coherence of the superposition of $|0\rangle$ and $|1\rangle$ in free-space by performing a complementary measurement in the time-domain. We fix the microwave frequency to be 980.390 MHz, corresponding to $\Delta/2\pi \approx -5$ kHz. To ensure the detuning is small, compared to our pulses' Fourier width ($\sim 1/\tau$), we increase the microwave power such that the $\pi/2$ pulses are now only 19 µs in duration. We then vary T and map out the Ramsey fringes. These fringes are shown in figure 4.4.

The reduction in the size of fringes could be the result of two mechanisms:

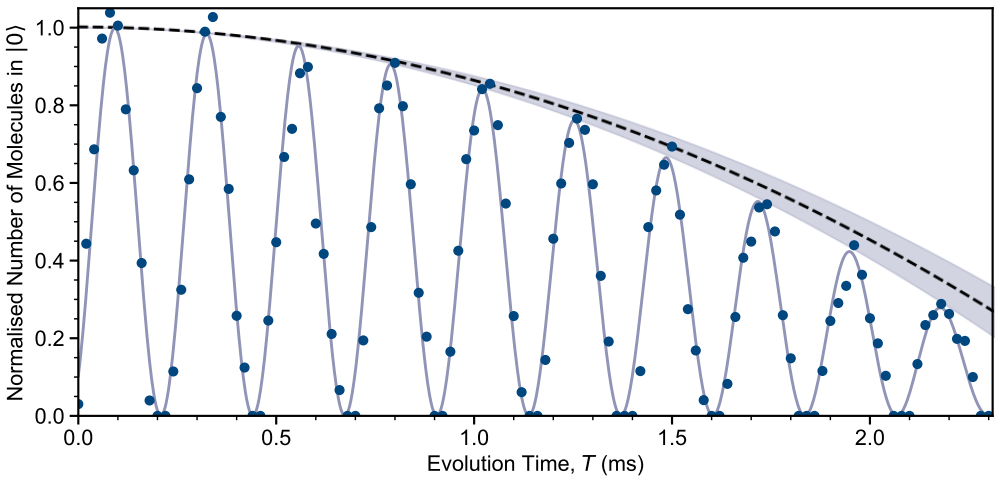

Figure 4.4: For a fixed microwave frequency of 980.390 MHz, we vary the free evolution time, T. We observe Ramsey fringes with a negligible loss of contrast over the 2.3 ms interrogation time. However, we observe a reduction in the molecule number with time as the cloud of molecules falls and expands. The dashed line shows the result of an independent measurement of this effect with an uncertainty indicated by the shaded region. The solid line is a fit to $(1-(T/T_0)^2)\times P_0$, with P_0 given by equation (4.8).

the total number of molecules can decrease or the molecular superposition can decohere, as described in section 4.4. We can discriminate between the two by comparing the changes in the maximum number in a fringe and in the minimum. A change in only the maximum indicates that the total number of molecules is decreasing whereas a change in the minimum and maximum, *i.e.* a reduction in contrast, indicates a loss of coherence. From our a measurements we therefore conclude there is no loss of coherence as the hold time increases to 2.3 ms, there is however a loss of molecules: likely as they fall out of the detection region defined by the STIRAP beams. Although the STIRAP beams have a waist of $\sim 30\,\mu$m, the STIRAP transfer efficiency depends sensitively on the intensity and is optimised only near the focus. To test our hypothesis we independently measure the population in $|0\rangle$ as a function of time in free space; the result is indicated by the dashed line in figure 4.4. We fit $(1-T/T_0)\times|\langle 0|\psi\rangle|^2$ to this measurement (as given by equation (4.8)), with $T_0 = 2.57(4)$ ms. We are additionally able to extract a transition frequency of $f_0 = 980.385\,698(3)$ MHz, where the quoted 3 Hz uncertainty is, as in the spectroscopy from figure 4.3, purely statistical.

The centre frequency extracted from the time domain measurement in figure 4.4 differs from that shown in figure 4.3 by 129(8) Hz, given that our statistical uncertainty is $\sim$ Hz, this is statistically significant. As the microwave source was referenced to an external 10 MHz GPS reference, we believe that the measured frequency difference stems from a difference in the conditions of the experiment on the separate days that the measurements were performed. The Zeeman shift of the transition is -4.8 Hz G^{-1} [116], indicating that the difference is not attributable to a change in the magnetic field (which is $\lesssim 50$ mG day-to-day). The transition is very sensitive to stray electric fields which can be present in the UHV glass cell when not actively controlled [42]. A DC Stark shift of the transition by 129 Hz requires a DC electric field of only 1.2 V cm^{-1}. We discount the possibility of the difference being due to dipole-dipole interactions as, in our bulk gas of peak density $\sim 10^{11}$ cm^{-3}, the interaction strength associated with the transition dipole moment for $(N = 0, M_F = +5) \rightarrow (1, 6)$ is only $\sim h \times 10$ Hz. Alternatively, the difference may result from a more subtle systematic effect such as coupling to nearby hyperfine states; the Fourier widths of the microwave pulses (21 kHz and 53 kHz for figure 4.3 and figure 4.4 respectively) are similar to the spacing between neighbouring hyperfine states. As two different pulse times are used it would be reasonable to expect that this effect would create a difference between the two Ramsey measurements presented.

4.3.1 The Phase Control Method

An alternative implementation of the Ramsey method is to use phase modulation rather than the detuning to map out fringes. This method can be interpreted as changing the axis x in figure 4.2 by rotating it by an angle ϕ about z, corresponding to the phase difference between the two pulses. This method allows us to directly measure the phase that has accumulated due to the finite detuning between the microwave source and the molecular resonance.

To observe Ramsey fringes we choose $|0\rangle = |N = 0, M_F = +5\rangle$ and $|1\rangle = |1, +4\rangle_2$, where the subscript indicates that this is the second state with these quantum numbers counting up in energy at 181.5 G. In figure 4.5 we

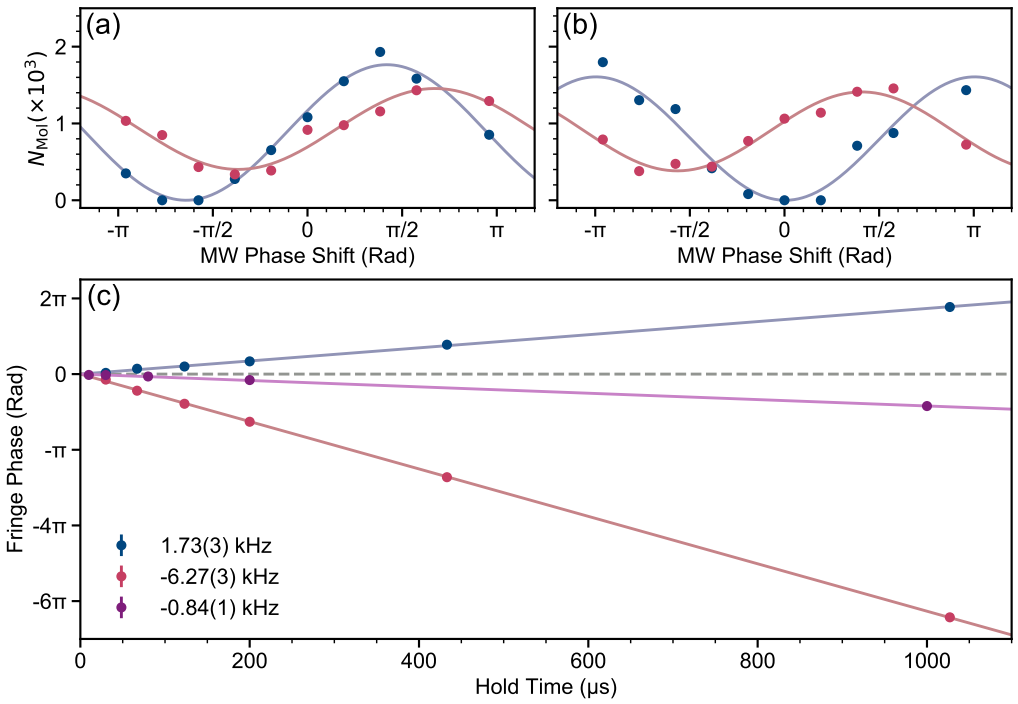

Figure 4.5: Ramsey fringes measured with the phase control method for $|0\rangle = |N = 0, M_F = +5\rangle$ and $|1\rangle = |1, 4\rangle_2$. (a)The ground state molecule number (N_{mol}) as a function of the phase of the second $\pi/2$ pulse. Fringes are measured by varying the phase of the second pulse with respect to the first after an evolution time of 30 μs for red and blue detuning as indicated by the red and blue colour respectively. (b) As in (a) with a 200 μs evolution time. (c) By mapping the evolution of the phase of the fringes as a function of the evolution time (T in figure 4.2) the detuning for fixed frequencies can be extracted, in this panel an additional detuning is shown in purple, corresponding to a near resonance condition. The dashed line shows the behaviour when the microwave field is fixed to resonance. Combined these measurements give a resonant frequency of 980 321.300(12) kHz.

show the evolution of the phase of Ramsey fringes with time. For various hold times up to 1 ms we map out phase fringes, examples can be seen in figure 4.5(a) and (b) for 30 μs and 200 μs respectively. Because we are varying the microwave axis around the Bloch sphere the phase is only defined modulo 2π. To overcome this we fit the detuning using as few phase windings as possible and unpack the phase parameter. We expect that this is reasonable as previous measurements have given us estimates of the transition frequency to ~ 1 kHz precision [116]. We combine the three measurements in figure 4.5(c) using a weighted mean to give the best estimate of the resonant

frequency $f_0 = 980\,321.300(12)$ kHz [123]. We highlight that as in our previous Ramsey measurements the error quoted is the statistical error due to the fit and we have not investigated potential systematic effects. The value of f_0 found using this method disagrees with the previous best estimate of $980\,320.4(2)$ kHz [116] by almost 1 kHz which we cannot definitively explain however it is likely for the same reason as the discrepancies observed earlier in this section.

4.4 Decoherence of Ramsey Fringes

The Ramsey fringes presented in the preceding section were free of measurable decoherence. For many of the proposals using ultracold molecules in a quantum simulator an optical lattice is a necessary component [124]. Additionally, by trapping the molecules the interrogation time can be increased improving the resolution of the Ramsey measurement, for molecules in a $^1\Sigma$ state only optical traps are suitable due to the lack of appreciable magnetic moment. When optically trapped there is the possiblity that the differential AC Stark shift between the rotational states can provide a decoherence mechanism. In this section we will briefly review the ways in which decoherence can manifest in a general two-level system before investigating the effect of the AC Stark shift on the coherence we observe in superpositions of states in $N = 0$ and 1.

4.4.1 Decoherence mechanisms

There are two possible mechanisms for the loss of contrast in a superposition state each of which has a characteristic $1/e$ time scale. The first timescale T_1 is related to loss of population from the excited state. The second T_2 is related to the loss of coherence, mathematically this is the decay of the off-diagonal elements of the density matrix.

The first mechanism, loss of population, is due to spontaneous emission of the excited state in our case. The decay rate of these transitions is given

by [118]

$$\Gamma = \frac{\omega_0^3}{3\pi\epsilon_0\hbar c^3} |\langle e| \boldsymbol{d} |g\rangle|^2. \tag{4.10}$$

Substituting values appropriate for the $N = 0 \rightarrow 1$ transitions in RbCs ($|\boldsymbol{d}| = d_0/\sqrt{3}$ and $\omega_0/2\pi = 980$ MHz) gives a decay rate of $\Gamma/2\pi = 5.5 \times 10^{-12}$ s^{-1} which corresponds to an excited state lifetime of $1/\Gamma \approx 6 \times 10^3$ years. This is sufficiently long that we will neglect the amplitude damping mechanism.

The second possible mechanism is also known as "phase damping" and is modelled as a series of infinitesimal "kicks" in the transition frequency, changing the rate of phase progression at random. In general the characteristic timescale for the decay of coherence depends on the exact noise distribution. A general discussion can be made which provides some experimental expectations. Firstly we note that the populations, ρ_{00} and ρ_{11}, will not be affected by phase kicks whilst the correlations, ρ_{01} and ρ_{10}, will. Secondly if we assume that the phase kicks follow a Gaussian distribution with variance σ^2 then the coherences will have time dependence [125]

$$\rho_{01}(t) = e^{-(\sigma)^2/2} e^{i\phi_0}. \tag{4.11}$$

where ϕ_0 is the mean phase accumulated in t. If we assume that the phase kicks follow a Brownian path, *i.e.* are delivered at random, then $\sigma^2 = \Gamma t$ and so we arrive at exponential decay of coherences.

4.4.2 Dephasing in an optical potential

We now study the effect of a simple optical trapping on the rotational coherence time of the molecules. We achieve this by recapturing the molecules in an optical trap after the STIRAP transfer to the ground state. The trap consists of two linearly polarised beams with $\lambda = 1550$ nm and waists of $w_{01} = 80$ µm and $w_{02} = 98$ µm, crossing at an angle of 27° in the horizontal plane. We set the polarisation of both beams to be along the direction of the magnetic field with an uncertainty of $< 3°$. The peak intensity of the trap light prior to STIRAP is 37.3 kW cm^{-2} for all the measurements. We vary the intensity of the trap used to recapture the molecules, thereby exploring the effect on the Ramsey sequence of different AC Stark shifts. Creating a trap deep enough to prevent evaporation of the molecules requires a peak

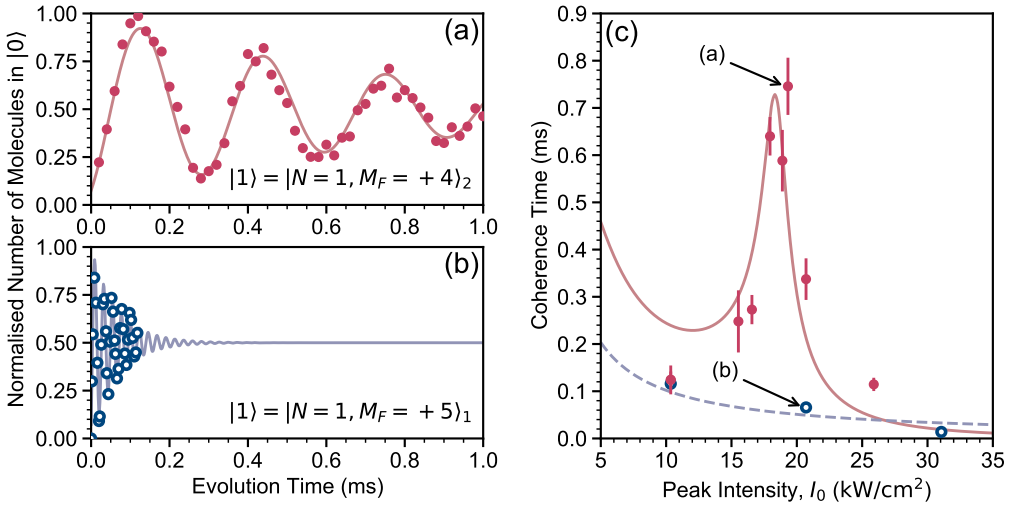

Figure 4.6: Ramsey measurements using RbCs molecules confined in an optical trap. (a) Long-lived Ramsey fringes in a trap with a peak intensity of $I_0 = 19.3$ kW cm^{-2} using a superposition of $|0\rangle = |N = 0, M_F = +5\rangle$ and $|1\rangle = |1, +4\rangle_2$. (b) Rapid dephasing of the Ramsey fringes in a trap with a peak intensity of $I_0 = 20.7$ kW cm^{-2} using a superposition of $|0\rangle$ and $|1\rangle = |1, +5\rangle_1$. In both (a) and (b) each point represents the result of a single experimental run and the solid line is a damped sine-function fit ($\chi^2_{\text{red}} = 0.2, 0.4$ respectively) to the data used to extract a coherence time. (c) The coherence time as a function of the peak intensity of the trap for superpositions of $|0\rangle$ with $|1\rangle = |1, +4\rangle_2$ (filled red points) and $|1\rangle = |1, +5\rangle_1$ (open blue points). The lines represent fits of the simple model described in the text and equation (4.13), showing qualitative agreement with our expectation that the coherence is maximised when the differential AC Stark shift across the sample is minimised.

intensity > 20 kW cm^{-2}, and matching the potential to that experienced by the Feshbach molecules requires a peak intensity of 43 kW cm^{-2}.

The trap holds the molecules in space, removing the loss mechanism we observed in figure 4.4. In principle this increases the time the molecules can be interrogated and therefore the precision of the Ramsey sequence. However, molecules in different parts of the trap experience different intensities, resulting in a spatially varying AC Stark shift of the microwave transition. The initial distribution of the ground-state molecules reflects that of the Feshbach molecules, as the molecules move a negligible distance during the 50 µs that the trap is turned off for STIRAP. The distribution is Gaussian, with standard deviations of $\sigma_z = 6.6$ µm in the vertical direction and $\sigma_{\text{axial}} = 24$ µm in the axial direction. Due to gravitational sag, the centre of the distribution is

$z_0 = 8.1$ μm below the position of peak intensity. Under these conditions, the variation of intensity across the cloud is dominated by the vertical direction and we estimate the 2σ intensity difference to be

$$\Delta I \approx \frac{8 z_0 \sigma_z}{w_0^2} I_0 \approx 0.04 \times I_0. \tag{4.12}$$

Crucially, this depends on the peak intensity I_0, indicating that the spread of intensities is greater for deeper traps. This analysis assumes that the light is switched instantaneously and that the width of the cloud along the vertical does not change. For simplicity, we assume that the molecular distribution and the associated intensity variation remains constant during the measurements. Typical trap oscillation periods are ~ 5 ms, we therefore expect that this approximation is valid for measurements performed in under ~ 0.5 ms. For longer times, the intensity variation will be greater than the above estimate, as the molecular cloud will fall and expand, since all the intensities investigated are below the 43 kW cm^{-2} needed to match the trap potential. Although this effect is undoubtedly important for some of our measurements, this approximate model gives sufficient insight for the present work.

To measure the effect of the trap light on the coherence time, we perform Ramsey measurements by varying T. We use different hyperfine levels of $N = 1$ compared to the free space measurement in section 4.3. Specifically, we investigate superpositions of $|0\rangle = |N = 0, M_F = +5\rangle$ with either $|1\rangle = |1, +4\rangle_2$ or $|1\rangle = |1, +5\rangle_1$. We choose these states as, unlike $(1, +6)$, their transitions are well separated in frequency from other nearby transitions minimising the possibility of off-resonant coupling. To perform each measurement, we turn on the trap light to recapture the molecules in $|0\rangle$. We then wait 400 μs before performing the Ramsey sequence. This ensures that the intensity of the light is stable prior to the measurement; the laser intensity is monitored on a photodiode and stabilised by an active servo loop with a bandwidth of ~ 50 kHz. For each trap intensity, we first determine the transition frequency and measure the Rabi frequency at zero detuning to define the $\pi/2$ pulse duration, τ. For $(1, +5)_1$ we typically use $\tau \approx 2.5$ μs, whilst for $(1, +4)_2$ we use $\tau \approx 12$ μs. The times chosen are a compromise, the shorter times ensure that all molecules within the trapped cloud are addressed while the microwaves have a non-zero detuning Δ. The pulse must also be long enough such that h/τ is smaller than the splittings between

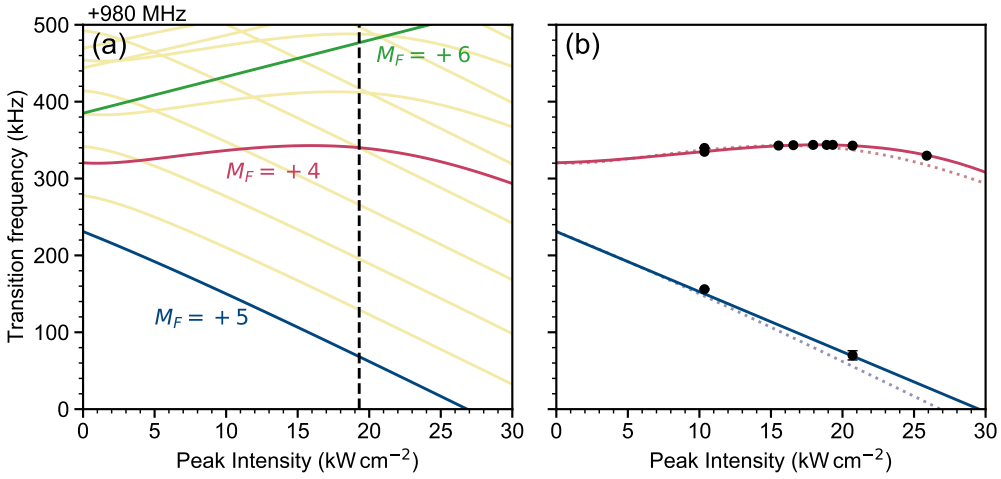

Figure 4.7: (a)The AC Stark shift of relevant transitions for our Ramsey work at a wavelength of $\lambda = 1550$ nm with polarisation along the magnetic field. Transition frequencies are measured from $(N = 0, M_F = +5)$ for $(1, +5)_1$ (red), $(1, +4)_2$ (blue) and (1,+6) (green). The vertical dashed line indicates the intensity of 19.3 kW cm^{-2} where the maximum coherence time was measured in figure 4.6(c). (b) The models used for the fit functions in figure 4.6(c) are shown as solid lines, colours are consistent with (a). The dashed lines are the theory values from (a). The extracted transition frequencies from Ramsey measurements are shown as points, with error bars that cannot be seen at this scale.

neighbouring hyperfine states. Note that the transition to the $M_F = +4$ state is considerably weaker and its strength varies appreciably with trapping laser intensity. For this transition, we must therefore use a longer τ and are limited to smaller detunings, as we can only interact with a smaller frequency range. Figure 4.6(a) and (b) show typical results of such measurements for the two different hyperfine levels. We observe Ramsey fringes which decohere with time as the spatially dependent AC Stark shift across the cloud leads to dephasing. To quantify this effect, we fit each dataset to a sine wave with an exponentially decaying amplitude in order to extract a coherence time τ_c.

The results shown in figure 4.6(a) and (b) exhibit significantly different coherence times for the two transitions, with the peak laser intensity differing by $< 10\%$. The AC Stark shifts of the transitions to $N = 1$ from $N = 0, M_F = 5$ are shown in figure 4.7 for a single beam polarised along the magnetic field[2].

[2]The AC Stark shift is discussed in detail in section 3.5.2 and chapter 5.

For $(N = 1, M_F = +5)_1$, the AC Stark shift is very close to linear. The spread of transition frequencies across the cloud is then simply $\Delta f = (\mathrm{d}f/\mathrm{d}I) \times \Delta I$ and the associated dephasing time is expected to scale inversely with the peak intensity. For the peak intensity of 20.7 kW cm^{-2} shown in figure 4.6(b), we find that a superposition between $(0, +5)$ and $(1, +5)_1$ has a coherence time of 66(5) µs. In contrast, the transition to $(1, +4)_2$ displays a broad avoided crossing around 16 kW cm^{-2}, where $(\mathrm{d}f/\mathrm{d}I) \simeq 0$ and the variation of transition frequency across the cloud is minimised. We observe a significant increase in the coherence time for this state around the avoided crossing, as shown in figure 4.6(c). The maximum coherence time that we measure for $(1, +4)_2$ in the trap is 0.75(6) ms, and is approximately an order of magnitude greater than that achieved using $(1, +5)_1$.

To model the results in figure 4.6(c) we need accurate knowledge of the AC Stark shift of the transitions. The prediction shown in figure 4.7(b) is for the polarisation of the trap light *exactly* aligned with the direction of the magnetic field for a single trapping beam. Even small deviations from this condition can lead to significantly different AC Stark shifts, particularly around an avoided crossing [1]. We therefore use the period of the Ramsey fringes to determine the transition frequency for each intensity, effectively mapping out the AC Stark shift under the conditions of the experiment (i.e. accounting for any small misalignment of the polarisation of the trap beams). For the transition to $(1, +4)_2$, we fit the measured frequencies to a third-order polynomial constrained to the known zero-intensity transition frequency [116]. For the transition to $(1, +5)_1$, we use a simple linear fit.

For a given intensity I, we extract the minimum and maximum transition frequencies in the range $I - \Delta I/2 \rightarrow I + \Delta I/2$ to determine the spread of transition frequencies $\Delta f(I)$ responsible for the dephasing of the Ramsey signal. The total coherence time τ_c is modelled using [126]

$$\tau_\mathrm{c} = \left[\left(\frac{1}{T_2} \right)^2 + (2\pi \times \Delta f(I))^2 \right]^{-\frac{1}{2}}, \tag{4.13}$$

where T_2 is the coherence time from all other sources of decoherence in the experiment, whilst the factor of 2π with $\Delta f(I)$ converts from cycles to radians. The solid lines in figure 4.6(c) show the results of fitting the simple

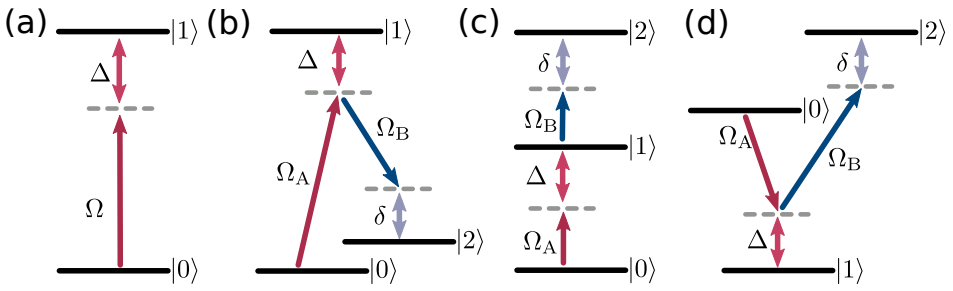

Figure 4.8: A sketch of the two and three level schemes described in this chapter. (a) The two-level molecule. A ground state $|0\rangle$ is coupled to the excited state $|1\rangle$ by radiation detuned by Δ from resonance and driving with a Rabi frequency Ω. (b) The three-level Λ molecule. $|0\rangle$ and $|1\rangle$ are coupled as in (a), the additional level $|2\rangle$ is coupled only to $|1\rangle$ by an additional field of Rabi frequency Ω_B. δ represents the "two-photon" detuning. (c) The ladder three-level system. (d) The V three-level system. In (c) and (d) the couplings and labels are as in (b).

model described by equation (4.13) to the measurements of the coherence time, with T_2 and ΔI as fit parameters. For the transition to $(1, +4)_2$, we find $T_2 = 0.7(2)$ ms and a spread of intensities equal to 3.4(9) % of the peak intensity. The measurements using $(1, +5)_1$ are adequately described by the intensity-dependent dephasing term alone and the fit yields a 2(1) % intensity variation. In both cases, the spread in intensity is in reasonable agreement with the simple estimate of equation equation (4.12). The fitted T_2 time is considerably shorter than the coherence time observed in free space. This is most likely due to the lack of a full dynamical model of the molecular motion leading to an underestimate of the intensity variation for longer evolution times.

4.5 Two-photon Spectroscopy

There are many proposals which utilise multiple resonant fields to couple the rotational states in a coherent manner for applications such as quantum computation [70, 71, 127] and simulation [79, 124]. One which is of particular interest is to use the rotational states of a molecule to form synthetic dimensions [128, 129]. These synthetic dimensions are an interpretation of the internal rotational ladder, where the population in a given rotational state

corresponds to a spin excitation on a lattice of hard-core bosons, *i.e.* constrained to one excitation per "site". In this system control of the tunnelling rates (or spin-exchange rates) between sites is given by the Rabi frequencies on different transitions. It is advantageous to use rotational excitations in molecules for studying synthetic dimensions because the energy level splitting increases with N, allowing individual level couplings to be tuned. To perform these types of experiments we must first develop the tools to couple multiple states simultaneously. In this section we will present our experimental results using two microwave fields simultaneously, first to spectrally observe the dressing of rotational states with a second microwave field then secondly for Raman transfer between hyperfine states of the rotational ground state without populating $N = 1$.

4.5.1 Three Level Molecule

We begin our study of multi-level phenomena by considering the next-simplest case to the two level molecule: the three-level molecule, example systems are shown in figure 4.8. In this case we need two microwave fields, which we will label A and B coupling $|0\rangle \rightarrow |1\rangle$ and $|1\rangle \rightarrow |2\rangle$ respectively. If we set the zero of energy to be the ground state ($|0\rangle$) the Hamiltonian is

$$H = \frac{\hbar}{2}\begin{pmatrix} 0 & \Omega_A & 0 \\ \Omega_A & -2\Delta & \Omega_B \\ 0 & \Omega_B & -2\delta \end{pmatrix}, \tag{4.14}$$

where we have defined the one photon detuning $\Delta = \omega_A - \omega_1 = \Delta_A$ as in the two-level system. The two-photon detuning has been defined to include the one-photon detuning: $\delta = \Delta - \omega_B + (\omega_1 - \omega_2) = \Delta_A - \Delta_B$, where Δ_B is the detuning of the second microwave field from resonance and ω_0, ω_1 and ω_2 describe the energies of states $|0\rangle$, $|1\rangle$ and $|2\rangle$ respectively. We can find the population in the ground state after some time by solving the time-dependent Schrödinger equation

$$i\hbar\frac{\mathrm{d}\psi}{\mathrm{d}t} = H\psi, \tag{4.15}$$

and integrating up to a pulse time τ.

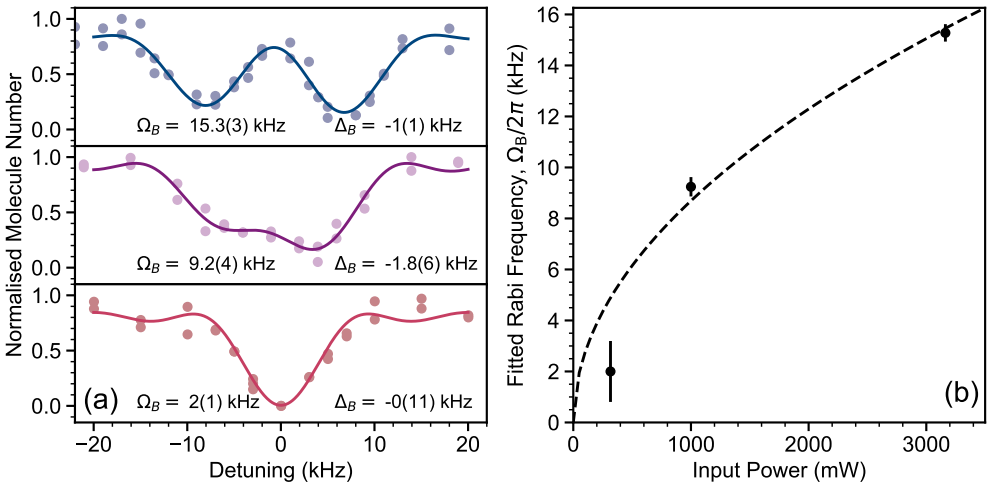

Figure 4.9: Autler-Townes splitting of the $N = 0 \rightarrow 1$ transition in RbCs.(a) The observed spectra for three different powers of microwave applied on the $N = 1 \rightarrow 2$ transition. Each point is the result of a single experimental run. The solid lines are fits to the optical Bloch equations. The fitted upper microwave field detunings Δ_B and Rabi frequencies Ω_B are shown. (b) The upper Rabi frequencies Ω_B extracted from a fit to the optical Bloch equations as a function of input microwave power. A line $\propto \sqrt{P}$ is shown to guide the eye.

4.5.2 The Autler-Townes Effect

The first system we will consider is the Autler-Townes doublet. With a microwave field near-resonant from $|1\rangle \rightarrow |2\rangle$, *i.e.* $|\Delta_B| \rightarrow 0$, we can split state $|1\rangle$ into two dressed states, each with energy given by

$$E_{\pm} = \pm\frac{\hbar}{2}\sqrt{\Delta_B^2 + \Omega_B^2} = \pm\frac{\hbar\Omega_B'}{2}. \tag{4.16}$$

In the limit where $\Delta_B = 0$ the energy splitting between the two features in the doublet is given simply by the Rabi frequency Ω_B. The state vectors associated with these two states are superpositions of $|1\rangle$ and $|2\rangle$. To probe this system we use the third level of our three-level Hamiltonian, keeping $\Omega_A \ll \Omega_B$ to ensure that our probe field doesn't itself create Autler-Townes doublets. We can realise Autler-Townes spectroscopically in separate rotational transitions of the RbCs molecule.

In figure 4.9 we show Autler-Townes spectroscopy of the $N = 0 \rightarrow 1 \rightarrow 2$ ladder system. The lower $(0, 5) \rightarrow (1, 6)$ transition is used as the weak probe with Rabi frequency $\Omega_A/2\pi = 5$ kHz whilst the power, and therefore Rabi frequency, on the upper $(1, 6) \rightarrow (2, 7)$ transition is varied. For an input

microwave power of ~ 3 W a splitting of 15.3(3) kHz is observed. There is a slight asymmetry in the observed lines, by fitting the spectroscopy to the optical Bloch equations we can determine that this is likely due to a detuning of the second microwave field of $\Delta_B/2\pi = -1.7(5)$ kHz. Whilst this was not anticipated it is not surprising, given that the spectral width of our initial one-photon spectroscopy was ~ 10 kHz.

By measuring the splitting as a function of the applied microwave power we can extract the Rabi frequency of the upper transition. This is shown in figure 4.9(b) alongside the expected $\sqrt{P}$ scaling. We see that for the lowest Rabi frequency, the two features cannot be resolved, demonstrating that the Autler-Townes splitting is only significant for $\Omega_B \gg \Omega_A$.

4.5.3 Raman Spectroscopy

When using single-photon pulses to transfer between rotational and hyperfine states we require that there is a non-zero electric dipole moment between the two. This restricts us to transitions between neighbouring rotational states, however there are many interesting applications for ultracold molecules which could utilise either transitions between the same rotational levels or accessing higher rotational levels with no population loss. Both of these can be achieved by using Raman spectroscopy. This section will briefly describe a proof-of-principle measurement on Raman spectroscopy using a rotational ladder system.

Starting from equation (4.14), we can form a quasi-two-level system by fixing the microwave fields to be two-photon resonant (*i.e.* $\delta = 0$) but with a significant one photon detuning *i.e.* when Δ is large compared to the Rabi frequencies Ω_A, Ω_B. By considering the time-dependent Schrödinger equation it can be shown that the $|1\rangle$ component of the state vector evolves as

$$\langle 1|\psi(t)\rangle \approx \left(\frac{1-e^{i\Delta t}}{\Delta}\right)\left[\Omega_{\mathrm{A}} c_0(t) + \Omega_{\mathrm{B}} c_2(t)\right], \tag{4.17}$$

where $c_i = \langle i|\psi\rangle$. Writing the effective two-level Hamiltonian in the new $|0\rangle$, $|2\rangle$ basis

$$H = \frac{\hbar}{4\Delta}\begin{pmatrix} \Omega_{\mathrm{A}}^2 & \Omega_{\mathrm{A}}\Omega_{\mathrm{B}} \\ \Omega_{\mathrm{A}}\Omega_{\mathrm{B}} & \Omega_{\mathrm{B}}^2 - 4\Delta\delta \end{pmatrix}. \tag{4.18}$$

So our new effective Hamiltonian has Rabi frequency $\tilde{\Omega} = \Omega_{\mathrm{A}}\Omega_{\mathrm{B}}/4\Delta$. The advantage of this "Raman" system is that it enables the coupling of levels for which direct transitions are forbidden by selection rules. The mathematics presented here is applicable to any of the three-level systems shown in figure 4.8.

In figure 4.10 we demonstrate the Raman system using the same energy level scheme as we did for the Autler-Townes in section 4.5.2. We first use single-photon spectroscopy to locate the intermediate state ($N = 1, M_F = +6$) and final state $(2, 7)$ and measure Rabi frequencies of $\Omega_A/2\pi = 5.16(6)$ kHz and $\Omega_B/2\pi = 4.25(6)$ kHz respectively. To transfer between $N = 0$ and $N = 2$ without populating $N = 1$ we must setup our Raman system, we do this by detuning the first microwave field from resonance such that $\Delta_A \gg \Omega_A$. In our case we choose $\Delta_A \approx +30$ kHz, this shifts the resonant frequency of the $1 \rightarrow 2$ transition by $-\Delta_A$, spectroscopy of which can be seen in figure 4.10(a). In figure 4.10(d) we show the evolution of the population with both microwave fields on and $\delta = 0$. We compare our measurements to a numerical solution to the three-level optical Bloch equations with our known values of Ω_A and Ω_B. As the effective Rabi frequency scales as $1/\Delta_A$ we expect that the Raman transition dynamics would be much slower than the dynamics of the individual single photon transitions, this can be seen in the Rabi oscillations in figure 4.10(b-d). This slower dynamics gives a longer π-pulse time and so narrower spectroscopy. Future work in this direction will need to utilise a higher power microwave field.

4.5.4 Ramsey Inteferometry in the Rotational Ground State

We are, of course, not limited to the ladder systems presented in the preceding sections. If we instead use a Λ configuration we can use the hyperfine mixing of the rotationally excited state to change the nuclear spin, accessing a different hyperfine level in the rotational ground state. There are numerous reasons why accessing different nuclear spin states is advantageous: firstly it increases the number of energy levels available for quantum computation [4], secondly because the transitions between hyperfine states are electric dipole

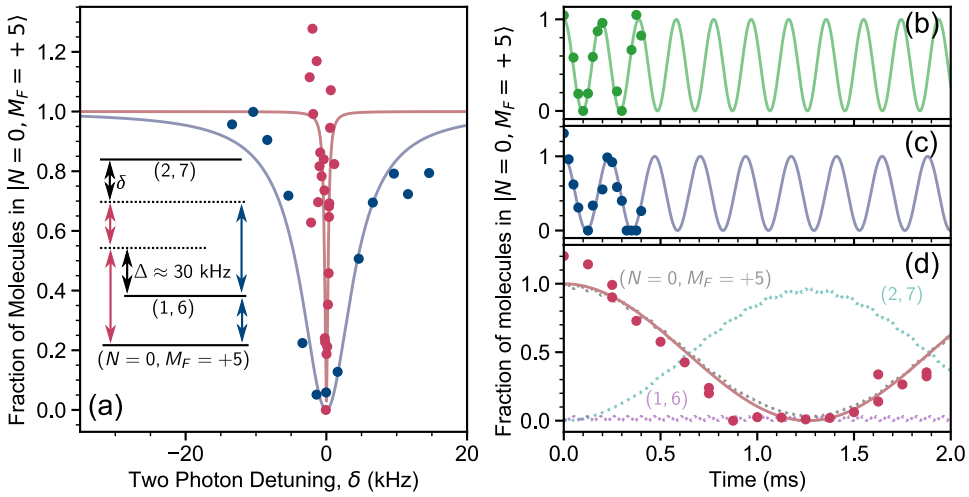

Figure 4.10: Raman transitions between $N = 0$ and $N' = 2$. (a) Spectroscopy of the $(N = 0, M_F = +5) \rightarrow (2, 7)$ transition using two one-photon transition (blue points) and a two-photon Raman transition (red points). The solid lines are Lorentzian fits to the data. For the single-photon transitions we extract a full width at half-maximum (FWHM) of 9(2) kHz, the two-photon transition lineshape has FWHM of 0.55(12) kHz. The energy levels and transitions used are shown inset. (b-c) Single photon Rabi oscillations on the (b) $(0, 5) \rightarrow (1, 6)$ (c) $(1, 6) \rightarrow (2, 7)$ transitions. (d) Two-photon Rabi oscillations on the $(0, 5) \rightarrow (2, 7)$ Raman transition, the solid line is a fit using an effective two-level model. The dashed lines show the expected populations in $N = 0, 1, 2$ (grey, purple, blue) in a true three-level system given the Rabi frequencies in (b) and (c).

forbidden the lifetime of state $|1\rangle$ is longer even than the rotationally excited states meaning there is a possibility of using the molecular levels as a quantum memory.

As a proof-of-concept measurement we use a Raman system to make a two-photon transition between the ground state $(N = 0, M_F = +5)$ and an additional state in $N = 0$: $(0,4)_2$. These two states are split by ~ 200 kHz by the applied 181.5 G magnetic field. In a similar manner to the experiments shown in figure 4.6 we use a $\pi/2$ pulse, of duration 361.5 µs, to create a superposition of the two hyperfine levels of the ground state we are interested in, allow this superposition to evolve for some time T and then, through another $\pi/2$ pulse make a projective measurement of the population in $(0, +5)$. The superposition is able to evolve freely, whilst trapped in the $\lambda = 1550$ nm optical dipole trap. We find that, in this measurement dephasing happens far more rapidly than expected, with a $1/e$ decay time of 0.08(3) s. This is

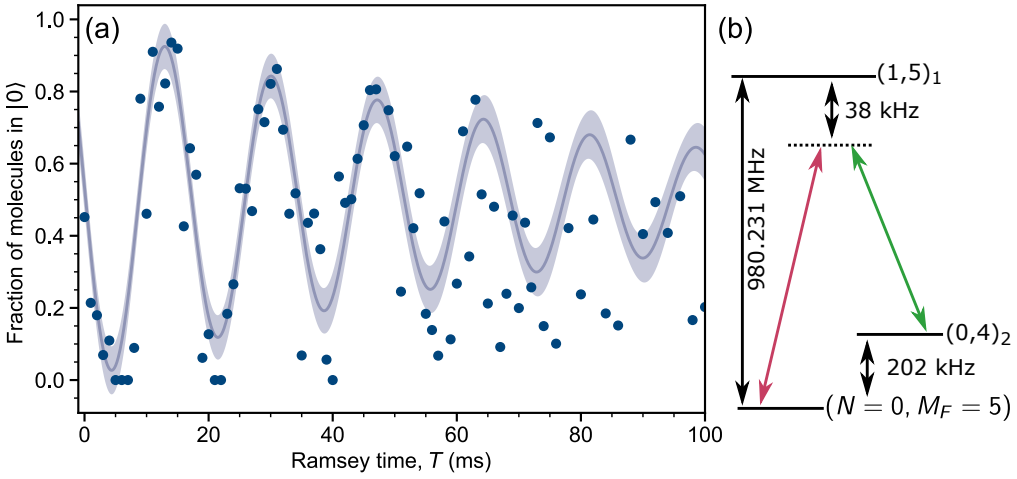

Figure 4.11: Ramsey interferometry using a Raman system (a) Ramsey fringes measured between the $(N = 0, M_F = +5)$ and $(0, +4)_2$ states of RbCs. The solid line shows the line of best fit to a damped sine function, the shaded region shows the error on the fit. The fringes rapidly decay with a coherence time of 0.08(3) s. (b) The transitions used in the Λ energy level configuration for this measurement. The resonant $(0, 5) \rightarrow (1, 5)_1$ transition frequency is shown.

two orders-of-magnitude faster than was observed in a more detailed study of the nuclear spin coherence times of ground state NaK [130].

We have not rigorously investigated the loss of contrast in the ground state, however by considering several possible mechanisms we can estimate potential decoherence times. Firstly we can discount the trapping potential, unlike in the single-photon Ramsey measurements shown in section 4.4 the two states we consider have almost identical AC Stark shifts with leading terms $\propto \alpha^{(0)} I$, we note that the prior work in [130] was able to measure $\sim$ Hz AC Stark shifts between the hyperfine levels in the NaK ground state, these are orders-of-magnitude too small to explain our decoherence. Additionally the trapping light is switched off ~ 100 µs before the two microwave pulses to remove any spatial AC Stark shifts during the microwave transfer, ensuring that the Raman pulses interact with all the molecules. There is however a differential magnetic moment between the two states of approximately 1.3 kHz G^{-1}, our expectation is that the magnetic bias field has approximately 55 mG of Gaussian noise. Combined we would expect 73 Hz of noise on the transition frequency which corresponds to a dephasing time of 14 ms. This estimate

based on the Zeeman shift agrees to an order-of-magnitude with our measurement, suggesting that the nuclear spin coherence time is limited by our magnetic field noise. This effect was not significant for the work of Park *et al.* where the differential magnetic moment was 200 Hz G^{-1} [130, 131] and the magnetic field noise was ±10 mG [132], giving them Hz-level transition frequency noise due to the differential magnetic moment.

To improve upon this measurement with our current experimental hardware we should identify a superposition with less sensitivity to magnetic field. The quantity we compare is

$$\delta\mu = |\langle 0|\,\mu_z\,|0\rangle - \langle 1|\,\mu_z\,|1\rangle\,|, \tag{4.19}$$

where $|0\rangle, |1\rangle$ are the state vectors of the two components of the superposition and μ_z is the magnetic moment operator for a magnetic field along z. We tabulate the value of the magnetic moment for several states in Table 4.2. By choosing two states which have similar magnetic moment we could extend the coherence time of hyperfine states, we are able to identify two such pairs of states: one in $N = 0$ and another in $N = 1$. For $N = 0$ the pair of states $(0,4)_2$ and $(0,3)_1$ has a differential magnetic moment of 71 Hz G^{-1}, corresponding to 4 Hz of frequency noise with our magnetic field stability (or an expected coherence time of $\sim$ 250 ms). For $N = 1$ the states $(1,5)_2$ and $(1,4)_1$ perform even better, with a differential magnetic moment of 27 Hz G^{-1} which could extend the coherence time of hyperfine states to > 0.5 s. Though the sub-levels in $N = 1$ will experience a differential AC Stark shift.

4.6 Outlook: Synthetic Dimensions

In this section we will describe an extension to our coherent control work that, by using more microwave fields, can be used to simulate quantum systems. We will focus our efforts on one model: the Su-Schrieffer-Heeger (SSH) model. This model was originally created to explain the movement of defects in $(CH)_x$ polymer chains [133]. It is also one of the simplest models to study which also has been shown to exhibit topological invariants and edge states [59, 134].

$(N, M_F)_i$	$\mu_z(\mu_N)$
(0,5)	-5.310
$(0,4)_1$	-4.464
$(0,4)_2$	-3.593
$(0,3)_1$	-3.686
$(0,3)_2$	-2.685
$(0,3)_3$	-1.872
$(1,5)_2$	-4.481
$(1,4)_1$	-4.445

Table 4.2: The magnetic moment μ_z is given for selected states in units of the nuclear magneton ($\mu_N \approx 762$ Hz G^{-1}) for various states of RbCs at an applied magnetic field of 181.5 G. States are identified by $(N, M_F)_i$, where i is used to identify states with the same quantum numbers by their energy at 181.5 G.

The many-body Hamiltonian of this SSH system is given by [59]

$$H_{\text{SSH}} = -\sum_{i\in\text{even},j\in\text{odd}} t_{ij}\left[\hat{b}_i^\dagger \hat{b}_j + \hat{b}_j^\dagger \hat{b}_i\right], \tag{4.20}$$

where the $\hat{b}_i(\hat{b}_i^\dagger)$ operator is the bosonic annihilation (creation) operator for site i. This bosonic formulation also includes a hard-core constraint such that $\hat{b}_i^\dagger \hat{b}_i^\dagger = 0$ so that only one bosonic particle occupies one site. The model is fixed such that only the nearest neighbour terms are non-zero, with two values t_1 for hopping from odd sites to even sites and t_2 for the reverse. We can, of course, write this explicitly as a matrix

$$H_{\text{SSH}} = \begin{pmatrix} 0 & t_1 & 0 & 0 \\ t_1 & 0 & t_2 & 0 \\ 0 & t_2 & 0 & t_1 \\ 0 & 0 & t_1 & 0 \end{pmatrix}. \tag{4.21}$$

In this form we have only considered four sites, a schematic of this is shown in figure 4.12. It is well known that there are two configurations of this Hamiltonian one known as the trivial configuration where $t_1 > t_2$ and another, known as the "topological" configuration where $t_1 < t_2$. The configurations are so named because, in momentum space, the trivial configuration has a winding number of zero whilst the topological configuration has a winding number of one [135].

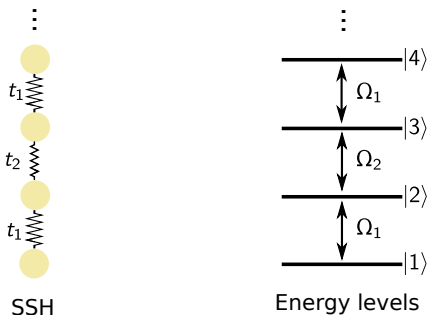

Figure 4.12: A mapping of the Su-Schrieffer-Heeger (SSH) model to the rotational transitions in a molecule. The SSH model represents a periodic modulation of the tunnelling rates between sites in a lattice, we can map this to the rotational states of the molecule using resonant microwave fields with Rabi frequencies Ω_1 and Ω_2.

If we compare equation (4.21) to equation (4.14) we can see that the mapping from the many-body Hamiltonian to the rotational energy states is simple: we have multiple microwave fields of periodic strengths Ω_A and Ω_B with the microwave fields tuned exactly to resonance. We can then make the connection that, in this arrangement, the relative tunnelling parameters are given by the Rabi frequencies Ω_A and Ω_B. In the SSH model the tunnelling amplitudes t_1, t_2 only couple nearest neighbour sites whilst for our rotational states we can only consider nearest neighbours because of the electric dipole selection rules. Additionally each microwave field only couples two rotational states as the rotational splitting between N and $N+1$ increases with N.

Using the internal states of the molecule we can spectroscopically probe the many-body energy levels: to view the spectrum we include an extra state in our model to represent the rotational ground state ($|0\rangle$). We allow $|0\rangle$ to couple only to the first of our simulation states $|1\rangle$ and it does so weakly, with a probe Rabi frequency $\Omega_{\mathrm{P}} \ll \Omega_A, \Omega_B$ and detuning Δ_{P}. We can then solve the time-dependent Schrödinger equation

$$i\hbar \frac{\mathrm{d}}{\mathrm{d}t} |\psi\rangle = \frac{\hbar}{2} \begin{pmatrix} 0 & \Omega_{\mathrm{P}} & 0 & 0 & 0 \\ \Omega_{\mathrm{P}} & -2\Delta_{\mathrm{P}} & \Omega_A & 0 & 0 \\ 0 & \Omega_A & -2\Delta_{\mathrm{P}} & \Omega_B & 0 \\ 0 & 0 & \Omega_B & -2\Delta_{\mathrm{P}} & \Omega_A \\ 0 & 0 & 0 & \Omega_A & -2\Delta_{\mathrm{P}} \end{pmatrix} |\psi\rangle \,, \tag{4.22}$$

to predict where our populations will be for various experimentally relevant parameters.

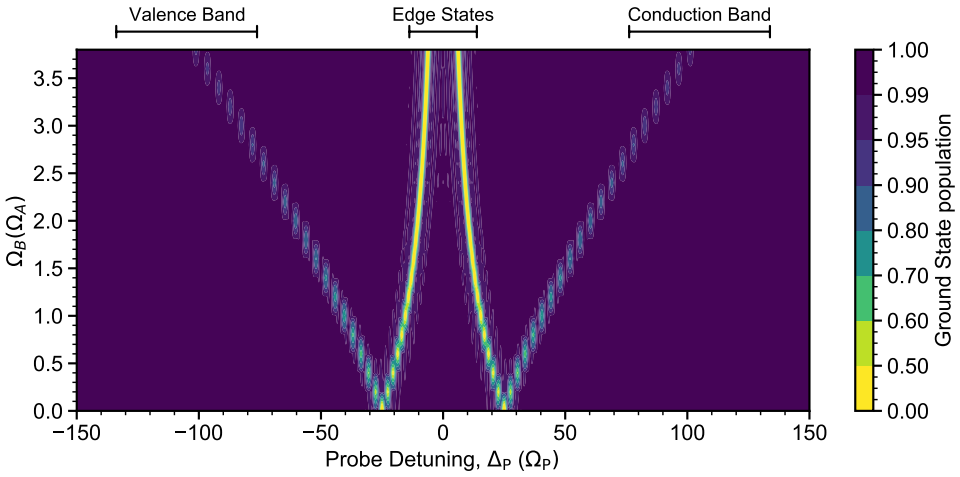

Figure 4.13: Numerical modelling of the rotational SSH model with 3 microwave fields. The ground state population is shown after a microwave pulse with $\Omega_p t = \pi$ as a function of probe detuning (Δ_p) and the second coupling Rabi frequency (Ω_B) in units of Ω_A, which has been chosen to be $\gg \Omega_p$. As Ω_B increases the topological phase becomes more apparent, shown by the splitting of the outermost spectral features and the convergence of the innermost. The innermost features are the topological edge states for $\Omega_B > \Omega_A$. When $\Omega_B < \Omega_A$ these states are part of the conduction and valence bands. Note the non-linear colour map, chosen to keep the outermost features visible as they become weaker.

The first experiment one would likely perform is to study the transition between trivial and topological matter. In figure 4.13 we show this phase transition, as would be seen spectroscopically, for various ratios of Ω_B to Ω_A. For the numerics Ω_A is fixed to $50 \times \Omega_p$ and we use only three microwave fields (four rotational states) which represents the simplest SSH system we could experimentally realise. At $\Omega_B = 0$ the model reduces to the Autler-Townes Hamiltonian explored experimentally in section 4.5.2. As we increase Ω_B the overall spectral splitting increases, however the two strongest spectral features tend towards zero detuning as is expected for edge states. The "true" topological configuration would have these edge states degenerate and there should be a sharp phase transition between the trivial and topological configurations, however due to the small system size this is more gradual.

We now investigate the effects of finite sizes on the numerical spectra, by extending equation (4.22) to include more microwave fields, restricting ourselves to odd numbers (such that the number of simulated lattice sites remains even). These spectra are shown in figure 4.14. For both the trivial and topo-

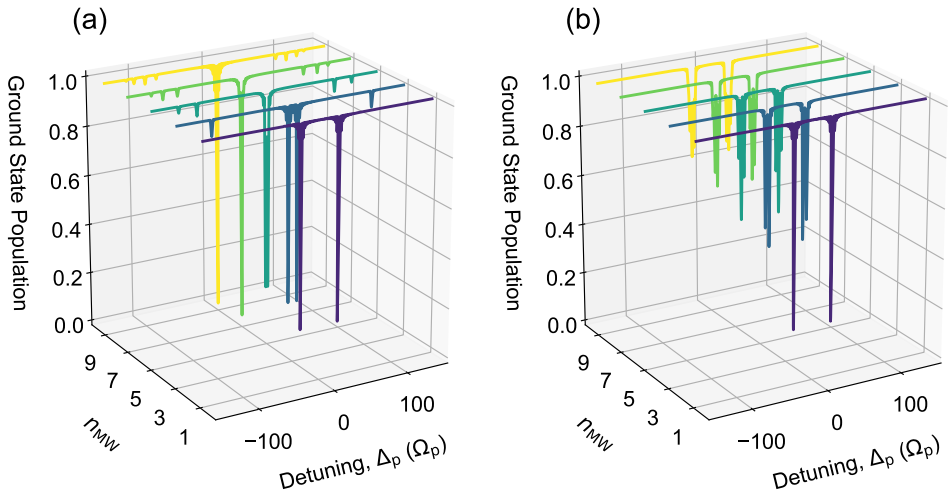

Figure 4.14: Numerical modelling of the rotational SSH model. The ground state population is shown as a function of probe detuning, Δ_p, with a varying number of microwave fields (n_MW). (a) $\Omega_B > \Omega_A$: the topological configuration. Two edge states are clearly visible until $n_\mathrm{MW} = 7$ where the limited frequency resolution merges the states together. (b) $\Omega_B < \Omega_A$: the trivial configuration. No edge states are visible, only the valence and conduction bands. Note that for one microwave field the trivial and topological configurations are identical as the rotational SSH model reduces to an Autler-Townes doublet.

logical configurations we see that the size of the conduction and valence bands increases as the system size grows, this is expected, with their splittings remaining the same: again this is expected as the energy differences are determined by the strengths of Ω_A and Ω_B. The splitting between the edge states however does change as the number of microwave fields is increased. For the topological configuration shown in figure 4.14, $\Omega_A = 50 \times \Omega_\mathrm{p}$, $\Omega_B = 4 \times \Omega_A$, we can see that by the time that $n_\mathrm{MW} = 7$ the two edge states are no longer resolvable with $\Omega_\mathrm{p} t = \pi$. This suggests that only a small number of states is necessary to remove the finite-size effects seen in figure 4.13.

To summarise, within this section we have discussed a possible mapping between a many-body SSH Hamiltonian and a multi-level molecular system. We showed that by varying the strength of Ω_B with respect to Ω_A we can explore both topological and trivial states of the system, with the characteristic topological edge states visible even for three microwave fields. We then examined the point at which finite-size effects are not spectrally resolvable, concluding that by $n_\mathrm{MW} = 7$ we could access true many-body states with

this synthetic dimensional simulator. Whilst this system will require coupling more rotational states than we have previously we can avoid differential AC Stark shifts by using untrapped molecules, for ~ 1 kHz uncertainties a typical spectroscopic pulse will have $\Omega_{\mathrm{p}}/2\pi \sim$ kHz. Thus for the numerical parameters we have chosen: $\Omega_A/2\pi \approx 50$ kHz and $\Omega_B/2\pi \approx 200$ kHz, these are larger than typically used in experiment but not impossible. To avoid subtle effects relating to the hyperfine structure a simple DC electric field of order $\sim 100\ \mathrm{V\,cm^{-1}}$ should suffice.

4.7 Summary

In this chapter we have described the coherent control we have over the internal states of the RbCs molecule. We began by describing proof of concept Ramsey measurements in free-space, which were decoherence free, in which we achieved hertz-level statistical uncertainty. We found that the limiting factor in free-space is the falling and expansion of the molecules from the optimal STIRAP region, after which they are lost. To investigate the effects that optical trapping had on the Ramsey coherence time we performed similar measurements in the presence of $\lambda = 1550$ nm laser light for two distinct superposition states $|N = 0, M_F = +5\rangle + |1, +5\rangle_1$ and $|0, +5\rangle + |1, +4\rangle_2$. We found that the dephasing rate depends strongly on the gradient of the AC Stark shift as a function of laser intensity, finding an optimum coherence time of 0.75(6) ms.

Moving from single-photon measurements we expanded our control scope to include coherent control over a three-level molecule in ladder and Λ configurations. In the ladder system we first investigated the Autler-Townes splitting, demonstrating hyperfine state specific mixing of two rotational levels. We later used this same configuration of states to optimise our equipment for coherent Raman transitions between $N = 0$ and $N = 2$ which is dipole-forbidden. In the Λ configuration we used a Raman transition to create an equal superposition of two hyperfine states in the rotational ground state, where we found dephasing which we attribute to the differential magnetic moment of the two states coupled with our magnetic field noise.

Finally we discussed the possibility of using the many rotational states in RbCs molecules as a synthetic lattice for studying the Su-Schrieffer-Heeger many-body Hamiltonian. We concluded that topological effects are visible with only four simulated lattice sites and that finite-size effects are no longer spectrally resolvable with eight simulated sites.

Chapter 5

The AC Stark Effect and External Fields

There are many proposals that use polar molecules confined in optical lattices for the simulation of novel problems in many-body physics [76–78, 124, 136–140]. These all exploit the long-range dipole-dipole interactions between molecules that can be engineered using applied electric fields and/or superpositions of rotational states. If the molecules are permitted to tunnel between lattice sites, novel quantum phases, including super-solids and spin glasses, are predicted to emerge [76, 77, 136–140]. In contrast, if the molecules are pinned to the lattice sites, pseudo-spin excitations encoded in the rotational states of the molecule can still propagate in the lattice due to spin exchange interactions. Exploiting the rich internal structure of the molecule enables a large range of tunable Hamiltonians to be explored, relevant to quantum magnetism [78–80, 124, 141–143]. In both cases, the majority of proposals require high occupancy in the lattice. This is readily achieved using molecules associated from ultracold atomic gases where uniform filling of the lattice can be achieved via the Mott-insulator transition [144]. Extending this to two atomic species and then forming molecules from the pre-formed pairs on each lattice site leads to high occupancy for the molecules, as demonstrated for ground-state KRb [145] and RbCs Feshbach molecules [146].

To realise a useful simulator, the lattice confining the molecules needs to fulfil several criteria. Firstly, the one-body lifetime, limited by evaporation and

off-resonant scatter, of the molecules in the lattice should be much greater than the timescales associated with the evolution of the Hamiltonian under investigation. Secondly, the light shifts in the lattice need to be controlled such that the coherence of the quantum states under investigation is longer than the characteristic inter-site interaction time. Bialkali molecules typically have permanent electric dipole moments $\sim 1\,\mathrm{D}$, which for a lattice spacing $\sim 500\,\mathrm{nm}$ leads to a dipole-dipole interaction energy $\sim h \times 1$ kHz. Rotational coherence times greater than 10 ms are therefore essential. Finally, for associated molecules it is also desirable that the Feshbach state and the rovibrational ground state of the molecule have identical, or at least very similar, polarisabilities. This is necessary to prevent the molecules being excited into higher bands of the lattice during the optical transfer to the ground state [40, 147]. In the case of RbCs molecules, it has been predicted [148] that this last condition should be satisfied for a lattice wavelength near to 1064 nm.

In this chapter we will study the effect of external AC and DC fields on the rotational and hyperfine structure of RbCs. The effect of a DC magnetic field on the internal structure of RbCs has already been studied in [116], we therefore start by mapping out the DC Stark shift of the first rotational transition, then through comparison to theory are able to locate a region where the molecule is in a "pendular" state. We then study the AC Stark shift at two wavelengths $\lambda = 1550$ nm and 1064 nm, the latter chosen as it is predicted to satisfy the first and third of our criteria for an optical lattice [148]. Finally, to satisfy our second criterion, we study how we can use the DC Stark and Zeeman effects to control the AC Stark shift, finding that with an applied electric field we can reduce the differential Stark shift greatly.

5.1 The DC Stark Effect

Heteronuclear molecules posses a permanent electric dipole moment due to the charge imbalance along the internuclear axis. This means that they interact strongly with electric fields.

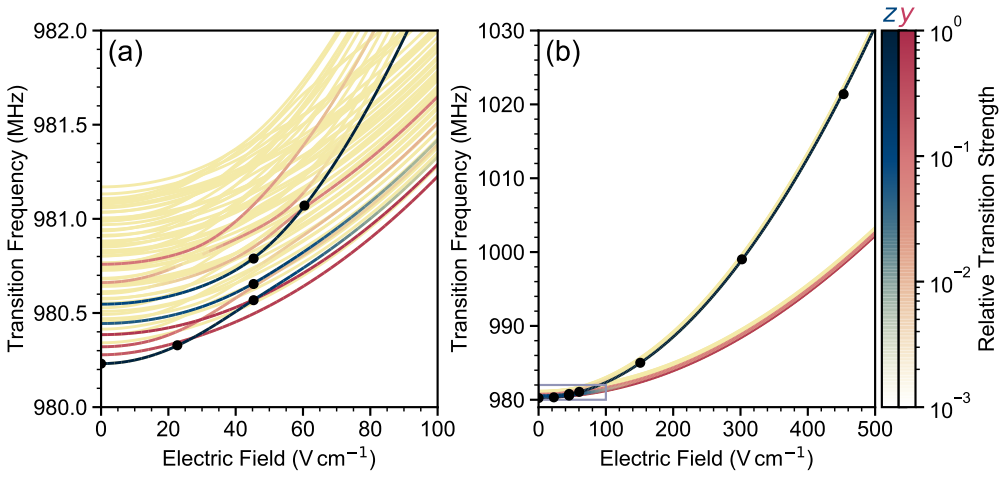

Figure 5.1: The DC Stark shift of transitions to $N = 1$ from $(N = 0, M_F = +5)$ in RbCs as a function of electric field strength, the electric field is directed along the 181.5 G magnetic field. The inset shows the highlighted region at low field. The relative transition strengths are coded as in Fig.4. Each point is the fitted centre frequency from a measured microwave spectrum, with uncertainties of ∼kHz, which are too small to be seen at this scale. As the electric field increases in magnitude the energy levels in $N = 1$ are split into $M_N = 0$ and $M_N = \pm 1$ branches. At high field only one transition can be driven with microwaves polarised along z, whilst at lower fields hyperfine mixing allows multiple transitions, which can be seen clearly at 50 V cm^{-1} where three transitions are observed.

The interaction between the molecule's dipole moment and a static electric field $\boldsymbol{E}_{\mathrm{DC}}$ is described by the expression

$$H_{\mathrm{DC}} = -\boldsymbol{d} \cdot \boldsymbol{E}_{\mathrm{DC}}. \tag{5.1}$$

The matrix elements of the dipole moment operator, $\boldsymbol{d}$, in equation (5.1) are given by[1] [98]

$$\begin{aligned} &\langle N, M_N | \, \boldsymbol{d} \, | N', M_N' \rangle = \\ &\sum_{i=-1,0,+1} d_0 \hat{i} \sqrt{(2N+1)\,(2N'+1)} \cdot (-1)^{M_N} \\ &\times \begin{pmatrix} N & 1 & N' \\ -M_N & i & M_N' \end{pmatrix} \begin{pmatrix} N & 1 & N' \\ 0 & 0 & 0 \end{pmatrix}. \end{aligned} \tag{5.2}$$

where $\hat{i}$ is a unit vector along the axes $x - iy$, z and $x + iy$ for -1, 0, +1 respectively. d_0 is the molecule's permanent molecule-frame dipole moment

[1] A full derivation is in Chapter 3.

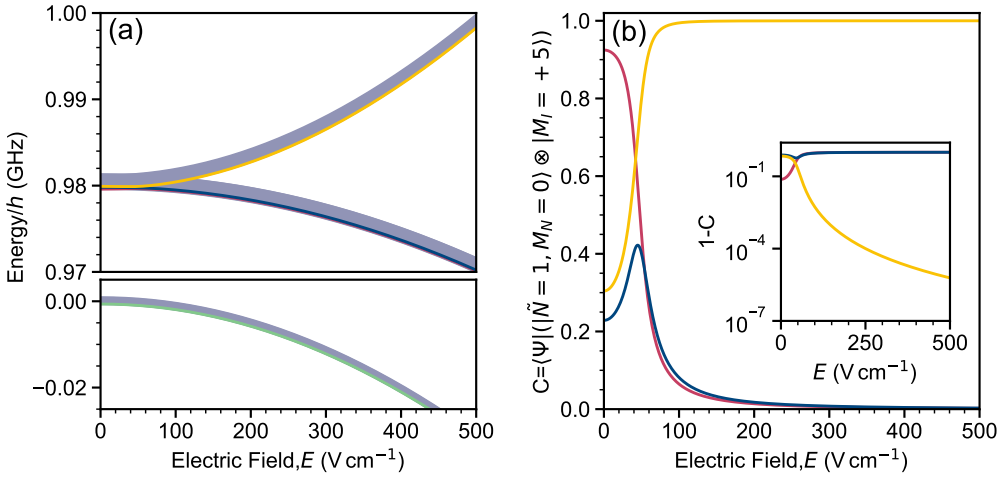

Figure 5.2: The decoupling of the nuclear spin from the rotational angular momentum by an applied electric field. (a) The energy level structure of RbCs in a DC electric field. The states which initially have $M_F = +5$ are highlighted in $\tilde{N} = 0$ (lower panel) and $\tilde{N} = 1$ (upper panel). (b) The overlap of the hyperfine states highlighted in (a) with the pendular state with $\tilde{N} = 1, M_N = 0$ and $M_I = 5$. As the electric field increases only one hyperfine state maintains any overlap with the pendular state. Shown inset is this overlap subtracted from 1 to show the deviation. Note the logarithmic scale.

and the symbols in parentheses are Wigner-3j symbols [108]. In the above expression $i = -1,\ 0,\ 1$ correspond to σ_+, π, σ_- transitions, respectively these can change M_N by $+1,\ 0,\ -1$. We have chosen to restrict that $\boldsymbol{E}_{\mathrm{DC}}$ lies along $\boldsymbol{B}$, which we have designated the z axis, so only the term with $i = 0$ contributes to the DC Stark effect.

We can spectroscopically probe the structure of the excited state within an electric field by using our microwave spectroscopy techniques. We are limited to using pulses with a Fourier width of 50 kHz by a slow drift in the electric field over the ~ 0.1 ms timescale of the experiment.

The experiments are performed in a glass cell, which can be polarised by the electric field applied by our external electrodes. To remove charge build up between shots we irradiate the chamber with up to 3 W of UV light ($\lambda_0 = 365$ nm) which removes the accumulated charges from the surfaces. Additionally we restrict our maximum electric field to 500 $\mathrm{V\,cm^{-1}}$ to limit the rate of charge build up which can cause instabilities within a single experimental run. This field is also the highest we can access with the limited

bandwidth of our microwave antennas.

In figure 5.1 we show the exploration of the first rotational state of RbCs using microwave spectroscopy in an applied electric field. We follow the lowest π transition as a function of applied electric field, until ~ 50 V cm^{-1} where the strongest transition becomes the highest energy. Because of the roughly quadratic dependence on electric field the DC Stark shift very quickly separates the energy levels, by ~ 100 V cm^{-1} there is approximately 1 MHz between the π and $\sigma_\pm$ transitions from $(N = 0, M_F = 5)$[2]. To account for movement in the external electrodes we fit the value of the electric field to the known dipole moment of RbCs, $d_0 = 1.225(3)(8)$ D [42], using our model of the molecule's hyperfine structure.

From the fitted model we can also extract how the state evolution evolves. In figure 5.2(a) we show the energy levels, as extracted from the fitting to figure 5.1 and have highlighted the energy levels that have $M_F = +5$ in $N = 0, 1$. We can calculate the overlap between each of these states and an ideal pendular state by first calculating the DC Stark shift of a rigid rotor, as described in Chapter 3.5.1. We choose the rigid rotor state of interest to be $|\psi_{\mathrm{RR}}\rangle = \left|\tilde{N} = 1, M_N = 0\right\rangle$. We then create a state vector in the hyperfine space by taking the outer product of $|\psi_{\mathrm{RR}}\rangle$ with the spin-stretched nuclear spin state: $|M_I = +5\rangle = |i_{\mathrm{Rb}} = 3/2, m_{\mathrm{Rb}} = 3/2\rangle\,|i_{\mathrm{Cs}} = 7/2, m_{\mathrm{Cs}} = 7/2\rangle$. We show the evolution of the overlap of this state with the hyperfine states with $M_F = +5$ as a function of electric field in figure 5.2(b). It is clear that initially the pendular basis is not a good representation of the hyperfine states, with all three states initially having some overlap with the single target state. However as the electric field increases past 100 V cm^{-1} the overlap with the highest energy state (shown in yellow) increases rapidly with the overlap two lower energy states (blue and red) decreasing. Because there is now only one state with good overlap with the pendular state we conclude that we have decoupled the nuclear spins from the rotational angular momentum.

[2]We are using the same labelling scheme as Chapter 4 when there are multiple states with the same values of N, M_F.

5.2 Determining the Polarisability at $\lambda = 1550$ nm

Our first work on studying the polarisability was performed in a $\lambda = 1550$ nm optical dipole trap. This is the trap in which our molecules are produced and so has some advantages to continuing to use it. Additionally the wavelength of 1550 nm is longer than that associated with the $X^1\Sigma \rightarrow A^1\Sigma, b^3\Pi$ transitions, reducing the risks of off-resonant excitation.

The molecular polarisability for an off-resonant laser beam polarised at an angle θ to the internuclear axis is given by

$$\alpha(\theta) = \alpha^{(0)} + \alpha^{(2)} P_2[\cos(\theta)], \tag{5.3}$$

where $P_2(x) = (3x^2 - 1)/2$ is the second Legendre polynomial. The two parts of the polarisability, $\alpha^{(0)}$ and $\alpha^{(2)}$ are called the isotropic and anisotropic parts respectively. The matrix elements for the AC Stark shift of these components in the lab frame are given in equation (3.34a) and equation (3.36). In short: the isotropic part contributes equally and only to the trapping potential for all rotational levels, the anisotropic part is responsible for the differential AC Stark shift and affects transition frequencies as well as the trapping potential for $N \geq 1$.

This section will describe the determination of the polarisability at $\lambda = 1550$ nm. We begin by describing how we determined the isotropic part of the polarisability, which is the only contributor to the trapping potential in the rotational ground state. We will then describe high precision microwave spectroscopy of the $N = 0 \rightarrow 1$ rotational transitions, from which we can extract the anisotropic part of the polarisability.

5.2.1 Isotropic Polarisability

As described in section 3.5.2 the isotropic part of the polarisability, $\alpha^{(0)}$, corresponds to an equal energy shift of all (N, M_N) whilst the term proportional to $\alpha^{(2)}$ is only non-zero for $N > 0$. Therefore in the rotational ground state only $\alpha^{(0)}$ contributes to the trapping potential. The value of this component can be found either by direct trap frequency measurements, *e.g.* through

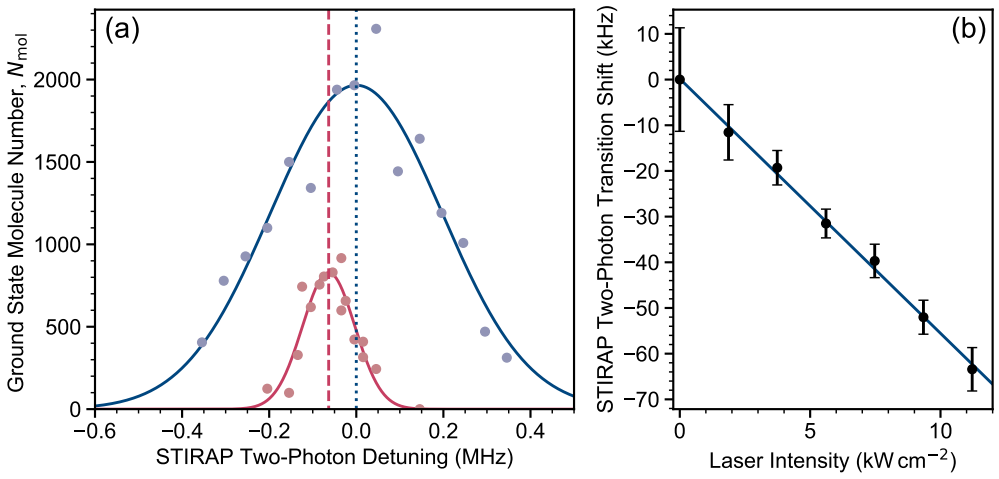

Figure 5.3: Measurement of the isotropic polarisability of RbCs in the rovibrational ground state using the AC Stark shift of the two-photon STIRAP resonance. (a) Spectroscopy of the two-photon STIRAP transition in free-space (blue points) and in a 1550 nm laser of peak intensity 11.2(3) kW cm^{-2} (b) The shift of the STIRAP two-photon resonance as a function of peak laser intensity. The error on peak laser intensity is estimated at ±3%.

parametric heating, or by the differential AC Stark shift between two states. For our measurements at $\lambda = 1550$ nm we will use both methods to determine $\alpha^{(0)}$. We start by measuring the AC Stark shift of the two-photon transition used for STIRAP. At 1550 nm the Feshbach and ground states have different polarisabilities, by measuring the differential Stark shift we can determine this difference and as the Feshbach molecules' polarisability is simply the sum of that for the free atoms, which are well known [149], we can uniquely determine $\alpha^{(0)}$. We show an example spectrum in figure 5.3(a) for a peak intensity of 12 kW cm^{-2}, where we measure a shift of ∼50 kHz. In figure 5.3(b) we show the results of repeating this spectroscopy for different peak intensities, the data agree well with the expected straight line which we can fit to extract a gradient of: -5.6(6) Hz (W cm^{-2})$^{-1}$. This corresponds to a ground state polarisability of $\alpha^{(0)}/4\pi\epsilon_0$ =878(12) a_0^3. This method however requires accurate knowledge of the absolute value of the intensity, which for our $\lambda = 1550$ nm apparatus, is approximately 3%.

To verify our result and determine the impact of a possible systematic shift we perform a measurement of the trapping frequency. Immedately after STIRAP we load the ground state molecules into a trap, consisting of both

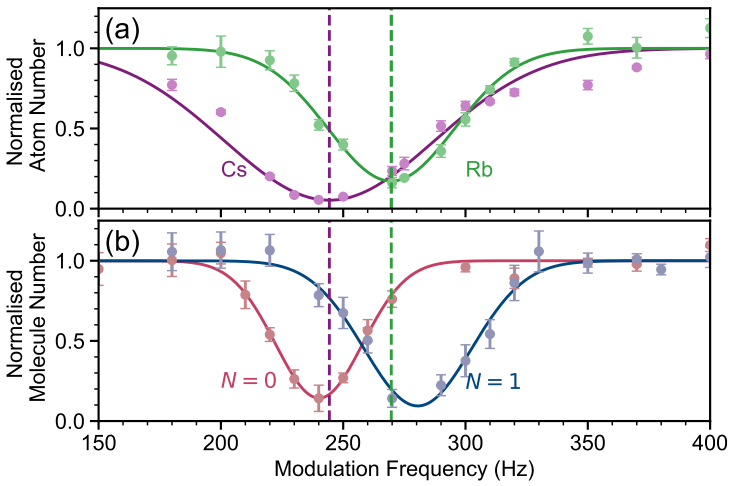

Figure 5.4: Parametric heating in the $\lambda = 1550$ nm optical dipole trap. (a) Parametric heating measurements of the two atomic species available in our apparatus: data for ^{133}Cs (^{87}Rb) are shown in purple (green). (b) Parametric heating of the RbCs molecules in the rotational ground state (red) and first rotationally excited state (blue). We can the value of $\alpha^{(0)}$ from the ratios between the trapping frequencies for the atoms and ground state molecule, with no dependence on the absolute value of the intensity.

beams of $\lambda = 1550$ nm light crossing at an angle of 27° in the plane defined by the magnetic field vector, with a peak intensity of 36 kW cm^{-2}. We then modulate the intensity of one beam by ±20% at a variable frequency. When the modulation frequency is twice one of the trapping frequencies the molecules are resonantly heated and so become untrapped. Because, as shown in figure 5.3(b), the AC Stark effect is linear we know that the trapping frequency goes as $(\alpha/m)^{1/2}$. By comparing the measured trapping frequency for molecules to that of atoms we can therefore determine the value of the molecular polarisability. We show the results for this measurement in figure 5.4(b) with a comparison to atoms in figure 5.4(a). Using this method we can determine the ground state polarisability to be $\alpha^{(0)}/4\pi\epsilon_0 = 8.8(1) \times 10^2$ a$_0{}^3$, with no systematic error due to the intensity. This value is in good agreement with the value measured spectroscopically. When we compare our result with theory we also find excellent agreement, with a ratio of ground-state to Feshbach polarisability of 0.88(1) compared to the prediction of 0.874 [148].

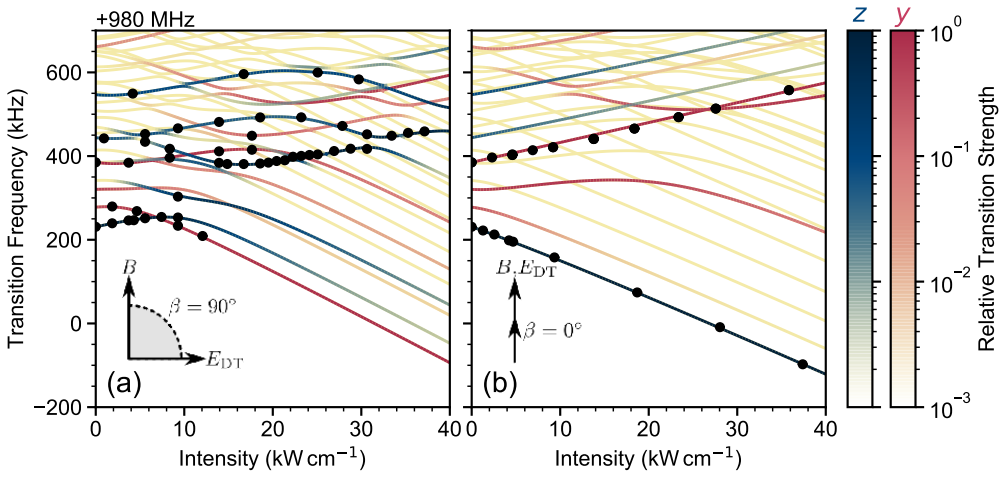

Figure 5.5: Transition frequencies from the lowest-energy hyperfine state of the rovibronic ground state ($N = 0, M_F = 5$) to the hyperfine states for $N = 1$ as a function of laser intensity, for laser polarisation angle (β) (a) perpendicular to and (b) parallel to the 181.5 G magnetic bias field. Each point is the fitted centre frequency from a measured microwave spectrum, with uncertainties of ∼kHz, which are too small to be seen at this scale. The transition strengths $|\boldsymbol{d}|^2$, relative to that of a rigid rotor, for microwaves polarised along z and y are shown as blue and red colour maps respectively.

5.2.2 Anisotropic Polarisability

To characterise the polarisability of the RbCs molecule we also require a measurement of $\alpha^{(2)}$. This can be measured through the intensity-varying differential frequency shift of the rotational transitions. We measure the transition frequencies using our two microwave antennae polarised along z and y (at zero intensity these correspond to π and $\sigma_{\pm}$ transitions respectively). To probe the AC Stark structure we switch a single laser beam, with waist 95 μm and $\lambda = 1550$ nm, on 0.5 ms before the microwave pulse. This time allows the laser intensity to fully stabilise, the molecules then experience a laser intensity which varies by only 2% across the cloud. We fix the time of the microwave pulse such that the Fourier-limited linewidth is $\gamma_{\mathrm{FWHM}}/2\pi \approx 10$ kHz, corresponding to times $\tau \sim 0.1$ ms. This timescale keeps the fraction of molecules which interact with the microwave field high, maximising our signal to noise ratio. Additionally we keep $\Omega\tau < \pi$ such that we only observe one spectral feature, we are able to achieve this either through coarse tuning of the microwave power or by decreasing τ.

In figure 5.5 the Stark maps for $\beta = 90°$ and $0°$ are shown in panels (a) and (b) respectively. The hyperfine mixing of states causes a complex pattern of crossings and avoided crossings as laser intensity is increased, however by using a model of the complete hyperfine structure of the molecule (basis states up to $N = 3$) it is possible to fit these maps to experimental microwave spectra. We find that we are unable to fit both sets of spectra with the same value of $\alpha^{(2)}$ instead finding that $\alpha^{(2)}_{90°}/4\pi\epsilon_0 = 602(2)$ $a_0{}^3$ and $\alpha^{(2)}_{0°}/4\pi\epsilon_0 = 507(1)$ $a_0{}^3$, in both cases we get excellent agreement between theory and experiment. Both uncertainties are the statistical errors extracted from the fitting, however as with $\alpha^{(0)}$ the data are subject to approximately $\pm 3\%$ error in the absolute value of the intensity. Unlike when determining $\alpha^{(0)}$ however we cannot remove the dependence on the intensity as, due to the complex behaviour, the value of the combined polarisability of the excited states *i.e.* the effect of $\alpha^{(0)}$ *and* $\alpha^{(2)}$, is strongly non-linear with intensity.

5.3 Determining the polarisability at $\lambda = 1064$ nm

Theoretical analysis predicts that the polarisability of ground state RbCs molecules is identical to the polarisability of the initial Feshbach state at $\lambda = 1064$ nm, we therefore choose to install a second optical potential operating at this wavelength to replace our $\lambda = 1550$ nm ODT. In this region of the spectrum the polarisability should be dominated by transitions to the $A^1\Sigma$ and $B^1\Pi$ potentials [148, 150], all of which occur at higher energies than the $\sim h \times 281$ THz provided by the 1064 nm photons. It is worth noting that due to spin orbit coupling the lowest levels of the $b^3\Pi$ potentials have significant singlet character, giving strong resonant behaviour from $h \times 262$ THz to $h \times 270$ THz despite singlet→triplet transitions being forbidden by spin selection rules.

During initial attempts to load RbCs molecules into the ODT of $\lambda \approx 1064$ nm, we observed loss in the ground state which was orders of magnitude faster than the collisional losses which typically dominate our experiments (these losses will be discussed in greater detail in Chapter 6). This

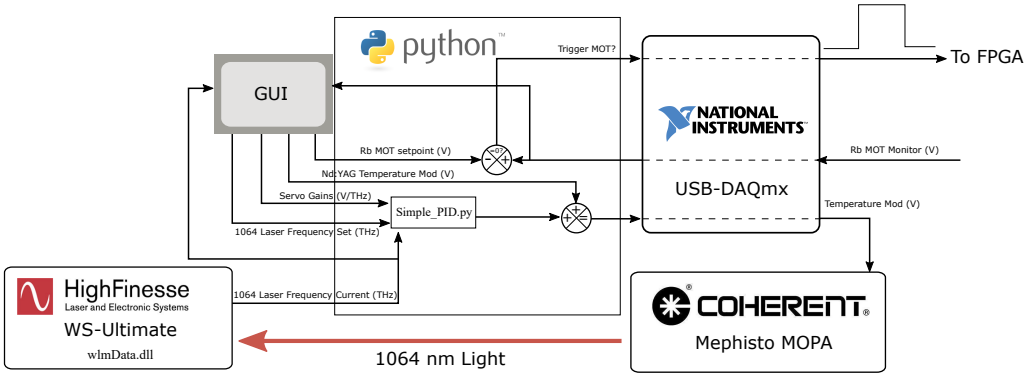

Figure 5.6: A schematic illustration of the communication between different hardware required to stabilise the frequency of the Mephisto MOPA system. A GUI powered by tkinter is used for user inputs, this controls the MOT servo and the laser lock. A HighFinesse WS ultimate wavemeter is used as a frequency reference on the Mephisto, the output is then compared to the setting supplied by the user and used in `Simple_PID.py` to generate the response of a servo loop. All of the code to create this software was written in Python 3.7.

was not expected. Although a single 1064 nm photon has enough energy to drive transitions to states in the electronically excited $b^3\Pi$ potential, as mentioned earlier, resonant behaviour is strongly suppressed by negligible Franck-Condon factors for transitions from 270 THz to 300 THz [148, 150].

In this section we will first describe the laser system in use and the method by which we stabilise the output frequency. We then will determine that the mechanism by which molecules are lost is a two-photon transition to another molecular state before identifying regions of the spectrum suitable for optical trapping where we characterise both components of the polarisability.

5.3.1 Laser stabilisation

The 1064 nm laser light is derived from a commercial Nd:YAG laser in a master-oscillator power amplifier (MOPA) configuration[3] which can output up to 25 W of laser power. The laser frequency is entirely controlled by the pump laser and can be adjusted within a range of $\sim$ 30 GHz by using an internal piezo and controlling the temperature of the Nd:YAG crystal.

For reliable measurements of resonant phenomena we must actively stabil-

[3] A Coherent Mephisto MOPA.

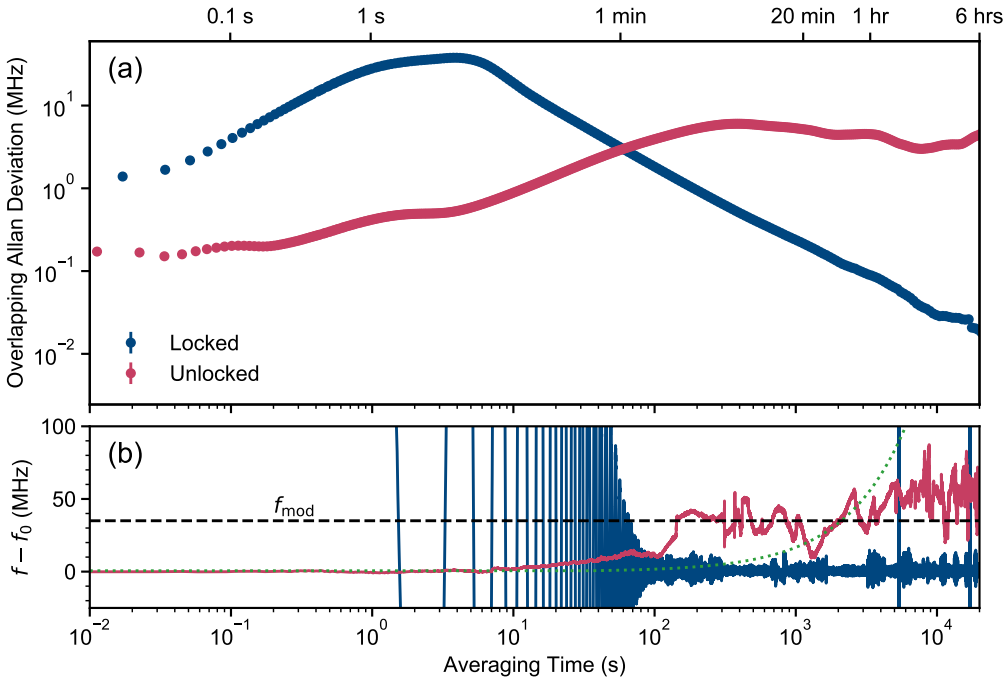

Figure 5.7: Frequency stability of the $\lambda = 1064$ nm set-up. (a) Overlapping Allan deviation with (blue) and without (red) the software lock running. When locked the laser is initially +500 MHz from the desired frequency (f_0) but surpasses the unlocked stability within 60 s. (b) Recorded deviation of laser frequency (f) from f_0 as a function of time. f_0 is defined as the lock set-point for the blue data and the initial set-point for the red. The width, in frequency, of modulation used for the spectroscopic measurments is shown as a dashed line.

ise the output frequency of this laser. In practice, for these wavelengths, lasers are either stabilised to an I_2 molecular reference or to a high-finesse optical cavity. We do not have the hardware for either of these solutions, as such we use a simpler, software based solution. The off-the-shelf frequency stability is claimed to be a drift of 1 MHz/min and is shown by the dotted line in figure 5.7. We choose to use a HighFinesse WS-Ultimate wavemeter for our frequency reference. We calibrate the wavemeter with our cooling lasers which are independently stabilised to ^{87}Rb and ^{133}Cs atomic frequency references.

The frequency stabilisation loop is contained entirely within software. Briefly: the software monitors the output of the wavemeter, which the drivers store in a `.dll` file on Windows: `wlmData.dll`. This value, in Hz, is filtered

by a 3$^{\text{rd}}$-order Butterworth low-pass filter in the time domain to remove jitter associated with repeatedly accessing the wavemeter output. This frequency is then used as the input to an external python library `simple_PID` which implements a proportional-integrator-derivative control loop outputting a single voltage in the range ± 10 V. Finally this output is relayed to a National Instruments USB-DAQmx board (which also controls the Rb MOT servo), the output of which is buffered using a trans-impedence amplifier circuit and connected to the temperature modulation input on the Mephisto pump laser. A schematic of this process is shown in figure 5.6. Currently this technique is limited by the Hz-level I/O refresh rates available and the ~ 10 Hz filter required to remove jitter.

To quantify the drift of the laser we fit a straight line to the frequency measured as a function of time, whilst the MOPA is free-running we find that there is an average drift of 343.6(3) Hz/s, well within the specification. By implementing our software servo we improve this to: -3(2) Hz/s, indicating that not only is the software functioning but it has removed all of the slow frequency drift. In figure 5.7 we show the overlapping Allan deviation with and without the servo loop in place, at short times the Allan deviation is actually higher when the servo loop is active, we attribute this to the low gain of the overall loop initially driving the laser frequency to oscillate. At the longer times, which are more relevant for our experiments, the Allan deviation averages down, indicating that we have correctly stabilised the output frequency of the laser.

5.3.2 Determining the loss mechanism

To investigate the optical losses, we trap ground-state molecules in the $\lambda = 1550$ nm crossed optical dipole trap and pulse on the 1064 nm light in a single beam to perform spectroscopy. We find that the loss of molecules is very sensitive to laser frequency, with several resonances in the region accessible to us. To determine the nature of these resonances we designate one of the resonant frequencies $f_0 = 281.634\,630(2)$ THz and stabilise the laser to this frequency, we apply additional modulation of 35 MHz at a rate of 5 kHz to remove error due to frequency tuning. We first measure the loss

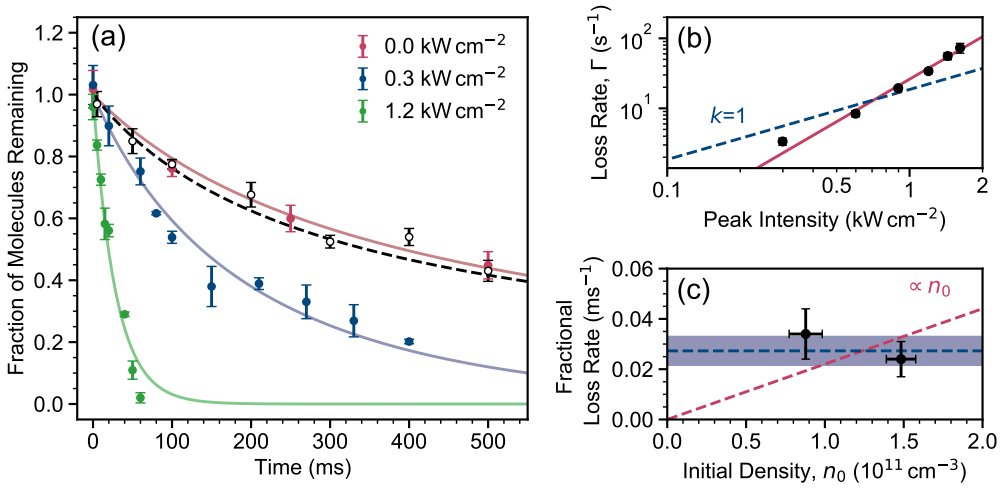

Figure 5.8: Determination of molecular loss mechanism. (a) Molecule loss as a function of time for various peak laser intensities. For the filled points the laser frequency is f_0 and an additional $\lambda = 1550$ nm dipole trap is used for confinement. For the unfilled black points the laser is detuned by -12.3 GHz, and the intensity is increased to 11.2 kW cm^{-2} without the 1550 nm dipole trap. (b) Rate of resonant loss (Γ) of molecules as a function of peak laser intensity (I). The solid line shows a fit to the data of the form $\Gamma \propto I^k$ which yields a best-fit ($\chi^2_{\text{red}} = 4$) value of $k = 2.02(8)$, the shaded region indicates the error on the fit. The dashed line shows the expected scaling for a one-photon process. (c) Initial fractional loss rate of molecules as a function of peak molecular density. The dashed lines indicate the expected scaling for single-(blue) and two-(red) molecule processes.

of molecules as a function of time due to the resonant light. By modelling the rate of change of density n as

$$\dot{n}(r,t) = -k_2 n(r,t)^2 - \Gamma n(r,t), \tag{5.4}$$

we can extract the resonant loss rate Γ. In equation (5.4) k_2 is the two-body inelastic loss rate coefficient, in this analysis we fix it to the value of 4.8×10^{-11} cm^3 s^{-1} as measured in [3]. Example loss measurements, with fit curves, can be seen in figure 5.8(a). To investigate the mechanism behind the loss, we measure Γ as a function of the peak intensity of the 1064 nm beam (see figure 5.8(b)). We fit the resulting variation with the function $\Gamma = AI^k$, with A as a free parameter. We fix $k = 1, 2, 3$ corresponding to loss due to a one, two, or three photon process, and find χ^2_{red}=31, 4 and 17 respectively. We confirm this fitting by additionally allowing k to vary, where we find that $k = 2.02(8)$ with no significant change in the best value for χ^2_{red}. This suggests that the loss is a two-photon process, with $A_{k=2} = 25(1)$ s^{-1} (kW cm^{-2})$^{-2}$.

We examine the density dependence of the loss by reducing the starting number of ground-state molecules, while keeping all other experimental parameters the same. Figure 5.8(c), shows loss rates for samples with a factor of 2 difference in the initial density; the largest change that we can make whilst still being able to measure an accurate lifetime. Both measurements agree within 1-σ so we conclude that there is no dependence on density [123]. This allows us to discount the possibility of, for example, two-photon photo-association of molecules or the resonant loss of molecular collision complexes [151]. As the loss appears to be a one-body process and the intensity dependence is quadratic, we believe it is caused by driving a two-photon transition to an electronically excited state. A pair of 1064 nm photons have sufficient energy to drive to the low-lying states in the $(5)^1\Sigma^+$ potential, shown in figure 5.9(b), which has a minimum of energy at $h \times 557$ THz ($\lambda = 538$ nm) [91, 152].

5.3.3 Spectroscopy of two-photon transitions

As the loss process we observe appears to be a two-photon transition to a different electronic state we expect there to be several resonances around f_0. To resolve these transitions we reduce the intensity to ~ 1 kW cm^{-2} and continue to dither the frequency as in the previous section, pulsing the light on for 50 ms. The dithering artificially broadens the transitions to the level where we can resolve individual lines with our current spectroscopy apparatus. In figure 5.9(a) we show results for spectroscopy from the ground rotational state $N = 0$, where two doublets separated by ≈ 1 GHz in laser frequency are observed. This energy splitting is typical for rotational transitions. We are able to fit the observed lines with a Gaussian function to extract centre frequencies with $\sim$ MHz error.

To ensure that we can reliably trap excited state molecules we repeat our spectroscopy measurements for molecules that have be transferred to $N = 1$ by microwaves. The results for this spectroscopy are shown in figure 5.9, offset by the microwave transition frequency 980.231 MHz. In this spectroscopy we see markedly different structure, with two doublets spaced by ~ 2 GHz in laser frequency and an additional singlet transition at $f \approx f_0 - 1.25$ GHz. Due to the different lines observed we can conclude that the individual transitions

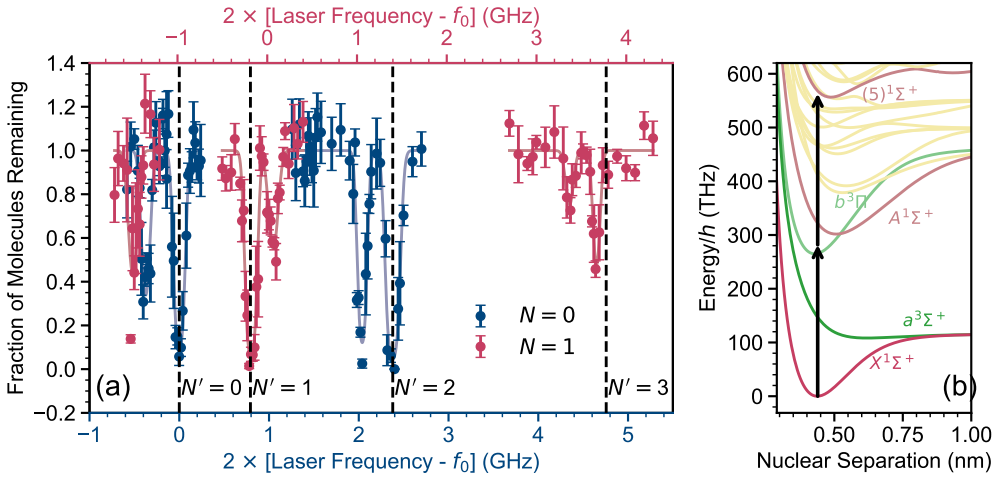

Figure 5.9: Resonant two-photon loss of ground state molecules in the presence of 1064 nm light. (a) The fraction of molecules remaining in the 1550 nm trap after exposure to 1064 nm light as a function of the laser frequency for molecules prepared in $N = 0$ (blue) or $N = 1$ (red). To display the results on a continuous scale corresponding to the excited state energy we plot the horizontal axes as twice the laser frequency (offset from $f_0 = 281,634.630(2)$ GHz) and offset the $N = 1$ measurements by $2 \times B_{v=0}/h = 980.231$ MHz on the top axis. Each data point is the average of 3 runs, with error bars indicating the standard deviation, the solid lines are Gaussian fits to the data. The vertical dashed lines highlight the excited state rotational structure using a rotational constant of $B_{v'} = h \times 400$ MHz. (b) The potential energy curves for RbCs [152]. The black arrows indicate the energies of one- and two-photon transitions at 1064 nm.

are likely to be due to transitions of the form $X^1\Sigma, v = 0, N \rightarrow (5)^1\Sigma, v', N'$. As each transition involves the absorption of two photons we have the selection rule $N - N' = -2,\ 0,\ +2$ to maintain angular momentum conservation. We fit the strongest of each pair of lines in the spectra to the eigenvalues of the rotational Hamiltonian $B_v \times N'(N'+1)$, weighted by the error in the centre frequencies extract from the fits. This gives a value of $B_v = h \times 389.9(4)$ MHz, which compares favourably to the theoretical prediction of 408 MHz calculated in [152]. We again note that there is an additional transition at $f_0 - 1.25$ GHz for molecules initially in $N = 1$, we are not certain of the origin of this line.

We can suppress the losses, such that they become unobservable in our experiments, by tuning the laser frequency ∼GHz away from the observed transitions. By doing this, we have been able to successfully load RbCs mo-

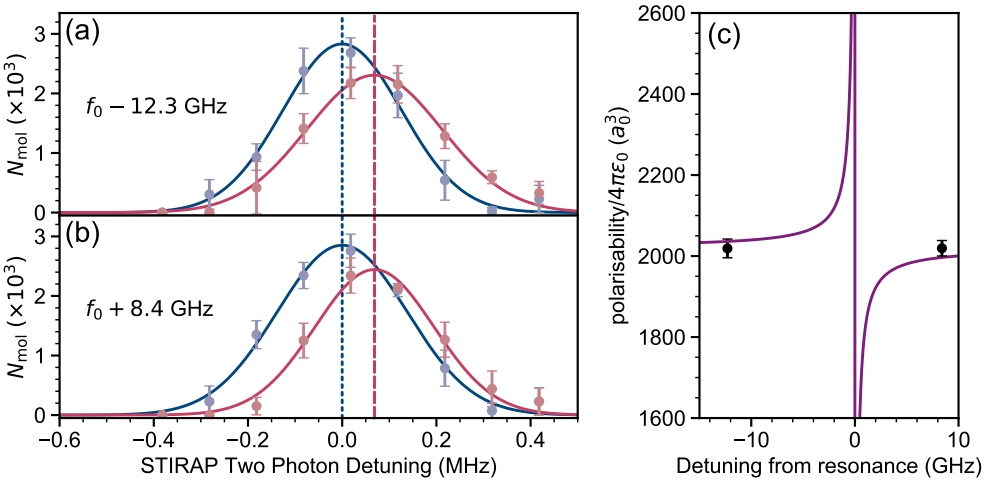

Figure 5.10: Measurement of the isotropic polarisability of RbCs in the rovibrational ground state using the AC Stark shift of the two-photon STIRAP resonance. (a) Spectroscopy of the two-photon STIRAP transition in free-space (blue points) and in a 1064 nm laser of peak intensity 8.60(7) KW cm^{-2}. The 1064 nm laser is -12.3 GHz detuned from the two-photon resonance at f_0. (b) As in (a) with the 1064 nm laser +8.4 GHz detuned from f_0. (c) The real part of the polarisability as given by: equation (5.5). The linewidth used is $\Gamma/2\pi = 8$ Hz which is the upper bound from the measurements in (a) and (b).

lecules into an ODT made with $\lambda = 1064$ nm light, where the lifetime is once again limited by two-body collisions [3]. This is shown in figure 5.8(a) by the dashed line and unfilled points.

5.3.4 Isotropic polarisability

For our measurements at $\lambda = 1064$ nm we choose to repeat the spectroscopy of the STIRAP transition to measure the intensity dependent energy shift of the ground state with respect to a weakly-bound Feshbach state. This is given by the AC Stark shift of the two-photon transition used in STIRAP [92], which we measure with and without the 1064 nm light in figure 5.10. The light is delivered in a single beam with a waist of 173(1) µm, and peak intensity of 8.60(7) kW cm^{-2}.

To check for off-resonant effects from the two-photon transition, we perform measurements for the 1064 nm laser tuned ±10 GHz of the loss features observed in Fig. 5.9. The energy shifts measured above and below the trans-

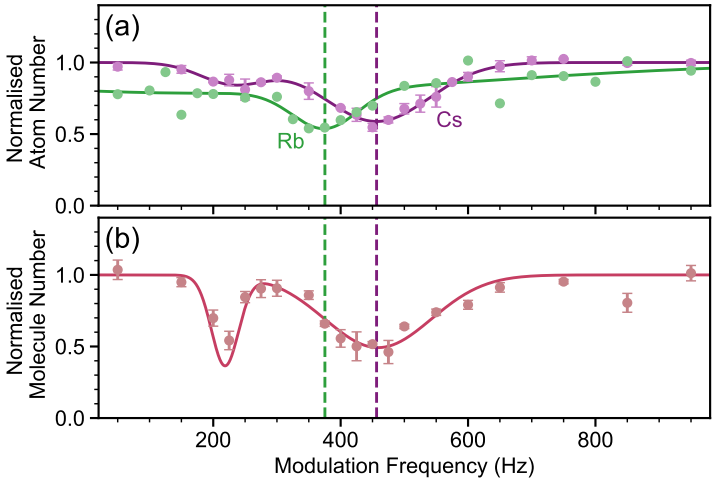

Figure 5.11: Parametric heating in the $\lambda = 1064$ nm dipole trap for (a) atoms and (b) ground state molecules. The weighted average polarisability from these measurements is $\alpha^{(0)}/4\pi\epsilon_0 = 2.03(4) \times 10^3$ $a_0{}^3$, in agreement with that measured using the AC Stark shift of the STIRAP transitions.

ition are $h \times 68(8)$ kHz and $h \times 68(9)$ kHz respectively. The identical shifts confirm that the laser frequency is far from resonance with the two-photon transition. Note that the shift in frequency is in the opposite direction to that shown in figure 5.3, indicating that the polarisability of the ground state is higher than the Feshbach state.

We can also use the polarisability to put an upper bound on the linewidth of the two-photon transition. By considering the dominant contribution to the polarisability to be that of the transition at $f_0 = \omega_0/2\pi$ and assuming that it has a form given by [153]

$$\alpha(\omega) = \alpha_{\text{Back}} + \frac{\Gamma/\omega_0^2}{\omega_0^2 - \omega^2 - i\Gamma(\omega^3/\omega_0^2)}, \tag{5.5}$$

where Γ is the linewidth of the transition of interest and α_{Back} is the background polarisability. We can then vary the value of γ until both measurements of the AC Stark shift of the STIRAP transitions agree with the curve to 1-σ. This occurs at $\Gamma/2\pi = 8$ Hz, this should not be interpreted as a measurement of the excited state lifetime.

The measured energy shift gives the difference in polarisability between the ground and Feshbach states, and the polarisability of the Feshbach state can be readily calculated by simple addition of the atomic polarisabilities α_{Rb}, α_{Cs}

which are well known [149]. The weighted average of our two measurements yields a polarisability in the ground state:

$$\begin{aligned}\alpha^{(0)} &= \alpha_{\mathrm{Rb}} + \alpha_{\mathrm{Cs}} + 4\pi\epsilon_0 \times 1.70(14) \times 10^2 \; a_0^3 \\ &= 4\pi\epsilon_0 \times 2019(14) \; {a_0}^3.\end{aligned}$$

Our measurement corresponds to a ratio of the ground-state to Feshbach polarisabilities ($\alpha^{(0)}/(\alpha_{\mathrm{Rb}} + \alpha_{\mathrm{Cs}})$) of 1.09(2). This is significantly different from the value of 1.00006 predicted by Vexiau *et al.* [148]. This may be a reflection that at 1064 nm there are many one and two-photon transitions that can contribute to the polarisability with both red and blue detunings, therefore the polarisability is likely sensitive to small differences in the relative transition strengths.

We confirm our spectroscopic measurement by again using parametric heating, shown in figure 5.11. We find that the polarisability is $\alpha^{(0)}/4\pi\epsilon_0 = 2.03(4) \times 10^3 \; {a_0}^3$ which agrees with the spectroscopic measurement. We attribute the larger error on this measurement to pointing instability in the 1064 nm crossed optical dipole trap, which has a much longer beam path than the 1550 nm trap. This leads to, over the course of the experiment, the trapping beams crossing and uncrossing thereby changing the trapping frequency.

5.3.5 Anisotropic polarisability

In this section we determine the value of the second term in the expansion of the polarisability, $\alpha^{(2)}$, using microwave spectroscopy of the $N = 0 \rightarrow 1$ rotational transition in RbCs, with an applied magnetic field of 181.5 G. We repeat the microwave spectroscopy of section 5.2.2, using similar techniques and with the 1064 nm laser frequency fixed to $f_0 - 12$ GHz. We again fit the complex AC Stark map to our spectra, however as the complex structure has been confirmed already in figure 5.5 we need only a few points to establish the scaling with laser intensity. By fitting this to our hyperfine model, using basis states up to $N = 3$, we can extract that $\alpha^{(2)}/4\pi\epsilon_0 = 1997(6) \; {a_0}^3$. We note that for $\lambda = 1064$ nm only a single value of $\alpha^{(2)}$ is necessary to fit the spectra at both $\beta = 90°$ and $0°$, which are shown in figure 5.12.

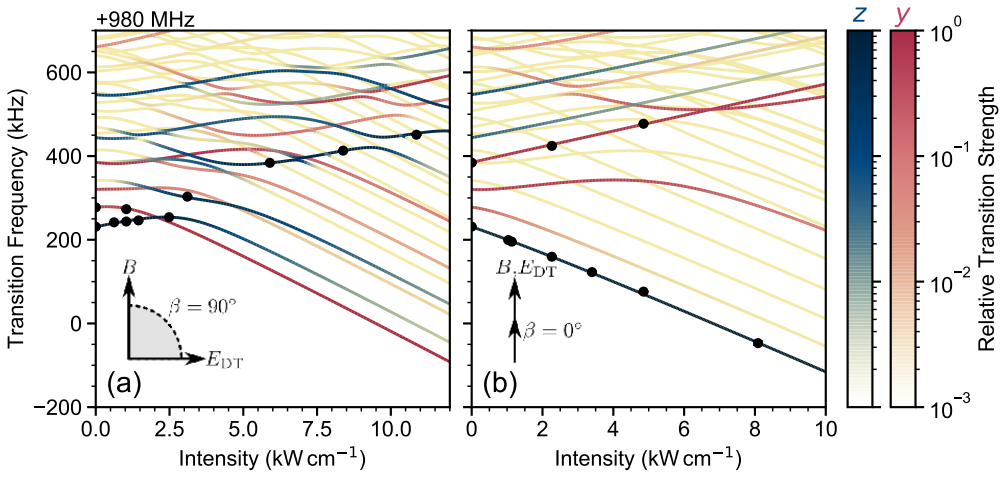

Figure 5.12: Transition frequencies from the lowest-energy hyperfine state of the rovibronic ground state ($N = 0, M_F = 5$) to the hyperfine states for $N = 1$ as a function of laser intensity, for laser polarisation angle (β) (a) perpendicular to and (b) parallel to the 181.5 G magnetic bias field. Each point is the fitted centre frequency from a measured microwave spectrum, with uncertainties of ∼kHz, which are too small to be seen at this scale. The relative transition strengths for microwaves polarised along z and y and are shown as blue and red colour maps respectively.

Knowing both parts of the polarisability allows us to fix all the parameters in both the hyperfine and pendular models described in Chapter 3.

5.4 Controlling the AC Stark effect with external fields

Molecules with $^1\Sigma$ ground states only have the nuclear contributions to their magnetic moments. Therefore they require a larger magnetic field gradient than molecules with $^2\Sigma$ ground states or atoms need to be trapped. As such it is simplest to trap these molecules with optical potentials as these are often a pre-requisite to produce the initial ultracold atomic gases from which they are associated. In the two previous sections we demonstrated that the AC Stark effect in the presence of a DC magnetic field creates a polarisation dependent, complex structure of crossings and avoided crossings between hyperfine states. In this section we will cover the interplay between the hyperfine structure, the AC Stark effect and the DC Stark and Zeeman

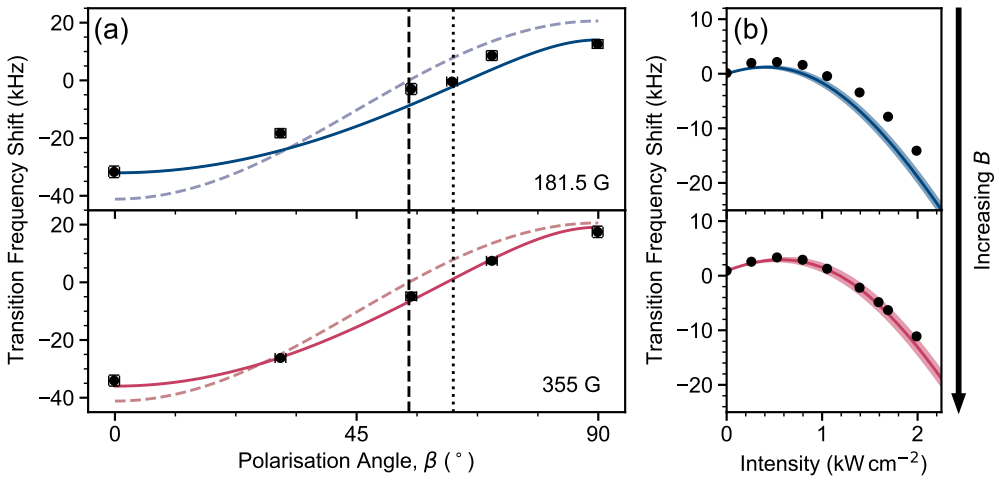

Figure 5.13: The anisotropic light shift of the $(N = 0, M_F = +5) \rightarrow (1, +5)_1$ transition in an applied magnetic field of (i) 181.5 G and (ii) 355 G as a function of (a) polarisation angle (β) for a fixed intensity of 1.05(1) kW cm^{-2} and (b) the laser intensity for β set to the zero crossing measured in (a), as indicated by the dotted line. Each point is the fitted centre frequency from a measured microwave spectrum, with uncertainties of ∼kHz. The solid lines are a model of the AC Stark effect which includes the full hyperfine and Zeeman structure, the shaded regions in (b) indicate the ±1° uncertainty in setting the polarisation angle to the zero crossing. On both axes the coloured dashed line indicates the expectation in a hyperfine-free model, with the vertical dashed line indicating the associated "magic angle". The intensity dependence makes it clear that the zero crossings are not due to magic angle behaviour and are instead due to turning points in the Stark map.

effects. We will show that when the AC Stark effect is combined with the DC Stark effect the molecules' internal structure is greatly simplified and there is a magic angle. We then extend this analysis to find the polarisation dependence of an optimum trapping condition. Finally we briefly describe an extension to higher rotational states.

5.4.1 In an applied magnetic field

We begin investigating the anisotropy of the polarisability in a magnetic field by fixing the intensity of the 1064 nm light to 1.05(1) kW cm^{-2} at the position of the molecules and varying the polarisation angle to find β_{magic}. In figure 5.13(a) the polarisation dependent Stark shift is shown at (i) 181.5 G and (ii) 355 G. In both cases the AC Stark shift does not follow the $\propto P_2[\cos(\beta)]$

form expected from models which ignore hyperfine structure. The transition frequency's zero crossing is also significantly different to the expected β_{magic}, instead crossing at 63(1)°. To find whether this is due to "magic angle" behaviour we fix the polarisation angle to 63° and vary the intensity at both magnetic fields, these measurements are shown in figure 5.13(b). In both cases we observe that the zero-crossing in the transition frequency is due to a low intensity turning point in the AC Stark map.

The data in figure 5.13 indicates that the hyperfine effects are playing a significant role in the AC Stark effect. Because the hyperfine interactions (described in section 3.6) mix different M_N the AC Stark effect has a different dependence on angle to the expected $\propto P_2\left[\cos\left(\theta\right)\right]$ form. It is expected that as the magnetic field increases the nuclear spin components of the wavefunction should decouple from the rotational angular momentum components. What we observe is that this does not happen over an experimentally relevant regime, which is unsurprising due to the small magnetic moment of the molecule, compared to the electric dipole moment. Our calculations including hyperfine structure show that the field would need to be ~ 700 G for the $|N=1, M_N=0, m_{\text{Rb}}=3/2, m_{\text{Cs}}=7/2\rangle$ component of $(N=1, M_F=5)_1$ to be $> 99\%$, we are currently limited to exploring up to ~ 400 G with our current configuration.

5.4.2 In an applied electric field

Because of the permanent electric dipole moment in the molecule frame there is a stronger coupling to DC electric fields than to the DC magnetic field. This means that only an experimentally modest electric field is sufficient to decouple the rotational and nuclear angular momenta. We have already discussed the effect of just applying the DC electric field in section 5.1. Once a field > 100 V cm^{-1} is applied to the molecules the rotational level has split into $|M_N| = 1$ and $M_N = 0$ branches. To reach a 99% state purity in the DC electric field requires only 100 V cm^{-1}.

We study the polarisation dependence of the AC Stark shift in an electric field using a fixed intensity of 3.12 kW cm^{-2} in figure 5.14(a) with an applied electric field of 300 V cm^{-1}. The model used here is hyperfine-free which

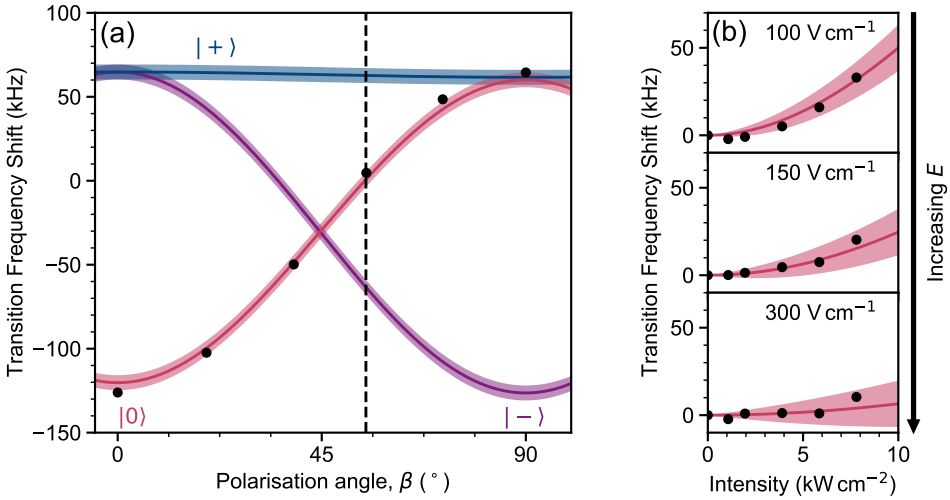

Figure 5.14: AC Stark shifts of the $N = 0 \rightarrow N = 1$ transitions with an applied DC electric field along the 181.5 G magnetic bias field. The shift of each transition is shown as a function of (a) the polarisation angle (β) of the 1064 nm laser with an applied electric field of 300 V cm^{-1} and a laser intensity of 3.12 kW cm^{-2}. The energy level of the state with $M_N = 0$ is labelled $|0\rangle$, the energy levels labelled $|+\rangle$ and $|-\rangle$ are even and odd combinations of (1,1) and (1,-1) respectively. (b) As a function of the peak laser intensity with β fixed to the magic angle (indicated in (a) by the dashed line). Each point is the fitted centre frequency from a measured microwave spectrum, with uncertainties of ∼kHz, which are too small to be seen at this scale. The solid lines are the results of a hyperfine free model, with the shaded regions indicating the error due to the uncertainty in $\alpha^{(2)}$.

agrees well with the data, as all measured points agree, within $1-\sigma$, with the previously measured value of $\alpha^{(2)}$. This shows that even a modest electric field can decouple $\boldsymbol{N}$, $\boldsymbol{i}_{\mathrm{Rb}}$ and $\boldsymbol{i}_{\mathrm{Cs}}$. To test the remanant AC Stark shift we fix the polarisation angle of the 1064 nm laser to the predicted magic angle of 54.7° and vary the intensity of the light. The results of these experiments at three electric fields are shown in figure 5.14(b). We see that the AC Stark shift scales approximately as I^2, this phenomenon is often termed "hyper-polarisability", it is important to recognise that this effect is completely described within equation (3.36) which contains only *electronic* polarisabilities. At higher electric fields this term is reduced, with only a maximum frequency shift of 10.0(1.6) kHz being measured at 300 V cm^{-1}. The remaining noise on our spectroscopy we expect is due to electric field noise which we anticipate to be on the level of $\sim 10^{-3}$.

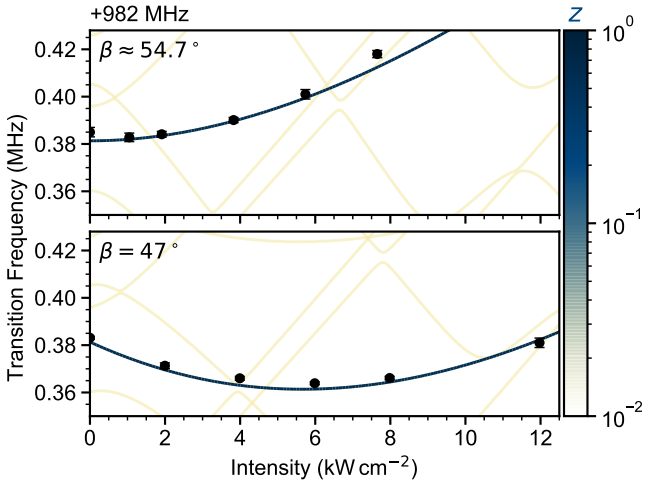

Figure 5.15: The AC Stark shift of the $(\tilde{N} = 0, M_N = 0, M_F = 5) \rightarrow (1, 0, 5)$ transition in RbCs as a function of peak 1064 nm laser intensity. An electric field of 100.8 V cm^{-1} is applied, and the resulting shifts for two polarisation angles, β, of the applied 1064 nm laser are compared. Only transition strengths for microwaves along z are shown, coded as in figure 5.13. Each point is the fitted centre frequency from a measured microwave spectrum, with uncertainties of ∼kHz. The continuous lines are the results from the hyperfine-containing model.

5.4.3 Beyond the Magic Angle

At the magic angle the diagonal terms of equation (3.36) are reduced to zero, in a perfect $|N, M_N\rangle$ state this removes the $\alpha^{(2)}$ component of the AC Stark shift. Previous works have focused on finding the magic angle [126, 154]. However due to the quadratic intensity behaviour of the remnant AC Stark shift, as seen in figure 5.14(b) and figure 5.15(a), the differential polarisability is only reduced to zero at $I = 0$. Here we describe a tunable arrangement for which the total frequency shift is reduced to near-zero at an intensity suitable for trapping. Because this technique doesn't require the full decoupling of the nuclear spins from the rotation it can be used in much smaller electric fields, reducing the sensitivity to electric field noise.

In figure 5.15(a) we compare the AC Stark shifts of the $(\tilde{N} = 0, M_N = 0, M_F = 5) \rightarrow (1, 0, 5)$ transition in RbCs with a model that includes the hyperfine structure initially using our data from figure 5.14(b). We see that by tuning the polarisation angle away from the magic angle (in this case $\beta = 47°$) a broad minimum is engineered at $I_0 \approx 6$ kW cm^{-2}, shown in fig-

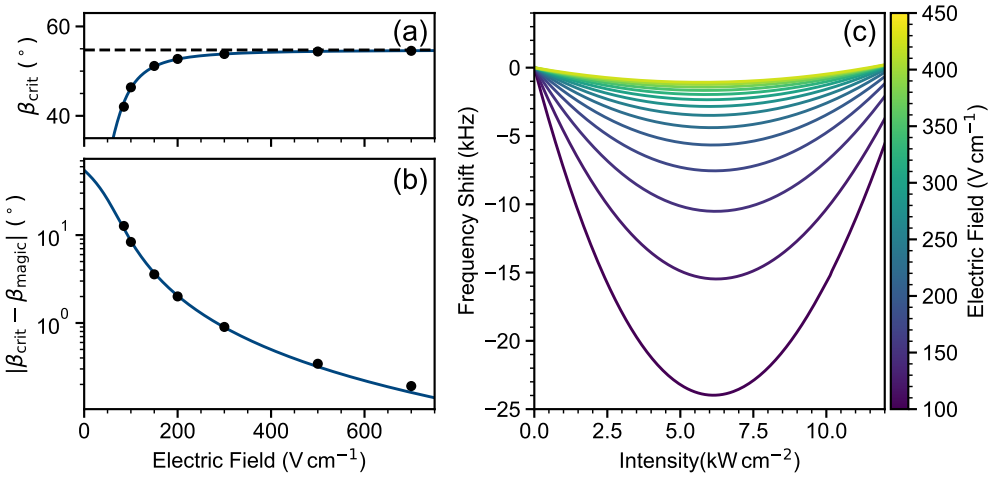

Figure 5.16: Tuning the AC Stark shift with polarisation and applied electric fields. (a) The critical angle for $I_0 = 6$ kW cm^{-2} as a function of applied electric field. The magic angle $\beta_{\text{magic}} \approx 54.7°$ is shown as a dashed line. (b) The difference between the critical angle and the magic angle as a function of applied electric field. Note the logarithmic scale for the vertical axis. In (a) and (b) the solid line is a solution to equation (5.9) whilst the points are obtained by optimising for a particular electric field by varying β in a calculation of the full hyperfine structure. (c) The optimum AC Stark maps, showing difference in transition frequency as a function of 1064 nm laser intensity, from the points in (a) and (b).

ure 5.15(b). This intensity corresponds to a trap depth of 27 μK in the rotational ground state, so would be suitable for trapping molecules at our current molecular temperatures of 1.5 μK.

We quantify the expected transition frequency spread Δf for a 4% spread in intensity by evaluating the Taylor expansion of the AC Stark map at $I = I_0$ and $I_0 - \Delta I$ for the two cases shown in figure 5.15. For $\beta = 54.7°$ we expect $\Delta f = 1.5$ kHz. In comparison for $\beta = 47°$, where we have optimised to minimise differential Stark shifts, $\Delta f = 33$ Hz. We expect that the coherence time in this arrangement should scale with $1/\Delta f \sim 30$ ms. Seeßelberg *et al.* trapped ^{23}Na^{40}K in an applied electric field in a spin-decoupled optical lattice where a coherence time of 8.7(6) ms was observed [154]. Our analysis indicates that we should observe similar coherence times with reduced sensitivity to electric field variation.

To find the angle with the minimum AC Stark shift for a given electric field and peak trap intensity we start with a Taylor expansion of the AC Stark

shift of a given transition

$$\Delta f = AI + BI^2, \tag{5.6}$$

where A is often referred to as the polarisability and B the hyper-polarisability both are given by: [126, 154]

$$A = \frac{[1 - 3\cos^2(\beta)]}{5}\alpha^{(2)}, \tag{5.7}$$

$$B = \frac{2}{5} \times \frac{B_{\text{Rot}} \sin^2(2\beta)}{(d_0 E)^2}\alpha^{(2)}. \tag{5.8}$$

To find the optimum angle of polarisation we take the derivative of equation (5.6) with respect to intensity to find the turning point, which will have the minimum variation in transition frequencies. We then have a function which, for a given electric field and peak intensity, gives the optimum angle of polarisation to use to minimise the AC Stark shift

$$I_0 = \frac{d_0^2 E^2 [1 + 3\cos(2\beta)] \csc^2(2\beta)}{8B_{\text{Rot}}}, \tag{5.9}$$

where I_0 is the intensity at which the transition frequency has a turning point. This is shown in figure 5.16(a) and (b) for an intensity of 6 kW cm^{-2}. We validate the simple model by calculating the full Stark map, including hyperfine structure, for various electric fields and optimising the polarisation such that the minimum is located within $\sim 1\%$ of the desired value of 6 kW cm^{-2}. The accuracy of this technique is limited by the coarse intensity axis of the hyperfine calculation, which must be repeated many times. The optimised AC Stark maps are shown in figure 5.16(c) for ($\tilde{N} = 1, M_N = 0, M_F = +5$). We find that this simplified model agrees well with our full calculations with deviations only becoming significant at large electric fields. Qualitatively we observe that as the electric field increases, what we have termed as the "critical angle" tends towards the magic angle, differing by $< 1^\circ$ by $E = 300$ V cm^{-1}. This is expected as at high electric field the molecular states become more pendular and so the differential polarisability becomes better represented by the term proportional to $\alpha^{(2)}$ in equation (5.3), which has a zero at the magic angle.

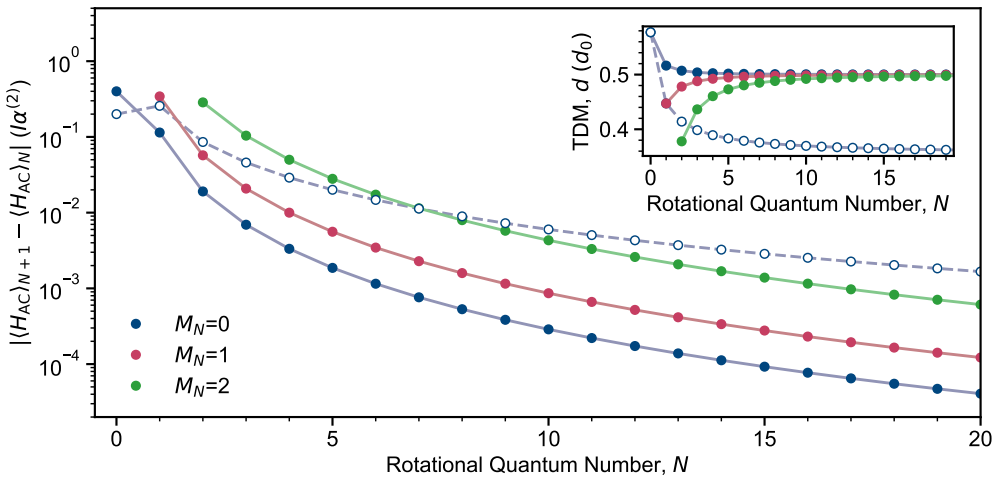

Figure 5.17: The difference in polarisability in units of the anisotropic polarisability, $\alpha^{(2)}$, is shown for the transitions $N \rightarrow N+1$ with $N \leq 20$ for π transitions $M_N = M'_N$. For $M_N = 0$, the $\sigma^{\pm}$ transitions are shown as open points. The ratio of the transition dipole moment, d, to the permanent dipole moment d_0 is shown inset for $N \leq 20$.

5.4.4 Higher Rotational States

One of the key advantages of molecules is the number of internal states which can be accessed. There are many possible applications for these but one of the most promising is to use the internal molecular states as a synthetic dimension [128, 129]. In the simplest case this only requires a single molecule, however more advanced models can be made with lattices of interacting molecules. To experimentally realise these systems requires many resonant microwave fields, which could make them very sensitive to time or space-varying AC Stark shifts. It is also desirable to maintain as large a dipole moment between the states as possible, such that nearest neighbour interactions can still be used if necessary. Here we will use the pendular theoretical model covered in Chapter 3 to analyse the AC Stark effect for pairs of high rotational states.

In figure 5.17, we evaluate the differential polarisability between various rotational levels for the hyperfine and Zeeman-free Hamiltonian. Our measure of the differential polarisability is the difference between the diagonal matrix elements, for polarisation along z, in equation (3.36) for N and $N+1$ *i.e.* $|\langle N+1, M'_N| H_{AC}(\beta = 0) |N+1, M'_N\rangle - \langle N, M_N| H_{AC}(\beta = 0) |N, M_N\rangle|$. We

find that if a two level system formed by levels with $(N = 10, M_N = 0)$ and $(11, 0)$ is used, the differential polarisability reduces by almost four orders of magnitude with respect to $(0, 0)$ and $(1, 0)$.

For applications to synthetic dimensions in lattices we must also consider the variation of the transition dipole moments between these higher rotational states. Partly this is because the transition dipole moment indicates what Rabi frequencies are possible between the states, which maps onto the tunneling rate between synthetic lattice sites. In lattices the interactions between the real sites will also be governed by the transition dipole moments. Inset to figure 5.17 we show how the transition dipole moment varies for the same states, measuring it as $\langle N+1, M_N | \, d_z \, | N, M_N \rangle$. This indicates that the reduction in differential polarisability would not come at the cost of reduced interaction strength.

5.5 Outlook and Summary

To summarise, we have explored the effect of external fields on the internal energy level structure of the RbCs molecule. Starting with a DC electric field we find that, as expected, the molecule couples strongly to the field with large energy shifts for experimentally modest electric fields. We compared our observations in the DC electric field with a model including the hyperfine structure and were able to conclude that of the three initially drivable π transitions only one has significant strength above 100 $\mathrm{V\,cm^{-1}}$. We conclude that this is because above this field the molecule is in a pendular state, as described in section 3.7.

We then moved to determining the interaction between the molecule and optical frequency AC fields. We started with $\lambda = 1550$ nm, as it was already in use for trapping the atomic mixture. Our initial measurements were on the isotropic part of the polarisability, where we found a ratio of ground to Feshbach state polarisability $\alpha^{(0)} / \left[\alpha_{\mathrm{Rb}} + \alpha_{\mathrm{Cs}}\right] = 0.88(1)$ which agrees well with theory [148]. We then studied the effect of the trapping light on the microwave transitions to the first rotationally excited state, finding that there is a complex pattern of crossings and avoided crossings. We

are able to fit each set of spectra independently to find best-fit values of $\alpha^{(2)}/4\pi\epsilon_0 = 602(2)\ \mathrm{a_0}^3, 507(1)\ \mathrm{a_0}^3$ for $\beta = 90°, 0°$ respectively. We are not able to determine the origin of this discrepancy.

We also investigated $\lambda = 1064$ nm as this wavelength has been predicted to be magic for the STIRAP transitions, with equal values for $\alpha^{(0)}$ and $\alpha_{\mathrm{FB}} = \alpha_{\mathrm{Rb}} + \alpha_{\mathrm{Cs}}$. Our initial experiments found rapid losses from the rotational ground state, which we were able to attribute to two-photon single-molecule transitions of the form $X^1\Sigma^+ N \rightarrow (5)^1\Sigma, (N-2, N, N+2)$. We found that rather than the expected ratio of 1.00006 [148] the ratio of ground state to Feshbach polarisability is 1.09(2), and therefore not a magic wavelength. Using the same microwave spectroscopic techniques as used for the $\lambda = 1550$ nm dipole trap we were able to determine that $\alpha^{(2)}/4\pi\epsilon_0 = 1997(6)\ \mathrm{a_0}^3$, we were unable to reproduce the discrepancy between $\beta = 90°$ and $\beta = 0°$ seen at $\lambda = 1550$ nm: suggesting that this was experimental in origin.

We extended our study of the polarisability by studying the interplay between the AC Stark effect and the DC Stark and Zeeman effects on the internal structure of the molecule, which required we constrain $\alpha^{(2)}/4\pi\epsilon_0 = 1997(6)\ \mathrm{a_0}^3$. For both cases we were able to compare our experiment directly to theoretical predictions, finding good agreement. Additionally we are able to verify our expectation that only a small electric field ($E \approx 100\ \mathrm{V\,cm^{-1}}$) is necessary to enter the limiting "pendular" case. Using this pendular case we were then able to engineer a turning point in our AC Stark maps for $\tilde{N} = 1$ such that the minimum variation in transition frequency was at $I_0 = 6\ \mathrm{kW\,cm^{-2}}$. We predict that this arrangement will give a sufficient trap depth for 1.5 μK molecules with coherence times > 10 ms. Finally we discussed how the AC Stark effect could impact the theoretical proposals which require higher rotational states to be used, with a particular focus on synthetic dimensions. Combined our results indicate that higher rotational states in the presence of a DC electric field have reduced sensitivity to differential Stark shifts without loss of interaction strength. This is promising for using molecules as a system for studying synthetic dimensions.

The control that we have developed over the internal structure in this chapter will be necessary for the future use of molecules in quantum simulations. By being able to isolate individual transitions by $\sim$ MHz using DC electric fields

large Rabi frequencies can be used in multi-photon synthetic dimension experiments [128, 129]. Additionally knowledge of the the complex behaviour of the internal structure of the molecule as a function of intensity and polarisation will allow for the generation of novel traps which could support long coherence times, either through exploiting magic angles [154] or by removing the intensity dependence in a magic wavelength trap [155].

Chapter 6

Collisions of RbCs Molecules

With decades of experimental and theoretical research we now possess a detailed understanding of collisions in ultracold atomic systems [37, 156]. Experiments are able to control inter- and intra-species scattering properties at magnetic Feshbach resonances [146, 157–159]. This control is aided by the availability of highly-accurate quantitative calculations of the scattering length. The corresponding calculations for ultracold molecule-molecule collisions have proved far more difficult. This is, in part, due to the added complexity of the possible collisions between two molecules. A collision between two atoms depends only on one coordinate: the separation, a collision between two diatomic molecules instead depends on multiple as we must represent the distance between the molecular centres-of-mass, their orientations and the separation of the atoms in the molecules. Despite this theoretical difficulty the densities reached in experiments on associated ultracold molecules are now sufficiently high that molecule-molecule collision processes are proving important and measurable.

The first measurements of ultracold molecular collisions were in fermionic ^{40}K^{87}Rb, where the lifetime was limited by the two-body exchange process $2\mathrm{KRb} \rightarrow \mathrm{K}_2 + \mathrm{Rb}_2$ [160–162]. However even in species for which this, and other chemical processes, are strongly energetically forbidden such as in the bosons ^{87}Rb^{133}Cs [3, 41] or ^{23}Na^{87}Rb [163, 164] and in the fermion ^{23}Na^{40}K [43, 165] the lifetime of the molecule is limited by two-body processes and remains on the same order-of-magnitude as in the reactive case.

This suggests that there is an unknown loss mechanism which is limiting the lifetime of these species.

In this chapter we will discuss our work studying the collisional properties of the RbCs molecule. First we will determine that the molecule follows second-order kinetics in molecule density. Then, using results from an intensity-modulated trap, we will determine that the molecule loss mechanism is conclusively explained by complex-mediated photoinduced losses. Finally we will conclude by studying the difference in the losses in mixtures of RbCs and Rb or RbCs and Cs.

6.1 Collisions of Ground State RbCs

The key to understanding the molecular loss is to establish a mechanism. This begins by determining the density dependence. In this section we begin by reviewing prior theoretical predictions for the molecular loss. We then study the molecular lifetime experimentally to determine that the kinetics of the rate-limiting step are second order in molecular density.

There are multiple collisional processes that can occur if we restrict ourselves to 2-body chemistry:

$$\mathrm{RbCs} + \mathrm{RbCs} \rightarrow \mathrm{Rb_2Cs_2}, \quad \Delta E/hc = -2641 \text{ cm}^{-1} \text{ [166]} \tag{6.1a}$$

$$\mathrm{RbCs} + \mathrm{RbCs} \rightarrow \mathrm{Rb_2} + \mathrm{Cs_2}, \quad \Delta E/hc = +29.1 \text{ cm}^{-1} \text{ [167]} \tag{6.1b}$$

$$\mathrm{RbCs} + \mathrm{RbCs} \rightarrow \mathrm{Rb_2Cs} + \mathrm{Cs}, \quad \Delta E/hc = +1981 \text{ cm}^{-1} \text{ [167]} \tag{6.1c}$$

$$\mathrm{RbCs} + \mathrm{RbCs} \rightarrow \mathrm{Rb} + \mathrm{RbCs_2} \quad \Delta E/hc = +2101 \text{ cm}^{-1} \text{ [167]}. \tag{6.1d}$$

Only the tetramer formation process in equation (6.1a) is energetically allowed, however due to the large exothermicity it is expected that this should not be significant at ultracold temperatures [166]. As the other three possible processes are forbidden by $\Delta E \gg hc \times 1 \text{ cm}^{-1} = k_\mathrm{B} \times 1.4 \text{ K}$, they also do not occur at ultracold temperatures. For these reasons we will refer to RbCs as "unreactive".

Given that the molecule is stable against two-body chemical reactions we must consider other possible mechanisms. One such mechanism was proposed by Mayle *et al.* [168, 169]. In their work they argue that the large

number of rovibrational states available supports a dense manifold of Feshbach resonances. The lifetime of the complex formed at a collision resonance is given by $\tau_c = \hbar/\Gamma$, where Γ is the resonance width. The key assumption of the Mayle *et al.* work is that the motion is fully ergodic *i.e.* energy within the complex is fully randomised. This enables them to use Rice-Ramsperger-Kassel-Marcus (RRKM) theory to determine the mean width:

$$\langle \Gamma \rangle = \frac{N_{\mathrm{Open}}}{2\pi\rho}. \tag{6.2}$$

In the above ρ is the density of states and N_{Open} is the number of open channels for the pair, for RbCs molecules in the absolute ground state $N_{\mathrm{Open}} = 1$. The cited work then calculates an estimate of the density of states of $\rho/k_{\mathrm{B}} = 942\ \mu\mathrm{K}^{-1}$; this corresponds to a lifetime for the $(\mathrm{RbCs})_2$ complex of 45 ms. These complexes can in principle decay back into molecules, however the predicted lifetime is sufficiently long that a third molecule is likely to collide with the complex and cause loss of all three.

The work of Mayle *et al.* includes a critical error. They count states for which the overlap $\langle n, m_n, L, M_L | J, M \rangle \neq 0$. For each J, M this includes a factor of $(2n + 1)$ where n of the order 10^2 contribute to the calculation of the density of states. This leads to several orders of magnitude overestimate in the density of states, and therefore also in the lifetime of $(\mathrm{RbCs})_2$. More recent work from Christianen *et al.* [151, 170] corrected this error, only counting the states of well-defined J, M. Their calculations imply a complex lifetime of $\tau_{\mathrm{c}} = 253\ \mu\mathrm{s}$ for $(\mathrm{RbCs})_2$, though the calculation was initially only performed for the $(\mathrm{NaK})_2$ complex, and scaled appropriately for the different bialkalis. This timescale is too short to reasonably expect loss by three-body collisions given current experimental densities. A different mechanism would therefore be necessary to explain the rate of observed losses. By considering a full potential energy surface for NaK+NaK it was determined in [151] that the complex has a significant number of possible transitions at typical trapping wavelengths, the loss was then hypothesised to be dominated by optical excitation of a molecular complex formed by a two-body collision.

In this section we will discuss the losses in our ultracold RbCs gas. We begin by determining the order of the kinetics, finding that the rate-limiting step is second-order in molecular density and sub-universal. We are able

to explain this data using a single channel model which uses some results from quantum defect theory (QDT), this enables us to determine, for each collision, the probability that the molecules will be lost. We exploit the thermal averaging to fully constrain the model, extracting a short-range loss parameter y and phase shift δ^{s}. We then explore the effect of the internal state, finding that there is a trend towards universality with increasing state. Additionally we see evidence that in a mixture of rotational states there is resonant dipole-dipole enhancement to the collision rate. Finally we conclude by exploring the magnetic field dependence, finding that even when the state with $M_F = +5$ is not the ground state there is no change to the collisional properties.

6.1.1 Determining the Kinetics

Before we can determine what the loss mechanism is we must first determine how many molecules are involved. For that we look at the kinetics of the rate-limiting step. For a generic γ-order process we can describe the reduction in molecular density as

$$\frac{\mathrm{d}n(\vec{r},t)}{\mathrm{d}t} = -k_\gamma n^\gamma(\vec{r},t). \tag{6.3}$$

In a harmonic trap the density of molecules n as a function of the position vector $\vec{r} = (x, y, z)$ and number of molecules N_{mol} is given by

$$n(\vec{r},t) = \frac{N_{\mathrm{mol}}\bar{\omega}^3 m^{3/2}}{(2\pi T)^{3/2}} \exp\left[-\frac{m\left(\omega_x^2 x^2 + \omega_y^2 y^2 + \omega_z^2 z^2\right)}{2k_{\mathrm{B}}T}\right], \tag{6.4}$$

note that we have allowed for the number of molecules N_{mol} and temperature T to be implicit functions of time t and $\bar{\omega} = (\omega_x\omega_y\omega_z)^{1/3}$ is the harmonic trapping frequency and ω_i is the trap frequency along the i-th axis. In the experiment, we typically cannot probe the density as a function of time, instead we measure the total number of molecules. This number is simply the integral of the density over all space. Our loss rate from equation (6.3) therefore becomes

$$\frac{\mathrm{d}N_{\mathrm{mol}}}{\mathrm{d}t} = \int \frac{\mathrm{d}n}{\mathrm{d}t}\mathrm{d}^3 r = -k_\gamma C^{\gamma-1}\left[\frac{N_{\mathrm{mol}}^\gamma}{\gamma^{3/2}T^{(\gamma-1)\times(3/2)}}\right], \tag{6.5}$$

where we have included the parameter $C = (m\bar{\omega}^2/2\pi k_{\mathrm{B}})^{3/2}$. The loss of molecules is preferentially from the densest region of the cloud, therefore as

losses continue the cloud is expected to heat as the average energy of the particles increases. The average energy of the colliding molecules is then given by summing the potential and kinetic energy contributions

$$\bar{E} = \int p_{\text{loss}} \frac{m}{2} \left(\omega_x^2 x^2 + \omega_y^2 y^2 + \omega_z^2 z^2\right) \mathrm{d}^3 r + \frac{3k_{\text{B}}T}{2} = \frac{3(\gamma+1)k_{\text{B}}T}{2\gamma}, \tag{6.6}$$

where the probability of loss (p_{loss}) can be calculated as $n^\gamma / \int n^\gamma \mathrm{d}^3 r$. From the average energy per molecule we can arrive at the total energy through $E = 3k_{\text{B}}TN_{\text{mol}}$. The total energy of the gas must be conserved and so, comparing the energy at time t and $t + \delta t$

$$3k_{\text{B}}T(t+\delta t)N_{\text{mol}}(t+\delta t) = 3k_{\text{B}}T(t)N_{\text{mol}}(t) - \bar{E}\left[N_{\text{mol}}(t+\delta t) - N_{\text{mol}}(t)\right]. \tag{6.7}$$

In this expression we have made the implicit time dependence of T and N_{mol} explicit. If we take the infinitesimal limit for δt we can construct a differential equation for the temperature

$$\frac{\mathrm{d}T}{\mathrm{d}t} = \frac{1}{N_{\text{mol}}} \frac{\mathrm{d}N_{\text{mol}}}{\mathrm{d}t} \left(\frac{\bar{E}}{3} - T\right). \tag{6.8}$$

We have assumed that the molecules remain in thermal equilibrium, such that a single temperature can describe the entire sample, experimentally we observe that losses occur on a timescale longer than a quarter trapping period implying that the molecules will thermalise on a time-scale comparable to the losses. As this behaviour depends on the time derivative of N_{mol} we can substitute equation (6.5) to reach a pair of coupled equations for T and N_{mol}

$$\frac{\mathrm{d}N_{\text{mol}}}{\mathrm{d}t} = -k_\gamma C^{\gamma-1} \left[\frac{N_{\text{mol}}^\gamma}{\gamma^{3/2} T^{(\gamma-1)\times(3/2)}}\right], \tag{6.9a}$$

$$\frac{\mathrm{d}T}{\mathrm{d}t} = k_\gamma C^{\gamma-1} \left(\frac{\gamma-1}{2\gamma}\right) \left(\frac{N_{\text{mol}}^{\gamma-1}}{\gamma^{3/2} T^{(3\gamma-5)/2}}\right). \tag{6.9b}$$

For $\gamma = 1$, *i.e.* a 1-body process, the temperature has no time dependence.

We establish what the relevant kinetics are for the RbCs loss process by measuring the time-dependent molecule number in our crossed optical dipole trap at $\lambda = 1550$ nm, the results are shown in figure 6.1(a). The molecules are initially prepared in the spin-stretched rotational ground state ($N = 0, M_F = +5$) at a magnetic field of 181.5 G, the STIRAP process used to

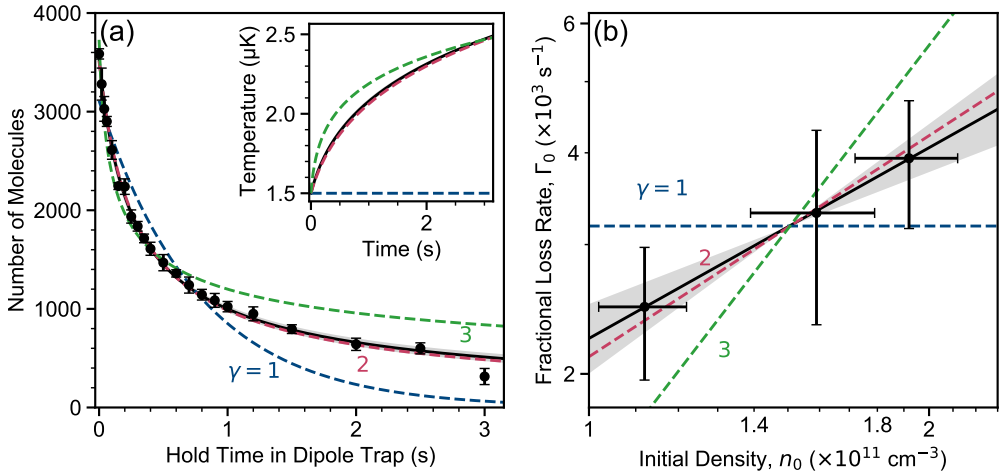

Figure 6.1: Determining the rate limiting step for the molecule-molecule loss process. (a) Lifetime of RbCs molecules in an optical dipole trap. Each data point is the mean of at least 5 experimental runs, with error bars indicating the standard error. The black solid line is a fit to the coupled equations in equation (6.9) with k_γ and γ as free parameters, with a shaded 1σ error bar. Constrained fits for $\gamma = 1, 2, 3$, corresponding to 1, 2 and 3-body loss processes are shown as blue, red and green dashed lines respectively. The expected variation in temperature for each model is shown inset. (b) The loss rate over the first 200 ms is shown as a function of peak molecular density. The expected trends for $\gamma = 1, 2, 3$ are shown as in (a), with the solid black line indicating the line of best fit. Combined (a) and (b) indicate that only a two-body process can fit both data sets well.

transfer the molecules to this state is hyperfine state selective, molecules that are in different states (or form complexes) will appear to be lost alongside those that are ejected from the trap. The initial temperature and density are 1.5(1) μK and $1.9(2)\times10^{11}$ cm^{-3} respectively. Currently we can only measure the temperature of the Feshbach molecules. This is because only ground-state molecules that undergo a second STIRAP sequence can be imaged, if we were to allow the cloud to expand due to its thermal energy it would also fall out the region where STIRAP is optimised. Measuring the temperature as a function of time is further complicated by the collisional losses reducing the number of molecules, greatly reducing the optical depth of the clouds being imaged.

To determine what order process we are observing we fit the experimental data to equation (6.9) allowing both γ and k_γ to vary freely, we assume that only one loss process is significant, noting that the vacuum limited lifetime

for Rb atoms is in excess of 100s. The parameter $T_{\mathrm{mol}}(t = 0)$ is fixed to match the measured temperature of the Feshbach molecules, $N_{\mathrm{mol}}(t = 0)$ is used as a fitting parameter. Using this method we find that $\gamma = 2.07(7)$ and $k_\gamma = 4.8(6) \times 10^{-11}$ cm^3 s^{-1}, we quantify the goodness-of-fit with the reduced χ^2 parameter: $\chi^2_{\mathrm{red}} = 0.998$. This suggests that the loss is rate-limited by a second-order process. In figure 6.1(a) we also compare the results to models that have γ constrained to $1, 2$ or 3, respectively these have $\chi^2_{\mathrm{red}} = 22.9, 1.27, 10.4$. We have repeated this analysis excluding the temperature variation from the model and are able to retrieve the same result: the loss manifests as a two-body process, we do not believe therefore that only being able to measure the initial temperature of the Feshbach molecules is a limiting factor.

As an independent verification of the second-order behaviour we measure the rate of molecule loss as a function of initial density over a 200 ms period. To do so we first fix the trap frequencies and molecular temperature and then vary the number of molecules after STIRAP. We extract a loss rate by linearly fitting the molecule loss over this time period to extract an average rate of change. We then confirm the order of the kinetics by plotting on a log-log scale, shown in figure 6.1(b). We fit a further three functions of the loss rate $-\mathrm{d}N_{\mathrm{mol}}/\mathrm{d}t$ against the initial density n_0

$$\log\left(\frac{\mathrm{d}N_{\mathrm{mol}}}{\mathrm{d}t}\right) = [\gamma - 1]\log(n_0) + C. \tag{6.10}$$

Gradients of 0, 1 and 2 correspond to first, second and third-order kinetics[1]. If we allow γ to be a free parameter we find that the best-fit value is 0.9(3), again in agreement with second-order kinetics. For these reasons we will, from this point onwards, constrain all fitting to $\gamma = 2$ and parametrise our loss curves using k_2.

6.1.2 The Single-Channel Model and Universal Losses

For a "simple" system, such as collisions of the form alkali atom + alkali atom, it is possible to accurately and fully model the scattering processes using close

[1]The $\gamma - 1$ exponent coefficient to $\log(n_0)$ from the conversion between rate of change of number and rate of change of number density.

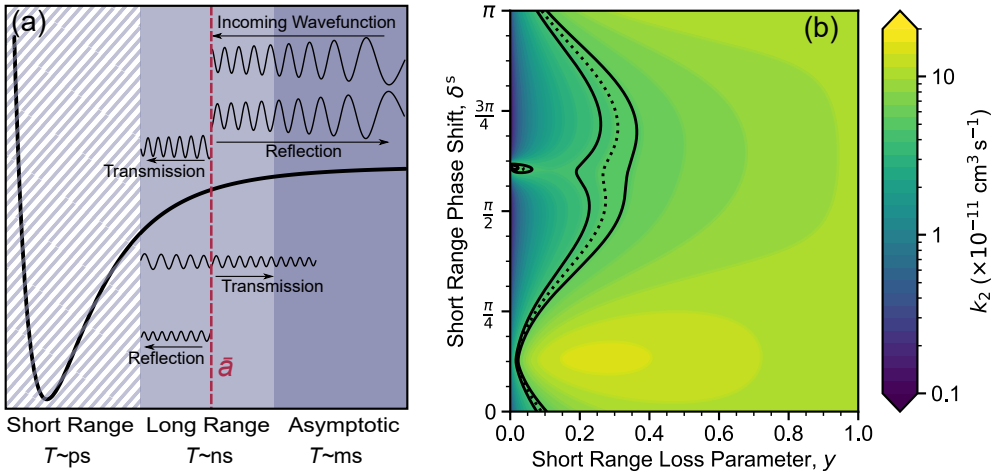

Figure 6.2: (a) An illustration of the processes that enter into the single channel model. The two parameters that enter the model are the short range loss parameter y and phase shift δ^S. The model considers the scattering off the long range C_6 potential at a distance $\bar{a}$ and for $y < 1$ can include multiple reflection and transmission processes. (b) Thermally averaged two-body loss rate coefficient at 1.5 μK, plotted as a function of the loss parameter y and phase shift δ^S. The dashed line shows the contour corresponding to the k_2 measured in figure 6.1(a) whilst the solid lines indicate the 1σ error bars.

coupled-channel methods to directly solve the many-body Schrödinger equation using software such as MOLSCAT [171, 172]. It was this ability to do accurate calculations that enable atomic scattering to be so well understood and for magneto-association to be first attempted. In the more complex molecule-molecule scattering systems this type of theory is simply not possible. We therefore use a different technique, based on quantum defect theory (QDT) [173, 174]. The model we use breaks the interaction processes into two components: a long-range part and a short-range part. We consider the long range part to be the $1/R^6$ part of the molecule-molecule potential energy surface (where R is the distance between the two molecules). At low collision energies a large amount of particle flux is scattered off the long-ranged potential and so never reaches short range. This gives a non-zero elastic cross-section. The component that does not scatter off the long-ranged potential therefore interacts with the short-ranged part of the potential, because the behaviour will depend strongly on the exact shape of the potential we

parametrise the loss from this potential using the short-range S-matrix [174]

$$S_c = \left(\frac{1-y}{1+y}\right) e^{2i\delta^{\mathrm{s}}}, \tag{6.11}$$

where we have introduced two new parameters: a loss parameter y which quantifies the amount of molecular flux loss at short range and δ^{s} which is a phase shift of the wavefunction that comes from short range[2]. We can relate the parameter δ^{s} to a scattering length a through

$$\frac{a}{\bar{a}} = 1 + \cot\left(\delta^{\mathrm{s}} - \frac{\pi}{8}\right). \tag{6.12}$$

The parameter y is related to the probability of loss at short range

$$p_{\mathrm{out}} = |S_c|^2 = \left|\frac{1-y}{1+y}\right|^2, \tag{6.13a}$$

$$p_{\mathrm{loss}} = 1 - p_{\mathrm{out}} = \frac{4y}{(1+y)^2}. \tag{6.13b}$$

The limiting case where $y \to 1$ has been termed the "universal loss" regime as $p_{\mathrm{loss}} \to 1$. In this regime there is no dependence on δ^{s} and the scattering properties are limited by the long ranged part of the potential [173]. In the universal loss limit and at zero temperature the two-body loss coefficient is given by [173]

$$k_2^{\mathrm{Univ}}(T=0) = \frac{2gh\bar{a}}{\mu} \tag{6.14}$$

where μ is the reduced mass, $g = 2$ for identical bosons and $\bar{a} = 0.477988... \times (mC_6/\hbar^2)^{1/4}$ is the mean scattering length [175]. For RbCs in the rovibrational ground state: $C_6 = d_0^4/6B_{\mathrm{rot}} = 141 \times 10^3 E_{\mathrm{h}} a_0^6$, which gives $\bar{a} = 233\ a_0$ and $k_2^{\mathrm{Univ}}(T=0) = 1.79 \times 10^{-10}\ \mathrm{cm^3\,s^{-1}}$ [3].

Away from the zero energy limit the value of k_2 has a strong energy dependence. Initially the second-order loss coefficient falls away: this is due to a falling contribution from the s partial wave. The next contribution to k_2 (d-wave) increases with temperature. However this contribution is zero at $T = 0$ and so it is not until higher temperatures (greater than 1 μK) that the second-order loss rate starts to increase again. Our model, which is described in greater detail in [174] uses Gao's analytic wavefunctions for a $1/R^6$ potential [176, 177], this accounts for the reflections off the long-range part.

[2]The superscript s is not for S-wave and instead stands for "short-ranged".

We are able to freely vary y and include multiple partial waves to get the full energy dependence. As the experiments are performed at finite temperature we thermally average the second-order loss coefficient

$$k_2(T) = \frac{2}{\sqrt{\pi}} \int_0^\infty k_2(E)\theta^{1/2} e^{-\theta}\, \mathrm{d}\theta, \tag{6.15}$$

where $\theta = E/k_\mathrm{B}T$. In figure 6.2(b) we plot the thermally averaged contours of constant $k_2(T = 1.5\ \mu\mathrm{K})$ as a function of y and δ^s. At this temperature the universal limit is $k_2^\mathrm{Univ}(T = 1.5\ \mu K) = 9.93 \times 10^{-11}\ \mathrm{cm}^3\,\mathrm{s}^{-1}$, nearly a factor of 2 reduced from the value at $T = 0$. In the region of parameter space for $y < 1$ we see the strong dependence on δ^s we expect. For $\delta^\mathrm{s} \approx \pi/8$ there is strong enhancement to loss, in excess of the universal limit, caused by resonant s-wave scattering. We also observe an enhancement to the loss coefficient at $\delta^\mathrm{s} \approx 5\pi/8$ due to a d-wave shape resonance. We note here that because RbCs is a boson only the even partial waves contribute. There are other shape resonances in $k_2(E)$ but have been washed out in the thermal averaging for $k_2(T)$ [174].

We have marked the region of 1-σ agreement between the value of k_2 measured in figure 6.1(a) and our thermally averaged k_2 in figure 6.2(b) with solid lines, the dashed line indicates the best fit value. From our single measurement we are able to determine that the collisional losses between RbCs molecules is sub-universal, with the highest acceptable value of y being 0.4, however we are not able to constrain the value of δ^s with only a single measurement.

6.1.3 Temperature Dependence

To constrain δ^s we choose to exploit the extra information that is contained within the temperature dependence of k_2. We vary the temperature of the molecules by using an adiabatic compression such that the final temperature T_f of the molecules, depends on the initial temperature T_i and the ratio of trapping frequencies

$$T_\mathrm{f} = T_i \times \left(\frac{\bar{\omega}_\mathrm{f}}{\bar{\omega}_i}\right). \tag{6.16}$$

Using the $\lambda = 1550$ nm optical dipole trap we are able to explore $\bar{\omega}_\mathrm{f}/2\pi$ in the region 79 Hz to 149 Hz, corresponding to temperatures of 0.85(5) μK

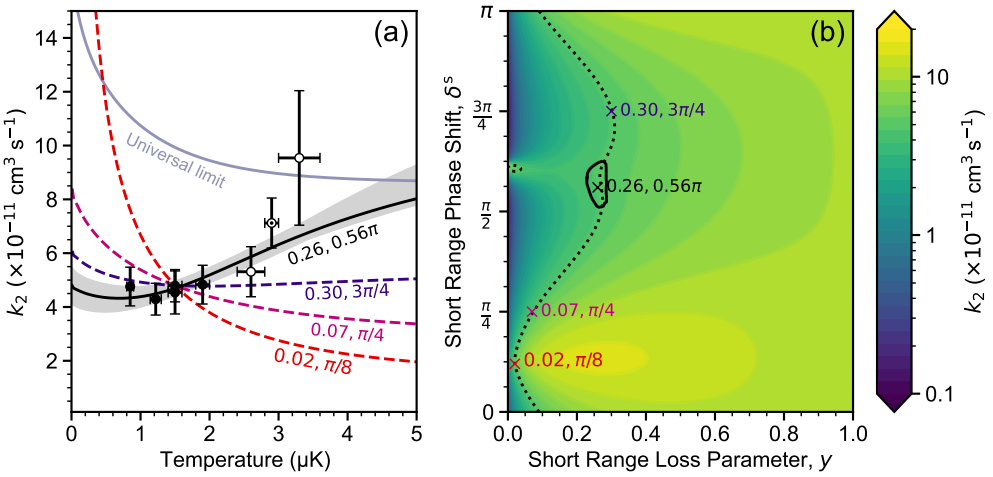

Figure 6.3: Exploiting the temperature dependence of the second-order loss coefficient k_2 to constrain the short-range phase and loss parameter δ^s and y. (a) The temperature dependence of k_2 as a function of initial molecule temperature. The filled black points use the $\lambda = 1550$ nm trap, the unfilled points use the $\lambda = 1064.52$ nm trap and the dotted point ($\odot$) uses a hybrid 1550 nm + 1064.52 nm trap. Each of the coloured dashed lines show the temperature dependence for a particular value of y, δ^s. The black line and shaded region correspond to the best-fit parameters and their error respectively. The temperature dependence of the universal limit ($y = 1$) is shown by the solid blue line. (b) The thermally averaged contours of $k_2(T = 1.5\ \mu\text{K})$ as a function of y and δ^s. The dashed line corresponds to the best-fit value of k_2 measured in figure 6.1(a). The crosses ($\times$) show the locations in parameter space for the continuous lines in (a). The solid line indicates the $\chi^2 \leq \chi^2_{\text{min}} + 1$ region.

and 1.9(1) μK respectively. To access higher temperatures we compress into a $\lambda = 1064.52$ nm potential, with waists 64 μm and 67 μm for which we perform measurements at $T = 2.6(2)$ μK and $T = 3.3(3)$ μK. To remove the possibility of additional losses due to heating or scatter caused by the $\sim$ 100 MHz beat frequency between the optical trapping beams we form a hybrid potential: crossing one beam of $\lambda = 1550$ nm and one of $\lambda = 1064.52$ nm.

We use a χ^2 minimisation method to determine the best-fit values of the short range parameters y and δ^s. To narrow the parameter space, we fit the loss as the temperature dependence as a function of δ^s with y constrained to give $k_2(T = 1.5\ \mu\text{K}) = 4.8 \times 10^{-11}\ \text{cm}^3\,\text{s}^{-1}$, we show several of these functions in figure 6.3(a). These slices through the (y, δ^s) parameter space show that

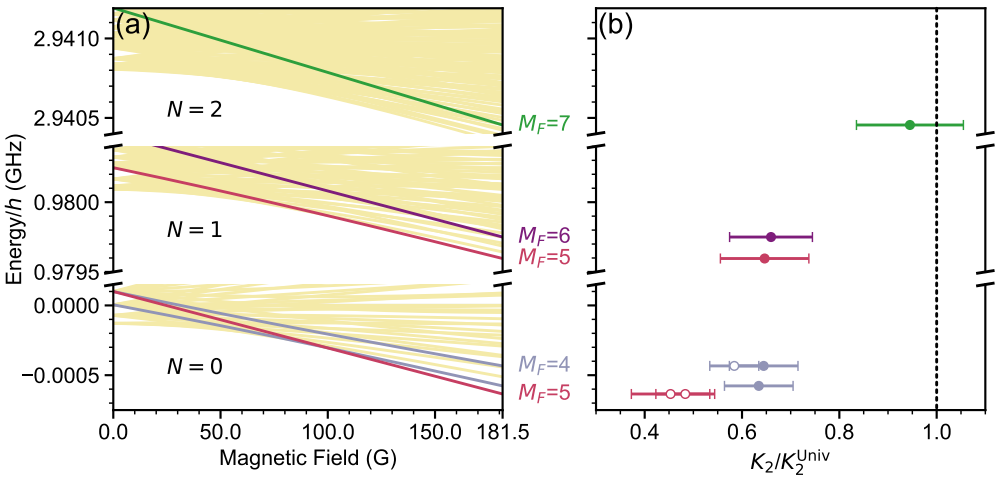

Figure 6.4: Measurements of k_2 in different hyperfine and rotational states. (a) The Breit-Rabi diagram for the first three rotational levels of RbCs, relevant hyperfine levels are highlighted. All experiments are performed at a magnetic field of 181.5 G. (b) The normalised values of k_2 for the highlighted states in (a). Unfilled points represent experiments where the state was populated using STIRAP, filled points represents experiments where the state was populated using coherent microwave π-pulses. The numerical values of k_2^{Exp} and k_2^{Univ} are given in table 6.1

temperature dependence of k_2 is strongly affected by the short range phase. We find that $y = 0.26(3)$ and $\delta^{\text{s}} = 0.56^{+0.07}_{-0.05} \times \pi$, where we have extracted the errors as the maximum extent on the $\chi^2_{\text{min}} + 1$ contour shown in figure 6.3(b) along the y and δ^{s} axes. As expected these data confirm that the loss is sub-universal, the value of y measured corresponds to $p_{\text{loss}} = 66(4)\%$ indicating that a third of the molecule flux that reaches short range is able to return to long range. Using equation (6.12) we can put the first constraint on the scattering length for molecule-molecule collisions: $231\ a_0 < a < 319\ a_0$, we note that this scattering length is not the same as the background scattering length.

6.1.4 Internal State Dependence

We can also explore the dependence of loss on the internal state of the molecule to shed light on the underlying two-body loss mechanism. As we are limited to only probing the number of molecules that are in the state that STIRAP can address any process which changes the state that molecules

State $(N, M_F)_i$	Energy/h (GHz)	$k_2^{\mathrm{Exp}} \times 10^{11}$ ($\mathrm{cm^3\,s^{-1}}$)	$k_2^{\mathrm{Univ}}(0) \times 10^{11}$ ($\mathrm{cm^3\,s^{-1}}$)	$k_2^{\mathrm{Univ}}(1.5\ \mu\mathrm{K})$ $\times 10^{11}$ ($\mathrm{cm^3\,s^{-1}}$)
$(0, 5)$	-0.000635	4.8(6)*	17.9	9.9
$(0, 5)$	-0.000635	4.5(8)*	17.9	9.9
$(0, 4)_1$	-0.000577	6.3(7)	17.9	9.9
$(0, 4)_2$	-0.000433	5.8(5)*	17.9	9.9
$(0, 4)_2$	-0.000433	6.4(7)	17.9	9.9
$(1, 5)_1$	0.979596	6.4(9)	17.9	9.9
$(1, 6)$	0.979750	6.2(8)	16.3	9.4
$(2, 7)$	2.940456	8.6(1.0)	15.8	9.1

Table 6.1: The values of k_2 for different rotational and hyperfine states. Experimental values where the state was directly populated using STIRAP are marked by an asterisk (*), all others were populated using coherent microwave π-pulses. The zero of energy is the ground rotational state in the absence of hyperfine structure and Zeeman shifts.

occupy would present as loss.

We have measured second-order loss coefficients for three hyperfine states in $N = 0$ (including the hyperfine ground state), two in $N = 1$ and one in $N = 2$. These are shown in figure 6.4 and the numerical values are summarised in table 6.1. Transfer between the ground state and the excited states is achieved using a mixture of STIRAP and coherent microwave π-pulses. We compare the losses for each state to the universal rate, which is not independent of state. The value of k_2^{Univ} changes with state due to the different rotational contributions to the value of C_6. We show the fractional loss coefficient k_2/k_2^{Univ} in figure 6.4(b) for each of the hyperfine states investigated. We see that the ratio increases significantly in the excited states. In $N = 2$ the ratio is consistent with 1, indicating that the collisions are near-universal. The measured increase is likely due two-body inelastic collisions, but could also also be caused by an increased formation of collision complexes. In the excited states the higher angular momentum allows the incoming channel to couple to a larger number of states in the $(\mathrm{RbCs})_2$ complex.

We have also studied the collisions where we put only half of the molecules into a rotationally excited state. We start with a pure sample of molecules in $(N = 0, M_F = +5)$, using a microwave $\pi/2$-pulse we transfer half of the

population into $(1, +6)$ where, because of the differential AC Stark effect the superposition rapidly dephases within 10 μs[3]. The resulting density matrix which describes the molecule sample therefore has only diagonal elements and so the molecules occupy a statistical mixed state. The two states that we have chosen are connected by an electric dipole allowed transition, so the collisions between them experience an additional resonant dipole interaction. For S-wave scattering this interaction cancels to first order because of spherical averaging, for the higher partial waves the interaction dies off as $1/R^3$. These terms die off much more slowly than the $1/R^6$ dispersion interaction at long ranges and could reasonably be expected to produce higher loss rates.

To model this system we use a modification of our coupled rate equations. We consider the density $n_N(\vec{r}, t)$ of molecules in the two rotational states to be governed by the coupled rate equations

$$\frac{\mathrm{d}n_0(\vec{r},t)}{\mathrm{d}t} = -k_2^{00}(n_0(\vec{r},t))^2 - \frac{1}{2}k_2^{01}n_0(\vec{r},t)\ n_1(\vec{r},t), \tag{6.17a}$$

$$\frac{\mathrm{d}n_1(\vec{r},t)}{\mathrm{d}t} = -k_2^{11}(n_1(\vec{r},t))^2 - \frac{1}{2}k_2^{01}n_0(\vec{r},t)\ n_1(\vec{r},t). \tag{6.17b}$$

We use the values of k_2 measured for molecules in a single rotational state, as shown in table 6.1 for k_2^{00} and k_2^{11}. We are then able to fit these loss equations to our experimental data, finding $k_2^{01} = 7.9 \times 10^{-10}\mathrm{cm}^3\,\mathrm{s}^{-1}$. This is a significant increase over molecules in a single rotational and hyperfine state, indicating that the resonant dipole-dipole interactions are enhancing the loss rate. As the two states used have a difference in polarisability of $\sim 10\%$ we repeat the experiment twice, once matching the trap frequency between the Feshbach molecules and $N = 0$ and once matching between the Feshbach state and $N = 1$. In both measurements we measure the same value of k_2^{01}.

6.1.5 Magnetic Field Dependence

The single channel model we have been using has no explicit dependence on magnetic field, however at fields below 98.8 G ($N = 0, M_F = +5$) is no longer the hyperfine ground state. This implies that hyperfine state changing collisions could occur between RbCs molecules. If this were the case it

[3]See chapter 5 and chapter 4 for more information.

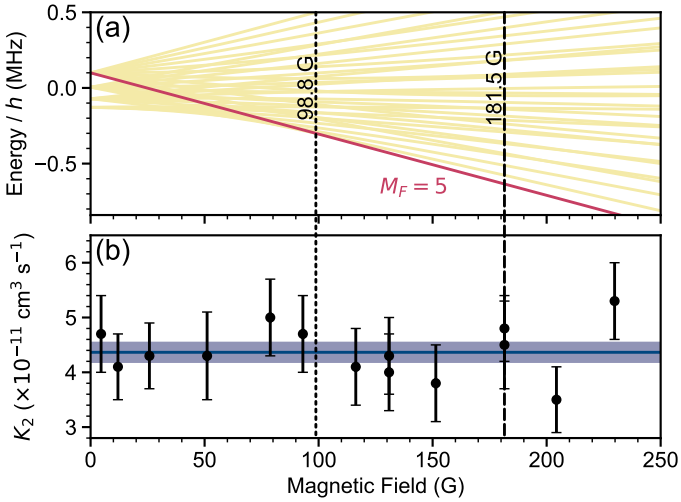

Figure 6.5: The two-body loss coefficient k_2 as a function of applied magnetic bias field. (a) The Breit-Rabi diagram for the ground rotational state ($N = 0$) of RbCs. The magnetic field at which molecules are produced (181.5 G) and the magnetic field where the populated state with $M_F = +5$ is no longer the absolute ground state (98.8 G) are shown as dashed and dotted lines respectively. (b) The two-body loss coefficient, as extracted from a fit to equation (6.9), as a function of magnetic bias field. The solid line shows the mean value of k_2 and the shaded region the error on the mean. We see no statistically significant variation in the scattering properties as a function of magnetic field.

would manifest in the experiment as an increased loss rate because of the state-selective nature of STIRAP. We note here that previous measurements by Takekoshi *et al.* at 8.7 μK did indeed see an increase in loss rate by approximately an order of magnitude when the magnetic field was held below 90 G [41].

To measure the dependence of k_2 over a range of magnetic fields we ramp the applied magnetic bias field linearly from 181.5 G to the target field in 50 ms. After a variable hold time we must ramp back to 181.5 G, again over 50 ms, to bring the STIRAP lasers back into resonance. In figure 6.5 we show the values of k_2 extracted by repeating this process for target fields from 4.6 G and 229.8 G. As can clearly be seen we do not observe any increased loss of molecules as a function of magnetic field, even when $(0, 5)$ is not the hyperfine ground state by ~ 0.1 MHz. We therefore discount the possibility of hyperfine state changing collisions as a loss mechanism. Our data instead supports the hypothesis that molecule loss is entirely mediated by the formation of $(\mathrm{RbCs})_2$ collision complexes, which is unlikely to be

strongly affected by the small changes in asymptotic states and therefore will be independent of magnetic field.

6.1.6 Conclusions

From the measurements presented in this section we can determine that the rate-limiting step is second-order in molecule density. This supports the "sticky collisions" hypothesis that molecules are lost to $(RbCs)_2$ complex formation. However the prediction of Mayle *et al.* and Christianen *et al.* [168, 170] predict universal losses at short range, whilst we observe only 66(4)% losses. This could be due to a number of reasons, firstly the RRKM theory assumes that the averaged with of the complex states is proportional to the spacing between them, an alternative way to arrive at the same result is through random matrix theory, which assumes there is no structure to the energy levels: clearly this is only an approximation and it is unsurprising that the real system has a loss rate below this prediction. Another interpretation is that $(RbCs)_2$ complexes are only formed at a small subset of relative orientations of the RbCs molecules. Currently we have no way to determine which of these mechanisms is the true cause of the sub-universal loss rate.

Acknowledgement

The single channel theory and thermally averaged calculations of k_2 presented in this section were produced by Matthew D. Frye. Additional detail on the model can be found in [174, 178].

6.2 Complex-mediated Photoinduced Losses

Our measurements on collisions of RbCs molecules told us that the kinetics are second-order, indicating that the rate-limiting step is two-body. We have already discounted the possibility of chemical reactions by consideration of the energetics involved. The remaining mechanisms are those which involve "sticky collisions". The historical prediction for the lifetime of the $(RbCs)_2$ was calculated by Mayle *et al.* to be $\tau_c = 45$ ms [168]. More recent work

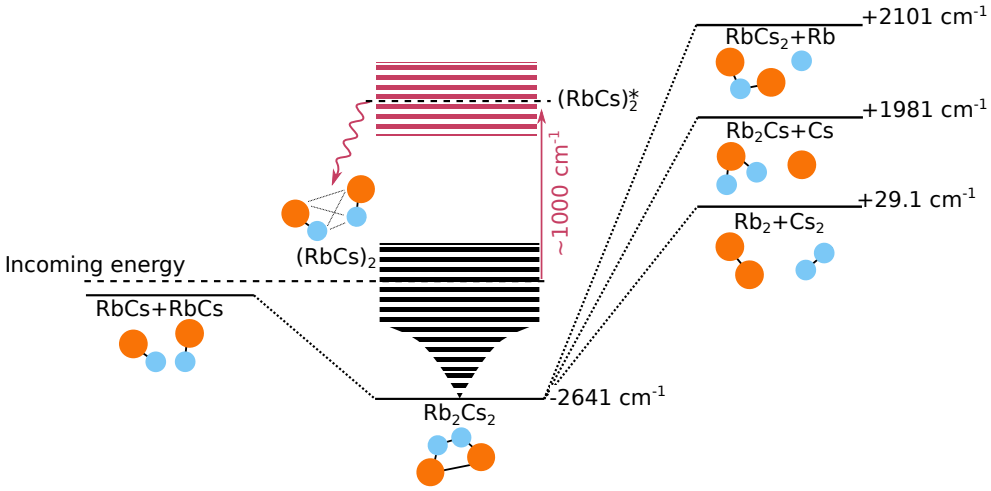

Figure 6.6: An illustration of the energetics of the photoinduced loss mechanism. Energy levels are taken from [166, 179] and are given with respect to the pair of free RbCs molecules. All available atom transfer reactions are forbidden energetically, however due to the high density of states near the incoming energy the transient complex $(RbCs)_2$ can form. These complexes can then be excited to the $(RbCs)_2^*$ states by light from the trapping potential. It is important to note that these transitions are at much longer wavelengths than those in the RbCs molecule. Once a complex has absorbed a photon it appears as a lost pair of RbCs molecules.

by Christianen *et al.* corrected an error in the historical calculation of the density-of-states [170], and therefore also in τ_c. Their prediction was that $\tau_c = 505$ µs [151]. Christianen *et al.* also predicted that at experimental densities sticking-amplified three-body losses would lead to a lifetime on the order of minutes in RbCs [170], as such it is expected that photoinduced losses of molecular collision complexes forms the dominant loss mechanism. In this section we will show that this is the case for RbCs.

We measure the photoinduced loss of complexes by introducing a time-dependent intensity to our optical dipole trap. The trap itself is a crossed optical dipole trap with $\lambda = 1064$ nm in a bow-tie configuration. The first pass through the cell has a waist of 107(1) µm, whilst the second is 74(1) µm. Between the two passes there is an acousto-optic modulator to introduce an 80 MHz frequency difference between the two beams and is included to avoid interference effects. We introduce the modulation by using a ThorLabs MC2000 optical chopper, the motor for which can spin at up to 100 Hz. We use a custom-made laser-cut blade which gives us an accessible modulation

frequency range of 120 Hz to 6 kHz. The duty cycle, that is the ratio of "bright time" to "dark time", is fixed to 25% or a ratio of 1:3. To imprint the intensity modulation onto the trapping light we focus the output of the 1064 nm laser through the aperture in the blade. Focussing the beam in this manner minimises the time where the laser beam is being diffracted, this is important as it makes the laser output better match our desired square-wave intensity profile. This minimises the light that leaks through to the molecules during the "dark time", any additional light during this time will continue to drive the optical losses of $(RbCs)_2$. The intensity profiles expected for differently sized beams are shown in figure 6.7(a).

The experiments we perform start with Feshbach molecules being produced in the $\lambda = 1550$ nm crossed dipole trap. To transfer from this trap into the time averaged potential we first increase the intensity of the $\lambda = 1064$ nm laser over 50 ms before the magnetic levitation gradient and 1550 nm light are ramped off in 10 ms. When not in use we block the $\lambda = 1550$ nm light with a pair of mechanical shutters, one for each beam. Typically we must turn the trapping light off to efficiently perform STIRAP. This avoids spatially dependent AC Stark shifts. In the time-averaged trap we exploit the intensity modulation and synchronise the STIRAP sequence to only occur during the time where the molecules are in the dark.

6.2.1 Measuring the lifetime of $(RbCs)_2$

The photoinduced loss mechanism is predicted to be saturated by multiple orders of magnitude, this means that as the laser intensity is increased for the intensity-modulated trap the rate of loss of complexes is fixed as the limiting step is their formation. Therefore whilst the light is off the molecule density is determined entirely by the decay and formation of $(RbCs)_2$ complexes. We can then use the time that the trap is off to probe these dynamics. We model the rate of change of the density of molecules, n_{mol} and complexes n_{c} using the coupled rate equations

$$\frac{\mathrm{d}n_{\mathrm{mol}}}{\mathrm{d}t} = -k_2 n_{\mathrm{mol}}^2 + \frac{2}{\tau_c} n_{\mathrm{c}}, \tag{6.18a}$$

$$\frac{\mathrm{d}n_{\mathrm{c}}}{\mathrm{d}t} = \frac{1}{2} k_2 n_{\mathrm{mol}}^2 - \frac{1}{\tau_c} n_{\mathrm{c}} - k_1 I(t) n_{\mathrm{c}}. \tag{6.18b}$$

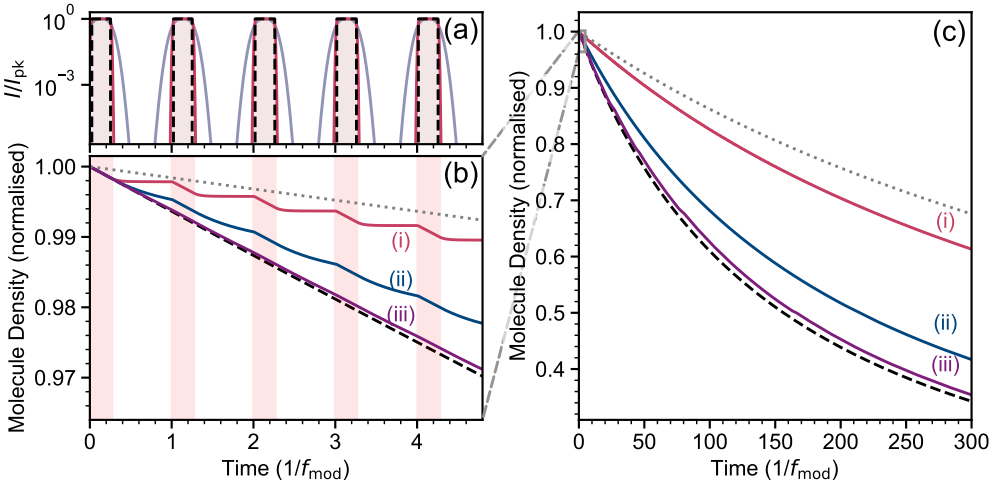

Figure 6.7: An illustration of a lifetime measurement in the intensity-modulated potential. (a) The intensity of the dipole trap as a function of time, shown on a logarithmic intensity scale. An ideal square wave is shown as a dashed black line, the solid red line shows the behaviour for our small laser beam. The blue line shows the same for a larger beam waist. (b) The molecule density on short time scales for $\tau_c/t_{dark} = 0.1$ (i), 1 (ii), 10 (iii). The dashed line shows the time-dependent density for a CW trap. The dotted line shows a CW trap with $k_2/4$. (c) As in (b) but on longer time scales. It can be seen that as the time is extended the behaviour in the intensity-modulated potential results in slower losses.

In the above k_2 is the second-order loss coefficient for molecules, where we have presumed that molecule loss is entirely governed by the formation of $(RbCs)_2$ complexes. We have included another parameter: τ_c which is the lifetime of the complex before it decays back into a pair of molecules. There is a factor of 2 difference in the first two terms of the coupled rate equations because it takes a pair of molecules to form a single complex. To model the photoinduced loss we include k_1, which is the first-order loss coefficient for the complexes.

Over multiple cycles the difference in molecule density between the intensity-modulated and continuous-wave (CW) potentials becomes much larger, as can be seen in the simulation of the mechanism in figure 6.7(b-c). For this simulation we use a fixed $f_{mod} = 1.5$ kHz, a 25% duty cycle and a second-order molecule-molecule loss coefficient appropriate for RbCs. For our initial analysis we assume that $k_1 I_0 \gg \tau_c^{-1}$, an assumption which is supported by theoretical predictions and that we shall justify later.

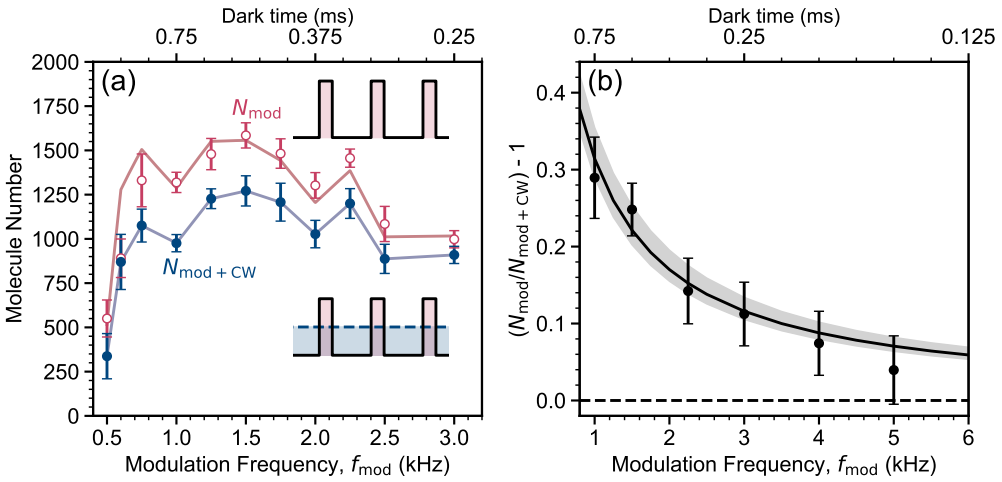

Figure 6.8: Measuring the lifetime of $(RbCs)_2$ in the time-averaged potential. (a) The number of molecules in the intensity-modulated trap with and without additional CW light ($N_{\mathrm{mod+CW}}$ and N_{mod} respectively) as a function of the modulation frequency of the trap. Each point is the mean and standard error of 8 measurements. The solid line is a linear interpolation of the points for $N_{\mathrm{mod+CW}}$, the dashed line is this function multiplied by the best-fit curve in (b). Sketches of the time-dependent intensities are shown inset. (b) The fractional difference in the molecule number with and without the CW light. Each point is the ratio of the mean of 50 measurements of N_{mod} and $N_{\mathrm{mod+CW}}$. The solid line is an exponential fit to the results with $\tau_c = 0.53(6)$ ms, the shaded region showing the error bar.

Before we can extract the behaviour of the complexes we have to determine the parameters associated with their formation. To do this we measure two-body loss curves in the CW 1064 nm trap, which operates in the same geometry as the intensity-modulated trap. We use the same procedure as in figure 6.1, finding that the best fit is still $\gamma = 2$ and $k_2 = 5.4(9) \times 10^{-11}$ cm^3 s^{-1}. This is in agreement with the theory prediction in figure 6.3(a). For our analysis of the lifetime we fix this value of k_2 in the CW and time-averaged traps.

We measure the lifetime of the complex by varying the dark time t_{dark}, as the duty cycle is fixed this is achieved by changing the modulation frequency. Introducing the intensity modulation also introduces another source of heating through parametric heating and therefore additional losses through evaporation. This extra loss is likely strongly frequency dependent with a highly complex structure due to the presence of high harmonics of all three trap

frequencies. We therefore need to perform a comparative measurement, where the heating and evaporative losses are common to both data sets. To produce such a comparative measurement we choose to add a second, low-intensity, CW beam at $\lambda = 1550$ nm. The light is sourced from the same laser as is used to trap the atomic mixture, but we have significantly reduced the peak intensity to 0.31(1) kW cm^{-2}. This intensity was chosen as it should be large enough to maintain $k_1 I \gg \tau_c^{-1}$ yet is low enough that it does not significantly perturb the trapping potential that the molecules experience[4]. We label the number of molecules after a 200 ms hold in N_{mod} when only the time averaged potential is used and $N_{\mathrm{mod+CW}}$ when we have introduced the low-intensity beam. We show the ratio of the two values as a function of modulation frequency in figure 6.8(a), averaged over 8 measurements. The trap frequencies experienced by the molecules are $[\omega_x, \omega_y, \omega_z]/(2\pi) = [96(2), 160(3), 185(3)]$ Hz. At low frequency ($f_{\mathrm{mod}} < 1$ kHz) we observe significant losses from the time-averaged potential, this is consistent with parametric heating effects [180–183]. At higher frequencies we observe a broad band where losses caused by the trap are low and where N_{mod} is greater than $N_{\mathrm{mod+CW}}$ by more than 1σ, indicating that there is an observable reduction in the rate of loss.

The expected suppression of photoinduced loss depends strongly on the ratio τ_c/t_{dark}, that is what fraction of a lifetime the complexes are not scattering light: the larger this fraction the higher the probability that the complexes dissociate back into individual RbCs molecules. To accurately determine the lifetime of $(\mathrm{RbCs})_2$ we perform 50 interleaved measurements each of N_{mod} and $N_{\mathrm{mod+CW}}$. The measurements are interleaved so that slow changes over the $\sim$ hours taken for the data to be gathered are equally included in both datasets. In figure 6.8(b) we show the data from these measurements, presented as the fraction difference $(N_{\mathrm{mod}}/N_{\mathrm{mod+CW}})-1$ as a function of f_{mod}. The solid line is a fit to equation (6.18a), where the only free parameter is τ_c, as we assume that no complexes remain between light pulses. We find that $\tau_c = 0.53(6)$ ms with an additional systematic uncertainty of ± 0.11 ms, associated with our density calibrations. As a simplification we have assumed that the molecules do not get heated as a function of time by either the

[4]Typical traps at this wavelength have peak intensities of ~ 10 kW cm^{-2}.

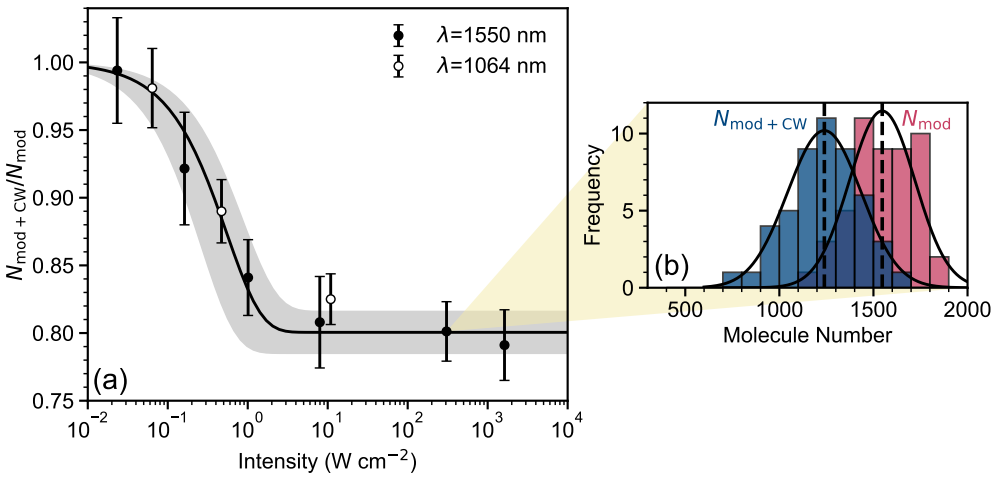

Figure 6.9: The intensity dependence of the loss of $(RbCs)_2$ complexes. We fix the modulation frequency to 1.5 kHz (dark time = 0.67 ms) and measure the ratio between molecule number with and without the CW light, for which we vary the intensity. Each data point is the result of 50 measurements each of N_{mod} and N_{mod+CW}, errorbars show the standard error. (b) An example histogram with N_{mod} shown in red and N_{mod+CW} shown in blue. The mean values are indicated by dashed vertical lines and the Gaussian distribution of the data is shown as a solid line.

intensity modulation or by the two-body loss, our model indicates that a 25% increase in temperature would shorten τ_c by $\sim 20\%$.

The measured value of the lifetime for $(RbCs)_2$ compares favourably with theory. The prediction of Christianen *et al.* is $\tau_c = 0.253$ ms [170]. We note that their prediction is from a detailed calculation for the $(NaK)_2$ complex, where they have scaled the result to $(RbCs)_2$ using approximate scaling laws. Performing such a calculation for $(RbCs)_2$ would be a large undertaking in itself. We note that the expected density of states increases with the reduced mass of the molecule, where NaK is the lightest of the non-reactive bialkalis and RbCs is the heaviest.

6.2.2 Measuring the Intensity Dependence

In the previous section we assumed that the intensity of our additional CW beam was sufficient to continuously remove complexes. In this section we will use the time-averaged trapping potential to probe the intensity depend-

ence of the photo-induced loss mechanism and in the process will test this assumption.

To perform this measurement we fix the modulation frequency to 1.5 kHz, corresponding to $t_{\mathrm{dark}}/\tau_{\mathrm{c}} \approx 1.25$ and vary the intensity of the CW beam. For intensities above 10^2 W cm^{-2} we can use the CW beam described previously. To reduce the intensity further we use a larger beam of the same $\lambda = 1550$ nm light. As for our measurement of τ_{c} for each intensity we perform 50 interleaved measurements of N_{mol} and $N_{\mathrm{mol+CW}}$, in figure 6.9(a) we present this data as the ratio: $N_{\mathrm{mod+CW}}/N_{\mathrm{mod}}$.

To extract the value of k_1 we fit the model

$$\frac{N_{\mathrm{mod+CW}}}{N_{\mathrm{mod}}} = (1 - B) \times \exp\left(-\frac{I}{I_0}\right) + B, \tag{6.19}$$

to our data. We leave B and $I_0 = (k_1 \times \tau_{\mathrm{c}})^{-1}$ as free parameters. The best fit is achieved for $I_0 = 5^{+5}_{-3} \times 10^{-1}$ W cm^{-2}. We can convert this into the first order loss coefficient k_1 from equation (6.18) by including our measured value for τ_{c}. Doing so gives $k_1 = 3^{+4}_{-2} \times 10^3$ s^{-1} (W cm^{-2})$^{-1}$. A typical trap for our molecules will have depth ~ 10 μK, for RbCs this is an intensity of ~ 5 kW cm^{-2} and gives a scattering rate (excitation time) of 15×10^6 s^{-1} (66 ns). This excitation time is over three orders of magnitude smaller than τ_{c}, confirming that not only was our earlier assumption that $k_1 I \gg 1/\tau_{\mathrm{c}}$ is valid but also that the photoinduced loss process is heavily saturated. With the process being so heavily saturated as soon as a complex is formed from a pair of molecules it scatters a photon and is removed.

We have also repeated the intensity dependence tests using a $\lambda = 1064$ nm beam. These data are shown in figure 6.9(a) as unfilled points. We see that the change in wavelength does not significantly affect the saturation behaviour. This was expected: Christianen *et al.* predicted that signficicant changes in the laser excitation rate would require an increase of the wavelength to ~ 10 μm [151].

6.2.3 Summary and Conclusions

By using an intensity-modulated trap we have been able to suppress photo-induced loss of RbCs molecules. This simple addition to our existing appar-

atus has offered a powerful insight into the lifetime of the collision complex, both in the dark and in the optical trapping light. We have found that the lifetime in the dark *i.e.* the time to decay back to a pair of RbCs molecules agrees within a factor of two with the rescaled value of [151], which is excellent given the complexity of the calculation. By measuring in the light we have seen that as the intensity increases fewer complexes break back apart into molecules. We have to reduce the intensity by many orders of magnitude from a typical trapping intensity to suppress this. Recently Liu *et al.* have performed a complementary experiment using a bulk gas of KRb, and reached the same conclusions [184].

Our results indicate that there are two ways now to reduce the effect of loss of molecules on current and next-generation molecule experiments. The first is to remove the formation of complexes entirely: this can be achieved using techniques for trapping single molecules in tweezers, or in sites of an optical lattice. Another possibility if a bulk gas is required is to shield individual molecules from collisions using DC electric fields [185] or by dressing using microwaves [186, 187]. The other way that losses can be mitigated is to not use a red-detuned optical trap with saturated losses. A blue detuned box trap could be used to reduce the scattering rates as molecule spend more time in low-intensity regions [153] as could a significant increase in wavelength [151]. If the molecule possess a magnetic moment, such as the $^2\Sigma$ molecules currently used in laser cooling, then magnetic traps [188] avoid the possibility of optical excitation altogether.

We have conclusively determined the dominant loss mechanism for ultracold ground state RbCs, and likely the other non-reactive bialkalis, to be photo-excitation of a collision complex by the infra-red trapping laser, which at typical intensities is very highly saturated. The complexes are formed by a two-body collision of the form RbCs+RbCs$\rightarrow$(RbCs)$_2$.

6.3 Collisions Between Atoms and Molecules

Throughout this chapter we have been considering the processes that occur between pairs of RbCs molecules. Of course because we associate our mo-

lecules from pre-cooled gases of ^{87}Rb and ^{133}Cs we can also study collisions in mixtures of these atomic species with our molecules. Studying collisions between atoms and molecules could open up a promising new avenue for cooling of RbCs further than is currently possible, collisional cooling has been observed in a mixture of $^3\Sigma$ NaLi and Na [189] suggesting that workable parameters are possible to find.

There are multiple loss mechanisms that are possible in a mixture between atoms and molecules, the most obvious of which are chemical reactions. By comparing the binding energies of the different homonuclear dimers we can consider the energetics of the RbCs + atom processes

$$\mathrm{RbCs} + \mathrm{Rb} \rightarrow \mathrm{Rb_2} + \mathrm{Cs}, \quad \Delta E/hc = -181.9(2)\ \mathrm{cm}^{-1}\ [167], \tag{6.20a}$$

$$\mathrm{RbCs} + \mathrm{Cs} \rightarrow \mathrm{Cs_2} + \mathrm{Rb}, \quad \Delta E/hc = +161.88(2)\ \mathrm{cm}^{-1}\ [167]. \tag{6.20b}$$

By studying atom+molecule collisions we can therefore access reactive collisions with Rb atoms and non-reactive with Cs atoms. For both atomic species the reaction of the form RbCs + X → XRbCs is energetically allowed by $\sim 10^3\mathrm{cm}^{-1}$ [167]. However, like the reaction RbCs+RbCs → $\mathrm{Rb_2Cs_2}$, this should be unlikely at ultracold temperatures [166]. In the case of the non-reactive reaction RbCs+Cs there are multiple mechanisms that we could consider. These are similar to the RbCs+RbCs mechanisms in that they rely on an intermediate collision complex. When compared to the molecule-molecule case the predicted density of states should be lower for the atom-molecule system by a factor of $\sim 10^5$ [168, 169], this would shorten the lifetime of the complex significantly and so reduces the likelihood of collision-enhanced three body losses.

In this section we present early data on collisions between RbCs molecules and Rb, Cs atoms. First we present our method of removing a single species from the mixture. We perform comparable measurements at two magnetic fields, with no significant differences between the two.

6.3.1 Species-Selective Removal

Typically in experiments on molecules we use the Stern-Gerlach effect to separate the Feshbach molecule cloud from the atoms. We achieve this by

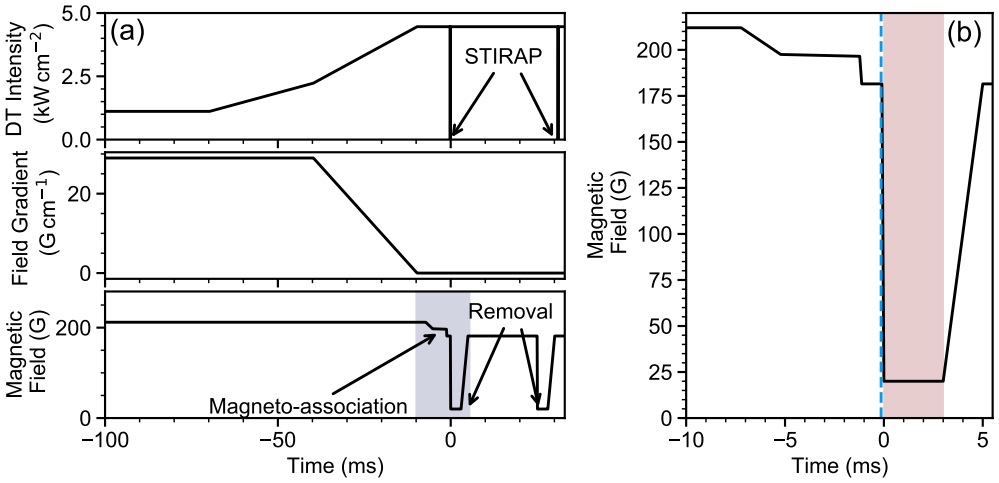

Figure 6.10: (a) The sequence used to measure collisions between molecules and atoms. Key points in the sequence are labelled. (b) A zoom in on the highlighted region in (a). The time when the STIRAP pulse sequence begins is shown by the blue dashed line. The shaded region shows where the MOT light is switched on for atom removal.

increasing a magnetic field gradient to levitate the molecules, held in the $n = -2$ Feshbach state, against gravity which gives the dipole trap for the atoms a significant upwards tilt. This is very effective at removing both atomic species and leads to a pure sample of RbCs. However it is not species selective as the magnetic moment to mass ratio is approximately the same for both Rb and Cs. As such we need a new method to selectively remove only one atomic species from our mixture.

There are several possibilities: microwave ARP between hyperfine states followed by optical cycling on a closed transition [190] or tuning a repump and "blaster" beam to resonance at high field. Both of these require an understanding of the internal atomic structure in a magnetic field, our calculations of which are presented in Appendix A. An alternative implementation involves bringing the atoms back to resonance with our existing laser light using the magnetic field. We choose to use this option as it does not require any additional hardware. Briefly the sequence is as follows:

1. The atoms are transferred into a pure optical potential adiabatically.

2. The Feshbach molecules are produced as usual at 181.5 G and transferred into the state with $n = -6$.

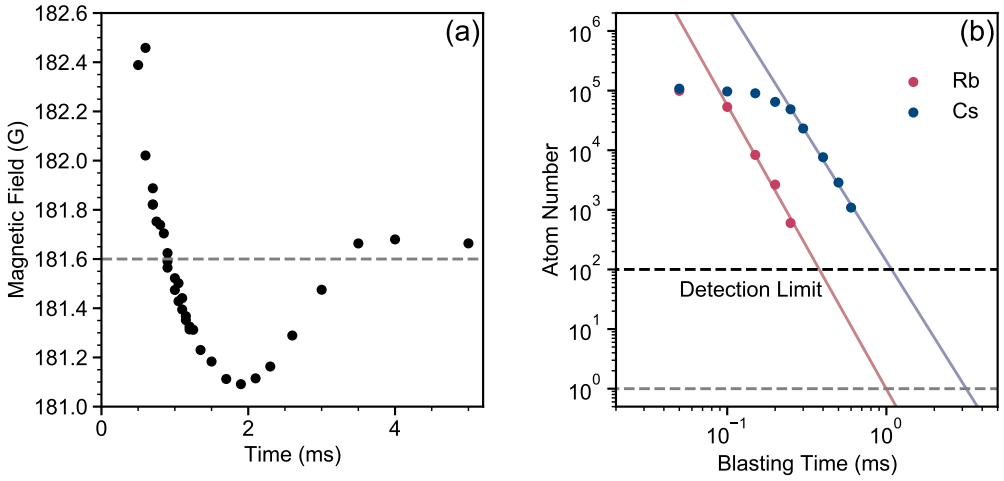

Figure 6.11: Determining the timescales for single-species removal. (a) The variation in magnetic field following magneto-association, measured using microwave spectroscopy of the ^{87}Rb ($f_{\mathrm{Rb}} = 1, m_{\mathrm{Rb}} = 1$) $\rightarrow$ $(2, 2)$ transition. The target field value is shown as a dashed line. We fix the wait between jumping the magnetic field and the STIRAP sequence to 1 ms based on this crossing point. (b) The loss of ^{87}Rb (red) ^{133}Cs atoms whilst the blaster light is switched on at 20 G. The minimum atom number we can detect using our absorption imaging is shown by a horizontal dashed black line. We extrapolate to total removal by fitting a straight line in log-log space.

3. The molecules are transferred via STIRAP to the absolute ground state.

4. The magnetic field is reduced to 20 G in 0.1 ms followed by 3 ms where the MOT light is switched on.

Finally if necessary the magnetic field is increased back to 181.5 G for the measurement. If one atomic species remains in the trap we repeat step 4 to remove it before increasing the magnetic field back to 181.5 G for STIRAP. This sequence is also shown diagramatically in figure 6.10.

We find that it is necessary to include a wait between the changing magnetic field and the STIRAP process to allow the field to settle. We determine this time using high-precision microwave spectroscopy of the ($f_{\mathrm{Rb}} = 1, m_{\mathrm{Rb}} = 1$) $\rightarrow$ $(2, 2)$ transition, the change in magnetic field with time is shown in figure 6.11(a). We aim to keep this time as short as possible as we observe fast loss ($1/e$ time of 1.2(1) ms) of Feshbach molecules when they are held in a mixture with free atoms of total density $\sim 10^{13}$ cm^{-3}. The blasting must take place after the STIRAP transfer to the ground state as the Feshbach

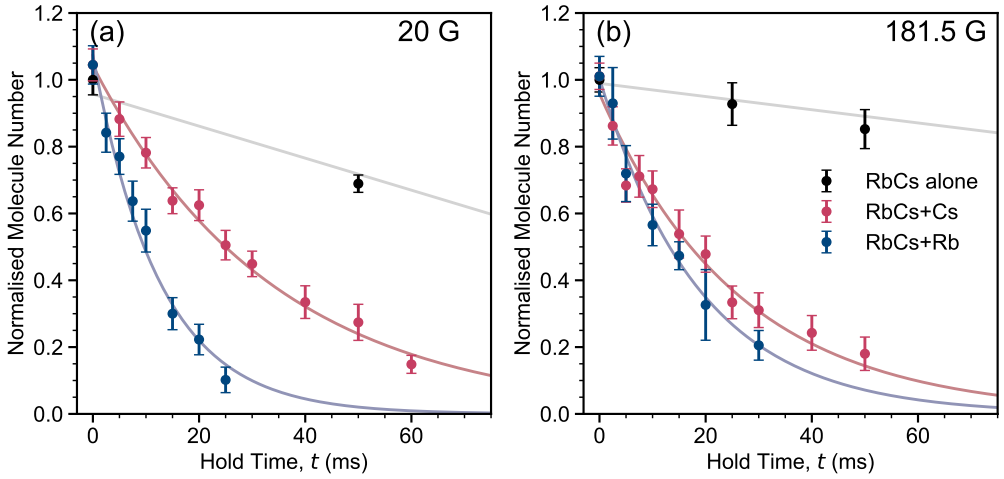

Figure 6.12: The lifetime of RbCs measured in a mixture with Rb and Cs. (a) The number of RbCs molecules as a function of time with Rb atoms (blue points) and Cs atoms (red points). The lifetime is measured at the magnetic field where the atomic species can be removed: 20 G. The lifetime of RbCs without either atomic species is also shown as a reference (black points). (b) As in (a) but at a magnetic field of 181.5 G.

molecules will scatter the light used for removal.

We identify the amount of time needed for full removal by using in-situ imaging of the atomic mixture and varying the length of the removal pulse. Using the in-situ measurement method has a minimum number of atoms that we can detect which is ~ 100. Because of this we cannot image to total removal and must extrapolate the exponential decay to find an appropriate amount of time. The loss of atoms as a function of time in the light is shown in figure 6.11(b). Based on these measurements we fix the removal pulse time, for both species, to 3 ms.

Using this sequence we are able to produces samples of RbCs molecules in the $(^1\Sigma, N = 0, M_F = +5)$ ground state at a temperature of 1.1(2) μK. These molecules are in a mixture with atoms of either species. Both atomic species are in their absolute ground state. The atoms are at a temperature of 0.73(5) μK and a mean density of $\sim 4 \times 10^{12}$ cm^{-3}, this is an order of magnitude greater than the density of the molecules.

6.3.2 Lifetime Measurements

Now that we are able to produce samples of RbCs and Rb or Cs atoms we can study the behaviour of the new mixture. In figure 6.12 we show the results for measuring the lifetime of RbCs with Rb and Cs atoms at ~ 20 G and ~ 181.5 G. It is immediately obvious that the loss between atoms and molecules is much faster than that between the molecules themselves, however this is not unexpected as the mean atom density is $\sim 10^{13}$ cm^{-3}, compared to the molecules $\sim 10^{11}$ cm^{-3}. This increase in density increases the rate of collisions, and therefore also of collisional losses. We find that these measurements fit well to exponentials with time constants of 17.0(1.8) ms [24.1(1.5) ms] for mixtures with Rb [Cs] at 181.5 G. At 20 G these time constants are 14.7(1.1) ms [48(3) ms] for mixtures with Rb [Cs]. The atomic densities are not equal however and so we cannot directly compare these time constants and must determine a density scaling law.

To determine the density scaling we desire to remove all atoms of one species and a portion of the atoms of the other. We choose to optically remove all of the Rb atoms. We cannot use the optical technique to remove only some of the Cs atoms as the light distributes atoms across multiple states. Instead we rapidly tilt the trapping potential using a magnetic field gradient. This over-levitates the atoms and causes a portion of them to leave. In figure 6.13 we show the $1/e$ lifetime of the molecule against the mean Cs atom density on a log-log scale. The two expectations for this data are that the additional losses are caused by RbCs+Cs collisions or by RbCs+Cs+Cs collisions. We expect the loss rate (the inverse lifetime) to scale linearly and quadratically with the mean atomic density respectively. A linear fit in log-log space to the data gives a gradient of -1.00(3) allowing us to discount the three-body process as a possibility.

Having determined the density scaling and desiring a more quantitative description, we consider the rate of change of density of molecules, in the presence of atoms, to be given by

$$\frac{\mathrm{d}n_{\mathrm{mol}}}{\mathrm{d}t} = -k_2^{\mathrm{mol}} n_{\mathrm{mol}}^2 - k_2^i n_i n_{\mathrm{mol}}. \tag{6.21}$$

where i =Rb, Cs. We will assume that $\mathrm{d}T_{\mathrm{mol}}/\mathrm{d}t = 0$. As in section 6.1 we are actually measuring the number of molecules and not the density. The

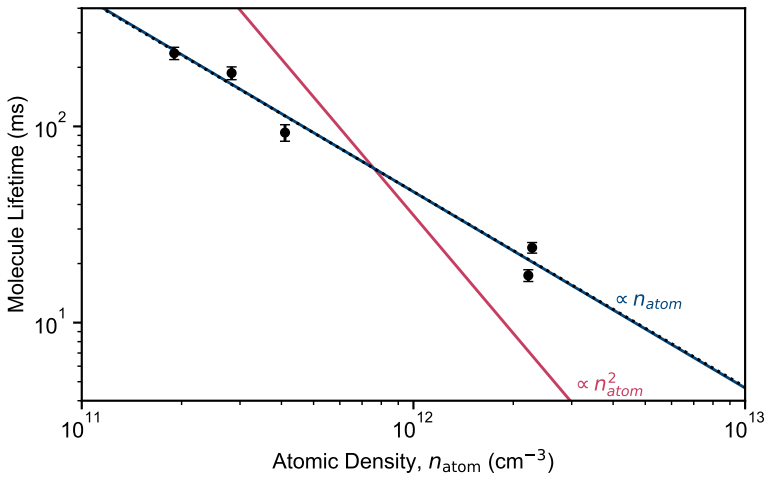

Figure 6.13: The $1/e$ lifetime of RbCs molecules when in a mixture with Cs is shown as a function of mean Cs atomic density. The dotted black line is a fit to the data to extract the density dependence as a power law, the fitted gradient is -1.00(3). The solid blue and red lines are expectations for a linear and quadratic density dependence.

rate of change is therefore the integral of equation (6.21) over all space. We have already determined the first term in the derivation of equation (6.9). To determine the second term we must consider the interspecies density. We can arrive at an approximation if we assume that the trap for the molecules and atoms are centred at the same point and that they are spherical *i.e* $\omega_x = \omega_y = \omega_z = \bar{\omega}$

$$\begin{aligned} N_{\mathrm{mol}}\bar{n}_i &= \int n_{\mathrm{mol}} n_i \, \mathrm{d}^3 r \\ &= N_{\mathrm{mol}} N_i \left(\frac{(m_{\mathrm{mol}}\bar{\omega}_{\mathrm{mol}}^2)(m_i\bar{\omega}_i^2)}{2\pi k_{\mathrm{B}} \left[(m_i\bar{\omega}_i^2) T_{\mathrm{mol}} + (m_{\mathrm{mol}}\bar{\omega}_{\mathrm{mol}}^2) T_i \right]} \right)^{3/2} . \end{aligned} \tag{6.22}$$

In our case there is actually a significant gravitational sag, which is different between the atoms and molecules. We can correct for this using the dimensionless factor

$$F(\Delta z) = \exp\left[-\frac{(m_{\mathrm{mol}}\omega_{z,\mathrm{mol}}^2)(m_i\omega_{z,i}^2)\Delta z^2}{2k_{\mathrm{B}}(m_i T_{\mathrm{mol}}\omega_{z,i}^2 + m_{\mathrm{mol}} T_i \omega_{z,\mathrm{mol}}^2)} \right] . \tag{6.23}$$

We are only concerned with the trap frequencies along the z (vertical) axes as for our purposes the difference in position, Δz, is entirely due to the gravitational sag

$$\delta z = g \left(\frac{1}{\omega_{z,i}^2} - \frac{1}{\omega_{z,\mathrm{mol}}^2} \right) , \tag{6.24}$$

Process	$k_2^{\mathrm{Univ}}(T=0)$ $(\times 10^{-11}\mathrm{cm}^3\,\mathrm{s}^{-1})$	$k_2^{\mathrm{Exp}}(B=20\ \mathrm{G})$ $(\times 10^{-11}\mathrm{cm}^3\,\mathrm{s}^{-1})$	$k_2^{\mathrm{Exp}}(B=181.5\ \mathrm{G})$ $(\times 10^{-11}\mathrm{cm}^3\,\mathrm{s}^{-1})$
RbCs + Rb	6.51	1.0(2)	1.6(3)
RbCs + Cs	5.46	2.0(4)	1.2(2)

Table 6.2: The values of the second-order loss coefficient for collisions between RbCs molecules and Rb or Cs atoms extraced from fits to the data in figure 6.12

here g is the acceleration due to gravity. We now have a model for the rate of change of molecule number, whilst in a mixture with atoms

$$\frac{\mathrm{d}N_{\mathrm{mol}}}{\mathrm{d}t} = -k_2^{\mathrm{mol}} C \left(\frac{N_{\mathrm{mol}}^2}{2^{3/2} T^{3/2}} \right) - k_2^i F(\delta z) \bar{n}_i N_{\mathrm{mol}}. \tag{6.25}$$

We can remove the second-order dependence on molecule number in equation (6.25) by independently measuring the RbCs lifetime without the atomic species but using the optical removal technique, we note that the loss observed is faster than the sub-universal losses in section 6.1.1. We attribute this increased loss to evaporation of the RbCs molecules from the trap, to maintain a large enough sample to study we cannot compress as tightly as in prior experiments, the trap depth is only 8 μK. Coupled with increased heating from the removal process evaporative losses are now significant. We are able to confirm this hypothesis by further compressing the molecules into a trap of depth ~ 30 μK and to a temperature of 1.9(3) μK. Here we are able to recover losses at a rate consistent with the model presented in figure 6.3(a).

By fitting equation (6.25) to our data we can extract a value of k_2^i. We can compare these results to the universal limit at zero temperature using equation (6.14) and the values of C_6^{iso} from Kotochigova *et al.* [191]. We find that for both species at both low and high magnetic field the loss coefficients are below the zero-temperature universal limit by approximately a factor of 5, the numeric values are tabulated in table 6.2.

Recent results by Yang *et al.* suggest that Feshbach resonances between atoms and molecules should be resolvable [165]. From their results we expect that the widths of these resonances should be $\sim$ G. To verify that the rate constants we have measured are not due to resonant behaviour we scan the magnetic field ±5 G around the fields we have studied for lifetimes. We scan the magnetic field in steps of 0.11 G, which is a compromise

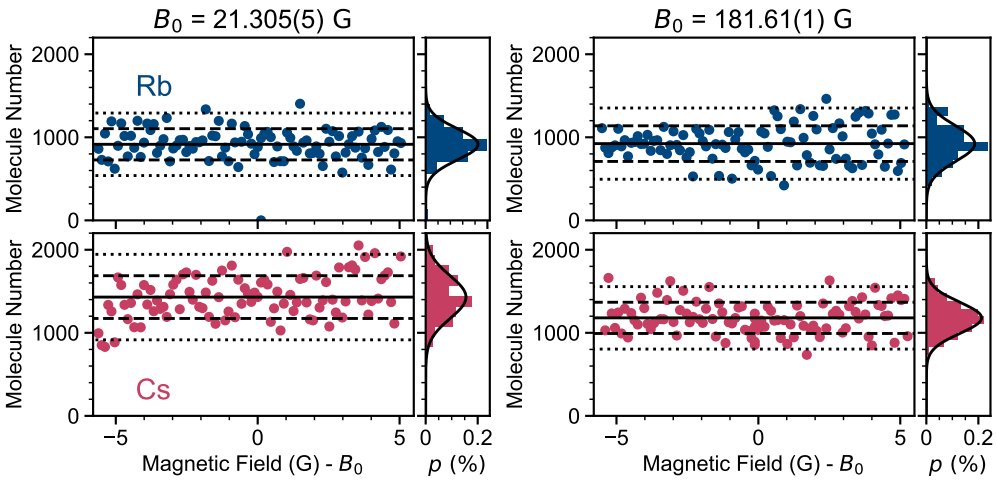

Figure 6.14: The number of molecules after a hold time with Rb (upper) and Cs (lower) atoms at 20 G (left panels) and 181.5 G (right panels) . In each case the magnetic field is scanned ±5 G around B_0. The mean value for each panel is shown as a solid horizontal line; $1-\sigma$ and $2-\sigma$ intervals are shown as dashed and dotted lines respectively. The data are also shown as a histogram and compared to a normal distribution, normalised to give the probability density p. We see no significant variation from normally distributed noise.

between resolution and experimental time. We perform the scan by fixing the molecules hold time with atoms to 10 ms (6 ms for the data with Rb at $\sim$ 181.5 G), the time is chosen such that our background number is $\sim$ 1000 molecules, this would enable us to see both increases and decreases in the lifetime. We present these results in figure 6.14. To determine if there is any variation from background we make a histogram of the results and extract a mean and standard deviation. For all four measurements we observe only $\sim$ 5% of the points are outside the mean $\pm 2\sigma$ interval, as would be expected for normally distributed noise. Additionally there are no signs of correlation between neighbouring points which also suggests that there is no structure to be found. We acknowledge that the region we have explored is small (only 10 G) when compared to the size of the magnetic bias field we apply (181.5 G), however it is expected that for RbCs and Cs the average spacing of resonances would be $\sim$ 5 G by rescaling the predictions of [168]. Our observations are therefore consistent with the hypothesis that there are no resolvable scattering resonances between atoms and molecules. This is potentially because the average spacing of resonances scales inversely with reduced mass, NaK is the lightest non-reactive bialkali currently being stud-

ied and RbCs is the heaviest. It is not impossible that the resonances in RbCs are overlapped to behave continuously and the resonances in NaK are more widely spread.

6.4 Summary

We have studied the collisional properties of RbCs molecules in a range of scenarios. Through our initial measurements we were able to determine that the kinetics of the rate-limiting step are second-order in molecule density and so agrees with the hypothesis that the loss is mediated by the formation of complexes. By comparing with a single-channel model we were able to determine that the losses were sub-universal with a short-range loss parameter $y = 0.26(3)$ and phase shift $\delta^{\mathrm{s}} = 0.56^{+0.07}_{-0.05} \times \pi$. This indicates that there is some limitation on the formation on complexes that prevents some molecules that reach short range from being lost.

To investigate the mechanism behind the losses of complexes we used an intensity-modulated optical dipole trap. We found that across a broad modulation frequency range the modulated trap gave an enhancement to the number of molecules observed after a fixed hold time when compared to when the complexes are continuously removed by CW light. By measuring this frequency response we are able to determine that the lifetime of the $(\mathrm{RbCs})_2$ complex is 0.53(6) ms, within a factor of two with theory [151]. This level of agreement is exceptional given the complexity of the theoretical calculation. We found that the intensity-normalised laser excitation rate is 3^{+4}_{-2} $\mathrm{s}^{-1}(\mathrm{kW\,cm}^{-2})^{-1}$ at $\lambda = 1550$ nm, indicating that at typical trap intensities the photo excitation of $(\mathrm{RbCs})_2$ highly saturated. Our results demonstrate that optical excitation of $(\mathrm{RbCs})_2$ complexes formed by collisions of RbCs molecules is the dominant loss mechanism for ultracold non-reactive molecules.

Finally we concluded by presenting data on collisions with atoms and molecules. As in the molecular complex formation we see sub-universal rates, with little difference between the exothermic $\mathrm{RbCs} + \mathrm{Rb}$ and endothermic $\mathrm{RbCs} + \mathrm{Cs}$ processes. Despite being sub-universal we see rapid loss of mo-

lecules due to collisions with atoms because of the high atomic density. We verified that this rapid loss was not due to resonant scattering by tuning the magnetic field, where our observations were consistent with the null hypothesis that there are no scattering resonances.

Chapter 7

Conclusions

Our goal throughout the work presented in this thesis has been to understand how we can use RbCs molecules in a quantum simulator. To this end we can create some necessary criteria for making a useable quantum simulator based upon ultracold polar molecules.

- For performing useful quantum simulations it is a requirement that we are able to engineer long-range interactions using the dipole-dipole interaction between molecules. This enables the simulation of more complex condensed matter models and is the chief advantage of a molecule-based quantum simulator over one based on atoms.

- We require that the coherence time of any superposition is longer than the molecule-molecule interaction time, typically this is $\sim$ ms. This maintains the quantum behaviour of the system for as long as possible and so preserves few-body interference effects over the many-body system.

- We must be able to coherently control the internal state of the molecule, even in the presence of external electromagnetic fields. This control is a necessary requirement to be able to initialise the molecules into a state for simulation, as well as for adding additional synthetic dimensions to a simulator.

- It is also desirable to know a great deal about the collisional properties of the molecule. This is because cooling the molecules to high phase-

space density is likely to be necessary prior to loading into any array for performing a simulation. If the lattice depth is low enough, there is also the possibility that molecules can tunnel between lattice sites and in these cases the collisional properties of the molecule will greatly affect the outcome of any quantum simulation experiment.

In this chapter we will summarise the key findings presented within this thesis and compare them to these listed criteria. We will then describe the next steps in molecular physics research our group will be undertaking and how the work presented in this thesis has helped to inform the development and trajectory of this future work.

7.1 Summary

Throughout this thesis we have investigated the internal structure of the RbCs molecule experimentally and theoretically. In Chapter 3 we provided a framework for understanding the structure. In order to demonstrate the behaviour of RbCs in different external fields we have developed a python package for performing this kind of theoretical calculation (the python 3.7 code is presented in Appendix B).

We have expanded our microwave control beyond coherent π pulses beginning with Ramsey measurements in free-space. Here we were able to observe a highly coherent superposition limited only by the time that molecules are detectable within our apparatus. Extending the interaction time necessitates an external trapping potential. The addition of a trap introduces spatially-dependent frequency shifts due to the differential AC Stark shift. We further investigated the coherence of superpositions of $|N = 0, M_F = 5\rangle$ and two states in $N = 1$: finding that we can maximise the coherence time by tuning the optical dipole trap to an avoided crossing, providing a first step towards our criterion on the coherence time. This work also helped us understand our criteria on engineering dipole-dipole interactions as the expectation value of the dipole moment for our rotational superposition is equal to the transition dipole moment, two molecules in such a superposition will therefore interact.

To begin to satisfy another one of our criteria we looked at coherently coup-

ling three internal states using two microwave fields. We demonstrated additional control over the internal structure of the molecule in two regimes. First, by using a resonant field on the $(N = 1, M_F = 6) \leftrightarrow (2, 7)$ transition, we were able to observe Autler-Townes splitting of the $(0, 5) \leftrightarrow (1, 6)$ transition. This system is an appropriate starting-point for considering how we might move towards using the internal levels of RbCs molecules as a synthetic dimension. Then by using a Λ configuration rather than a ladder we were able to transfer our molecules between different hyperfine levels of the rotational ground state. We tested the coherence of this process by producing a superposition of two states: $(0, 5)$ and $(0, 4)_2$. In this superposition we attributed loss of contrast to the differential magnetic moment between the two states. Through this attribution we were able to find two pairs of states, one in $N = 0$ and one in $N = 1$, which have lower sensitivity to magnetic field and would be suitable for use as a quantum memory.

We investigated the AC Stark shift of the rotational and hyperfine states at two different wavelengths in Chapter 5. A combination of trap frequency measurements and $\sim$ kHz precision microwave spectroscopy were used to find the isotropic $\alpha^{(0)}$ and anisotropic $\alpha^{(2)}$ components of the polarisability. We first investigated at $\lambda = 1550$ nm finding that two values of $\alpha^{(2)}$ are required to fully describe the experimental data. We repeated these experiments at $\lambda = 1064$ nm where we found an unexpected two-photon transition to a high-lying electronic state. We were, however, able to detune the laser sufficiently far that we can still maintain the long one-body lifetime at typical trapping intensities.

To expand our work on the polarisability at 1064 nm we explored how the AC Stark shift interacts with DC magnetic and electric fields. Our results show that, due to the hyperfine mixing of states, the AC Stark shift can only be minimised at local minima at experimentally relevant magnetic fields. However only a modest electric field is necessary to cause the molecule's rotation to decouple from the nuclear spin of its constituent atoms. In this electric field we are able to find the "magic angle": a polarisation where the AC Stark shift of $N = 0$ matches that for $N = 1$, however we observe a residual AC Stark shift. This shift is often called a hyper-polarisability term though it is caused by off-diagonal elements in the Hamiltonian and

requires us to add no extra terms to our analysis. We are able to use the applied electric field and the polarisation angle of the applied laser field to control this quadratic light shift. Control over the AC Stark shift will enable us to extend the coherence time of rotational superpositions to the level necessitated by the $\sim$ kHz interactions expected for a lattice spacing of 0.5 μm.

We began our investigation into the collisional properties of ground state RbCs molecules in Chapter 6 by attempting to determine the kinetic order of the rate-limiting steps. Our careful measurement of the lifetime of RbCs indicates that the loss follows a second-order process and so is therefore caused by collisions of the form RbCs+RbCs. By considering the possible processes of this form we can rule out chemical reactions: to rule out other processes we varied the internal state and energy of the molecule using a magnetic field and microwaves. We observed no change in the loss rate throughout these experiments. Therefore we conclude the loss of RbCs molecules is due to the formation of $(RbCs)_2$ complexes. To learn more about this complex formation process we varied the temperature of the molecular gas. By changing the temperature of the gas we are able to constrain the short-range loss coefficient and the short range phase shift. Across a wide range of parameters we measured less than universal losses: this suggests that there is a limitation to complex formation.

We continued to investigate the losses of RbCs molecules in a time-averaged trap. In this intensity-modulated potential we were able to measure the lifetime of the $(RbCs)_2$ complex in the dark which agrees well with a theoretical prediction. By measuring the intensity dependent suppression of the loss in this trap we were able to determine that at normal trapping intensities the loss of $(RbCs)_2$ complexes by laser scattering is saturated by many orders of magnitude. This allowed us to conclude that the dominant loss mechanism for ultracold RbCs is optical excitation of complexes formed by a two molecule collision. This work conclusively explains the source of loss observed in all non-reactive ultracold molecule experiments [3, 41, 43, 160, 161, 163].

The final results we presented concerned collisions in mixtures of RbCs molecules and free atoms. Continuing these studies may reveal a way that we can use collisions between atoms and molecules to perform additional sym-

pathetic cooling of RbCs. This cooling could lead to a higher occupancy in the lattice used for quantum simulation experiments.

7.2 Outlook

The results that we have presented in this thesis demonstrate proof-of-concept measurements towards performing quantum simulations in ultracold molecules. As the field progresses the knowledge that we have gained from these measurements can be put into practice. In this section we will describe how using two new apparatuses in our group in Durham will enable us to pursue these goals. We will also describe possible future upgrades to the existing RbCs apparatus which can extend the life of the existing experimental apparatus into the future.

7.2.1 New Apparatus

There are two new RbCs apparatuses currently in development in our group, both are focussed on solving the problem that optical excitation of collision complexes by preventing the initial RbCs+RbCs collision that forms an $(RbCs)_2$ complex. In both cases they will achieve this by confining individual molecules in optical potentials.

The first of the two new apparatuses that are in development aims to control individual RbCs molecules in optical microtraps. Recently laser-cooled CaF molecules were transferred into a small array of optical tweezer traps [192] and association of individual NaCs Feshbach molecules has also been shown to be possible in an optical tweezer [46]. Using a digital mirror device, acousto-optic deflector or spatial light modulator these traps can be manipulated in space. In Rydberg atoms this has been used to exploit the spatial dependence of the dipole-dipole interaction [59], as molecules can also have dipole-dipole interactions this could be replicated in tweezer trapped ultracold molecules.

The other new apparatus is a quantum gas microscope for RbCs. The key ingredient of a quantum gas microscope is the same as for the optical tweezers: a high numerical aperture objective lens. Using this lens it is possible to

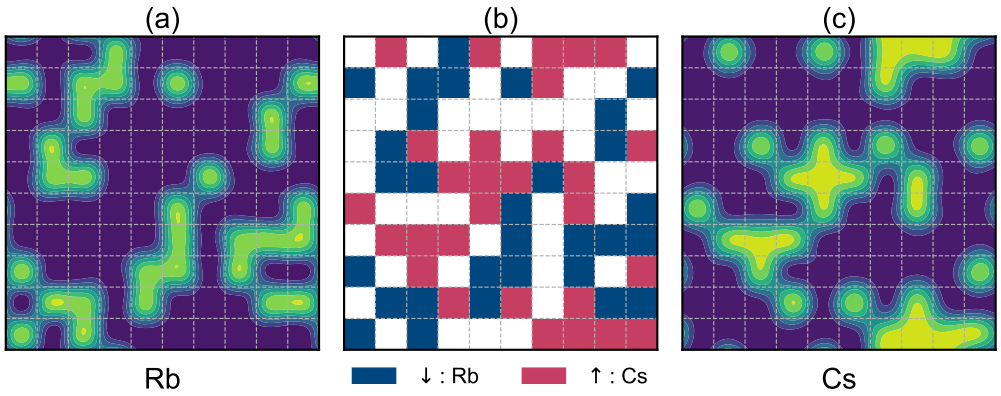

Figure 7.1: A pair of simulated output images for (a) Rb and (c) Cs from a quantum gas microscope for RbCs. (b) The initial lattice of RbCs molecules, with two molecular states identified with $\uparrow, \downarrow$ spins as shown in the legend, the white sites are empty. Each of these pseudo-spin states is mapped onto an atomic species as described in the text.

observe individual atoms confined to sites in an optical lattice, these atoms are spaced by half of the trapping wavelength, typically 0.5 μm. This technology has already been developed for atoms [193, 194] but extending it to molecules has additional benefits. The first benefit matches that in optical tweezers, the molecules possess an electric dipole moment which allows for interactions between sites in a lattice.

The other benefit that we shall consider is that we can leverage the two constituent atoms for imaging of a simulated spin-1/2 system. Because there are no closed transitions within the RbCs molecule that would be suitable for imaging through absorption or fluorescence we must break the molecule apart into its constituents. These atoms can then be imaged separately in either time, *i.e* sequentially or spatially for example using a species-selective lattice or similar. We can use this to account for the defects in the lattice by exploiting the hyperfine and rotational state selective nature of STIRAP. To illustrate this we can take an imperfect lattice of RbCs molecules, like that shown in figure 7.1(b). For our example we identify $|\uparrow\rangle$ with a hyperfine state in $N = 1$ and $|\downarrow\rangle$ with $(N = 0, M_F = 5)$, represented in the figure by the red and blue squares respectively.

We can image the molecules in $|\downarrow\rangle$ by performing a STIRAP and disassociation sequence (as we currently do), this leaves the molecules in $|\uparrow\rangle$ un-

touched. By removing just the Cs atoms every lattice site that was occupied by a $|\downarrow\rangle$ molecule is now a lone Rb atom, however in order to preserve this so we can repeat the process to form a Cs lattice to represent $|\uparrow\rangle$ we must protect the Rb atoms. One possibility is to physically offset the Rb lattice from the RbCs $|\uparrow\rangle$ lattice along the vertical direction. Another is to use a microwave field to transfer the Rb atoms from their $(f_{\mathrm{Rb}} = 1, m_{\mathrm{Rb}} = 1)$ ground state to $(2, 2)$. We also need to transfer the molecules between $|\uparrow\rangle$ and $|\downarrow\rangle$, though as we have shown, this can be achieved readily using microwave pulses. After the STIRAP and dissociation process we must remove the Rb in a spin-selective manner, at high magnetic field this is possible by using a microwave field and ARP to swap the populations $(1, 1) \leftrightarrow (2, 2)$, this has the added benefit of moving the "protected" Rb atoms from earlier back into the ground state. Removal of the unnecessary Rb atoms then takes place by cycling on the closed $(5S_{1/2}, f_{\mathrm{Rb}} = 2, m_{\mathrm{Rb}} = 2) \leftrightarrow (5P_{3/2}, 3, 3)$ transition. Two images can then be taken in the atomic quantum gas microscope to reconstruct the distribution of molecules in $|\uparrow\rangle$ and $|\downarrow\rangle$. Predicted images from following this sequence for a given spin-1/2 lattice are shown in figure 7.1(a) and (c).

7.2.2 Upgrades to the Existing Apparatus

As well as building two new apparatuses we can also take what we have learnt about the RbCs molecule to inform some upgrades to the existing apparatus.

We have determined that one of the limiting factors to using RbCs molecules for quantum simulation experiments is differential energy shifts between the rotational states. As we look towards the next generation of apparatus we should consider methods to reduce these. The most immediately applicable is to use a "magic wavelength" optical trap. In these traps the differential AC Stark shift is exactly zero as the two states have the same polarisability. Searching for these wavelengths is challenging both experimentally and theoretically however a magic wavelength trap has been demonstrated for NaK molecules [155] suggesting it would be possible for RbCs as well.

An alternative to magic wavelength traps, that we have already demonstrated proof-of-principle measurements for, is to use the polarisation dependence of

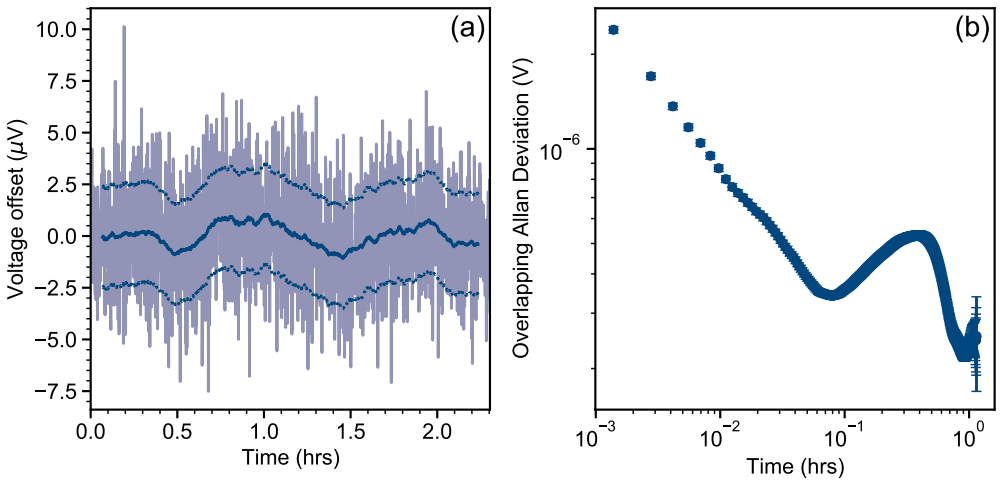

Figure 7.2: The performance of the high stability voltage source for our next-generation high voltage system. The source is an AD5791 evaluation board, externally referenced to a MAX6325 reference voltage. (a) Voltage trace measured in time over $\sim$ 2 hours. Measurements are logged at 0.2 Hz. The offset is measured from the set-point of 1 V. The solid line indicates the rolling average, the dashed lines indicate $\pm$ one standard deviation. (b) The overlapping Allan deviation of the data in (a). The peak at $\sim$ 0.5 hrs corresponds with the cycling period of the laboratory AC system.

the AC Stark shift to control the internal energy level structure. This will necessitate a reasonably large electric field to be applied, large enough that time-dependent variations in the electric field become a significant source of decoherence. At the largest electric field we are likely to use in the current apparatus, 300 $\mathrm{V\,cm^{-1}}$, the $\Delta M_N = 0$ transition frequency has a gradient of 121 $\mathrm{kHz\,(V\,cm^{-1})^{-1}}$. To stabilise the transition frequency to $<$ kHz we need to stabilise the field to 8 $\mathrm{mV\,cm^{-1}}$. This corresponds to the potential being stabilised to the $\sim$ 10ppm level. We have therefore begun to develop a high stability voltage source: which can operate up to $\pm$2 kV. The design follows the principles outlined in [195]: a low-noise voltage reference is the input to a control loop, the output is amplified by a high-gain amplifier, the amplified voltage is sampled by a potential divider and fed back into the control loop to stabilise the voltage applied onto our electrodes. The limit to the electric field stability comes form the voltage reference used for control. We plan to use a 20-bit AD5791 DAC referenced to temperature in-sensitive MAX 6325. The performance of our reference at 1 V is shown in figure 7.2 over 2 hours, which is able to achieve higher stability than the 10 ppm we required.

It has been a long time since the apparatus in our lab was designed and in that time the field of ultracold atomic gases has advanced significantly. Maintaining the efficient operation of the apparatus into the future will require some improvements to the early part of the sequence where we are focussed on cooling the atoms. These improvements will most likely come in the form of additional laser cooling of the Rb atoms using techniques like Λ-enhanced grey molasses cooling [196]. This additional cooling will provide a significant benefit to the continued operation of the experiment as additional cooling of the Rb atoms prior to the first stage of sympathetic cooling in the magnetic trap will lead to an increased number of Rb atoms being able to make it through to later stages of the sequence. This should improve the efficiency of the sympathetic cooling in the magnetic trap, allowing us to either cut the ~ 20 s RF-evaporation down and improve our repetition rate or, more likely, to improve the molecule number from our current limit of ~ 3500. Adding more atoms cannot increase the efficiency of the magnetoassociation process, as this is limited by the phase space density of the mixture which is limited as the Rb and Cs are immiscible.

7.2.3 Possible Future Experiments

Using the multi-photon control that we have developed within this work opens up new avenues for studies with ultracold molecules. In Chapter 4 we detailed a possible study where a many-body Hamiltonian (in that case the Su-Schrieffer-Heiger model) could be mapped on to the internal states of a molecule by dressing with multiple microwave fields. To be concise we will not cover this specific application again, instead we will outline how this technique could be expanded to produce simulations of more complex systems. One obvious extension to the one-dimensional system already explored is to take this to two-dimensions, this is clearly more difficult as it requires more microwave fields. An illustration of a possible mapping for two-dimensional studies in synthetic dimensions is shown in figure 7.3 for a 2×2 and 3×3 lattice. Because we now require multiple transitions to the same rotational manifold we cannot solely use the microwave frequency to avoid unwanted couplings, we must also use the polarisation. As such to build this system we

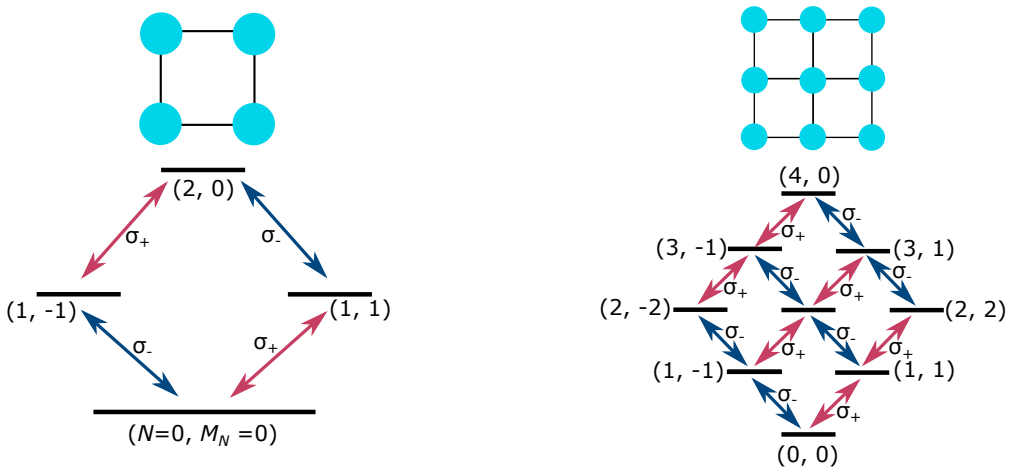

Figure 7.3: A diagram of a possible implementation of 2D synthetic dimensions using the rotational states of molecules. This implementation uses microwave fields of orthogonal polarisation to reduce cross talk between transitions to the same rotational manifold.

would require microwave fields to drive the $\sigma_{\pm}$ transitions from each level. Applying a large magnetic field as well as an electric field will separate transitions by multiple kHz to reduce the chance of off-resonant driving further. We have already seen that, due to the hardware that surrounds the glass cell, it is difficult to maintain a good microwave polarisation purity at low frequency. One solution to this would be to STIRAP molecules to $N = 2$ rather than $N = 0$, this would shorten the transition wavelength and lessen the effects of the surroundings.

Control over the scattering properties has proved vital for the development of ultracold atomic gas experiments. Previous works have shown that the dipole-dipole interactions between molecules can increase the collision rate between molecules in DC electric fields [197], and when dressed with near-resonant microwave fields [198]. Having demonstrated microwave dressing in Chapter 4 with Autler-Townes spectroscopy we can begin to imagine combining this with our work on two-body losses to control the scattering processes. This has already been addressed theoretically, with calculations that show that using blue-detuned microwaves can shield molecules from collisions [186, 187] and should not be limited by our ability to produce circularly polarised microwave fields [199]

7.3 Final Remarks

In this work we have explored the internal structure of the RbCs molecule. Understanding how we can control the internal state with microwave fields will be critical to using molecules for quantum simulation and computation. For molecules to be useful in a quantum simulator we must study how their internal structure is influenced by external electric and magnetic fields. Through our study we determined that it is possible to use these external fields to control the internal structure: provided that, as we do, you are able to understand the behaviour of the molecule in these fields.

When this work began the world of ultracold molecules faced one central problem: the unexplained loss of non-reactive molecules. There were, of course, multiple potential explanations given to explain the experimental observations. In this work we have conclusively shown that the cause of loss of ultracold RbCs molecules is optical excitation of the complex formed by two molecules colliding. Now that we know that the cause of this loss is a combination of the optical trap and the molecular density future experiments can truly exploit the potential of ultracold molecules. As the field expands with the continued growth in the number of associated and laser-cooled molecular species available we can expect more and more laboratories to embrace the challenges and benefits of ultracold molecules.

Appendix A

Atomic Transitions at High Magnetic Field

To determine the appropriate technique for the removal of a single species required extensive understanding of the relevant atomic structure. Here we present the transitions of the D_2 lines of ^{87}Rb and ^{133}Cs for magnetic fields between 0 and 181.7 G.

The atomic Hamiltonian is given by

$$H_{\text{atom}} = H_0 + H_{\text{fine}} + H_{\text{HF}} + H_{\text{Zeeman}}. \tag{A.1}$$

where H_0 is the coarse energy level structure (dependent on the principle quantum number n). H_{fine} is the fine structure and is given by

$$H_{\text{fine}} = \frac{\gamma_{\text{SO}}}{\hbar^2} (\boldsymbol{l} \cdot \boldsymbol{s}), \tag{A.2}$$

here γ_{SO} is the spin-orbit coupling constant and $\boldsymbol{l}$ and $\boldsymbol{s}$ are the orbital and spin angular momenta of the valence electron. H_{HF} is the hyperfine structure and has two components

$$H_{\text{HF}} = H_{\text{Dipole}} + H_{\text{Quad}}, \tag{A.3a}$$

$$H_{\text{Dipole}} = \frac{A_{\text{HF}}}{\hbar^2} (\boldsymbol{i} \cdot \boldsymbol{j}), \tag{A.3b}$$

$$H_{\text{Quad}} = \frac{B_{\text{HF}}}{\hbar^4} \left[\frac{3(\boldsymbol{i} \cdot \boldsymbol{j})^2 + \hbar^2 \frac{3}{2} (\boldsymbol{i} \cdot \boldsymbol{j}) - i(i+1) j(j+1) \hbar^4}{2i(2i-1) \times j(2j+1)} \right]. \tag{A.3c}$$

In the above H_{Dipole} describes the magnetic dipole interaction between the total electronic angular momentum $\boldsymbol{j} = \boldsymbol{i} + \boldsymbol{l}$ and the nuclear spin $\boldsymbol{i}$. H_{Quad}

is the Hamiltonian for the electric quadrupole interaction. H_{Zeeman} is the Zeeman interaction between the atom and the magnetic field

$$H_{\text{Zeeman}} = \frac{\mu_{\text{B}}}{\hbar} \left(g_l l_z + g_s s_z + g_i i_z \right) B_z. \tag{A.4}$$

Here, the assumption is that the magnetic field is along the quantisation axis z. The factors g_i, g_l and g_s are the g-factors for i, l and s respectively.

We are only concerned with the Zeeman shift of the ground state energy levels and the transitions on the D_2 line of each atomic species. The calculations were performed using the Elecsus python package [200, 201] which encapsulates all of the terms that we require.

A.1 Zeeman Shift of Transitions in ^{87}Rb

The first atom we focus on is ^{87}Rb. In figure A.1 the energy levels are shown at 0 G and 181.7 G. Our calculation indicates there are no closed transitions from the hyperfine ground state $5S_{1/2}(f_{\text{Rb}} = 1, m_{\text{Rb}} = 1)$. The "most closed transition" is the σ_- transition to the lowest energy hyperfine sub-level in $5P_{3/2}$, approximately 85% of the time the atom decays to (1,1). This transition is frequency shifted from the repump laser by approximately 600 MHz and requires the opposite polarisation to drive. All transitions from this state eventually lead to atoms being distributed across $5S_{1/2} f_{\text{Rb}} = 1, 2$, in the figure the ground states that can be decayed to are indicated by the grey circles. This distribution across multiple states is not ideal for the clean removal of atoms.

The pattern repeats for transitions from $5S_{1/2}(2, 2)$. The cooling transition $5S_{1/2}(2, 2) \rightarrow 5P_{3/2}(3, 3)$ remains closed even at high magnetic field because both states are spin-stretched, though there is a frequency shift of ~ 250 MHz.

Using the existing repump and cooling lasers at high field is also not a suitable option. Both lasers are far off-resonant, when compared to the natural linewidth, and would drive multiple transitions with similar strengths.

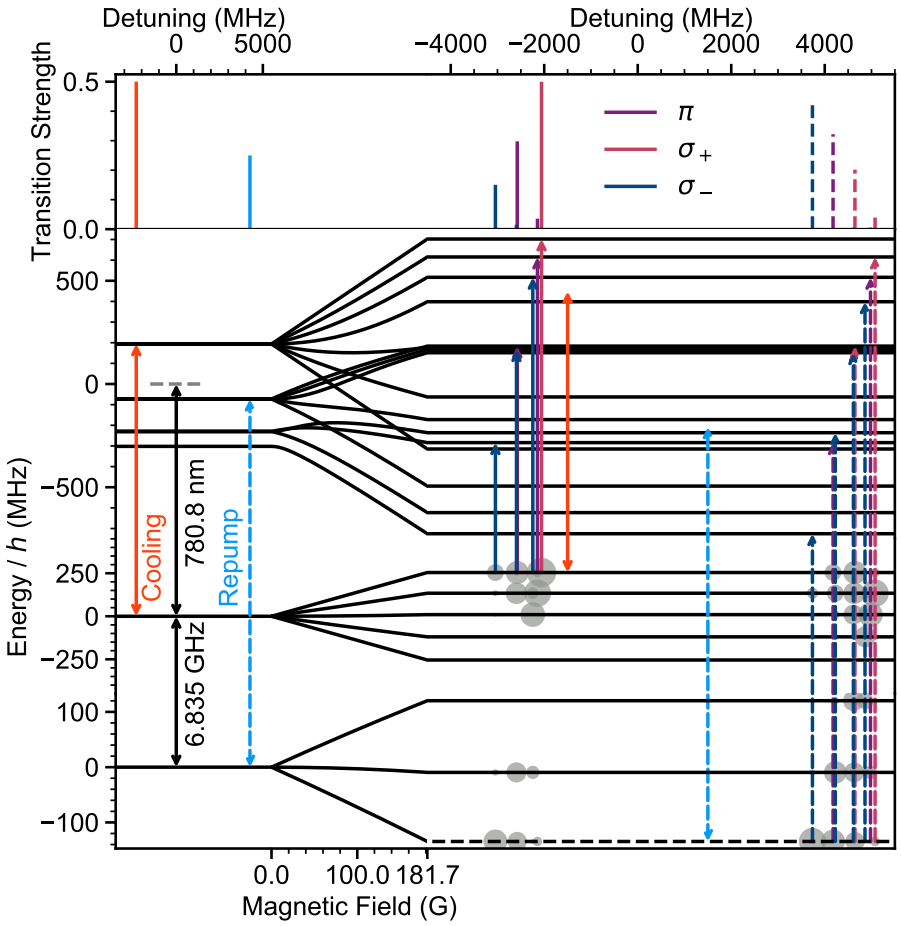

Figure A.1: The hyperfine energy levels for ^{87}Rb as a function of magnetic field. The cooling $5S_{1/2}(f_{\mathrm{Rb}} = 2, m_{\mathrm{Rb}} = 2) \leftrightarrow 5P_{3/2}(3,3)$ transition is shown in orange. The repump $5S_{1/2}(1,1) \leftrightarrow 5P_{3/2}(2,2)$ transition is shown as a blue dashed line. The magnetic field increases from left to right. The right hand panel is at the high magnetic field of 181.7 G, transitions from $5S_{1/2}(1,1)$ are shown as dashed lines and transitions from $5P_{3/2}(2,2)$ are shown by solid lines. The upper panel shows the transition strength in units of the reduced matrix element $|\langle J = 1/2||er||J' = 3/2\rangle|^2$.

A.2 Zeeman Shift of Transitions in ^{133}Cs

We repeat the calculation for ^{133}Cs. Near zero magnetic field the cooling light addresses the transition $6S_{1/2}(f_{\mathrm{Cs}} = 4, m_{\mathrm{Cs}} = 4) \leftrightarrow 6P_{3/2}(5, 5)$ while the repump addresses $6S_{1/2}(3, 3) \leftrightarrow 6P_{3/2}(4, 4)$. Because of the Zeeman shift these lasers are not resonant in a magnetic field.

There are no closed transitions from the ground $6S_{1/2}(f_{\mathrm{Cs}} = 3, m_{\mathrm{Cs}} = 3)$ to any hyperfine level of the $6P_{3/2}$ state. The lowest transition of the D_2 line is more closed than in ^{87}Rb with $> 90\%$ of the population returning to the (3,3) state. At the magnetic field we perform the calculation for, 181.7 G, the repump laser light is nearly resonant (within ± 80 MHz) with 6 separate transitions.

The $6S_{1/2}(f_{\mathrm{Cs}} = 4, m_{\mathrm{Cs}} = 4) \leftrightarrow 6P_{3/2}(5, 5)$ is therefore the only closed transition on the D_2 line of Cs at 181.7 G. This transition is shifted 250 MHz from the cooling light, there are three transitions within ± 80 MHz of the laser frequency.

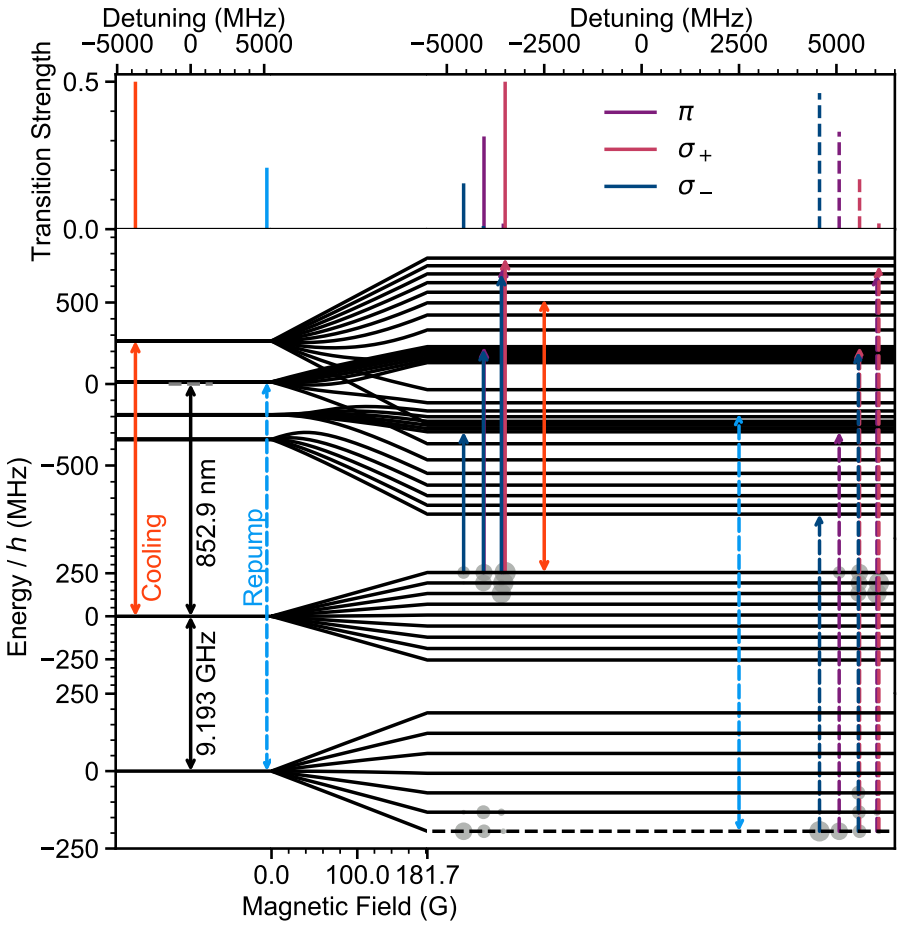

Figure A.2: The hyperfine energy levels for ^{133}Cs as a function of magnetic field. The cooling $6S_{1/2}(f_{\mathrm{Cs}} = 4, m_{\mathrm{Cs}} = 4) \leftrightarrow 6P_{3/2}(5,5)$ transition is shown in orange. The repump $6S_{1/2}(3,3) \leftrightarrow 6P_{3/2}(4,4)$ transition is shown as a blue dashed line. The magnetic field increases from left to right. The right hand panel is at the high magnetic field of 181.7 G, transitions from $6S_{1/2}(3,3)$ are shown as dashed lines and transitions from $6S_{1/2}(4,4)$ are shown by solid lines. The upper panel shows the transition strength in units of the reduced matrix element $|\langle J = 1/2||er||J' = 3/2\rangle|^2$.

Appendix B

Hyperfine code

This appendix gives the full hyperfine code necessary for the calculations in 5 as described in 3. The code is written using python 3.7 and requires the scipy stack [202]. The numerical values for the molecular constants used and their sources are given in Table 3.2. The code is also available from [203].

B.1 Python Source code

```
import numpy
from sympy.physics.wigner import wigner_3j,wigner_9j
from sympy.physics.quantum.spin import Rotation
from scipy.linalg import block_diag,eig,eigvals
import scipy.constants
import warnings

# Start by defininining a bunch of constants that are needed for the code

'''
    Important note!

    All units in this code are SI i.e. elements in the Hamiltonian have
        ↪ units
    of Joules. Outputs will be on the order of 1e-30

'''
```

```
h = scipy.constants.h
muN = scipy.constants.physical_constants['nuclear magneton'][0]
bohr = scipy.constants.physical_constants['Bohr radius'][0]
eps0 = scipy.constants.epsilon_0
c = scipy.constants.c


pi = numpy.pi

DebyeSI = 3.33564e-30

# RbCs Molecular Constants

RbCs = { "IRb":1.5,
           "ICs":3.5,
           "d0":1.225*DebyeSI,
           "binding":114268135.25e6*h,
           "Brot":490.173994326310e6*h,
           "Drot":213*h,
           "QRb":-809.29e3*h,
           "QCs":59.98e3*h,
           "CRb":98.4*h,
           "CCs":194.2*h,
           "C3":192.4*h,
           "C4":19.0189557e3*h,
           "MuN":0.0062*muN,
           "MuRb":1.8295*muN,
           "MuCs":0.7331*muN,
           "a0":2020*4*pi*eps0*bohr**3,
           "a2":1997*4*pi*eps0*bohr**3,
           "Beta":0}

# Functions for the calculations to use#

#first functions are mathematical and used to generate the structures that
    ↪ we
#will need to use

def Raising_operator(j):
    #produce the angular momentum raising operator J+
    dimension = numpy.rint(2.0*j+1).astype(int)
```

```
    J = numpy.zeros((dimension,dimension))
    for m_j in range(numpy.rint(2.0*j).astype(int)):
        J[m_j,m_j+1]=numpy.sqrt(j*(j+1)-(j-m_j)*(j-m_j-1))
    return J

# produce the three generalised projections of angular momentum:
# for S=1/2 these should return the Pauli matrices.
# for the source of these definitions see any good QM textbook e.g.
# Bransden & Joachain (or wikipedia)

def X_operator(J):
    '''
        input arguments:
        J: Magnitude of angular momentum (float)
    '''
    J_plus = Raising_operator(J)
    J_minus = numpy.transpose(J_plus)
    return 0.5*(J_plus+J_minus)

def Y_operator(J):
    '''
        input arguments:
        J: Magnitude of angular momentum (float)
    '''
    J_plus = Raising_operator(J)
    J_minus = numpy.transpose(J_plus)
    return 0.5j*(J_minus - J_plus)

def Z_operator(J):
    '''
        input arguments:
        J: Magnitude of angular momentum (float)
    '''
    J_plus = Raising_operator(J)
    J_minus = numpy.transpose(J_plus)
    return 0.5*(numpy.dot(J_plus,J_minus)-numpy.dot(J_minus,J_plus))

def vector_dot(x,y):
    '''
        A function that can do the dot product of a vector of matrices
            ↪ default
```

```
        behaviour of numpy.dot does the elementwise product of the matrices
            ↪ .
        input arguments:
        x,y: Vectors of Angular momentum operators, each element is a JxJ
            ↪ arrays
             (numpy.ndarray)
    '''
    X_Y = numpy.zeros(x[0].shape,dtype=numpy.complex)
    for i in range(x.shape[0]):
        X_Y += numpy.dot(x[i],y[i])
    return X_Y

def Generate_vecs(Nmax,I1,I2):
    '''
        Generate the vectors of the angular momentum operators which we
            ↪ need
        to be able to produce the Hamiltonian

        input arguments:
        Nmax: maximum rotational level to include in calculations (float)
        I1,I2: Nuclear spins of nuclei 1 and 2 (float)

    '''

    shapeN = int(numpy.sum([2*x+1 for x in range(0,Nmax+1)]))
    shape1 = int(2*I1+1)
    shape2 = int(2*I2+1)

    Nx = numpy.array([[]])
    Ny=numpy.array([[]])
    Nz= numpy.array([[]])

    for n in range(0,Nmax+1):
        Nx = block_diag(Nx,X_operator(n))
        Ny = block_diag(Ny,Y_operator(n))
        Nz = block_diag(Nz,Z_operator(n))

    #remove the first element of the N vectors, which are empty
    Nx = Nx[1:,:]
    Ny = Ny[1:,:]
    Nz = Nz[1:,:]
```

```
    #Each of the following corresponds to the product [N x 1Rb x 1Cs]
    #This gives the operators for N in the full hyperfine space.

    # numpy.kron is the function for the Kronecker product, often also
        ↪ called
    # the tensor product.

    N_vec = numpy.array([numpy.kron(Nx,numpy.kron(numpy.identity(shape1),
                                                  numpy.identity(shape2))),
                         numpy.kron(Ny,numpy.kron(numpy.identity(shape1),
                                                  numpy.identity(shape2))),
                         numpy.kron(Nz,numpy.kron(numpy.identity(shape1),
                                                  numpy.identity(shape2)))])

    # we also have to repeat for the nuclear spins
    I1_vec = numpy.array([numpy.kron(numpy.identity(shapeN),
                         numpy.kron(X_operator(I1),numpy.identity(shape2))),
                         numpy.kron(numpy.identity(shapeN),
                         numpy.kron(Y_operator(I1),numpy.identity(shape2))),
                         numpy.kron(numpy.identity(shapeN),
                         numpy.kron(Z_operator(I1),numpy.identity(shape2)))])

    I2_vec = numpy.array([numpy.kron(numpy.identity(shapeN),
                         numpy.kron(numpy.identity(shape1),X_operator(I2))),
                         numpy.kron(numpy.identity(shapeN),
                         numpy.kron(numpy.identity(shape1),Y_operator(I2))),
                         numpy.kron(numpy.identity(shapeN),
                         numpy.kron(numpy.identity(shape1),Z_operator(I2)))])

    return N_vec,I1_vec,I2_vec

# From here the functions will calculate individual terms in the
    ↪ Hamiltonian,
# I have split them up for two reasons 1) readability and 2) so that its
    ↪ obvious
# what is doing what.

def Rotational(N,Brot,Drot):
    '''
```

```
        Generates the hyperfine-free hamiltonian for the rotational levels
            ↪ of
        a rigid-rotor like molecule. Includes the centrifugal distortion
            ↪ term

        input arguments:
        N: Angular momentum vector for rotation (numpy.ndarry)
        Brot: Rotational constant (float)
        Drot: Centrifugal distortion (float)
    '''
    N_squared = vector_dot(N,N)
    return Brot*N_squared-Drot*N_squared*N_squared

def Zeeman(Cz,J):
    '''
        Linear Zeeman shift, fixed magnetic field along z so only need the
        last component of the angular momentum vector.

        input arguments:
        Cz: Zeeman Coefficient (float)
        J: Angular momentum vector (numpy.ndarray)
    '''
    Hzeeman = -Cz*J[2]
    return Hzeeman

def scalar_nuclear(Ci,J1,J2):
    '''
        Returns the scalar spin-spin term of the HF Hamiltonian
        Input arguments:
        Ci: Scalar spin coupling coefficient (float)
        J1,J2: Angular momentum vector (numpy.ndarray)

        returns:
        Quad: (2*Nmax+1)*(2*I1_mag+1)*(2*I2_mag+1)x
           (2*Nmax+1)*(2*I1_mag+1)*(2*I2_mag+1) array.
    '''
    return Ci*vector_dot(J1,J2)

def tensor_nuclear(C3,I1,I2,N):
    '''
        The tensor - nuclear spin spin interaction
```

```
    input arguments:
    C3: Tensor spin-spin coupling coefficient (float)
    I1,I2,N: Angular momentum Vectors (numpy.ndarry)
    returns:
    Quad: (2*Nmax+1)*(2*I1_mag+1)*(2*I2_mag+1)x
       (2*Nmax+1)*(2*I1_mag+1)*(2*I2_mag+1) array.
'''
with warnings.catch_warnings():
    # this is a statement to make the code nicer to use, python wants
        ↪ to
    # warn the user whenever the data type is changed from Complex. But
        ↪  we
    # know that it will always be real so it doesn't matter.
    warnings.filterwarnings("ignore",category=numpy.ComplexWarning)
    #find max values for angular momentum from their projections onto z
    Nmax = int(numpy.round(numpy.real(numpy.amax(N[2])),1))
    I1max = numpy.real(numpy.round(numpy.amax(I1[2]),1))
    I2max = numpy.real(numpy.round(numpy.amax(I2[2]),1))

I1shape = int(2*I1max+1)
I2shape = int(2*I2max+1)

# The tensor nuclear spin-spin interaction depends on the rotational
    ↪ level
# not its projection, so we have to create a new matrix that contains
    ↪ the
# values of N. Thankfully the terms are block-diagonal in N so we don'
    ↪ t have
# to worry what the term <N,MN|I1 dot T dot I|N',MN'> looks like
Narray = numpy.zeros((1,1))

for n in range(0,Nmax+1):
    #this loop iterates over all the values for N (indexed as n)
        ↪ allowed and
    # builds an nxn matrix of only one value.

    shape = int((2*n+1)*(2*I1max+1)*(2*I2max+1))
    nsub = numpy.zeros((shape,shape))+n
    Narray = block_diag(Narray,nsub)

#first element is fixed to be zero - get rid of it
```

```
    Narray = Narray[1:,1:]

    #Now calculate the terms as shown earlier
    prefactor = C3/((2*Narray+3)*(2*Narray-1))
    term1 = 3*numpy.dot(vector_dot(I1,N),vector_dot(I2,N))
    term2 = 3*numpy.dot(vector_dot(I2,N),vector_dot(I1,N))
    term3 = -2*vector_dot(I1,I2)*Narray*(Narray+1)
    return prefactor*(term1+term2+term3)


def Quadrupole(Q,I1,I2,N):
    '''
        from 10.1103/PhysRev.91.1403, which quotes the quadrupole
            ↪ interaction
         for KBr
         input arguments:

         Q:Tuple or list of the nuclear quadrupole moments as (Q1,Q2) (
             ↪ tuple)
         I1,I2,N: Nuclear spin of nucleus 1,2 and rotational angular
             ↪ momentum
                 vectory (numpy.ndarray)
        returns:
        Quad: (2*Nmax+1)*(2*I1_mag+1)*(2*I2_mag+1)x
           (2*Nmax+1)*(2*I1_mag+1)*(2*I2_mag+1) array.

    '''
    Q1,Q2 = Q
    with warnings.catch_warnings():
        # this is a statement to make the code nicer to use, python wants
            ↪ to
        # warn the user whenever the data type is changed from Complex. But
            ↪  we
        # know that it will always be real so it doesn't matter.
        warnings.filterwarnings("ignore",category=numpy.ComplexWarning)
        #find max values for angular momentum from their projections onto z
        Nmax = int(numpy.round(numpy.real(numpy.amax(N[2])),1))
        I1max = numpy.round(numpy.real(numpy.amax(I1[2])),1)
        I2max = numpy.round(numpy.real(numpy.amax(I2[2])),1)

    Narray = numpy.array([])
```

```
Narray=numpy.zeros((1,1))

for n in range(Nmax+1):
    # this loop iterates over all the values for N (indexed as n)
        ↪ allowed &
    # builds an (2*I1+1)*(2*I2+1)*(2*n+1)x(2*I1+1)*(2*I2+1)*(2*n+1)
        ↪ matrix
    # of only one value.
    shape = int((2*I1max+1)*(2*I2max+1)*(2*n+1))
    subarray = numpy.zeros((shape,shape))+n
    Narray= scipy.linalg.block_diag(Narray,subarray)
Narray = Narray[1:,1:]
# there is the possibility for division by zero here, so define a
    ↪ machine
# epsilon to avoid NaN errors. Epsilon is insignificantly small,
# particularly on modern 64-bit machines.
epsilon = (numpy.finfo(float).eps)

prefactor1 = numpy.zeros(Narray.shape)
prefactor2 = numpy.zeros(Narray.shape)

# Calculate the terms as earlier. This is presented in Sigma notation
    ↪ in the
# text but is actually just two terms.
prefactor1 = -Q1/(2*I1max*(2*I1max-1)*(2*Narray-1)\
                  *(2*Narray+3))

term1_1= 3*(numpy.dot(vector_dot(I1,N),vector_dot(I1,N)))
term2_1 = 1.5*vector_dot(I1,N)
term3_1 = -1*numpy.dot(vector_dot(I1,I1),vector_dot(N,N))
Quad1 = prefactor1*(term1_1 +term2_1+term3_1)

prefactor2 = -Q2/(2*I2max*(2*I2max-1)*(2*Narray-1)*\
                  (2*Narray+3))

term1_2= 3*(numpy.dot(vector_dot(I2,N),vector_dot(I2,N)))
term2_2 = 1.5*vector_dot(I2,N)
term3_2 = -1*numpy.dot(vector_dot(I2,I2),vector_dot(N,N))
Quad2 = prefactor2*(term1_2 +term2_2+term3_2)

return Quad1+Quad2
```

```
def DC(Nmax,d0,I1,I2):
    '''
       Generates the effect of the dc Stark shift for a rigid-rotor like
       molecule.

       This term is calculated differently to all of the others in this
           ↪ work
       and is based off Jesus Aldegunde's FORTRAN 77 code. It iterates
           ↪ over
       N,MN,N',MN' to build a matrix without hyperfine structure then uses
       kronecker products to expand it into all of the hyperfine states.


       input arguments:

       Nmax: maximum rotational quantum number to calculate (int)
       d0: Permanent electric dipole momentum (float)
       I1,I2: Nuclear spin of nucleus 1,2 (float)


       returns:
       H: Hamiltonian, (2*Nmax+1)*(2*I1_mag+1)*(2*I2_mag+1)x
          (2*Nmax+1)*(2*I1_mag+1)*(2*I2_mag+1) array.
     '''

    shape = numpy.sum(numpy.array([2*x+1 for x in range(0,Nmax+1)]))
    HDC = numpy.zeros((shape,shape),dtype= numpy.complex)

    I1shape = int(2*I1+1)
    I2shape = int(2*I2+1)

    i =0
    j =0
    for N1 in range(0,Nmax+1):
        for M1 in range(N1,-(N1+1),-1):
            for N2 in range(0,Nmax+1):
                for M2 in range(N2,-(N2+1),-1):
                    HDC[i,j]=-d0*numpy.sqrt((2*N1+1)*(2*N2+1))*(-1)**(M1)*\
                    wigner_3j(N1,1,N2,-M1,0,M2)*wigner_3j(N1,1,N2,0,0,0)
                    j+=1
```

```
            j=0
            i+=1
    return (numpy.kron(HDC,numpy.kron(numpy.identity(I1shape),
            numpy.identity(I2shape))))

def AC_iso(Nmax,a0,I1,I2):
    '''
        Generates the effect of the isotropic AC Stark shift for a rigid-
            ↪ rotor
        like molecule.

        This term is calculated differently to all of the others in this
            ↪ work
        and is based off Jesus Aldegunde's FORTRAN 77 code. It iterates
            ↪ over
        N,MN,N',MN' to build a matrix without hyperfine structure then uses
        kronecker products to expand it into all of the hyperfine states.

        input arguments:

        Nmax: maximum rotational quantum number to calculate (int)
        a0: isotropic polarisability (float)
        I1,I2: Nuclear spin of nucleus 1,2 (float)



        returns:
        H: Hamiltonian, (2*Nmax+1)*(2*I1_mag+1)*(2*I2_mag+1)x
           (2*Nmax+1)*(2*I1_mag+1)*(2*I2_mag+1) array.

     '''
    shape = numpy.sum(numpy.array([2*x+1 for x in range(0,Nmax+1)]))
    I1shape = int(2*I1+1)
    I2shape = int(2*I2+1)
    HAC = numpy.zeros((shape,shape),dtype= numpy.complex)
    i=0
    j=0
    for N1 in range(0,Nmax+1):
        for M1 in range(N1,-(N1+1),-1):
            for N2 in range(0,Nmax+1):
                for M2 in range(N2,-(N2+1),-1):
                    if N1==N2 and M1 ==M2:
```

```
                    HAC[i,j]=-a0
                j+=1
            j=0
            i+=1
    #final check for NaN errors, mostly this is due to division by zero or
    # multiplication by a small prefactor. it is safe to set these terms
        ↪ to 0
    HAC[numpy.isnan(HAC)] =0

    #return the matrix, in the full uncoupled basis.
    return (numpy.kron(HAC,numpy.kron(numpy.identity(I1shape),
                                            numpy.identity(I2shape))))

def AC_aniso(Nmax,a2,Beta,I1,I2):
    '''
        Generates the effect of the anisotropic AC Stark shift for a rigid-
            ↪ rotor
        like molecule.

        This term is calculated differently to all of the others in this
            ↪ work
        and is based off Jesus Aldegunde's FORTRAN 77 code. It iterates
            ↪ over
        N,MN,N',MN' to build a matrix without hyperfine structure then uses
        kronecker products to expand it into all of the hyperfine states.

        input arguments:

        Nmax: maximum rotational quantum number to calculate (int)
        a2: anisotropic polarisability (float)
        Beta: polarisation angle of the laser in Radians (float)
        I1,I2: Nuclear spin of nucleus 1,2 (float)

        returns:
        H: Hamiltonian, (2*Nmax+1)*(2*I1_mag+1)*(2*I2_mag+1)x
           (2*Nmax+1)*(2*I1_mag+1)*(2*I2_mag+1) array.
     '''
    I1shape = int(2*I1+1)
    I2shape = int(2*I2+1)
    shape = numpy.sum(numpy.array([2*x+1 for x in range(0,Nmax+1)]))
    HAC = numpy.zeros((shape,shape),dtype= numpy.complex)
```

```
    i=0
    j=0
    for N1 in range(0,Nmax+1):
        for M1 in range(N1,-(N1+1),-1):
            for N2 in range(0,Nmax+1):
                for M2 in range(N2,-(N2+1),-1):
                    M = M2-M1
                    HAC[i,j]= -a2*(Rotation.d(2,M,0,Beta).doit()*(-1)**M2*\
                              numpy.sqrt((2*N1+1)*(2*N2+1))*\
                              wigner_3j(N2,2,N1,0,0,0)*\
                              wigner_3j(N2,2,N1,-M2,M,M1))
                    j+=1
            j=0
            i+=1
    #final check for NaN errors, mostly this is due to division by zero or
    # multiplication by a small prefactor. it is safe to set these terms
        ↪ to 0
    HAC[numpy.isnan(HAC)] =0

    #return the matrix, in the full uncoupled basis.
    return (numpy.kron(HAC,numpy.kron(numpy.identity(I1shape),
            numpy.identity(I2shape))))

#Now some functions to take these functions and assemble them into the
    ↪ physical
#Hamiltonians where necessary.


def Hyperfine_Ham(Nmax,I1_mag,I2_mag,Consts):
    '''
        The field-free Hyperfine hamiltonian

        Input arguments:
        Nmax: Maximum rotational level to include (float)
        I1_mag,I2_mag, magnitude of the nuclear spins (float)
        Consts: Dict of molecular constants (Dict of floats)

        returns:
        H: Hamiltonian, (2*Nmax+1)*(2*I1_mag+1)*(2*I2_mag+1)x
           (2*Nmax+1)*(2*I1_mag+1)*(2*I2_mag+1) array.
    '''
```

```
    N,I1,I2 = Generate_vecs(Nmax,I1_mag,I2_mag)
    H = Rotational(N,Consts['Brot'],Consts['Drot'])+\
    scalar_nuclear(Consts['CRb'],N,I1)+scalar_nuclear(Consts['CCs'],N,I2)
        ↪ +\
    scalar_nuclear(Consts['C4'],I1,I2)+tensor_nuclear(Consts['C3'],I1,I2,N
        ↪ )+\
    Quadrupole((Consts['QRb'],Consts['QCs']),I1,I2,N)
    return H

def Zeeman_Ham(Nmax,I1_mag,I2_mag,Consts):
    '''
        assembles the Zeeman term and generates operator vectors

        Input arguments:
        Nmax: Maximum rotational level to include (float)
        I1_mag,I2_mag, magnitude of the nuclear spins (float)
        Consts: Dict of molecular constants (Dict of floats)

        returns:
        H: Hamiltonian, (2*Nmax+1)*(2*I1_mag+1)*(2*I2_mag+1)x
           (2*Nmax+1)*(2*I1_mag+1)*(2*I2_mag+1) array.
    '''
    N,I1,I2 = Generate_vecs(Nmax,I1_mag,I2_mag)
    H = Zeeman(Consts['MuRb'],I1)+Zeeman(Consts['MuCs'],I2)+\
              Zeeman(Consts['MuN'],N)
    return H

# This is the main build function and one that the user will actually have
    ↪  to
# use.

def Build_Hamiltonians(Nmax,I1,I2,Constants,zeeman=False,EDC=False,AC=
    ↪ False):
    '''
        This function builds the hamiltonian matrices for evalutation so
            ↪ that
        the user doesn't have to rebuild them every time and we can benefit
            ↪  from
        numpy's ability to do distributed multiplcation.
```

```
        Input arguments:
        Nmax: Maximum rotational level to include (float)
        I1_mag,I2_mag, magnitude of the nuclear spins (float)
        Constants: Dict of molecular constants (Dict of floats)
        zeeman,EDC,AC :Switches for turning off parts of the total
            ↪ Hamiltonian
                    can save significant time on calculations where DC
                        ↪ and
                    AC fields are not required due to nested for loops
                    (bool)

        returns:
        H0,Hz,HDC,HAC: Each is a (2*Nmax+1)*(2*I1_mag+1)*(2*I2_mag+1)x
           (2*Nmax+1)*(2*I1_mag+1)*(2*I2_mag+1) array.
    '''
    H0 = Hyperfine_Ham(Nmax,I1,I2,Constants)
    if zeeman:
        Hz = Zeeman_Ham(Nmax,I1,I2,Constants)
    else:
        Hz =0.
    if EDC:
        HDC = DC(Nmax,Constants['d0'],I1,I2)
    else:
        HDC =0.
    if AC:
        HAC = (1./(2*eps0*c))*(AC_iso(Nmax,Constants['a0'],I1,I2)+\
        AC_aniso(Nmax,Constants['a2'],Constants['Beta'],I1,I2))
    else:
        HAC =0.
    return H0,Hz,HDC,HAC

#These are the functions that the user will use to generate any
    ↪ interesting maps
#obviously these can be added to by writing custom scripts but these
    ↪ should
# cover most needs

def Vary_magnetic(Hams,fields0,Bz,return_states = False):

    '''
```

```
    find Eigenvalues (and optionally Eigenstates) of the total
        ↪ Hamiltonian

    input arguments:
    Hams: list or tuple of hamiltonians. Should all be the same size
    fields0: initial field conditions, allows for zeeman + Stark
        ↪ effects
    Bz: magnetic field to be iterated over
    return_states: Switch to return EigenStates as well as
        ↪ Eigenenergies

    returns:
    energy:array of Eigenenergies, sorted from smallest to largest
        ↪ along
           the 0 axis
    states:array of Eigenstates, sorted as in energy.
'''

H0,Hz,HDC,HAC = Hams
E,B,I = fields0

#warn the user if they've done something silly, so they don't waste
    ↪ time
if type(Hz) != numpy.ndarray:
    warnings.warn("Hamiltonian␣is␣zero:␣nothing␣will␣change!")
else:
    EigenValues = numpy.zeros((H0.shape[0],len(Bz)))
    if return_states:
        States = numpy.zeros((H0.shape[0],H0.shape[0],len(Bz)))
    for i,b in enumerate(Bz):
        with warnings.catch_warnings():
            warnings.filterwarnings("ignore",category=numpy.
                ↪ ComplexWarning)
            H = H0+E*HDC+I*HAC+b*Hz
            if return_states:
                Eigen = eig(H)
                order = numpy.argsort(Eigen[0])
                EigenValues[:,i]=Eigen[0][order]
                States[:,:,i] = Eigen[1][:,order]
            else:
                Eigen = eigvals(H)
```

```
                EigenValues[:,i]=numpy.sort(Eigen)
        if return_states:
            return EigenValues,States
        else:
            return EigenValues

def Vary_ElectricDC(Hams,fields0,Ez,return_states = False):

    '''
        find Eigenvalues (and optionally Eigenstates) of the total
            ↪ Hamiltonian

        input arguments:
        Hams: list or tuple of hamiltonians. Should all be the same size
        fields0: initial field conditions, allows for zeeman + Stark
            ↪ effects
        Ez: Electric field to be iterated over
        return_states: Switch to return EigenStates as well as
            ↪ Eigenenergies

        returns:
        energy:array of Eigenenergies, sorted from smallest to largest
            ↪ along
               the 0 axis
        states:array of Eigenstates, sorted as in energy.
    '''
    E,B,I = fields0
    H0,Hz,HDC,HAC = Hams
    EigenValues = numpy.zeros((H0.shape[0],len(Ez)))

    #warn the user if they've done something silly, so they don't waste
        ↪ time

    if type(HDC) != numpy.ndarray:
        warnings.warn("Hamiltonian␣is␣zero:␣nothing␣will␣change!")

    else:
        if return_states:
            States = numpy.zeros((H0.shape[0],H0.shape[0],len(Ez)))
        for i,e in enumerate(Ez):
            with warnings.catch_warnings():
```

```
                warnings.filterwarnings("ignore",category=numpy.
                    ↪ ComplexWarning)
                H = H0+e*HDC+I*HAC+B*Hz
                if return_states:
                    Eigen = eig(H)
                    order = numpy.argsort(Eigen[0])
                    EigenValues[:,i]=Eigen[0][order]
                    States[:,:,i] = Eigen[1][:,order]
                else:
                    Eigen = eigvals(H)
                    EigenValues[:,i]=numpy.sort(Eigen)
        if return_states:
            return EigenValues,States
        else:
            return EigenValues

def Vary_Intensity(Hams,fields0,I_app,return_states = False):
    '''
        find Eigenvalues (and optionally Eigenstates) of the total
            ↪ Hamiltonian

        input arguments:
        Hams: list or tuple of hamiltonians. Should all be the same size
        fields0: initial field conditions, allows for zeeman + Stark
            ↪ effects
        I_app: Laser
        return_states: Switch to return EigenStates as well as
            ↪ Eigenenergies

        returns:
        energy:array of Eigenenergies, sorted from smallest to largest
            ↪ along
               the 0 axis
        states:array of Eigenstates, sorted as in energy.
    '''

    H0,Hz,HDC,HAC = Hams
    E,B,I = fields0

    #warn the user if they've done something silly, so they don't waste
        ↪ time
```

```
    if type(HAC) != numpy.ndarray:
        warnings.warn("Hamiltonian is zero: nothing will change")
    else:
        EigenValues = numpy.zeros((H0.shape[0],len(I_app)))
        if return_states:
            States = numpy.zeros((H0.shape[0],H0.shape[0],len(I_app)))
        else:
            for i,Int in enumerate(I_app):
                with warnings.catch_warnings():
                    warnings.filterwarnings("ignore",
                                            category=numpy.ComplexWarning)
                    H = H0+E*HDC+Int*HAC+B*Hz
                    if return_states:
                        Eigen = eig(H)
                        order = numpy.argsort(Eigen[0])
                        EigenValues[:,i]=Eigen[0][order]
                        States[:,:,i] = Eigen[1][:,order]
                    else:
                        Eigen = eigvals(H)
                        EigenValues[:,i]=numpy.sort(Eigen)
            if return_states:
                return EigenValues,States
            else:
                return EigenValues

def Vary_Beta(Hams,fields0,Angles,Molecule_pars,return_states = False):
    '''
        find Eigenvalues (and optionally Eigenstates) of the total
            ↪ Hamiltonian
        This function works differently to the applied field ones. Because
            ↪ beta
        changes the matrix elements in the Hamiltonian we cannot simply
        multiply it through. Therefore we have to recalculate the matrix
        elements on each interation. This makes the function slower.

        input arguments:
        Hams: list or tuple of hamiltonians. Should all be the same size
        fields0: initial field conditions, allows for zeeman + Stark
            ↪ effects
        Angles: Polarisation angles to iterate over
```

```
    Molecule_pars: Nmax,I1,I2,a2, arguments to feed to regenerate the
                   anisotropic Stark shift matrix.

    return_states: Switch to return EigenStates as well as
        ↪ Eigenenergies

    returns:
    energy:array of Eigenenergies, sorted from smallest to largest
        ↪ along
          the 0 axis
    states:array of Eigenstates, sorted as in energy.
'''

Nmax,I1,I2,a2 = Molecule_pars
H0,Hz,HDC,HAC = Hams
E,B,I = fields0

#warn the user if they've done something silly, so they don't waste
    ↪ time

if I == 0:
    warnings.warn("Intensity␣is␣zero:␣nothing␣will␣change")
else:
    EigenValues = numpy.zeros((H0.shape[0],len(Angles)))
    if return_states:
        States = numpy.zeros((H0.shape[0],H0.shape[0],len(Angles)))
    for i,beta in enumerate(Angles):
        HAC = AC_aniso(Nmax,a2,beta,I1,I2)/(2*eps0*c)
        with warnings.catch_warnings():
            warnings.filterwarnings("ignore",category=numpy.
                ↪ ComplexWarning)
            H = H0+E*HDC+I*HAC+B*Hz
            if return_states:
                Eigen = eig(H)
                order = numpy.argsort(Eigen[0])
                EigenValues[:,i]=Eigen[0][order]
                States[:,:,i] = Eigen[1][:,order]
            else:
                Eigen = eigvals(H)
                EigenValues[:,i]=numpy.sort(Eigen)
```

```
if return_states:
    return EigenValues,States
else:
    return EigenValues
```

Bibliography

[1] P. D. Gregory, J. A. Blackmore, J. Aldegunde, J. M. Hutson, and S. L. Cornish, Physical Review A **96**, 021402(R) (2017).

[2] J. A. Blackmore, L. Caldwell, P. D. Gregory, E. M. Bridge, R. Sawant, J. Aldegunde, J. Mur-Petit, D. Jaksch, J. M. Hutson, B. E. Sauer, M. R. Tarbutt, and S. L. Cornish, Quantum Science and Technology **4**, 014010 (2018).

[3] P. D. Gregory, M. D. Frye, J. A. Blackmore, E. M. Bridge, R. Sawant, J. M. Hutson, and S. L. Cornish, Nature Communications **10**, 3104 (2019).

[4] R. Sawant, J. A. Blackmore, P. D. Gregory, J. Mur-Petit, D. Jaksch, J. Aldegunde, J. M. Hutson, M. R. Tarbutt, and S. L. Cornish, New Journal of Physics **22**, 013027 (2020).

[5] P. D. Gregory, J. A. Blackmore, S. L. Bromley, and S. L. Cornish, Physical Review Letters **124**, 163402 (2020).

[6] J. A. Blackmore, R. Sawant, P. D. Gregory, S. L. Bromley, J. Aldegunde, J. M. Hutson, and S. L. Cornish, arXiv e-prints , arXiv:2007.01762 (2020), arXiv:2007.01762 [physics.atom-ph] .

[7] J. A. Blackmore, P. D. Gregory, S. L. Bromley, and S. L. Cornish, arXiv e-prints , arXiv:2009.01944 (2020), arXiv:2009.01944 [cond-mat.quant-gas] .

[8] A. Gaëtan, Y. Miroshnychenko, T. Wilk, A. Chotia, M. Viteau, D. Comparat, P. Pillet, A. Browaeys, and P. Grangier, Nature Physics **5**, 115 (2009).

[9] E. Urban, T. A. Johnson, T. Henage, L. Isenhower, D. D. Yavuz, T. G. Walker, and M. Saffman, Nature Physics **5**, 110 (2009).

[10] K. Aikawa, A. Frisch, M. Mark, S. Baier, A. Rietzler, R. Grimm, and F. Ferlaino, Physical Review Letters **108**, 210401 (2012).

[11] M. Lu, N. Q. Burdick, S. H. Youn, and B. L. Lev, Physical Review Letters **107**, 190401 (2011).

[12] A. Griesmaier, J. Werner, S. Hensler, J. Stuhler, and T. Pfau, Physical Review Letters **94**, 160401 (2005).

[13] M. D. Di Rosa, The European Physical Journal D - Atomic, Molecular, Optical and Plasma Physics **31**, 395 (2004).

[14] J. F. Barry, D. J. McCarron, E. B. Norrgard, M. H. Steinecker, and D. DeMille, Nature **512**, 286 (2014).

[15] S. Truppe, H. J. Williams, M. Hambach, L. Caldwell, N. J. Fitch, E. A. Hinds, B. E. Sauer, and M. R. Tarbutt, Nature Physics **13**, 1173 (2017).

[16] L. Anderegg, B. L. Augenbraun, E. Chae, B. Hemmerling, N. R. Hutzler, A. Ravi, A. Collopy, J. Ye, W. Ketterle, and J. M. Doyle, Physical Review Letters **119**, 103201 (2017).

[17] A. L. Collopy, S. Ding, Y. Wu, I. A. Finneran, L. Anderegg, B. L. Augenbraun, J. M. Doyle, and J. Ye, Physical Review Letters **121**, 213201 (2018).

[18] I. Kozyryev, L. Baum, K. Matsuda, B. L. Augenbraun, L. Anderegg, A. P. Sedlack, and J. M. Doyle, Physical Review Letters **118**, 173201 (2017).

[19] J. Lim, J. R. Almond, M. A. Trigatzis, J. A. Devlin, N. J. Fitch, B. E. Sauer, M. R. Tarbutt, and E. A. Hinds, Physical Review Letters **120**, 123201 (2018).

[20] B. L. Augenbraun, Z. D. Lasner, A. Frenett, H. Sawaoka, C. Miller, T. C. Steimle, and J. M. Doyle, New Journal of Physics **22**, 022003 (2020).

[21] L. Baum, N. B. Vilas, C. Hallas, B. L. Augenbraun, S. Raval, D. Mitra, and J. M. Doyle, Physical Review Letters **124**, 133201 (2020).

[22] D. Mitra, N. B. Vilas, C. Hallas, L. Anderegg, B. L. Augenbraun, L. Baum, C. Miller, S. Raval, and J. M. Doyle, ArXiv 2004.02848 (2020), pre-print.

[23] R. L. McNally, I. Kozyryev, S. Vazquez-Carson, K. Wenz, T. Wang, and T. Zelevinsky, ArXiv 2004.09570 (2020), pre-print.

[24] A. Guttridge, S. A. Hopkins, M. D. Frye, J. J. McFerran, J. M. Hutson, and S. L. Cornish, Physical Review A **97**, 063414 (2018).

[25] A. Guttridge, M. D. Frye, B. C. Yang, J. M. Hutson, and S. L. Cornish, Physical Review A **98**, 022707 (2018).

[26] S. Schiller, D. Bakalov, and V. Korobov, Physical Review Letters **113**, 023004 (2014).

[27] M. Borkowski, Physical Review Letters **120**, 083202 (2018).

[28] J. Deiglmayr, A. Grochola, M. Repp, K. Mörtlbauer, C. Glück, J. Lange, O. Dulieu, R. Wester, and M. Weidemüller, Physical Review Letters **101**, 133004 (2008).

[29] P. Zabawa, A. Wakim, M. Haruza, and N. P. Bigelow, Physical Review A **84**, 061401 (2011).

[30] J. Banerjee, D. Rahmlow, R. Carollo, M. Bellos, E. E. Eyler, P. L. Gould, and W. C. Stwalley, Physical Review A **86**, 053428 (2012).

[31] C. D. Bruzewicz, M. Gustavsson, T. Shimasaki, and D. DeMille, New Journal of Physics **16**, 023018 (2014).

[32] Z. Li, T. Gong, Z. Ji, Y. Zhao, L. Xiao, and S. Jia, Physical Chemistry Chemical Physics **20**, 4893 (2018).

[33] C. Gabbanini and O. Dulieu, Physical Chemistry Chemical Physics **13**, 18905 (2011).

[34] M. McDonald, I. Majewska, C.-H. Lee, S. S. Kondov, B. H. McGuyer, R. Moszynski, and T. Zelevinsky, Physical Review Letters **120**, 033201 (2018).

[35] Z. Ji, T. Gong, Y. He, J. M. Hutson, Y. Zhao, L. Xiao, and S. Jia, ArXiv 2002.06390 (2020), pre-print.

[36] T. Köhler, K. Góral, and P. S. Julienne, Reviews of Modern Physics **78**, 1311 (2006).

[37] C. Chin, R. Grimm, P. Julienne, and E. Tiesinga, Reviews of Modern Physics **82**, 1225 (2010).

[38] K.-K. Ni, S. Ospelkaus, M. H. G. de Miranda, A. Pe'er, B. Neyenhuis, J. J. Zirbel, S. Kotochigova, P. S. Julienne, D. S. Jin, and J. Ye, Science **322**, 231 (2008).

[39] J. G. Danzl, E. Haller, M. Gustavsson, M. J. Mark, R. Hart, N. Bouloufa, O. Dulieu, H. Ritsch, and H.-C. Nägerl, Science **321**, 1062 (2008).

[40] F. Lang, K. Winkler, C. Strauss, R. Grimm, and J. Hecker Denschlag, Physical Review Letters **101**, 133005 (2008).

[41] T. Takekoshi, L. Reichsöllner, A. Schindewolf, J. M. Hutson, C. R. Le Sueur, O. Dulieu, F. Ferlaino, R. Grimm, and H.-C. Nägerl, Physical Review Letters **113**, 205301 (2014).

[42] P. K. Molony, P. D. Gregory, Z. Ji, B. Lu, M. P. Köppinger, C. R. Le Sueur, C. L. Blackley, J. M. Hutson, and S. L. Cornish, Physical Review Letters **113**, 255301 (2014).

[43] J. W. Park, S. A. Will, and M. W. Zwierlein, Physical Review Letters **114**, 205302 (2015).

[44] M. Guo, B. Zhu, B. Lu, X. Ye, F. Wang, R. Vexiau, N. Bouloufa-Maafa, G. Quéméner, O. Dulieu, and D. Wang, Physical Review Letters **116**, 205303 (2016).

[45] T. M. Rvachov, H. Son, A. T. Sommer, S. Ebadi, J. J. Park, M. W. Zwierlein, W. Ketterle, and A. O. Jamison, Physical Review Letters **119**, 143001 (2017).

[46] J. T. Zhang, Y. Yu, W. B. Cairncross, K. Wang, L. R. B. Picard, J. D. Hood, Y.-W. Lin, J. M. Hutson, and K.-K. Ni, ArXiv 2003.07850 (2020), pre-print.

[47] I. Ferrier-Barbut, H. Kadau, M. Schmitt, M. Wenzel, and T. Pfau, Physical Review Letters **116**, 215301 (2016).

[48] G. Semeghini, G. Ferioli, L. Masi, C. Mazzinghi, L. Wolswijk, F. Minardi, M. Modugno, G. Modugno, M. Inguscio, and M. Fattori, Physical Review Letters **120**, 235301 (2018).

[49] F. Böttcher, J.-N. Schmidt, M. Wenzel, J. Hertkorn, M. Guo, T. Langen, and T. Pfau, Physical Review X **9**, 011051 (2019).

[50] L. Tanzi, E. Lucioni, F. Famà, J. Catani, A. Fioretti, C. Gabbanini, R. N. Bisset, L. Santos, and G. Modugno, Physical Review Letters **122**, 130405 (2019).

[51] L. Chomaz, D. Petter, P. Ilzhöfer, G. Natale, A. Trautmann, C. Politi, G. Durastante, R. M. W. van Bijnen, A. Patscheider, M. Sohmen, M. J. Mark, and F. Ferlaino, Physical Review X **9**, 021012 (2019).

[52] A. L. Marchant, T. P. Billam, T. P. Wiles, M. M. H. Yu, S. A. Gardiner, and S. L. Cornish, Nature Communications **4**, 1865 (2013).

[53] C. A. Regal, M. Greiner, and D. S. Jin, Physical Review Letters **92**, 10.1103/physrevlett.92.040403 (2004).

[54] M. W. Zwierlein, C. A. Stan, C. H. Schunck, S. M. F. Raupach, A. J. Kerman, and W. Ketterle, Physical Review Letters **92**, 10.1103/physrevlett.92.120403 (2004).

[55] T. Bothwell, D. Kedar, E. Oelker, J. M. Robinson, S. L. Bromley, W. L. Tew, J. Ye, and C. J. Kennedy, Metrologia **56**, 065004 (2019).

[56] N. Poli, F.-Y. Wang, M. G. Tarallo, A. Alberti, M. Prevedelli, and G. M. Tino, Physical Review Letters **106**, 038501 (2011).

[57] Y. Eto, M. Sadrove, and T. Hirano, in *Principles and Methods of Quantum Information Technologies* (Springer Japan, 2016) pp. 111–133.

[58] J. Simon, W. S. Bakr, R. Ma, M. E. Tai, P. M. Preiss, and M. Greiner, Nature **472**, 307 (2011).

[59] S. de Léséleuc, V. Lienhard, P. Scholl, D. Barredo, S. Weber, N. Lang, H. P. Büchler, T. Lahaye, and A. Browaeys, Science **365**, 775 (2019).

[60] E. Brion, D. Comparat, and G. Harel, The European Physical Journal D **38**, 381 (2006).

[61] S. Truppe, R. J. Hendricks, S. K. Tokunaga, H. J. Lewandowski, M. G. Kozlov, C. Kenkel, E. A. Hinds, and M. R. Tarbutt, Nature Communications **4**, 2600 (2013).

[62] J. Kobayashi, A. Ogino, and S. Inouye, Nature Communications **10**, 3771 (2019).

[63] J. J. Hudson, D. M. Kara, I. J. Smallman, B. E. Sauer, M. R. Tarbutt, and E. A. Hinds, Nature **473**, 493 (2011).

[64] The ACME Collaboration, Nature **562**, 355 (2018).

[65] P. Aggarwal, , H. L. Bethlem, A. Borschevsky, M. Denis, K. Esajas, P. A. B. Haase, Y. Hao, S. Hoekstra, K. Jungmann, T. B. Meijknecht, M. C. Mooij, R. G. E. Timmermans, W. Ubachs, L. Willmann, and A. Zapara, The European Physical Journal D **72**, 197 (2018).

[66] F. Arute, K. Arya, R. Babbush, *et al.*, Nature **574**, 505 (2019).

[67] S. K. Moore, IBM edges closer to quantum supremacy with 50-qubit processor, IEEE Spectrum (2017).

[68] J. Hsu, CES 2018: Intel's 49-qubit chip shoots for quantum supremacy, IEEE Spectrum (2018).

[69] D. Leibfried, R. Blatt, C. Monroe, and D. Wineland, Reviews of Modern Physics **75**, 281 (2003).

[70] D. DeMille, Physical Review Letters **88**, 067901 (2002).

[71] K.-K. Ni, T. Rosenband, and D. D. Grimes, Chemical Science **9**, 6830 (2018).

[72] M. Hughes, M. D. Frye, R. Sawant, G. Bhole, J. A. Jones, S. L. Cornish, M. R. Tarbutt, J. M. Hutson, D. Jaksch, and J. Mur-Petit, Physical Review A **101**, 062308 (2020).

[73] M. J. Bremner, C. M. Dawson, J. L. Dodd, A. Gilchrist, A. W. Harrow, D. Mortimer, M. A. Nielsen, and T. J. Osborne, Physical Review Letters **89**, 247902 (2002).

[74] D. P. DiVincenzo, Fortschritte der Physik **48**, 771 (2000).

[75] C. Palacios-Berraquero, L. Mueck, and D. M. Persaud, Nature **576**, 213 (2019).

[76] L. Pollet, J. D. Picon, H. P. Büchler, and M. Troyer, Physical Review Letters **104**, 125302 (2010).

[77] B. Capogrosso-Sansone, C. Trefzger, M. Lewenstein, P. Zoller, and G. Pupillo, Physical Review Letters **104**, 125301 (2010).

[78] R. Barnett, D. Petrov, M. Lukin, and E. Demler, Physical Review Letters **96**, 190401 (2006).

[79] A. V. Gorshkov, S. R. Manmana, G. Chen, J. Ye, E. Demler, M. D. Lukin, and A. M. Rey, Physical Review Letters **107**, 115301 (2011).

[80] A. V. Gorshkov, S. R. Manmana, G. Chen, E. Demler, M. D. Lukin, and A. M. Rey, Physical Review A **84**, 033619 (2011).

[81] M. L. Wall, K. R. A. Hazzard, and A. M. Rey, in *From Atoms to Mesoscale*, edited by S. A. Malinovskaya and I. Novikova (WORLD SCIENTIFIC, 2015) Chap. 1, pp. 3–37.

[82] M. L. Harris, *Realisation of a cold mixture of rubidium and caesium*, Ph.D. thesis, Durham University (2008).

[83] P. Tierney, *Magnetic Trapping of an Ultracold ^{87}Rb - ^{133}Cs Atomic Mixture*, Ph.D. thesis, Durham University (2009).

[84] D. J. Mccarron, *A Quantum Degnerate Mixture of ^{87}Rb and ^{133}Cs*, Ph.D. thesis, Durham University (2011).

[85] D. L. Jenkin, *Feshbach spectroscopy of an ultracold Rb-Cs mixture*, Ph.D. thesis, Durham University (2012).

[86] M. P. Köppinger, *Creation of ultracold RbCs molecules*, Ph.D. thesis, Durham University (2014).

[87] P. K. Molony, *Creation of ultracold polar ground-state RbCs molecules*, Ph.D. thesis, Durham University (2016).

[88] P. D. Gregory, *Coherent Control of Ultracold Polar Molecules*, Ph.D. thesis, Durham University (2018).

[89] D. J. McCarron, H. W. Cho, D. L. Jenkin, M. P. Köppinger, and S. L. Cornish, Physical Review A **84**, 011603 (2011).

[90] M. P. Köppinger, D. J. McCarron, D. L. Jenkin, P. K. Molony, H. W. Cho, S. L. Cornish, C. R. Le Sueur, C. L. Blackley, and J. M. Hutson, Physical Review A **89**, 033604 (2014).

[91] H. Fahs, A. R. Allouche, M. Korek, and M. Aubert-Frécon, Journal of Physics B: Atomic, Molecular and Optical Physics **35**, 1501 (2002).

[92] P. K. Molony, A. Kumar, P. D. Gregory, R. Kliese, T. Puppe, C. R. Le Sueur, J. Aldegunde, J. M. Hutson, and S. L. Cornish, Physical Review A **94**, 022507 (2016).

[93] P. D. Gregory, P. K. Molony, M. P. Köppinger, A. Kumar, Z. Ji, B. Lu, A. L. Marchant, and S. L. Cornish, New Journal of Physics **17**, 055006 (2015).

[94] P. K. Molony, P. D. Gregory, A. Kumar, C. R. Le Sueur, J. M. Hutson, and S. L. Cornish, ChemPhysChem. **17**, 3811 (2016).

[95] D. A. Steck, Rubidium 87 D line data, Online (2019), available online.

[96] C. S. Adams and I. G. Hughes, *Optics f2f: from Fourier to Fresnel* (OUP Oxford, 2018).

[97] C. A. Balanis, *Antenna Theory: Analysis and Design, 3rd Edition* (Wiley-Interscience, 2005).

[98] J. M. Brown and A. Carrington, *Rotational Spectroscopy of Diatomic Molecules (Cambridge Molecular Science)* (Cambridge University Press, 2010).

[99] K.-K. Ni, *A Quantum Gas of Polar Molecules*, Ph.D. thesis, University of Colorado (2009).

[100] T. M. Dunn, K. N. Rao, and C. W. Mathews, *Molecular spectroscopy: modern research*, edited by K. N. Rao and C. W. Mathews (Academic Press, New York, 1985) Chap. 4, pp. 231 –259.

[101] C. Fellows, R. Gutterres, A. Campos, J. Vergès, and C. Amiot, Journal of Molecular Spectroscopy **197**, 19 (1999).

[102] H. J. Williams, *Producing, trapping and controlling ultracold CaF molecules*, Ph.D. thesis, Imperial College London (2018).

[103] R. J. Hendricks, D. A. Holland, S. Truppe, B. E. Sauer, and M. R. Tarbutt, Frontiers in Physics **2**, 51 (2014).

[104] B. H. Bransden and C. J. Joachain, *Physics of Atoms and Molecules* (Prentice Hall, 2003).

[105] G. Herzberg, *Spectra of Diatomic Molecules*, 2nd ed., Molecular Spectra and Molecular Structure, Vol. 1 (D. Van Nostrand Company, Princeton, New Jersey, USA, 1950).

[106] Q. Wei, S. Kais, B. Friedrich, and D. Herschbach, Journal of Chemical Physics **134**, 124107 (2011).

[107] R. N. Zare, *Angular Momentum* (John Wiley & Sons, 1988).

[108] E. W. Weisstein, From MathWorld–A Wolfram Web Resource. (2004).

[109] S. V. Syzranov, M. L. Wall, V. Gurarie, and A. M. Rey, Nature Communications **5**, 5391 (2014).

[110] D. J. Griffiths, *Introduction to Electrodynamics* (Cambridge University Pr., 2017).

[111] J. Aldegunde, B. A. Rivington, P. S. Żuchowski, and J. M. Hutson, Physical Review A **78**, 033434 (2008).

[112] J. Aldegunde and J. M. Hutson, Physical Review A **96**, 042506 (2017).

[113] J. Bardeen and C. H. Townes, Physical Review **73**, 97 (1948).

[114] B. P. Fabricand, R. O. Carlson, C. A. Lee, and I. I. Rabi, Physical Review **91**, 1403 (1953).

[115] T. A. Dixon, C. H. Joyner, F. A. Baiocchi, and W. Klemperer, The Journal of Chemical Physics **74**, 6539 (1981).

[116] P. D. Gregory, J. Aldegunde, J. M. Hutson, and S. L. Cornish, Physical Review A **94**, 041403 (2016).

[117] B. H. Bransden and C. J. Joachain, *Quantum Mechanics* (Pearson Education Limited, Harlow, England, 2000).

[118] D. A. Steck, *Quantum Optics* (available online at http://steck.us/teaching (revision 0.12.6, 23 April 2019), 2019).

[119] N. F. Ramsey, Physical Review **78**, 695 (1950).

[120] D. M. Kara, I. J. Smallman, J. J. Hudson, B. E. Sauer, M. R. Tarbutt, and E. A. Hinds, New Journal of Physics **14**, 103051 (2012).

[121] T. P. Heavner, E. A. Donley, F. Levi, G. Costanzo, T. E. Parker, J. H. Shirley, N. Ashby, S. Barlow, and S. R. Jefferts, Metrologia **51**, 174 (2014).

[122] G. E. Marti, R. B. Hutson, A. Goban, S. L. Campbell, N. Poli, and J. Ye, Physical review letters **120**, 103201 (2018).

[123] I. G. Hughes and T. P. A. Hase, *Measurements and their Uncertainties* (Oxford University Press, 2010).

[124] A. Micheli, G. K. Brennen, and P. Zoller, Nature Physics **2**, 341 (2006).

[125] S. Brouard and J. Plata, Physical Review A **68**, 012311 (2003).

[126] B. Neyenhuis, B. Yan, S. A. Moses, J. P. Covey, A. Chotia, A. Petrov, S. Kotochigova, J. Ye, and D. S. Jin, Physical Review Letters **109**, 230403 (2012).

[127] L. D. Carr, D. DeMille, R. V. Krems, and J. Ye, New Journal of Physics **11**, 055049 (2009).

[128] B. Sundar, B. Gadway, and K. R. A. Hazzard, Scientific Reports **8**, 3422 (2018).

[129] B. Sundar, M. Thibodeau, Z. Wang, B. Gadway, and K. R. A. Hazzard, Physical Review A **99**, 013624 (2019).

[130] J. W. Park, Z. Z. Yan, H. Loh, S. A. Will, and M. W. Zwierlein, Science **357**, 372 (2017).

[131] S. A. Will, J. W. Park, Z. Z. Yan, H. Loh, and M. W. Zwierlein, Physical Review Letters **116**, 225306 (2016).

[132] J. W. Park, *An Ultracold Gas of Dipolar Fermionic $^{23}Na^{40}K$ Molecules*, Ph.D. thesis, Massachusetts Institute of Technology (2016).

[133] W. P. Su, J. R. Schrieffer, and A. J. Heeger, Physical Review Letters **42**, 1698 (1979).

[134] D. Xie, W. Gou, T. Xiao, B. Gadway, and B. Yan, npj Quantum Information **5**, 55 (2019).

[135] N. Batra and G. Sheet, ArXiv 1906.08435 (2019), pre-print.

[136] H. P. Büchler, E. Demler, M. Lukin, A. Micheli, N. Prokof'ev, G. Pupillo, and P. Zoller, Physical Review Letters **98**, 060404 (2007).

[137] A. Micheli, G. Pupillo, H. P. Büchler, and P. Zoller, Physical Review A **76**, 043604 (2007).

[138] A. Macià, D. Hufnagl, F. Mazzanti, J. Boronat, and R. E. Zillich, Physical Review Letters **109**, 235307 (2012).

[139] W. Lechner and P. Zoller, Physical Review Letters **111**, 185306 (2013).

[140] A. V. Gorshkov, K. R. A. Hazzard, and A. M. Rey, Molecular Physics **111**, 1908 (2013).

[141] Y. L. Zhou, M. Ortner, and P. Rabl, Physical Review A **84**, 052332 (2011).

[142] S. R. Manmana, E. M. Stoudenmire, K. R. A. Hazzard, A. M. Rey, and A. V. Gorshkov, Physical Review B **87**, 081106 (2013).

[143] K. R. A. Hazzard, S. R. Manmana, M. Foss-Feig, and A. M. Rey, Physical Review Letters **110**, 075301 (2013).

[144] M. Greiner, O. Mandel, T. Esslinger, T. W. Hänsch, and I. Bloch, Nature **415**, 39 (2002).

[145] S. A. Moses, J. P. Covey, M. T. Miecnikowski, B. Yan, B. Gadway, J. Ye, and D. S. Jin, Science **350**, 659 (2015).

[146] L. Reichsöllner, A. Schindewolf, T. Takekoshi, R. Grimm, and H.-C. Nägerl, Physical Review Letters **118**, 073201 (2017).

[147] J. G. Danzl, M. J. Mark, E. Haller, M. Gustavsson, R. Hart, J. Aldegunde, J. M. Hutson, and H.-C. Nägerl, Nature Physics **6**, 265 (2010).

[148] R. Vexiau, D. Borsalino, M. Lepers, A. Orbán, M. Aymar, O. Dulieu, and N. Bouloufa-Maafa, International Reviews in Physical Chemistry **36**, 709 (2017).

[149] M. Safronova, B. Arora, and C. Clark, Physical Review A **73**, 022505 (2006).

[150] O. Docenko, M. Tamanis, R. Ferber, T. Bergeman, S. Kotochigova, A. V. Stolyarov, A. de Faria Nogueira, and C. E. Fellows, Physical Review A **81**, 042511 (2010).

[151] A. Christianen, M. W. Zwierlein, G. C. Groenenboom, and T. Karman, Physical Review Letters **123**, 123402 (2019).

[152] A. R. Allouche, M. Korek, K. Fakherddin, A. Chaalan, M. Dagher, F. Taher, and M. Aubert-Frécon, Journal of Physics B: Atomic, Molecular and Optical Physics **33**, 2307 (2000).

[153] R. Grimm, M. Weidemüller, and Y. B. Ovchinnikov, in *Advances In Atomic, Molecular, and Optical Physics* (Elsevier, 2000) pp. 95–170.

[154] F. Seeßelberg, X.-Y. Luo, M. Li, R. Bause, S. Kotochigova, I. Bloch, and C. Gohle, Physical Review Letters **121**, 253401 (2018).

[155] R. Bause, M. Li, A. Schindewolf, X.-Y. Chen, M. Duda, S. Kotochigova, I. Bloch, and X.-Y. Luo, ArXiv 1912.10452 (2019), pre-print.

[156] J. Weiner, V. S. Bagnato, S. Zilio, and P. S. Julienne, Reviews of Modern Physics **71**, 1 (1999).

[157] E. Tiesinga, B. J. Verhaar, and H. T. C. Stoof, Physical Review A **47**, 4114 (1993).

[158] S. Inouye, M. R. Andrews, J. Stenger, H.-J. Miesner, D. M. Stamper-Kurn, and W. Ketterle, Nature **392**, 151 (1998).

[159] O. J. Wales, A. Rakonjac, T. P. Billam, J. L. Helm, S. A. Gardiner, and S. L. Cornish, Communications Physics **3**, 51 (2020).

[160] S. Ospelkaus, K.-K. Ni, D. Wang, M. H. G. de Miranda, B. Neyenhuis, G. Quéméner, P. S. Julienne, J. L. Bohn, D. S. Jin, and J. Ye, Science **327**, 853 (2010).

[161] K.-K. Ni, S. Ospelkaus, D. Wang, G. Quéméner, B. Neyenhuis, M. H. G. de Miranda, J. L. Bohn, J. Ye, and D. S. Jin, Nature **464**, 1324 (2010).

[162] M.-G. Hu, Y. Liu, D. D. Grimes, Y.-W. Lin, A. H. Gheorghe, R. Vexiau, N. Bouloufa-Maafa, O. Dulieu, T. Rosenband, and K.-K. Ni, Science **366**, 1111 (2019).

[163] X. Ye, M. Guo, Guo, M. L. González-Martínez, G. Quéméner, and D. Wang, Science Advances **4**, eaaq0083 (2018).

[164] M. Duo, X. Ye, J. He, M. L. González-Martínez, R. Vexiau, G. Quéméner, and D. Wang, Physical Review X **8**, 041044 (2018).

[165] H. Yang, D.-C. Zhang, L. Liu, Y.-X. Liu, J. Nan, B. Zhao, and J.-W. Pan, Science **363**, 261 (2019).

[166] J. N. Byrd, H. H. Michels, J. A. Montgomery, R. Côté, and W. C. Stwalley, Journal of Chemical Physics **136**, 014306 (2012).

[167] P. S. Żuchowski and J. M. Hutson, Physical Review A **81**, 060703 (2010).

[168] M. Mayle, B. P. Ruzic, and J. L. Bohn, Physical Review A **85**, 062712 (2012).

[169] M. Mayle, G. Quéméner, B. P. Ruzic, and J. L. Bohn, Physical Review A **87**, 012709 (2013).

[170] A. Christianen, T. Karman, and G. C. Groenenboom, Physical Review A **100**, 032708 (2019).

[171] J. M. Hutson and C. R. L. Sueur, Computer Physics Communications **241**, 1 (2019).

[172] J. M. Hutson and C. R. L. Sueur, Molscat, bound and field, version 2020.0 (2020).

[173] Z. Idziaszek and P. S. Julienne, Physical Review Letters **104**, 113202 (2010).

[174] M. D. Frye, P. S. Julienne, and J. M. Hutson, New Journal of Physics **17**, 045019 (2015).

[175] G. F. Gribakin and V. V. Flambaum, Physical Review A **48**, 546 (1993).

[176] B. Gao, Physical Review A **58**, 1728 (1998).

[177] B. Gao, Physical Review A **78**, 012702 (2008).

[178] M. D. Frye, *Quantum Theory of Complex Ultracold Collisions*, Ph.D. thesis, University of Durham (2017).

[179] P. Żuchowski, M. Kosicki, M. Kodrycka, and P. Soldán, Physical Review A **87**, 022706 (2013).

[180] S. K. Schnelle, E. D. van Ooijen, M. J. Davis, N. R. Heckenberg, and H. Rubinsztein-Dunlop, Optics Express **16**, 1405 (2008).

[181] K. Henderson, C. Ryu, C. MacCormick, and M. G. Boshier, New Journal of Physics **11**, 043030 (2009).

[182] K. O. Roberts, T. McKellar, J. Fekete, A. Rakonjac, A. B. Deb, and N. Kjærgaard, Optics Letters **39**, 2012 (2014).

[183] T. A. Bell, J. A. P. Glidden, L. Humbert, M. W. J. Bromley, S. A. Haine, M. J. Davis, T. W. Neely, M. A. Baker, and H. Rubinsztein Dunlop, New Journal of Physics **18**, 035003 (2016).

[184] Y. Liu, M.-G. Hu, M. A. Nichols, D. D. Grimes, T. Karman, H. Guo, and K.-K. Ni, ArXiv 2002.05140 (2020), pre-print.

[185] M. L. González-Martínez, J. L. Bohn, and G. Quéméner, Phys. Rev. A **96**, 032718 (2017).

[186] T. Karman and J. M. Hutson, Phys. Rev. Lett. **121**, 163401 (2018).

[187] L. Lassablière and G. Quéméner, Phys. Rev. Lett. **121**, 163402 (2018).

[188] H. J. Williams, L. Caldwell, N. J. Fitch, S. Truppe, J. Rodewald, E. A. Hinds, B. E. Sauer, and M. R. Tarbutt, Phys. Rev. Lett. **120**, 163201 (2018).

[189] H. Son, J. J. Park, W. Ketterle, and A. O. Jamison, Nature **580**, 197 (2020).

[190] O. J. Wales, *Splitting and recombination of bright-solitary matter waves*, Ph.D. thesis, Durham University (2019).

[191] S. Kotochigova, New Journal of Physics **12**, 073041 (2010).

[192] L. Anderegg, L. W. Cheuk, Y. Bao, S. Burchesky, W. Ketterle, K.-K. Ni, and J. M. Doyle, Science **365**, 1156 (2019), https://science.sciencemag.org/content/365/6458/1156.full.pdf .

[193] D. Barredo, S. de Léséleuc, V. Lienhard, T. Lahaye, and A. Browaeys, Science **354**, 1021 (2016), https://science.sciencemag.org/content/354/6315/1021.full.pdf .

[194] M. Endres, H. Bernien, A. Keesling, H. Levine, E. R. Anschuetz, A. Krajenbrink, C. Senko, V. Vuletic, M. Greiner, and M. D. Lukin, Science **354**, 1024 (2016), https://science.sciencemag.org/content/354/6315/1024.full.pdf .

[195] J. Shaw, *External Electric Fields: A New Tool for Controlling Ultracold Polar Molecules*, Undergraduate Honors Thesis, University of Colorado Boulder (2001).

[196] S. Rosi, A. Burchianti, S. Conclave, D. S. Naik, G. Roati, C. Fort, and F. Minardi, Scientific Reports **8**, 1301 (2018).

[197] M. Guo, X. Ye, J. He, M. L. González-Martínez, R. Vexiau, G. Quéméner, and D. Wang, Physical Review X **8**, 041044 (2018).

[198] Z. Z. Yan, J. W. Park, Y. Ni, H. Loh, S. Will, T. Karman, and M. Zwierlein, ArXiv 2002.05140 (2020), pre-print.

[199] T. Karman, Physical Review A **101**, 042702 (2020).

[200] M. A. Zentile, J. Keaveney, L. Weller, D. J. Whiting, C. S. Adams, and I. G. Hughes, Computer Physics Communications **189**, 162 (2015).

[201] J. Keaveney, C. S. Adams, and I. G. Hughes, Computer Physics Communications **224**, 311 (2018).

[202] E. Jones, T. Oliphant, P. Peterson, *et al.*, SciPy: Open source scientific tools for Python (2001).

[203] J. Blackmore, Jakeblackmore/diatomic-py: Pre-publication release (2020).